R-87-62

CENTRIFUGAL MODELING OF UNDERGROUND STRUCTURES SUBJECTED TO BLAST LOADING

H. TABATABAI, D. [illegible]HST, M.C. MCVAY, J.J. GILL, F.C. TOWNSEND

UNIVERSITY OF FLORIDA
DEPT OF CIVIL ENGINEERING
GAINESVILLE FL 32611

MARCH 1988

FINAL REPORT

SEPTEMBER 1985-MAY 1987

AFESC

ENGINEERING & SERVICES LABORATORY
AIR FORCE ENGINEERING & SERVICES CENTER
TYNDALL AIR FORCE BASE, FLORIDA 32403

NOTICE

PLEASE DO NOT REQUEST COPIES OF THIS REPORT FROM HQ AFESC/RD (ENGINEERING AND SERVICES LABORATORY). ADDITIONAL COPIES MAY BE PURCHASED FROM:

NATIONAL TECHNICAL INFORMATION SERVICE
5285 PORT ROYAL ROAD
SPRINGFIELD, VIRGINIA 22161

FEDERAL GOVERNMENT AGENCIES AND THEIR CONTRACTORS REGISTERED WITH DEFENSE TECHNICAL INFORMATION CENTER SHOULD DIRECT REQUESTS FOR COPIES OF THIS REPORT TO:

DEFENSE TECHNICAL INFORMATION CENTER
CAMERON STATION
ALEXANDRIA, VIRGINIA 22314

UNCLASSIFIED

SECURITY CLASSIFICATION OF THIS PAGE

REPORT DOCUMENTATION PAGE

Form Approved OMB No. 0704-0188

1a. REPORT SECURITY CLASSIFICATION UNCLASSIFIED	1b. RESTRICTIVE MARKINGS
2a. SECURITY CLASSIFICATION AUTHORITY	3. DISTRIBUTION/AVAILABILITY OF REPORT Approved for public release. Distribution unlimited.
2b. DECLASSIFICATION/DOWNGRADING SCHEDULE	
4. PERFORMING ORGANIZATION REPORT NUMBER(S)	5. MONITORING ORGANIZATION REPORT NUMBER(S) ESL-TR-87-62
6a. NAME OF PERFORMING ORGANIZATION UNIVERSITY OF FLORIDA DEPT OF CIVIL ENGINEERING 6b. OFFICE SYMBOL (If applicable)	7a. NAME OF MONITORING ORGANIZATION
6c. ADDRESS (City, State, and ZIP Code) GAINESVILLE, FL 32611	7b. ADDRESS (City, State, and ZIP Code)
8a. NAME OF FUNDING/SPONSORING ORGANIZATION AIR FORCE ENGINEERING AND SERVICES CENTER 8b. OFFICE SYMBOL (If applicable)	9. PROCUREMENT INSTRUMENT IDENTIFICATION NUMBER Contract #F08635-83-C-0136
8c. ADDRESS (City, State, and ZIP Code) AFESC Tyndall AFB FL 32403-6001	10. SOURCE OF FUNDING NUMBERS PROGRAM ELEMENT NO. 6.2 / PROJECT NO. 2673 / TASK NO. 0048 / WORK UNIT ACCESSION NO. N/A

11. TITLE (Include Security Classification)
CENTRIFUGAL MODELING OF UNDERGROUND STRUCTURES SUBJECTED TO BLAST LOADING

12. PERSONAL AUTHOR(S)
Habibollah Tabatabai, D. Bloomquist, M.C. McVay, John J. Gill, F.C. Townsend

13a. TYPE OF REPORT	13b. TIME COVERED	14. DATE OF REPORT (Year, Month, Day)	15. PAGE COUNT
Final	FROM Sept 85 TO May 87	March 1988	319

16. SUPPLEMENTARY NOTATION
Availability of this report is specified on reverse of front cover.

17. COSATI CODES			18. SUBJECT TERMS (Continue on reverse if necessary and identify by block number)
FIELD	GROUP	SUB-GROUP	Scaled Structures, Blast Loads, Centrifuge
19	09		
14	02		

19. ABSTRACT (Continue on reverse if necessary and identify by block number) (Survivable underground military)

The survivability of underground military structures may be of critical importance in times of crisis. Reliable and economical design of ~~such~~ structures requires a better understanding of the complex parameters involved.

Small-scale model testing of such systems offers major cost savings compared to full-scale tests. The laws of similitude and scaling relationships require some form of dead-load compensation to account properly for the effect of gravity stresses in scaled models. This can be accomplished by subjecting the scaled model to an increased acceleration field by use of a centrifuge. The objectives of this research were to determine the significance of gravity stresses on the response of underground structures subjected to blast loading and to evaluate the scaling relationships.

A discussion of the scaling relationships and procedures for model construction are presented. A complete instrumentation set-up for the → (over)

20. DISTRIBUTION/AVAILABILITY OF ABSTRACT	21. ABSTRACT SECURITY CLASSIFICATION
☒ UNCLASSIFIED/UNLIMITED ☐ SAME AS RPT. ☐ DTIC USERS	UNCLASSIFIED

22a. NAME OF RESPONSIBLE INDIVIDUAL	22b. TELEPHONE (Include Area Code)	22c. OFFICE SYMBOL
STEVEN T. KUENNEN, 2LT, USAF	(904) 283-6298	HQ AFESC/RDCS

DD Form 1473, JUN 86 — Previous editions are obsolete. — SECURITY CLASSIFICATION OF THIS PAGE

UNCLASSIFIED

(Block 19. continued:)
measurements of shock pressures, strains and accelerations on the structure was designed, built and tested. This includes development of Polyvinyidene Fluoride ~~(PVDF)~~ piezoelectric shock pressure transducers and associated electronics.

A series of tests at high-gravity and low-gravity environments were performed on 1/60 and 1/82-scale models of an underground protective structure subjected to a scaled blast loading. Based on the tests' results, it is concluded that the structural responses in the two gravity fields are different and that such parameters as wave speed, pressure magnitudes and structural strains are higher in the high-gravity tests. The centrifuge is believed to be a necessary and viable tool for blast testing on small-scale models of underground structures.

→ (edo) 4-

PREFACE

This report was prepared by the Department of Civil Engineering, University of Florida, Gainesville, Florida, 32611 under Contract Number F0835-83-C-0136, TASK 85-1, for the Air Force Engineering and Services Center, Engineering Research Division, Tyndall AFB, Florida, 32403-6001.

This report is published as submitted to the University of Florida by Mr. Habibollah Tabatabai, as his Ph.D. dissertation. Dr. Tabatabai worked under the direction of Professors David Bloomquist (centrifuge and instrumentation aspects), M.C. McVay (numerical analysis) and F.C. Townsend (project PI and centrifuge aspects), with assistance from fellow graduate student Captain J.J. Gill, USAF (model construction and instrumentation). Mr. Dan Ekdahl, UF College of Engineering Digital Design Facility, designed the onboard centrifuge instrumentation system. Sergeant William Bache, Alachua County Sheriff's Department supervised and performed the explosive detonations. Mr. Paul L. Rosengren, Jr. and 2Lt Steven T. Kuennen, USAF, were the HQ AFESC/RDCS Project Officers. This report summarizes work performed between September 1985 and May 1987 and is published as submitted because of its interest to the USAF Scientific and Engineering Community.

The report describes scaling relationships, model construction, instrumentation, and methodology for performing centrifugal modeling of blast loadings on buried model structures. The results show that gravity stresses should be considered for models. The structural response at high g levels was different with wave speed, pressure magnitudes and structural strains, being higher in the high gravity environment than at earth's gravity (1 g). It was concluded that centrifugal modeling is a necessary and viable method for evaluating the structural response of underground structures.

This report has been reviewed by the Public Affairs Office (PA) and is releasable to the National Technical Information Service (NTIS). At NTIS, it is available to the general public, including foreign nationals.

This technical report has been reviewed and is approved for publication.

STEVEN T. KUENNEN, 2LT, USAF
Project Officer

ROBERT J. MAJKA, Maj, USAF
Chief, Engineering Research Division

WILLIAM S. STRICKLAND, GM-14
Chief, Facilities and Systems

JAMES R. VAN ORMAN
Deputy Director of Engineering and Services Laboratory

(The reverse of this page is blank.)

TABLE OF CONTENTS

(The reverse of this page is blank.)

CHAPTER 1
INTRODUCTION

1.1 General

The survivability of underground military structures may be of critical importance in times of crisis. Reliable and economical design of such structures requires a better understanding of the complex parameters involved. Although, in recent years, there have been advances made in the development of analytical methods for the study of such systems, structural testing is believed to be essential considering the existing uncertainties and complexities in evaluating the performance of underground structures subjected to blast loads. Defense-related agencies regularly perform full-scale or scaled model tests on buried protective structures. Although full-scale testing may be ideal in terms of evaluating structural response, the economic costs may be substantial. Small-scale model testing (1/10 to 1/80) offers major cost savings, thereby allowing a larger number of tests to be performed for the purpose of parametric studies or evaluating repeatability.

There are several important factors to be considered in blast tests on small-scale models. First, the development of model materials such as microconcrete and miniaturized

reinforcement with properties similar to the prototype is an important consideration. The ability to build small-scale models within acceptable tolerances is another major concern. Second, the development and proper understanding of the scaling relationships, based on which the scaled model is designed and the observed response on the model is extrapolated to predict the response of the full-scale (prototype) structure, are essential. Third, the development of instrumentation methods and devices for the measurements of such parameters as shock pressures, strains and accelerations on small-scale models is another important consideration.

Complete adherence to the scaling relationships developed on the basis of the laws of similitude would require some form of dead-load compensation to properly account for the effect of gravity stresses. For example, in static tests on model bridges, it is customary to account for the discrepancy between the prototype and model dead-load stresses by adding sufficient weight to the bridge in such a way as not to add stiffness to the structure. In dynamic tests on super small-scale models, this problem becomes more complicated because of the relatively small-size structures involved and the problem of accounting for increased mass in a dynamic test.

An alternative would be to subject the scaled model to an increased acceleration field through an elevator arrangement or, more suitably, a centrifuge. Researchers

have generally ignored the effect of gravity on the response of buried structures based on the argument that, for shallow-buried structures subjected to blast loading, gravity stresses are generally much smaller than blast-induced stresses. Also, the relative complexity of compensating for gravity stresses has been another important consideration. However, it is clear that in some soils, properties such as stiffness and strength are directly related to gravity stresses (or depth of soil). In addition, the degree of soil-structure interaction could very well be a function of gravity stresses. To answer some of these questions, the U. S. Air Force sponsored this research project to determine the significance of gravity stresses (centrifuge testing) on the response of models of underground structures subjected to blast loading.

1.2 Review of Previous Work

During the last 50 years, the centrifuge has been frequently used as a tool in geotechnical testing, especially in Europe and the Soviet Union. In recent years, there has been an increased interest in using this technique to study soil mechanics and soil-structure interaction problems including underground structures.

Many researchers have conducted centrifuge tests to study varied subjects such as offshore gravity structures (Prevost et al., 1981), coal waste embankments (Al-Hussaini et al., 1981), consolidation of phosphatic clay

(Bloomquist, 1982), buried large-span culverts (McVay and Papadopoulos, 1986), abutments (Randolph et al., 1985), embankment dams and dikes (Fiodorov et al., 1985), pile installations (Craig, 1985), and laterally loaded pile groups in sand (Kulkarni et al., 1985).

Schmidt and Holsapple (1980) conducted a number of blast tests in a centrifuge to study the effectiveness of the centrifuge technique for modeling explosive cratering in dry sand and to validate their derived similarity requirements. These experiments used 0.5-4 grams of Pentaerythritol-tetranitrate (PETN) and 1.7 grams of lead-azide explosives in tests at zero depth of burial and at gravities as high as 450 g's.

The authors conclude that the centrifuge is an effective tool for such tests. Based on the observed symmetrical cratering in these tests, they also suggest that the Coriolis effects are insignificant (Coriolis effects are explained in Chapter 4). In addition, the authors recommend a non-dimensional parameter (discussed in Chapter 2) for determining an equivalent charge for simulating large explosive yields with small charges at elevated gravities.

Nielsen (1983) conducted a number of blast tests in a centrifuge to evaluate the suitability of the centrifuge technique for the measurement of free-field blast pressures in soil. In some tests less than 1 gram of Cyclotrimethylenetrinitramine (RDX) and PETN explosive was placed in the sand and then detonated at 50 g's. The soil

pressures at different locations were measured. In other tests, the explosive was placed inside a microconcrete burster slab (which, in the design of underground protective structures, serves to prevent deep penetration of the weapon into the soil). The explosives were detonated at gravities of up to 90 g's and pressure measurements were taken at different locations in the sand beneath the burster slab.

The author suggests that the centrifuge is a suitable tool for such measurements. The author also recommends the use of larger centrifuges and improvements in the instrumentation and data-acquisition arrangements.

Baird (1985) presents a survey of the instrumentation problems for explosive centrifugal testing and provides a list of commercially available transducers and data-acquisition systems that have a potential for use in such tests. Bradley (1983) and Cunningham et al. (1986) discuss scaling relationships and model materials for blast testing in a centrifuge, respectively.

Kutter et al. (1985) report preliminary results of a number of blast tests on scaled aluminum models of a buried reinforced concrete pipe (tunnel) at 1, 50 and 100 gravities. The two types of explosive charges used contained 64 and 512 mg of PETN. Horizontal accelerations on one side of the models were measured. The authors suggest that the effect of gravity becomes more important

as the range from the blast source increases and as the relative size of the explosion decreases.

1.3 Objectives

The objectives of this research program are as follows:

1) To develop instrumentation methods and devices for the measurement of shock pressures, strains and accelerations in centrifuge blast tests on small-scale microconcrete models of underground structures and to develop general testing procedures for such tests.

2) To perform blast tests on small-scale models of an underground structure at low-gravity (1g) and high-gravity (centrifuge) environments, and to study the differences in response, if any, between the two testing conditions and thereby ascertain the significance of gravity stresses in the response of such structures.

3) To evaluate the validity of scaling relationships by performing and comparing blast tests on two different sized scaled models (1/60 and 1/82-scale models).

1.4 Scope Of Work

A complete discussion of the scaling relationships for blast tests on underground structures is presented. Research work performed by Cunningham et al. (1986) and Bradley (1983) in the development of model materials and scaling relationships are summarized.

A complete instrumentation and data acquisition set-up

for the measurements of pressures, strains and accelerations in a centrifuge is designed, built, and tested and detailed procedures for such measurements are recommended. This includes the development of Polyvinylidene Fluoride (PVDF) piezoelectric pressure transducers and associated electronics for pressure measurements at the soil-structure interface and design of electronic circuits for strain measurements.

A series of tests are performed on 1/60- and 1/82-scale models of an underground structure subjected to a scaled 500-lb bomb blast at low-gravity (1g) and high-gravity (60- or 82-g's) environments. The results are evaluated for the purpose of determining the significance of gravity stresses (centrifuge testing) and for evaluating the scaling relationships.

CHAPTER 2
SIMILITUDE AND MODELING

2.1 Introduction

Experimental evaluations of engineering systems are generally recommended especially when such systems are too complicated to yield accurate analytical solutions based on mathematical formulations of the problem. However, prototype testing can, in many cases, be prohibitively expensive. Tests on scaled-down models of the prototype offer an alternative to prototype testing at a generally reduced cost.

The design of a model and the relationships, based on which the prototype response can be predicted from the observed response on the model, are based on the laws of similitude. Murphy (1950) defines models and prototypes as follows: " A model is a device which is so related to a physical system that observations on the model may be used to predict accurately the performance of the physical system in the desired respect. The physical system for which the predictions are to be made is called the prototype" (p. 1). Murphy (1950) also comments that " the theory of similitude includes a consideration of the conditions under which the behavior of two separate entities or systems will be

similar, and the techniques of accurately predicting results on the one from observations on the other" (p. 1).

Structural models have been widely used to evaluate the performance of underground structures subjected to blast loading. Parametric studies can be performed on such models to evaluate the significance of different factors such as varying soil conditions, sizes of threat, structural configurations, etc.

The most common relationship in blast wave scaling is based on the Hopkinson or cube-root scaling. This law states that "self-similar blast (shock) waves are produced at identical scaled distances when two explosive charges of similar geometry and the same explosive, but of different size, are detonated in the same atmosphere" (Baker et al., 1973, p. 55). The dimensional scaled distance, Z, is defined by the following equation:

$$Z = \frac{R}{W^{1/3}} \qquad \text{Equation 2.1}$$

where R is the distance from the explosive and W is the energy (or weight) of the explosive. Figure 2.1 illustrates the Hopkinson blast scaling. Baker et al. (1973) reviewed several other scaling relationships developed for blast.

A more systematic approach to scaling is through the laws of similitude and the theory of models. The first and by far the most important step is to determine the pertinent variables in the problem. According to the Buckingham's Pi theorem, the relationship among these variables can be

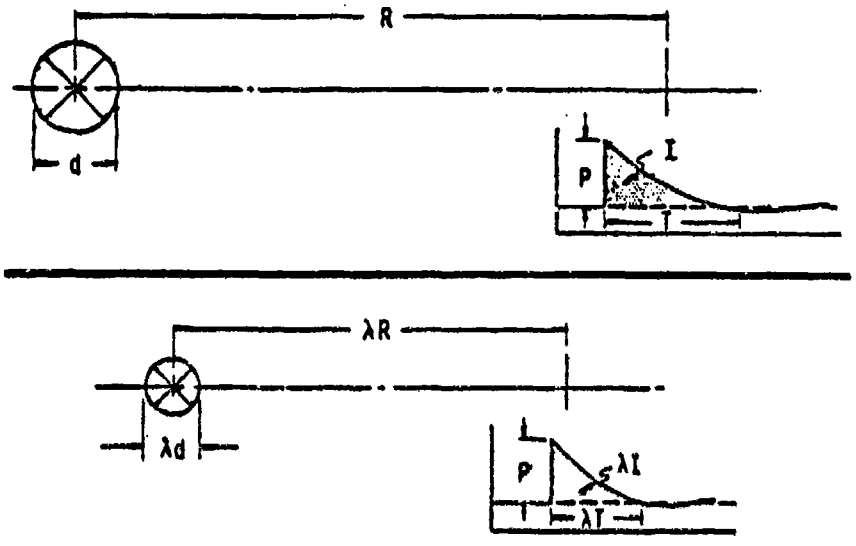

Figure 2.1. Hopkinson Blast Scaling (Baker et al., 1973)
(Reprinted by Permission of the Southwest Research Institute)

described by a set of S dimensionless and independent terms called Pi (π) terms which are products of the pertinent variables.

$$S = n - r \qquad \text{Equation 2.2}$$

Where S is the number of π terms, n is the number of variables and r is the number of fundamental dimensions. In a dynamic engineering problem, these fundamental dimensions are generally selected to be either force, length and time, or mass, length and time. There can be infinite sets of correct π terms. However, in each set the total number of dimensionless and independent terms is limited to S.

Similitude requirements establishing the relationship between model and prototype is determined by equating the dimensionless π terms in the model and prototype. Therefore

$$\pi_{im} = \pi_{ip} \qquad i = 1,2,\ldots,S \qquad \text{Equation 2.3}$$

where m and p denote model and prototype respectively.

More information on similitude requirements for static or dynamic modeling is presented by Murphy (1950), Langhaar (1951), Young and Murphy (1964), Tener (1964), Denton and Flathau (1966), Krawinkler and Moncarz (1973), Sabnis et al. (1983) and Bradley (1983).

2.2 Similitude for Underground Structures

Bradley (1983) presents a list of pertinent variables (Table 2.1), π terms (Table 2.2) and scaling relationships (Table 2.3) for underground structures subjected to blast loading. The relationships in Table 2.3 are based on the

Table 2.1

List Of Parameters (Bradley, 1983)

σ - Stress	E_s - Soil Modulus
d - Displacement	c - Soil Cohesion
a - Acceleration	p_c - Preconsolidation Pressure
P_o - Characteristic Pressure	g - Gravity
E_n - Energy	T - Time
R - Radius	o - Soil Angle of Friction
H - Thickness	ε_{st} - Steel Strain
ρ_c - Concrete Mass Density	ε_s - Soil Strain
C_c - Concrete P-Wave Speed	ε_c - Concrete Strain
F'_c - Concrete Strength	μ_{st} - Steel Poison's Ratio
E_c - Concrete Modulus	μ_c - Concrete Poisson's Ratio
F_{st} - Steel Strength	E_{st} - Steel Modulus
A_{st} - Area Of Steel	
ρ_s - Soil Mass Density	
C_s - Soil P-Wave Speed	

Table 2.2

Solution π Terms (Bradley, 1983)

$$\pi_1 = \frac{\sigma}{E_c}$$

$$\pi_2 = \frac{d}{H}$$

$$\pi_3 = \frac{a\ H\ \rho_c}{E_c}$$

$$\pi_4 = \frac{P_o}{E_c}$$

$$\pi_5 = \frac{E_n}{H^3\ E_c}$$

$$\pi_6 = \frac{R}{H}$$

$$\pi_7 = \frac{\rho_c\ C^2_c}{E_c}$$

$$\pi_8 = \frac{F'_c}{E_c}$$

$$\pi_9 = \frac{F_{st}}{E_c}$$

$$\pi_{10} = \frac{A_{st}}{H^2}$$

$$\pi_{11} = \frac{\rho_s}{\rho_c}$$

$$\pi_{12} = \frac{\rho_c\ C^2_s}{E_c}$$

$$\pi_{13} = \frac{E_s}{E_c}$$

$$\pi_{14} = \frac{c}{E_c}$$

$$\pi_{15} = \frac{P_c}{E_c}$$

$$\pi_{16} = \frac{H\ \rho_c\ g}{E_c}$$

$$\pi_{17} = \frac{E_c\ T^2}{H^2\ \rho_c}$$

Table 2.3

Scaling Relationships (Bradley, 1983)

Parameter	Symbol	Scaling Law
Stress	σ	$\sigma_m = \sigma_p$
Displacement	d	$d_m = d_p/n$
Acceleration	a	$a_m = n\ a_p$
Velocity	v	$v_m = v_p$
Explosive Pressure	P_o	$P_{om} = P_{op}$
Explosive Energy	E_n	$E_{nm} = E_{np}/n^3$
Radius	R	$R_m = R_p/n$
Thickness	H	$H_m = H_p/n$
Material Density	ρ	$\rho_m = \rho_p$
Material Modulus	E	$E_m = E_p$
Material Strength	F	$F_m = F_p$
Material Wave Speed	C	$C_m = C_p$
Area	A	$A_m = A_p/n^2$
Volume	V	$V_m = V_p/n^3$
Mass	M	$M_m = M_p/n^3$
Strain	ϵ	$\epsilon_m = \epsilon_p$
Dynamic Time	t	$t_m = t_p/n$
Poisson's Ratio	μ	$\mu_m = \mu_p$
Soil Cohesion	c	$c_m = c_p$
Soil Preconsolidation Pressure	P_c	$P_{cm} = P_{cp}$
Force	F_f	$F_{fm} = F_{fp}/n^2$
Acceleration of Gravity	g	$g_m = n\ g_p$

assumption that the same materials are used in the model as in the prototype, or at least the material properties are kept constant. Strict adherence to the geometric scaling requirements in Table 2.3 means that aggregates in concrete or soil particles would have to be scaled down to meet those requirements. For soils, large reductions in particle sizes can lead to major changes in soil properties. Therefore, such scaling down of all soil particles is not recommended and only large-size aggregates should be scaled down.
Sabnis and White (1967) suggest using a gypsum mortar mix to model concrete in small scale models. This would result in material properties similar to concrete.

Table 2.3 shows that the acceleration of gravity in the model (g_m) should be n times the acceleration of gravity in the prototype ($g_p = 1g$). This condition can be achieved by subjecting the model to an acceleration field. An elevator arrangement or, more suitably, a centrifuge can provide the desirable acceleration field.

Almost all research involving model tests on underground structures subjected to blast loads has been performed at 1g, i.e. ignoring the gravity effect and thereby violating one of the requirements for a true model. An evaluation of the significance or lack of significance of ignoring gravity effects in such model tests is presented in Section 2.3.

Modeling explosives is another important consideration in such tests. The geometric scaling of the shape of cased explosives may be an important parameter. For example,

cylindrical-shaped charges may be necessary to model some weapons. Table 2.3 shows that the energy of explosion is scaled by a factor of $1/n^3$. For example, a 500 lb bomb containing 267 lb of TNT can be simulated by a 0.267 lb TNT explosive in a 1/10 scale model test.

Schmidt and Holsapple (1980) suggest the following π term for scaling of energy for various types of explosives for centrifuge testing:

$$\pi = \left[\frac{G}{Q}\right]\left[\frac{W}{\delta}\right]^{1/3} \qquad \text{Equation 2.4}$$

where Q = Heat of detonation per unit mass of explosive

δ = Initial density of the explosive

W = Mass of the explosive

G = Gravity

By equating the above π term for the model and prototype, the scaling relationship can be established

$$\pi_m = \pi_p$$

$$\frac{G_m}{Q_m}\left(\frac{W_m}{\delta_m}\right)^{1/3} = \frac{G_p}{Q_p}\left(\frac{W_p}{\delta_p}\right)^{1/3}$$

Or

$$W_m = \left(\frac{G_p}{G_m}\right)^3 \left(\frac{Q_m}{Q_p}\right)^3 \left(\frac{\delta_m}{\delta_p}\right) W_p \qquad \text{Equation 2.5}$$

Based on this relationship, Table 2.4 shows calculated explosive weights for models simulating various size bombs at different scales or gravities (Nielsen, 1983). The type of

explosive used to model the prototype bombs in these calculations is Cyclotrimethylenetrinitramine (RDX).

Table 2.4

Theoretical Model Explosive Simulation Weights

(Nielsen, 1983)

Threat Designation (lb)	Centrifuge Environment (Gravities)				
	20 g	40 g	60 g	80 g	100 g
	Weight of RDX in Grams				
250	12.35	1.54	0.46	0.19	0.10
500	25.57	3.20	0.95	0.40	0.20
1000	53.43	6.68	1.98	0.83	0.43
2000	106.95	13.37	3.98	1.67	0.86

Schmidt and Holsapple's π term provides satisfactory results for centrifuge testing. However, this π term implies that, in order to compensate for the error introduced by ignoring gravity in simulating explosive energy, the mass of explosive in the model as predicted by Equation 2.5 should be increased by a factor of $(G_m/G_p)^3$ or n^3. This is of course an improper extension of the use of Schmidt and Holsapple's π term. To observe strict adherence to the similitude requirements, the type of explosive to be used for modeling should have the same detonating rate as the prototype explosives to simulate the blast effects correctly.

There are commercially available detonators such as the standard Reynolds RP-83 detonator (explained in Section 4.4)

with RDX charges that can be used for model tests. Based on the information on the available commercial detonators, the model scale can be calculated using the π term in Equation 2.4.

2.3 Gravity Effects

In this section the effect of ignoring gravity in model tests of underground structures subjected to blast loads is evaluated. In almost all such model tests in the literature, the effect of gravity is ignored on the basis of the fact that, for shallow-buried structures, the blast-induced pressures are generally much higher than gravity stresses.

The effect of neglecting gravity on dynamic time in models is dependent on the nature of dynamic forces. Consider the following π term in deriving a relationship for dynamic time:

$$\pi = \frac{F\ t^2}{M\ l} \qquad \text{Equation 2.7}$$

where F is dynamic force, M is mass, t is dynamic time and l is any relevant length. Equating this π term for model and prototype,

$$\pi_m = \pi_p$$

$$\frac{F_m\ t^2_m}{M_m\ l_m} = \frac{F_p\ t^2_p}{M_p\ l_p}$$

Therefore,

$$\frac{t^2_m}{t^2_p} = \left(\frac{M_m}{M_p}\right)\left(\frac{l_m}{l_p}\right)\left(\frac{F_p}{F_m}\right)$$

Considering the scaling relationships in Table 2.3,

$$\left(\frac{t_m}{t_p}\right)^2 = \left(\frac{1}{n^3}\right)\left(\frac{1}{n}\right)(n^2)$$

Or

$$t_m = \frac{1}{n}\, t_p \qquad \text{Equation 2.8}$$

If the force causing the dynamic response is applied on the system through gravity alone, then

$$\frac{F}{M} = g$$

where g is the acceleration of gravity. Therefore the term in Equation 2.7 can be rewritten in the following form

$$\pi = \frac{g\, t^2}{l}$$

Equating π terms for model and prototype

$$\pi_m = \pi_p$$

$$\frac{g_m\, t^2_m}{l_m} = \frac{g_p\, t^2_p}{l_p}$$

Therefore,

$$\frac{t^2_m}{t^2_p} = \left(\frac{g_p}{g_m}\right)\left(\frac{l_m}{l_p}\right)$$

If the effect of gravity is not neglected, then

$$t^2_m = \left(\frac{1}{n}\right)\left(\frac{1}{n}\right) t^2_p$$

Or

$$t_m = \frac{1}{n}\, t_p$$

Which is the same as the relationship in equation 2.8.

However, if the effect of gravity is neglected, then

$$t^2_m = (1)\left(\frac{1}{n}\right) t^2_p$$

Or

$$t_m = \frac{1}{\sqrt{n}}\, t_p \qquad \text{Equation 2.9}$$

which is substantially different from Equation 2.8. The following two examples illustrate this effect in systems where gravity is the only force causing the dynamic response of the system. An ideal pendulum is one such system in which gravity is the only force applied on the mass (Figure 2.2(a)). The period of vibration (T) of an ideal pendulum of length L is

$$T = 2\pi \sqrt{L/g} \qquad \text{Equation 2.10}$$

If a test is performed on a scaled-down version of this pendulum, the resulting period of vibration can be calculated as follows:

$$\pi = \frac{T}{\sqrt{L/g}}$$

$$\pi_m = \pi_p$$

$$\frac{T_m}{\sqrt{L_m/g_m}} = \frac{T_p}{\sqrt{L_p/g_p}}$$

Then

$$T_m = (\sqrt{L_m/L_p})(\sqrt{g_p/g_m})\, T_p$$

If gravity is not neglected, then

$$T_m = (1/n)\, T_p$$

If gravity is neglected, then

$$T_m = \sqrt{(1/n)(1)}\, T_p$$

Or

$$T_m = (1/\sqrt{n})\ T_p$$

Another similar example is the case of determining the time (t) that it takes for a point mass to drop from a height H with zero initial velocity (figure 2.2 (b)).

$$t = \sqrt{2H/g} \qquad \text{Equation 2.11}$$

This is similar to Equation 2.10 and yields the same results as in the previous example.

Consider a spring-mass system (Figure 2.2 (c)) which is in static equilibrium under its own weight. For the case of a linear spring, the period of vibration (T) of such a system is only a function of its mass M and its stiffness (spring constant K) and not a function of gravity

$$T = 2\pi \sqrt{M/K} \qquad \text{Equation 2.12}$$

Of course, stress in the spring is a function of gravity and any other external force applied on the mass. So, if the system is not linear, K and consequently T would be functions of gravity too.

Based on the above argument, it would appear at first that, for underground structures for which gravity stresses are small compared to blast induced stresses, the response time would be independent of gravity assuming the loading functions are the same. However, there are other factors that must be taken into account. Wong and Weidlinger (1983) suggest that, in box-type structures, a part of soil mass around the structure moves with it and therefore the effective mass for the vibration of the structure under

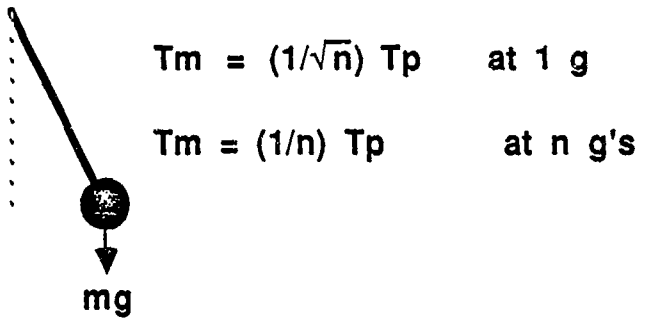

(a) Ideal Pendulum

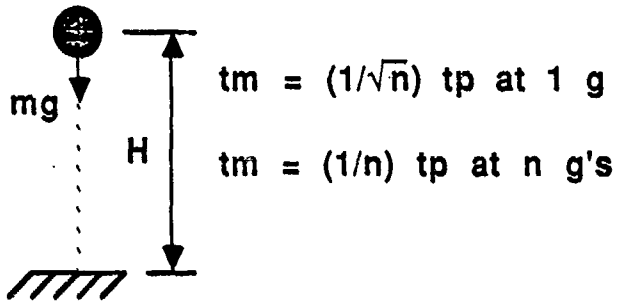

(b) Free Fall

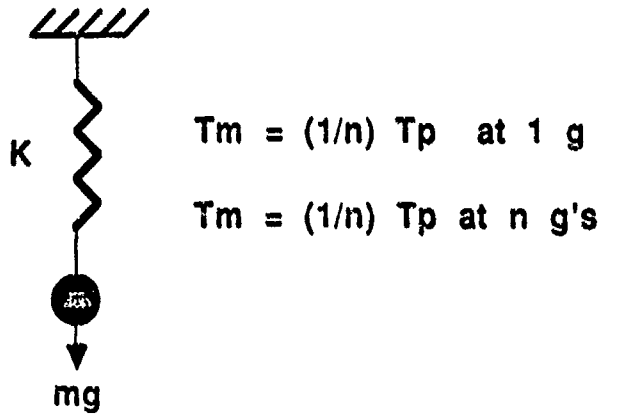

(c) Spring-Mass System

Figure 2.2. Gravity Effects on Dynamic Time

blast loading increases. If gravity stresses are not scaled properly, it is believed that the degree of interaction between soil and structure (in terms of movement of soil with structure) would be reduced and the effective mass for structural vibrations would be reduced. This results in reduced response times (Equation 2.12) and higher frequencies for models for which gravity effects are ignored. Other factors may be an increased apparent stiffness of the structure and soil confinement effects on the structure due to higher degree of soil-structure interaction.

Perhaps the most important factor to be considered is the possible change in characteristics of shock waves in soils due to gravity. For example, properties such as strength, wave speed, and stiffness of dry sand or gravel are highly dependent on gravity or overburden (Baker et al., 1973, Pan, 1981 and 1982 and Kutter et al., 1985). Therefore, it is expected that in models in which gravity is not properly accounted for, there would be a decrease in strength and stiffness of soil (compared to prototype) and thereby greater attenuation of shock waves could be expected. For models subjected to proper acceleration fields (gravity), it is expected that the shock wave will arrive faster with smaller rise times (higher frequency content) and higher magnitudes of pressure.

Denton and Flathau (1966) conducted a series of load tests on buried circular aluminum arches at different

scales. They reported relatively good agreement in strain and deflection results due to the applied loads even though gravity was ignored. However, the applied loads were quasi-static: that is the load durations were much greater than the period of vibrations for the structure (Baker et al., 1973).

Baker et al. (1973) report a study performed by Hanna et al. on half-buried steel containment shells subjected to an internal blast. It is reported that the peak strain did not appreciably change in different tests. However, large shells exhibited increased damping which was attributed to gravity effects which were not properly scaled.

Young and Murphy (1964) conducted tests on buried aluminum cylinders at different scales. Load was applied by dropping a weight on the surface of the sand. However, the drop height for different size models was kept constant (not scaled) in order to obtain the same velocity of impact in all tests. This is equivalent to scaling the drop height and subjecting the mass to an increased gravity field. The authors attribute some discrepencies in test results to the fact that the weight of soil was not scaled.

Gran et al. (1973) compared tests on 1/30 and 1/6-scale models of a buried cylindrical missile shelter. They reported good agreement in results. The soil wave speed in the 1/6 scale test (400 m/s) was higher than that in the 1/30 scale test (250 to 400 m/s). This was attributed to differences in soil density due to imperfect soil placement. They also reported that the concrete strain responses were

generally reproduced, although the magnitudes of the strains differed somewhat.

In summary, the use of centrifuge for model tests on underground structures subjected to blast loads is warranted based on the belief that the increased gravity field affects such things as the characteristics of shock waves in soils and the degree of interaction between soil and structure resulting in added mass, stiffness and confinement for the structure.

2.4 Construction of Small Scale Models

2.4.1 Micro-Concrete

The scaling relationships presented in Table 2.3 are derived on the assumption that the material properties in the models remain the same as the prototype. Therefore, it is essential that the micro-concrete used in the small scale models have the same properties as prototype concrete. Sabnis and White (1967) recommended gypsum mortar to be used for small scale model tests. Cunningham et al. (1986) give the following reasons for choosing gypsum over portland cement in super small scale modeling:

1. Relatively large particle sizes in portland cement can cause problems for models smaller than 1/60 scale.
2. Curing time for cement is generally 28 days while gypsum cures very rapidly and can be removed from its mold within an hour. In fact when micro-concrete reaches its desired strength, the surface is coated with shellac to prevent

further variations in strength and eventually brittleness.

3. In very small scale models, shrinkage problems with portland cement can be severe, while gypsum exhibits very low distortion upon curing.

The micro-concrete mix selected uses gypsum cement, sand and water in a ratio of 1:0.8:0.25 by weight. The resulting properties for such a mix are as follows:

f'_c = 4085 psi

f'_t = 327 psi

γ = 130 pcf

E_c = 3.3 X 10^6 psi

2.4.2 Reinforcement

The primary concern in developing reinforcement for small scale models is to have similar properties in the model and prototype. The following three properties and characteristics are considered important in the development of miniaturized reinforcement (Cunningham et al., 1986):

1. Yield strength
2. Modulus of elasticity
3. Bond development

The prototype steel generally has a yield strength of 60 ksi and a modulus of elasticity of 29000 ksi. Black-annealed steel wires (gages 28, 24, 22) were chosen as model reinforcement. Annealed steel wire has lower yield strength (40 to 60 ksi) than cold-rolled steel wire (80 to 100 ksi) and it is widely available. In order to provide sufficient bond

between micro-concrete and steel wire, a method developed at Cornell University was utilized. A deforming machine, made up of two pairs of perpendicularly mounted knurling wheels, was built.

2.4.3 Mold and Model Construction

An aluminum mold was used to build the micro-concrete box-type models and a cast acrylic mold was used to build the burster slab (Gill, 1985). The reason for using an aluminum mold for the box type model was that there were problems in removing the cast acrylic mold. The aluminum mold included a collapsible inner column and break-away outer walls. Miniaturized reinforcement was placed in the mold by drilling holes on the molds and stringing the micro-reinforcing wire prior to casting the concrete (Figure 2.3).

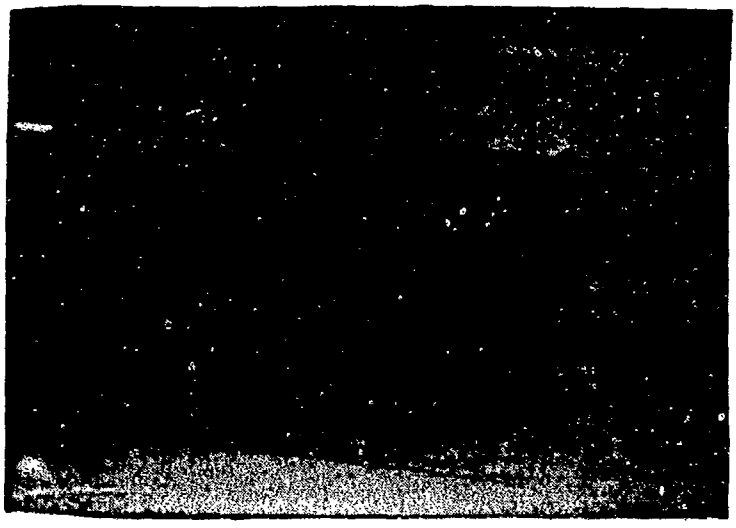

Figure 2.3. Aluminum Mold for Structural Model (Gill, 1985)

CHAPTER 3
TESTING EQUIPMENT AND SPECIMENS

3.1 Centrifuge

The University of Florida geotechnical centrifuge (Figure 3.1) has a radius of 1 meter and a capacity of 2125 g-kg. Two buckets containing the test specimen (Figure 3.2) and the counterweight (Figure 3.3) are attached at the two ends of the centrifuge arm by means of two aluminum support frames. The bucket containing the test specimen has inside dimensions of 10 in X 12 in X 10 in deep (McVay and Papadopoulos, 1986). The counterweight is used to balance the forces applied on the centrifuge arm by the test specimen.

The test specimen and the counterweight are placed in the buckets while the buckets are in an up-right position before spinning the centrifuge. Connections between the buckets and the support frames are built such that the buckets could rotate around the point of connection. Figure 3.4 shows that the center of mass of the bucket (with contents) is below the point of connection to the support frame. Therefore, when the centrifuge is accelerated from rest to full speed, the net centrifugal force acting on the center of mass of the bucket produces a net moment around the connection

Figure 3.1. University of Florida Geotechnical Centrifuge

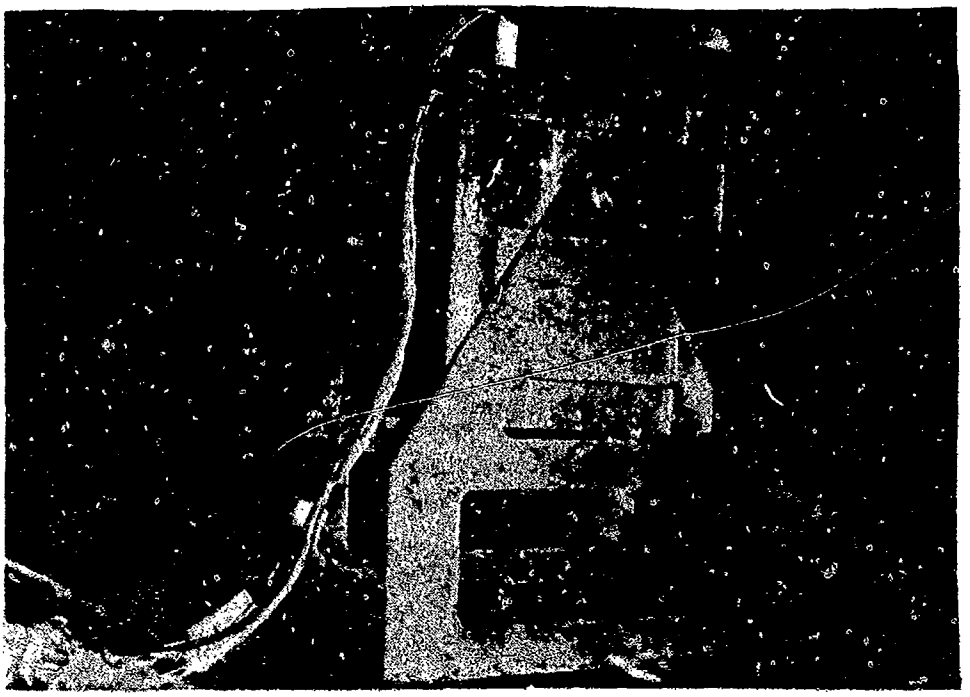

Figure 3.2. Bucket Containing Test Specimen

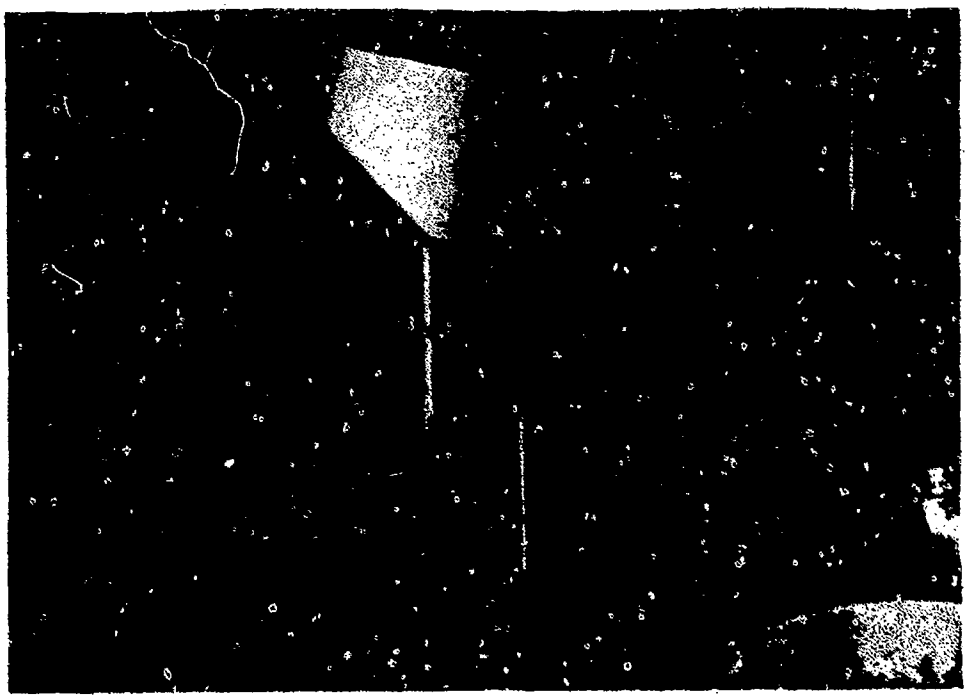

Figure 3.3. Bucket Containing Counterweight

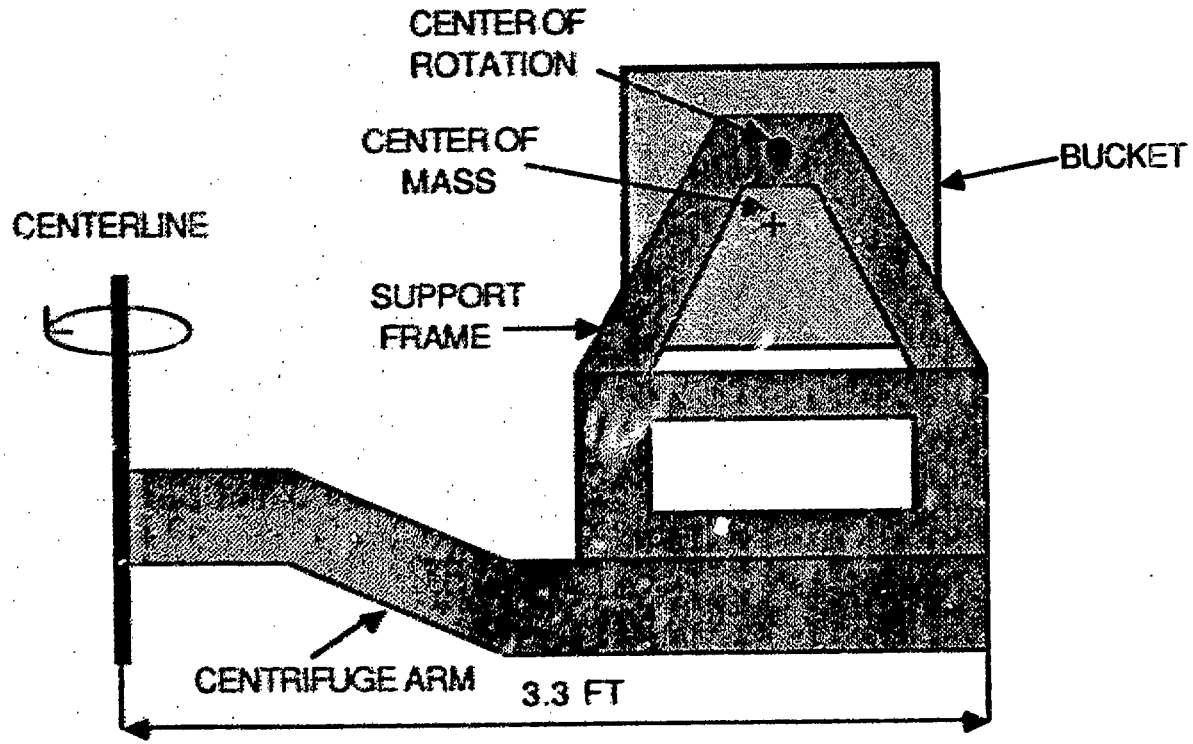

Figure 3.4. Attachment of the Bucket to the Centrifuge Arm

point. This results in the rotation of the bucket by 90 degrees at which point the net moment is zero (Figure 3.5).

The relationship between centrifugal acceleration (a) and angular velocity of the centrifuge (w) is given in the following equation:

$$a = r\,w^2 \qquad \text{Equation 3.1}$$

In this case, r is the distance from the center of rotation of the centrifuge to the center of mass of the test specimen (soil plus structure) in the rotated position. For example, to obtain a centrifugal acceleration of 60 g's for a radius of 36 inches:

$$(60\ g)(32.2\ ft/sec^2)(12\ in/ft) = (36\ in)\ (w^2)$$

Or

$$w = 25.4\ rad/sec \quad or \quad w = 242\ rpm$$

Since the height of the test specimen is small compared to the length of the centrifuge arm, variations of centrifugal accelerations along the height of the test specimen are believed to be negligible.

The rotating nature of a centrifuge makes it impossible to have instrumentation wires from inside the centrifuge directly connected to outside devices. These wires must pass through slip rings, unless other schemes such as telemetry or on-board data capture and storage are devised. Slip rings operate based on a sliding contact mechanism. A total of 64 slip rings are available on the U.F. centrifuge.

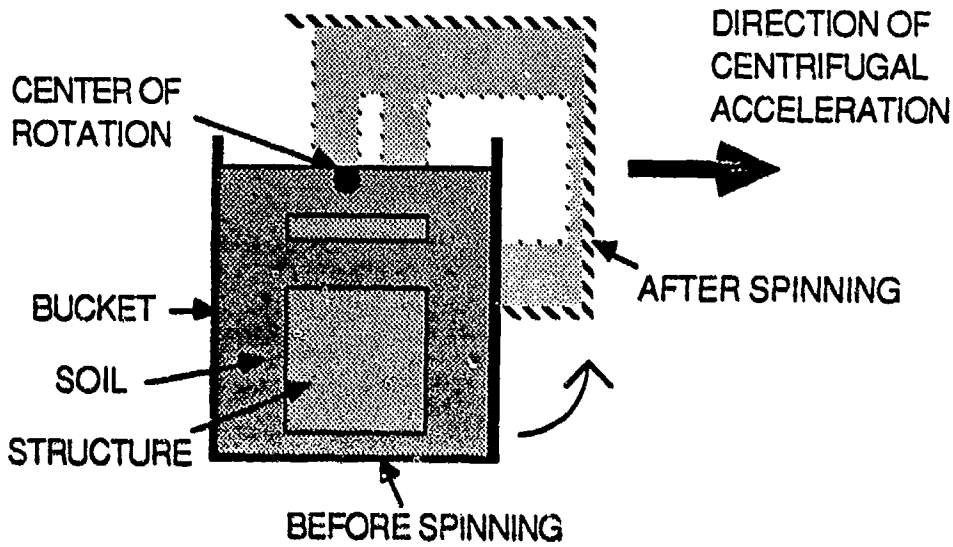

Figure 3.5. Orientation of Bucket Before and After Spinning

3.2 Test Specimens

The original prototype structure considered for centrifuge model testing in this research effort was a multi-bay underground structure (with burster slab) designed for use as shelter for Ground Launched Cruise Missiles (Bradley, 1983). However, the objectives of this research program are to develop methods and evaluate modeling relationships and techniques for centrifuge tests, rather than to be a detailed study of the performance of a specific structure. Therefore, a slightly simplified version of the prototype, which included a one-bay (box-type) structure (instead of 3 bays) with burster slab, was built at two different scales of 1/60 and 1/82. Figures 3.6 and 3.7 illustrate the shape and sizes of the models.

A total of three 1/60-scale and two 1/82-scale structures were built using a gypsum mortar mix as concrete and deformed steel wire as reinforcement (Chapter 2). Reinforcement details for 1/60 and 1/82-scale models are given in Gill (1985). The criteria, based on which, the size of models for such tests are selected are as follows:

1. Ability to construct small-scale models is a primary consideration. Super small-scale models may pose difficulties in terms of building molds or formwork within acceptable tolerances, designing and obtaining micro-concrete with specific properties, and providing for steel reinforcement and its placement within acceptable tolerances.

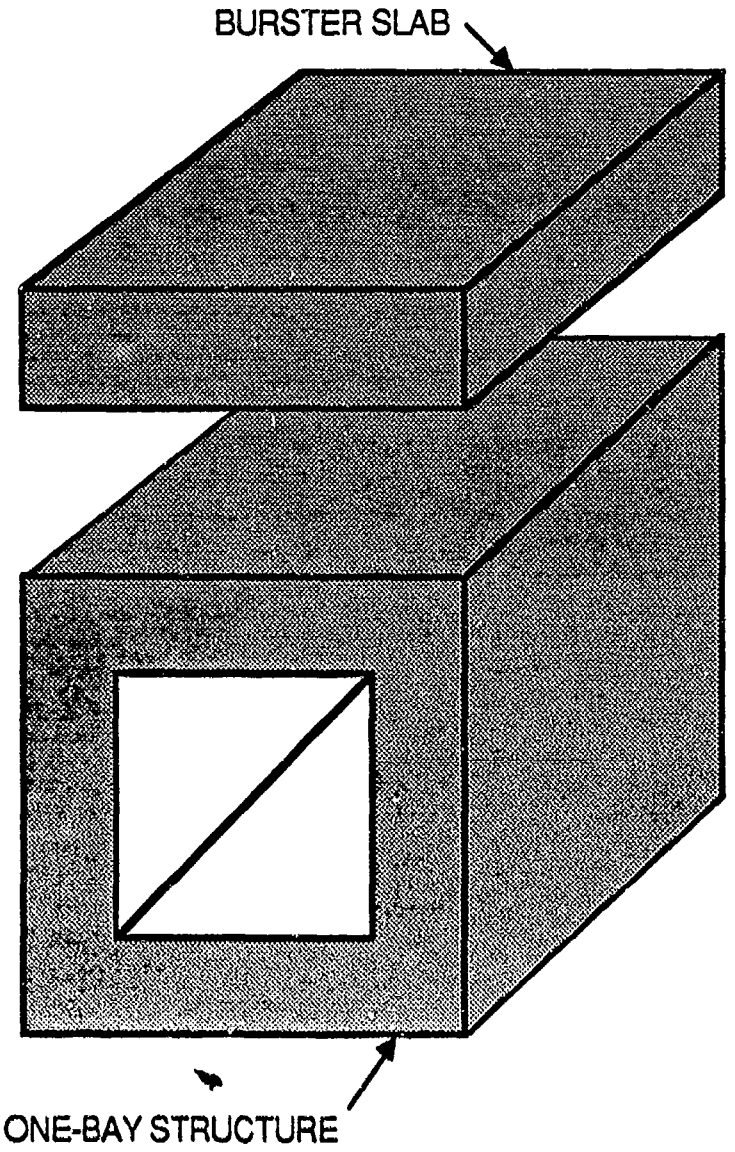

Figure 3.6. General Shape of the Structural Model

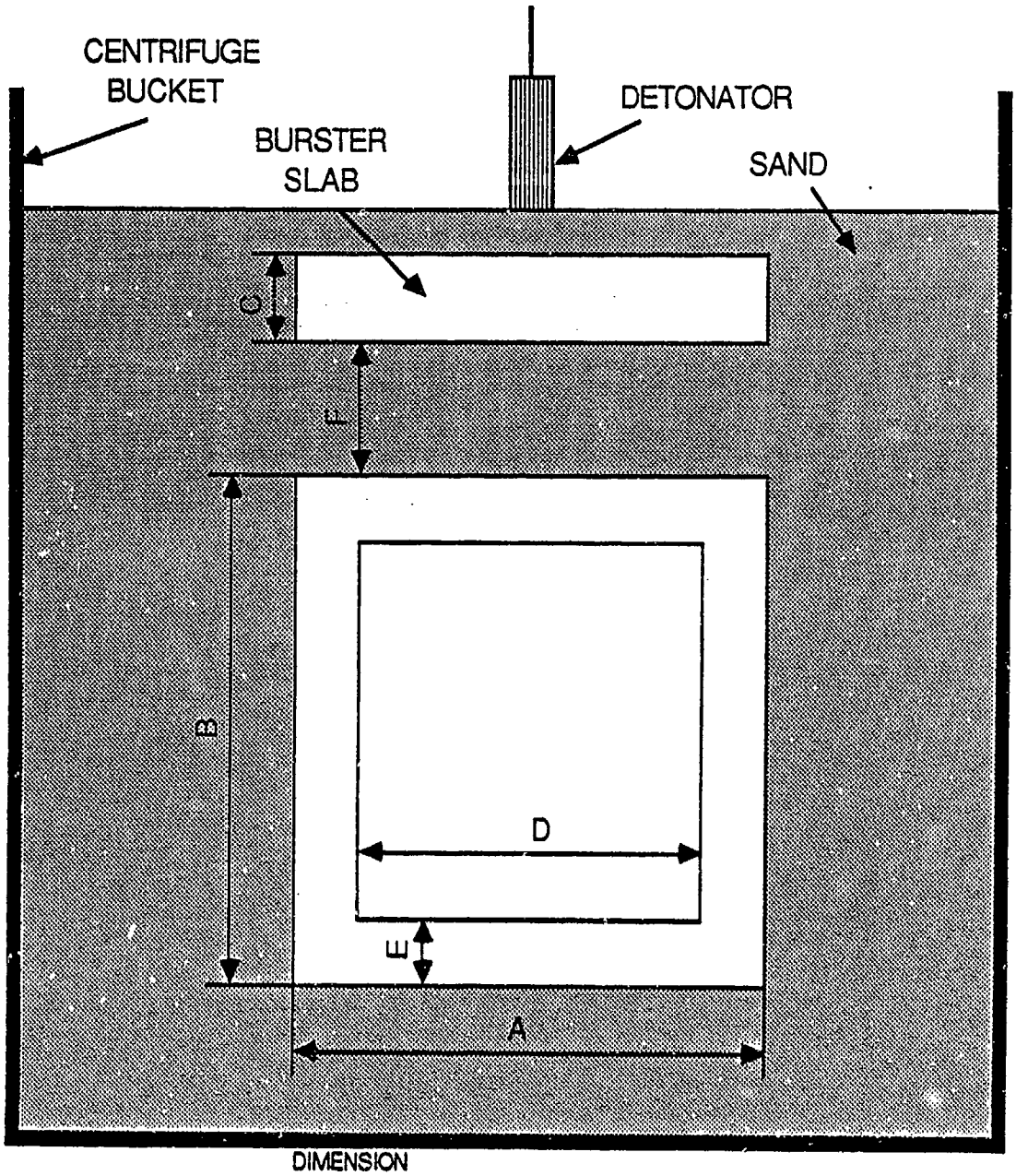

DIMENSION (INCH)

	A	B	C	D	E	F	Depth
1/60	4.0	4.4	1.0	2.8	0.6	1.4	4.0
1/82	2.93	3.22	0.73	2.05	0.44	1.02	2.93

Figure 3.7. Dimensions of 1/60 and 1/82-Scale Models

2. Simulating explosives in small-scale models generally involves very small-size charges that may have to be custom-made in order to satisfy geometry and size (explosive weight) requirements. Another, perhaps more convenient approach would be to choose from a limited number of commercially available explosive charges and calculate the model scale, for which, the commercial charge would be an appropriate simulation of the size of the threat on the prototype structure (Section 2.2). For example, two commercially available explosive charges (Standard and modified Reynolds RP-83) were used to simulate a 500-lb bomb threat on 1/60 and 1/82 scale models in this research work. Safety concerns with regard to detonating large explosive charges in a centrifuge is also a limiting factor on the model scale selected.
3. Size and capacity limitations for the centrifuge should also be considered in selecting a model scale. Models that are too large may cause obvious problems in centrifuge tests.
4. The type of instrumentation planned for model tests may also be dependent on, and limited by, the size of the model in super small-scale models. A complete review of instrumentation for centrifuge tests is given in Chapter 4.

Based on the above arguments, two model scale sizes (1/60 and 1/82) were selected for the tests reported here.

CHAPTER 4
INSTRUMENTATION AND DATA ACQUISITION

4.1 Introduction

Instrumentation and data acquisition in centrifugal model tests pose unique challenges in that the conventional methods and instruments may not be adequate to handle the special conditions associated with a centrifuge. Blast testing in such an environment also adds to the complications involved.

There are several factors that should be considered in the design of effective instrumentation and data acquisition methods for such a system. The primary concern is the existence of electrostatic and magnetic noise sources in the centrifuge which could affect the electrical signals. In fact, slip rings, through which all signals have to pass to exit the centrifuge, are inherently noisy because of their sliding contact mechanism.

Another factor to be considered in small-scale modeling is the necessity of having measuring instruments small enough, both in mass and size, compared to the model such as to minimize distortions in the model response. Finally, the relatively high frequency signals associated with blast

waves require accurate instruments with sufficiently high sampling rates to properly record the event.

In this chapter a complete explanation of the development of methods for the measurement of strains, pressures, and accelerations in centrifugal testing of small scale models subjected to blast loading is presented. However, most of the following discussions equally apply to other kinds of instrumented testing in a centrifuge.

4.2 Instrumentation

In this section the basic concepts of electrical resistance strain gages, piezoelectric pressure transducers and piezoelectric accelerometers are reviewed. Development of new procedures and modifications to conventional methods are also discussed.

4.2.1 Electrical Resistance Strain Gages

Electrical resistance strain gages function on the basis of the change in the electrical resistance of the gage in response to strain. When properly bonded to a test surface, these gages exhibit slight changes in resistance (relative to their original resistance) as a function of strain in the test specimen. Each gage has a constant factor, called the gage factor, which determines the relationship between the relative change in resistance and the strain, according to the following equation:

$$F = \frac{\frac{\delta R_g}{R_g}}{\varepsilon} \qquad \text{Equation 4.1}$$

where F is the gage factor, δR_g and R_g are the change in resistance and the resistance of the gage, respectively, and ε is the strain in the gage.

The usual way to monitor such changes in resistance is through a Wheatstone bridge (Figure 4.1). The four arms of the bridge consist of four resistors, one of which is the strain gage R_g. In such case the circuit is called a quarter bridge. The bridge is powered by a voltage power supply V_i.

A bridge is called balanced when the potential level at points b and d are equal or, in other words, the output voltage is zero (Figure 4.1). Therefore, voltage drop across a-d is equal to voltage drop across a-b.

$$V_{ad} = V_{ab} \quad \text{and} \quad V_{bc} = V_{dc}$$

or

$$R_g I_g = R_3 I_3 \quad \text{and} \quad R_1 I_1 = R_2 I_2$$

where I_1, I_2, I_3, and I_g represent electrical current in the four arms of the bridge as shown in Figure 4.1. Similarly, because of zero voltage across b-d,

$$I_1 = I_g \quad \text{and} \quad I_2 = I_3$$

Therefore,

$$R_g I_1 = R_3 I_2 \quad \text{and} \quad R_1 I_1 = R_2 I_2$$

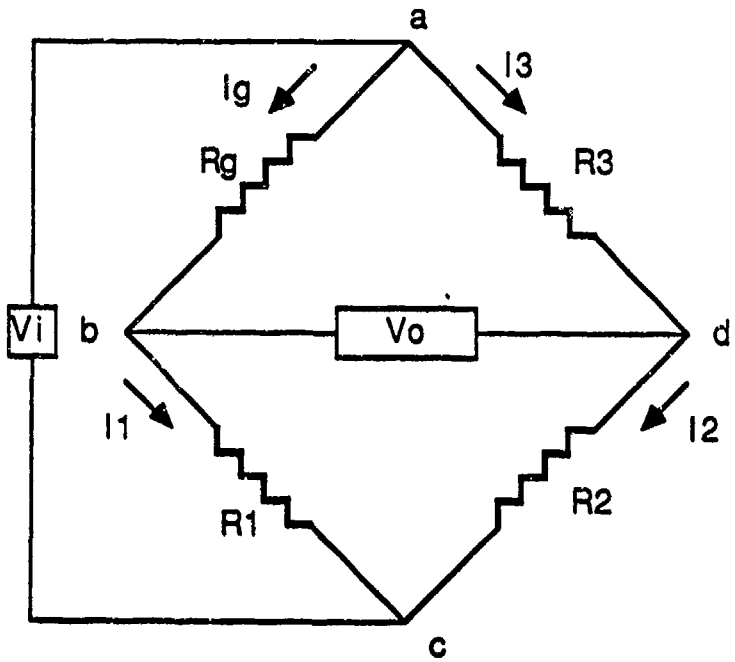

Figure 4.1. Basic Wheatstone Bridge

Thus, for a balanced bridge,

$$\frac{R_g}{R_1} = \frac{R_3}{R_2} \qquad \text{Equation 4.2}$$

In the balanced bridge method of calculating strains, the Wheatstone bridge has to be first balanced in the 'no-load' or unstrained condition. This can be accomplished by using a variable resistor for R_1 and changing it until the output voltage V_o becomes zero. The bridge must again be balanced in the strained condition by readjusting R_1.

$$\delta R_1 = R_1(\text{strained}) - R_1(\text{unstrained})$$

From equation 4.2:

$$R_g = (R_3/R_2)\, R_1$$

Since R_3 and R_2 are constant,

$$\delta R_g = (R_3/R_2)\, \delta R_1 \qquad \text{Equation 4.3}$$

However, substituting δR_g into Equation 4.1,

$$\epsilon = \frac{R_3}{R_2\, R_g F}\, \delta R_1 \qquad \text{Equation 4.4}$$

Equation 4.4 is valid only when the bridge is balanced. This is called the 'balanced bridge' method of calculating strains. Most regular strain gage indicators are based on this concept. However, in dynamic tests, where continuous monitoring of strain is required, the output signal does not stay constant for a sufficient time to balance the bridge, specially when several strain gages have to be monitored simultaneously. The 'unbalanced bridge' method

relates the output voltage of the bridge to the resistance change, or strain, in the gage. Therefore, bridge balancing is not required and equation 4.4 does not apply any longer. Williams and McFetridge (1983) present equations relating strains to the output voltages at unstrained and strained conditions, supply voltage and gage factor.

$$V_{ab} = R_g I_g$$

$$I_g = V_i/(R_g + R_1)$$

Therefore, in the unstrained or initial condition,

$$V^i_{ab} = \frac{R_g}{R_g + R_1} V_i$$

And in the strained or final condition,

$$V^f_{ab} = \frac{(R_g + \delta R_g)}{(R_g + \delta R_g) + R_1} V_i$$

$$\delta V_{ab} = V^f_{ab} - V^i_{ab} = \left[\frac{(R_g + \delta R_g)}{(R_g + \delta R_g) + R_1} - \frac{R_g}{R_g + R_1} \right] V_i$$

If R_1 is selected to be equal to R_g,

$$\delta V_{ab} = \frac{\delta R_g}{4R_g + 2\delta R_g} V_i$$

However,

$$\delta V_o = -\delta V_{ab}$$

This is because the potential at d is unchanged and therefore any change in potential across bd (δV_o) must be due to the change in potential at b. Therefore,

$$\delta V_o = - \frac{\delta R_g}{4R_g + 2\delta R_g} V_i$$

Or,

$$\frac{\delta R_g}{R_g} = - \frac{4\delta V_o}{V_i + 2\delta Vo}$$

Substituting equation 4.1 in the above equation,

$$\varepsilon = - \frac{4\delta V_o}{F\ (V_i + 2\delta V_o)} \qquad \text{Equation 4.5}$$

Therefore, any change in output voltage from the unstrained condition indicates a strain which can be calculated using the above equation. This equation indicates a nonlinear relationship between strain ε, and δV_o. However, for a strain gage with a gage factor close to 2 and a strain of 10000 micro in./in., the deviation from linearity is less than 1 percent (Dove and Adams, 1964). This indicates that δV_o is very small compared to V_i. Therefore, the linear approximation of equation 4.5 can be written as

$$\varepsilon = - \frac{4\ \delta V_o}{F\ V_i} \qquad \text{Equation 4.6}$$

In order to accurately measure strains, it is necessary to use accurate voltage measuring devices. Also, the power supply must be stable. Another factor to be considered is the effect of temperature changes on lead wires connecting the strain gage to the Wheatstone bridge. These changes can

cause resistance variations in the lead wires and thereby introduce errors in the measurements. For short-term tests this problem may not be critical because of the small probability of large temperature variations in a short period of time. However, this effect can be completely eliminated by employing a three-wire arrangement instead of a two-wire setup as shown in Figure 4.2. In this method, equal lengths of lead wires exist in two adjacent arms of the bridge and since resistance changes in adjacent arms make opposite contributions to the output voltage (Dove and Adams, 1964), the overall effect is thereby eliminated.

4.2.1.1 Strain Gage Measurements in a Centrifuge

The use of commercially available strain indicators may not be suitable for centrifugal testing. Because of the size and number of these indicators, they generally have to be placed outside the centrifuge. Therefore, the gage connection to the Wheatstone bridge passes through slip rings. This can cause serious problems because the slip rings are inherently noisy and resistance changes in slip rings can be as large as the resistance changes in the strain gages (Hetenyi, 1950). In addition, in regular strain indicators, the low-level output voltage of the bridge is increased with an amplifier. Depending on the gain, the amplifier has a frequency range in which that gain remains constant and the amplifier exhibits a linear response (Figure 4.3). If the signal frequency is beyond

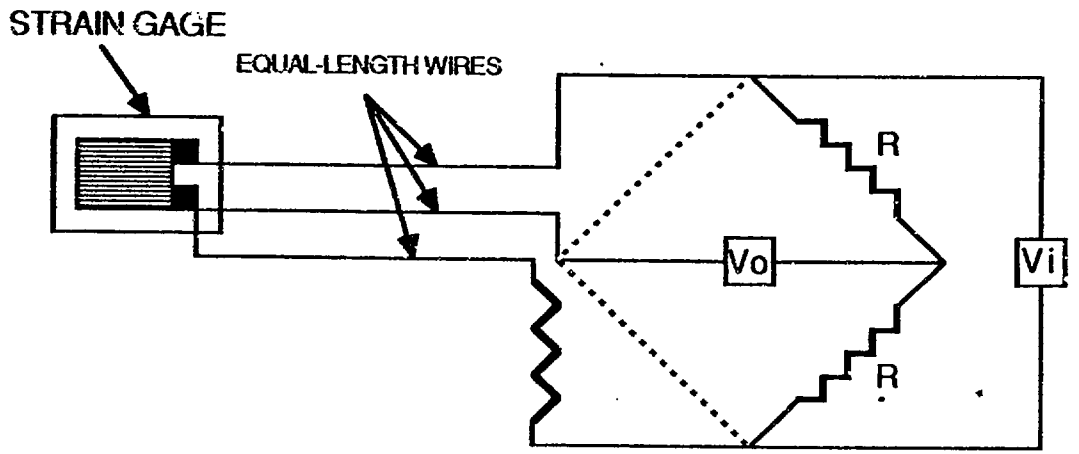

Figure 4.2. Three-Wire Circuit for Strain Measurements

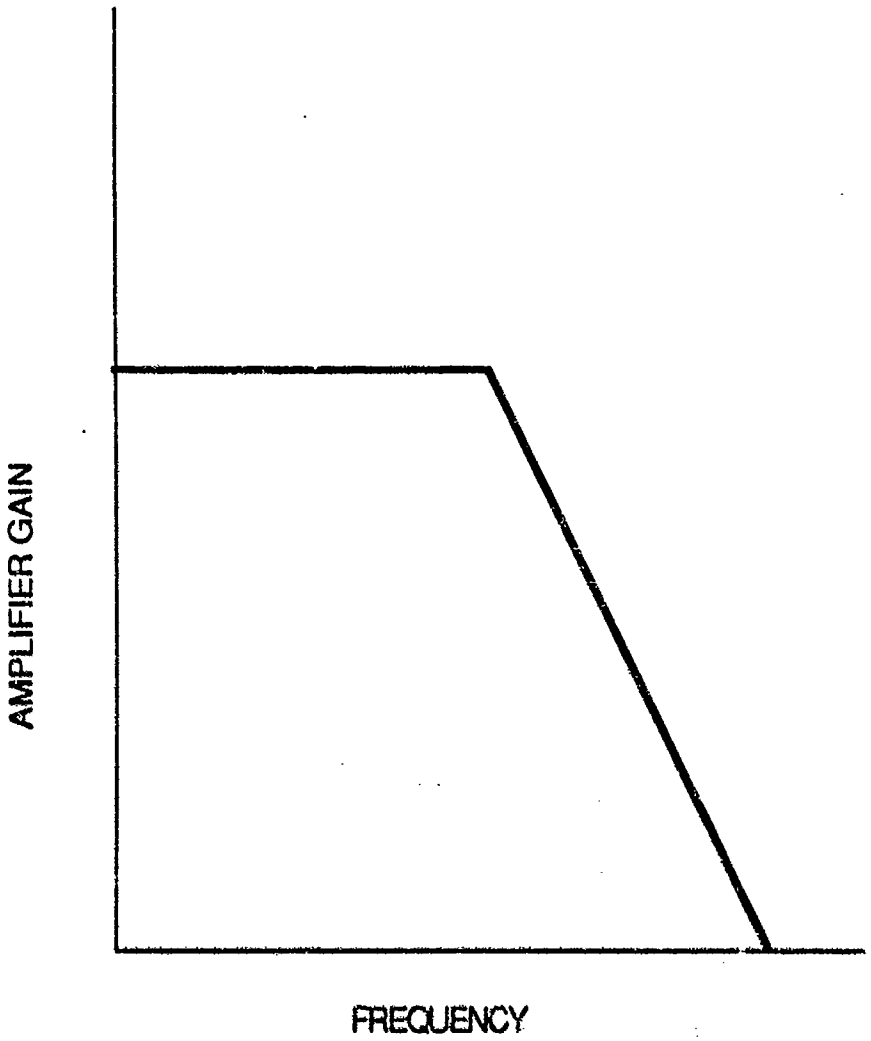

Figure 4.3. Gain Versus Frequency Response of Amplifiers

the frequency range of the amplifier, distortion of the response associated with that frequency will occur. Therefore, in blast testing, where higher frequency signals are expected, the characteristics of the regular strain indicator may not be suitable.

A solution to these problems can be achieved through on-board signal conditioning and circuitry. This means that electronic circuit boards containing multiple Wheatstone bridges and instrumentation amplifiers can be specially designed and built. The relatively small size of the electronic board would permit the attachment of the box containing the board on the arm of the centrifuge. Of course, the box has to be located as close to the center of rotation as possible to reduce unwanted centrifugal accelerations on the electronic components. Such an arrangement would eliminate the effect of resistance changes in the slip rings on the output voltage of the Wheatstone bridge due to the fact that the slip rings are not on the arm of the bridge anymore. Also, since the Wheatstone bridge is relatively close to the gage, the lead wires are shorter and noise pickup by those wires will be reduced. In addition, since the output voltage is amplified with an instrumentation amplifier before the signal passes through slip rings, the signal to noise ratio will be much higher.

4.2.1.2 Electronic Circuits For On-Board Strain Measurements

Figure 4.4 illustrates the basic electronic circuit for each strain gage. The strain gages used in the tests discussed in this report had a resistance of 120 ohms. The basic circuit consists of a quarter-bridge (one active gage) completion unit and an instrumentation amplifier. The quarter-bridge completion unit consists of one 120-ohm and two 1000-ohm precision resistors as shown in figure 4.4. It is very important that the resistors have high precisions in order to reduce errors. The bridge is powered with ± 3 DC volts. The same power supply is used to power the instrumentation amplifiers. In these tests the strain gage power supply unit was placed outside the centrifuge. However, batteries can be placed on-board to power the bridge and the amplifier. The amplifier used is Burr-Brown Model INA 101 which is a high-accuracy instrumentation amplifier. It responds only to the difference between the two input signals and has very high input impedance (10^{10} ohms).

Characteristics of INA 101 are presented in Appendix A. The gain for this amplifier is set through an external resistor. In this case, the gain was set at 100, which for frequencies below 10000 hertz remains constant.

4.2.1.3 Calibration of Strain Gage Bridges

The output voltage of the bridge can be theoretically related to strain through equation 4.6. Therefore, for a one

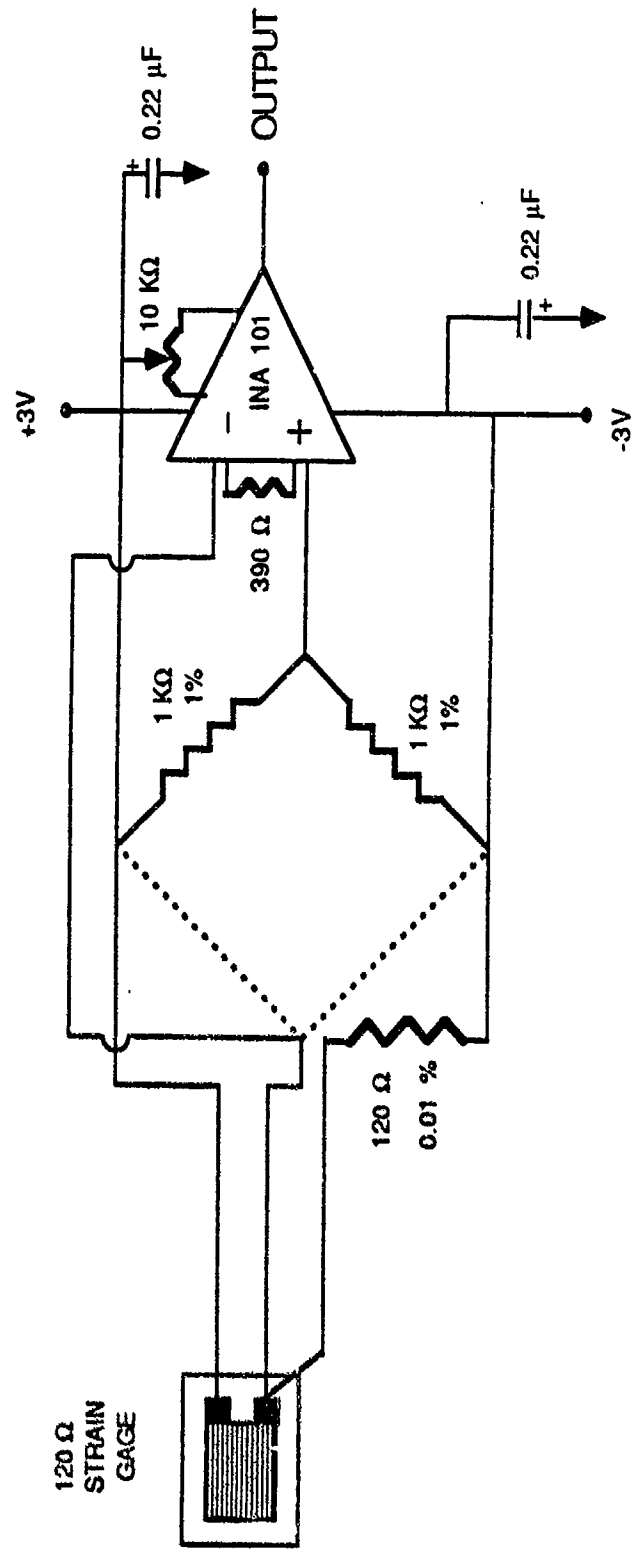

Figure 4.4. Electronic Circuit for Strain Gages

volt change in the output voltage of the amplifier (δV_{oA}), strain can be calculated as follows:

$$\varepsilon = - \frac{4\delta V_o}{F\ V_i}$$

$$\begin{bmatrix}\text{Amplifier Output} \\ \delta V_{oA}\end{bmatrix} = \begin{bmatrix}\text{Amplifier} \\ \text{Gain}\end{bmatrix} \text{ X } \begin{bmatrix}\text{Bridge Output} \\ \delta V_o\end{bmatrix}$$

$$\varepsilon = - \frac{4\delta V_{oA}}{F\ V_i\ (\text{Amplifier Gain})}$$

For F= 2.065, V_i = +_ 3 Volts = 6 Volts

$$\varepsilon = - \frac{4 \times 1}{2.065 \times 6 \times 100} = -3.22 \text{ X } 10^{-3} \text{ Strain/Volt}$$

This is equivalent to 3.22 microstrains per milivolt of amplifier output.

To verify this relationship, all eight strain gage channels were calibrated. An aluminium cantilever beam with a 120 ohm strain gage attached to it was loaded. Three different loads were applied which produced tensile strains in the gage. The three tests were then repeated with the beam in a reversed position which resulted in compressive strains. In each case the static strain in the gage was measured both by a commercial strain gage indicator (Vishay/ Ellis 10) and by each of the eight strain gage channels. Table 4.1 shows the results and the calibration values (sensitivities) obtained for a strain gage with a

gage factor of 2.10. Equivalent calibration values (sensitivities) for strain gages used in the tests which had gage factors equal to 2.065 and 2.05 are calculated using the following equation which is derived from equation 4.6.

$$\left[\begin{array}{c}\text{Sensitivity at}\\ \text{New}\\ \text{Gage Factor}\end{array}\right] = \left[\begin{array}{c}\text{Sensitivity at}\\ \text{Gage Factor}\\ \text{Equal to 2.10}\end{array}\right] \times \left[\frac{2.10}{\text{New Gage Factor}}\right]$$

Channel No. 3 shows a different calibration factor than the others which may be due to lack of precision of the resistors in the Wheatstone bridge.

For noise considerations, it is important that the lead wires connecting the strain gages to bridge completion units be twisted and shielded and the shield be grounded properly at the ground surface on the bridge completion board. The cable used in these tests was MicroMeasurements' type 326-DSV which is a stranded tinned-copper wire, 3-conductor twisted cable with vinyl insulation, braided shield and vinyl jacket. Separate ground wires were used for each amplifier. The two-wire outputs for all channels exited the centrifuge through slip rings. Each pair of wires corresponding to a strain gage channel was then connected to a coaxial cable through a BNC connector. Coaxial cables (30 feet long) then carried the signals to Nicolet digital storage oscilloscopes. Figure 4.5 shows the overall schematics of the strain gage setup.

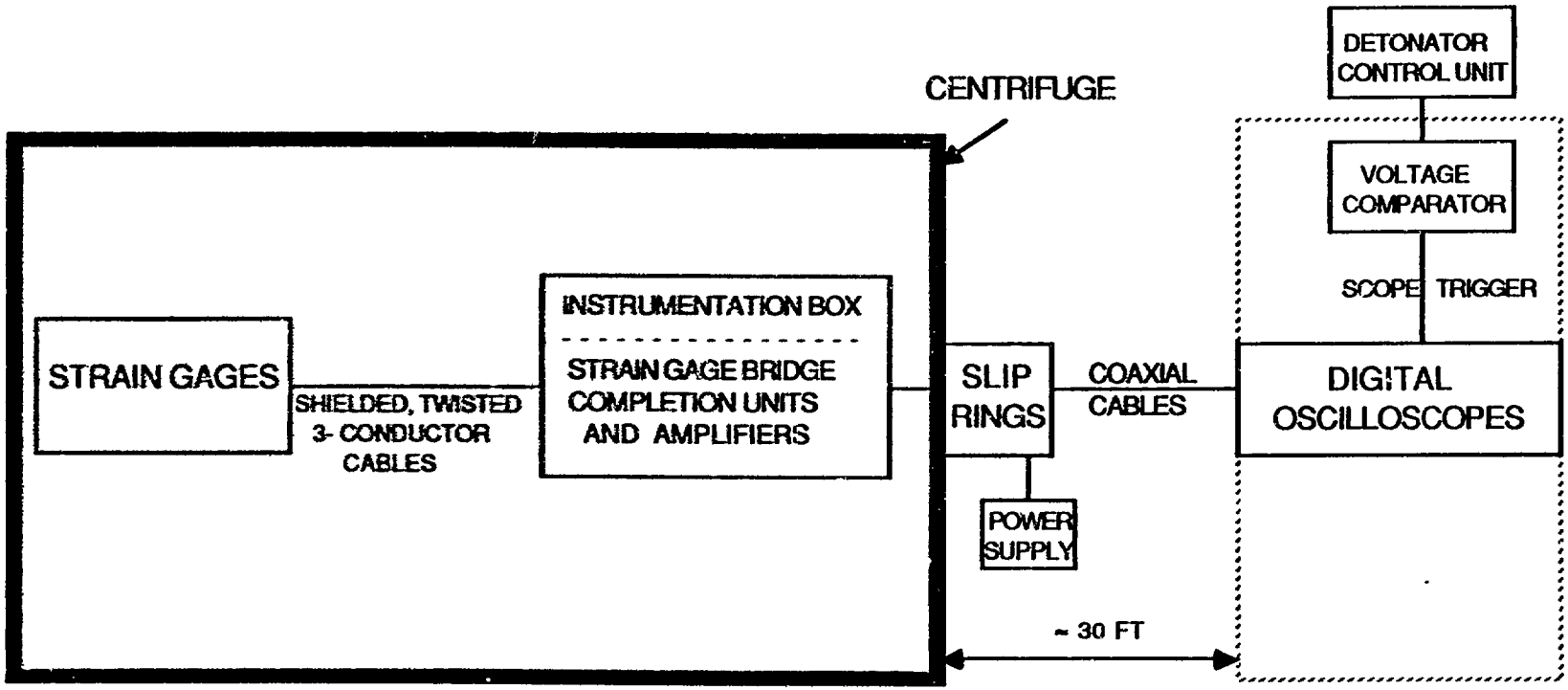

Figure 4.5. Block Diagram for Strain Gage Setup in the Centrifuge

Table 4.1
Strain Gage Sensitivity Measurements**

	Micro Strain	Amplifier Output Voltage (Milivolts) For Strain Gage Channels							
		1	2	3	4	5	6	7	8
TENSION	0	0	0	0	0	0	0	0	0
	500	158	159	202	155	159	162	160	158
	684	216	216	288	211	217	221	217	216
	860	273	274	373	268	274	279	273	273
COMPRES	0	0	0	0	0	0	0	0	0
	-500	-159	-158	*	-162	-162	-160	-160	-158
	-689	-215	-216	*	-215	-217	-220	-219	-216
	-868	-270	-274	*	-270	-271	-279	-278	-273
		Sensitivities (μstrain/mvolt)							
	F=2.10	3.179	3.161	2.069	3.181	3.159	3.104	3.138	3.169
	F=2.065	3.233	3.215	2.104	3.235	3.213	3.157	3.191	3.223
	F=2.05	3.257	3.238	2.120	3.259	3.236	3.180	3.215	3.246

** Excitation Voltage = ±3 Volts
* Out of Range

4.2.1.4 Strain Gage Setup on the Test Structure

A total of eight strain gages were used on each structure. Their locations are illustrated in Figure 4.6. Considering the existence of axial strains in the slabs and walls of the structure under loading in addition to flexural strains, the gages were applied in pairs, one on the outside and the other on the inside of the structure. This arrangement would allow calculation of axial and

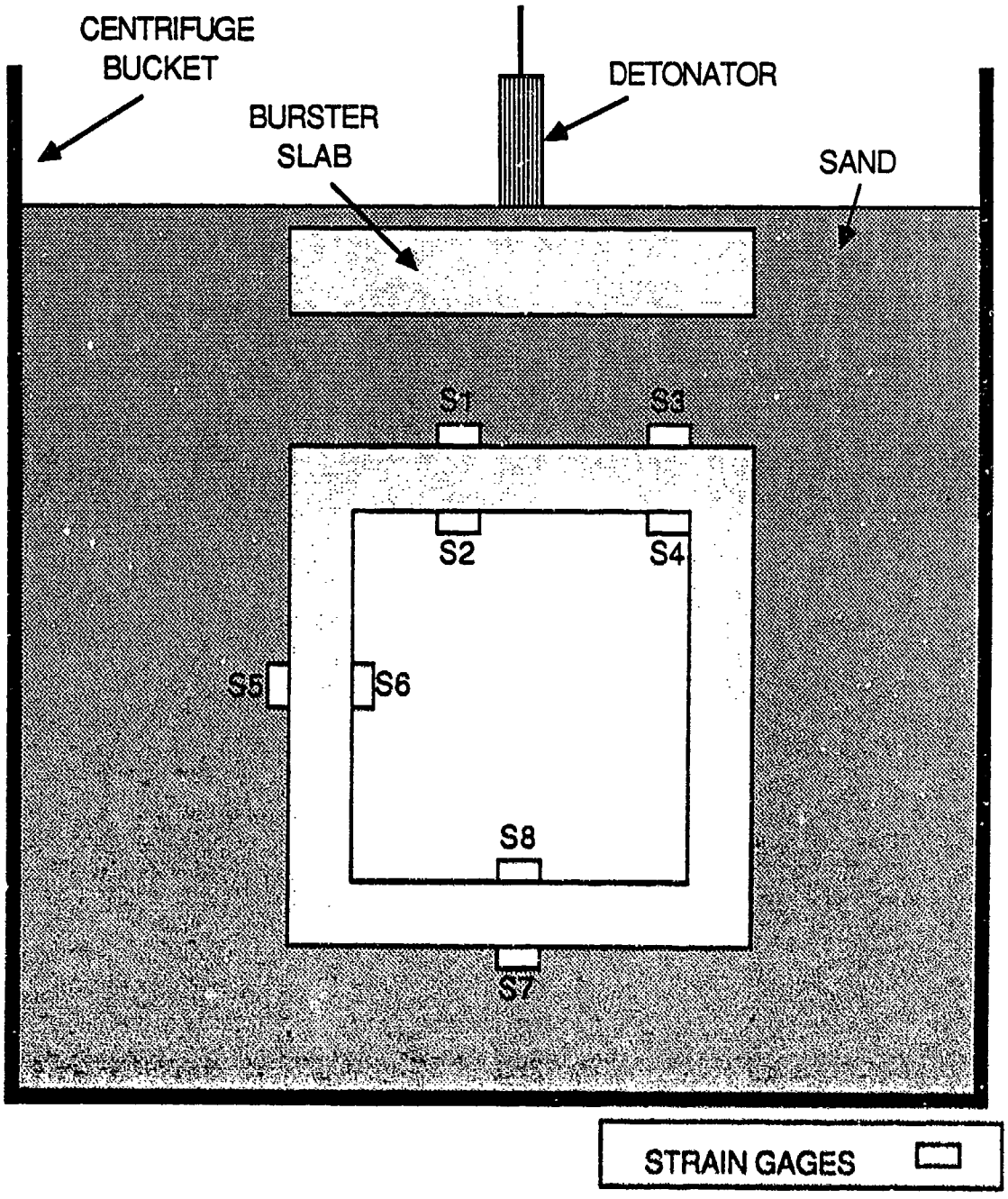

Figure 4.6. Strain Gage Locations on the Structural Model

flexural strains from the total strains measured on the two gages. Assuming linear strain distributions, total strains are the algebraic sum of axial and flexural strains (figure 4.7).

$$\varepsilon_a + \varepsilon_f = \varepsilon_o$$

$$\varepsilon_a - \varepsilon_f = \varepsilon_i$$

Therefore,

$$\varepsilon_a = \frac{\varepsilon_o + \varepsilon_i}{2} \qquad \text{Equation 4.7}$$

And,

$$\varepsilon_f = \varepsilon_o - \varepsilon_a \qquad \text{Equation 4.8}$$

Or

$$\varepsilon_f = \varepsilon_a - \varepsilon_i \qquad \text{Equation 4.9}$$

The size of strain gages used in the tests were chosen considering several factors. First, the gages have to be small relative to the size of the structural model. For example, a gage length of 1/4 inch in a 1/60 scale model is equivalent to a 15-inch long gage on the prototype structure. This may or may not be sufficiently small depending on the strain gradient in the immediate vicinity of the gage. Second, the gage length has to be several times larger than the maximum aggregate size in the microconcrete mix so that the gage readings would be indicative of overall structural strains rather than local strains in the aggregate. Third, physical restrictions related to the application of extremely small gages in

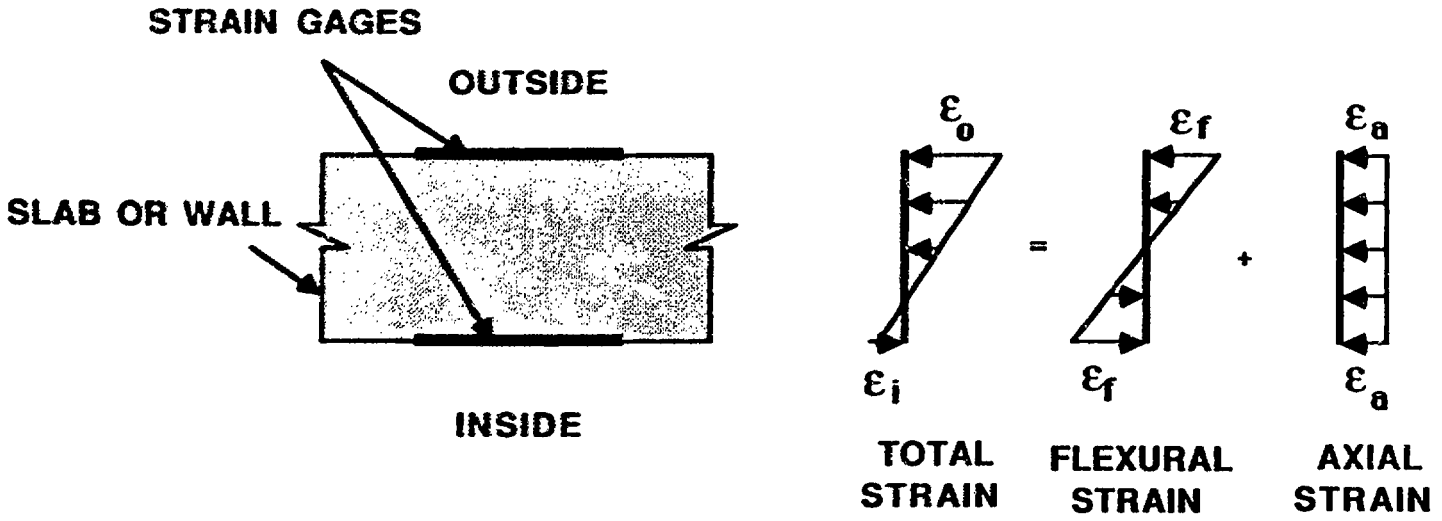

Figure 4.7. Combined Axial and Flexural Strains

hard-to-access areas may be important. Considering the above factors, a gage length of 1/4 inch was selected for these tests. The gages are manufactured by Micro-Measurements. The gages were installed according to the directions recommended by the manufacturer.

4.2.2 Piezoelectric Shock Pressure Transducers

In this study, the pressure transducers were used to determine the shock pressure applied on the structure due to blast loading. A piezoelectric material was chosen for transducer development because of the wide dynamic range and high resonant frequencies associated with piezoelectric transducers (Riedel, 1986).

4.2.2.1 Introduction to Piezoelectricity

Piezoelectricity is defined by W. G. Cady (1964) as "electric polarization by mechanical strain in crystals belonging to certain classes, the polarization being proportional to the strain and changing sign with it" (p. 4) In other words, piezoelectric materials generate electrical charge when subjected to pressure. In fact piezoelectricity means "pressure electricity" (Kantrowitz, et al., 1979, p. 308). Pierre and Jacques Curie discovered this property in 1880 (Cady, 1964).

Some materials such as Rochelle salt, tourmaline and quartz are naturally piezoelectric. Some other materials, called ferroelectric, can be made piezoelectric through

artificial polarization, in which material characteristics can be controlled through the manufacturing process (Endevco 101, 1986).

The major advantage of piezoelectric materials when used as shock pressure transducers is their large bandwidth. In addition, they are self-generating and do not need a power supply to generate an output.

In addition to their sensitivity to pressure, piezoelectric materials also generate electrical charges when subjected to temperature variations. This effect is called pyroelectricity and is not a favorable effect in shock pressure transducers because such pressure variations are not isothermal. Another disadvantage is that piezoelectric materials cannot be used for long-term static or steady-state pressure measurements.

Piezoelectric materials have been widely used in accelerometers and pressure transducers. Piezoelectric accelerometers are essentially "spring-mass" systems with the "spring" being the piezoelectric material and the mass applying compressive or shear forces (depending on the accelerometer design) on the spring when the system is subjected to accelerations.

The piezoelectric material used to develop shock pressure transducers for the tests reported here was artificially polarized Polyvinylidene Fluoride (PVDF). In the next section the general properties of PVDF are presented.

4.2.2.2 Polyvinylidene Fluoride (PVDF)

Polyvinylidene Fluoride (PVDF) is a semicrystalline polymer which has been widely used in commercial applications in chemical, food, and nuclear industries (Thorn EMI notes, 1986). The fact that this material could be made piezoelectric was discovered in 1969 (Meeks and Ting, 1983). The piezoelectric response is achieved through a special manufacturing process which includes electrical polarization. In addition to its strong piezoelectric properties, PVDF has a good acoustic impedance match to water which makes it suitable for use as hydrophones or underwater shock sensors (Meeks and Ting, 1984). The National Bureau of Standards has also conducted research on developing a stress gage for shock pressure measurements (Bur and Roth, 1985, Chung et al., 1985 and Holder et al., 1985). PVDF is manufactured in different shapes, sizes and thicknesses.

Figure 4.8 shows the three principal directions in a piezoelectric material with axes 1 and 2 in the plane and axis 3 perpendicular to the plane of the sample. The relationship between the generated charge per unit area, p, and the applied uniaxial stress, σ, can be written as (Nye, 1957)

$$P = d\,\sigma \qquad \text{Equation 4.10}$$

where d is the piezoelectric coefficient. In general for a

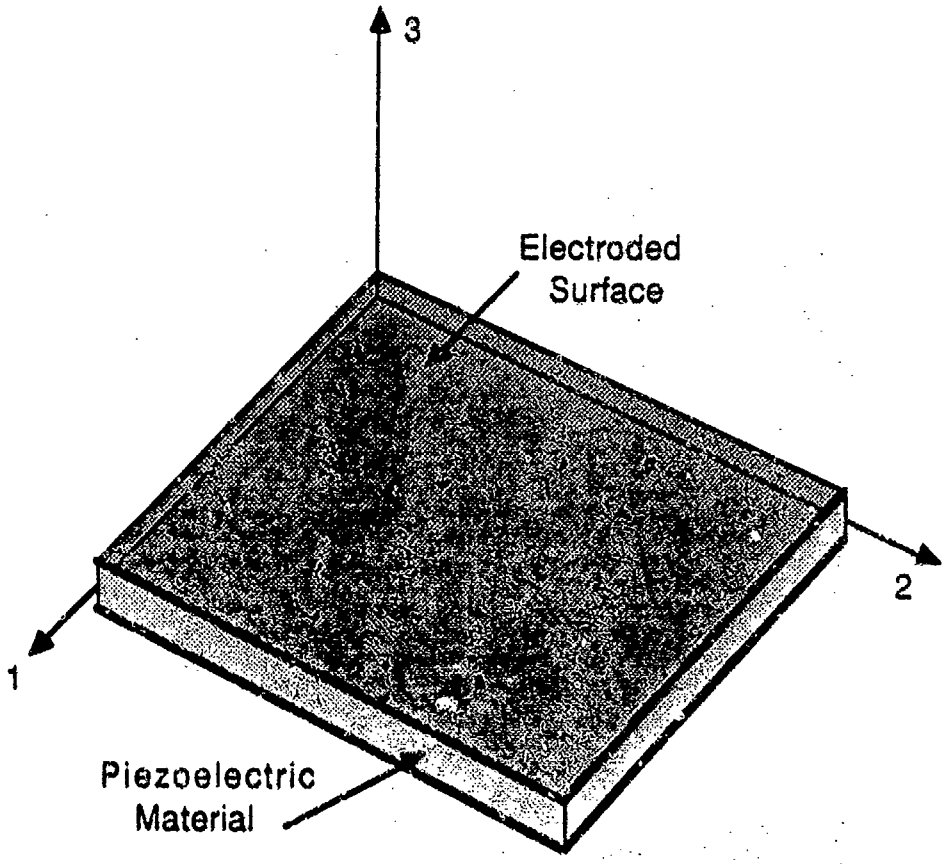

Figure 4.8. Principle Directions on a Piezoelectric Material

3-dimensional state of stress equation 4.10 can be rewritten in matrix form (Nye, 1957):

$$P_i = d_{ij}\,\sigma_j \quad (i= 1,2,3 : j= 1,2,3,\ldots,6) \qquad \text{Equation 4.11}$$

Or in expanded form,

$$\begin{bmatrix} P_1 \\ P_2 \\ P_3 \end{bmatrix} = \begin{bmatrix} d_{11} & d_{12} & d_{13} & d_{14} & d_{15} & d_{16} \\ d_{21} & d_{22} & d_{23} & d_{24} & d_{25} & d_{26} \\ d_{31} & d_{32} & d_{33} & d_{34} & d_{35} & d_{36} \end{bmatrix} \begin{bmatrix} \sigma_1 \\ \sigma_2 \\ \sigma_3 \\ \sigma_4 \\ \sigma_5 \\ \sigma_6 \end{bmatrix} \qquad \text{Equation 4.12}$$

where P_i is the vector of polarization charge per unit area, d_{ij} is the matrix of piezoelectric coefficients, and σ_j is the stress vector. The six components of σ_j represent the six independent terms in a general stress tensor

$$\sigma_1 = \sigma_{11}$$
$$\sigma_2 = \sigma_{22}$$
$$\sigma_3 = \sigma_{33}$$
$$\sigma_4 = \sigma_{23}$$
$$\sigma_5 = \sigma_{31}$$
$$\sigma_6 = \sigma_{12}$$

For PVDF, the d matrix has several zero components (Bur and Roth, 1985):

$$d_{ij} = \begin{bmatrix} 0 & 0 & 0 & 0 & d_{15} & 0 \\ 0 & 0 & 0 & d_{24} & 0 & 0 \\ d_{31} & d_{32} & d_{33} & 0 & 0 & 0 \end{bmatrix}$$

When the two surfaces perpendicular to axis 3 are electroded, the electrical charge, P_3 can be written as

$$P_3 = d_{31}\,\sigma_1 + d_{32}\,\sigma_2 + d_{33}\,\sigma_3$$

When there is a hydrostatic state of stress

$$\sigma_1 = \sigma_2 = \sigma_3 = \sigma$$

Therefore,

$$P_3 = d_{31}\,\sigma + d_{32}\,\sigma + d_{33}\,\sigma$$

$$P_3 = (d_{31} + d_{32} + d_{33})\,\sigma$$

Or

$$P_3 = d_h\,\sigma$$

where d_h is the hydrostatic piezoelectric coefficient. Therefore,

$$d_h = d_{31} + d_{32} + d_{33}$$

The PVDF sample used in the tests reported here is produced by Thorn EMI Central Research Laboratories in England. The sample contained microvoids in order to improve its piezoelectric properties. Table 4.2 shows the properties of the PVDF sample as reported by the manufacturer.

Meeks and Ting (1983,1984) conducted a series of hydrostatic and dynamic tests on voided and nonvoided, 0.5 mm thick, PVDF samples. They concluded that relatively high

Table 4.2

General Properties of PVDF Sample

SAMPLE NO	3717B1
PVDF THICKNESS	570 μm
ELECTRODE THICKNESS	≈ 10 μm Copper
ELECTRODE/POLYMER ADHESION	> 14 MPa
Er	7.8
dh	13.4 pCN^{-1}
gh	178 $mVm^{-1} Pa^{1}$
SENSITIVITY	-199.9 dB (rel 1V μPa^{-1})
d31	≈ 15 $pCN-1_{-1}$
d32	≈ 0.25 pCN^{-1}
d33	≈ -28 pCN^{-1}

Provided By THORN EMI Central Research Laboratories

pressures applied on voided samples can cause the collapse of microvoids and thereby result in a nonlinear, irreversible response while nonvoided samples exhibited linear response up to pressures as high as 10000 psi in both hydrostatic and dynamic tests. However, non-voided samples show smaller piezoelectric sensitivities. Test results indicate that for relatively low amplitude pressures (less than 2000 psi), the response of voided samples are also close to linear. The degree of linearity increases with a decrease in the number of voids at the cost of a decrease in the value of piezoelectric coefficients. Meeks and Ting (1984) also evaluated the frequency response of non-voided PVDF for underwater shock-wave sensor applications. They reported a 2-MHZ bandwidth and very little high-frequency ringing. These factors are both favorable in shock-wave sensors which may encounter high frequency signals.

4.2.2.3 PVDF Pressure Transducer

The transducer used for the tests reported here was a 1/4 in X 1/4 in square which was cut from a sheet of 570 μm thick, copper electroded PVDF material. The selection of size was based on several factors. First, the gage size should be small compared to the size of the structural model. Second, the gage dimensions have to be at least 10 times the mean soil grain size (Bur and Roth, 1985). Third, the aspect ratio of gage thickness to gage size should be

less than 1/5 (Bur and Roth, 1985). Of course, the size is also limited by the practical restrictions in building and working with small gages.

Two 30-gage stranded wires were attached to the two electroded surfaces on the gage. These wires can be satisfactorily soldered to the copper electrodes by following the procedures recommended by the manufacturer:

1. Clean the solder area by dipping it in a 3% solution of sulfuric acid for a few seconds. Then wash thoroughly in water and dry it.

2. Place a small piece of solder on the electrode surface and place the tinned wire on top of, and perpendicular to the solder.

3. Apply the soldering iron to the wire and remove it quickly as soon as the solder melts.

The above procedure provides for a satisfactory connection. However, when the gage is used at the soil-structure interface, the gage surface must be smooth enough to have full contact with the concrete surface. This might not be possible if there is a blob of solder on the surface. In addition, if extreme care is not taken, heat from the soldering iron may deform or damage the PVDF. Based on these considerations, it was decided to use silver filled epoxy to attach wires to the electrode surfaces as suggested by Meeks and Ting (1983, 1984). The following is a step-by-step procedure used in these tests to obtain satisfactory wire connections.

1. To clean the gage, dip it in a 3% solution of sulfuric acid for a few seconds. Then wash it thoroughly in water and dry it.

2. Expose a few millimeters of a 30 gage stranded wire and place it on top of the electroded surface in such a way that only the exposed wire is on the surface. Tape it down as shown in Figure 4.9.

3. Mix the two components of silver-filled conductive epoxy.

4. Apply a small amount of epoxy on the exposed wire.

5. Use a piece of masking tape to cover the epoxy, wire and the gage. This procedure would level the epoxy to a smooth surface. Let the epoxy cure for a few hours.

6. Remove the masking tape and check the wire connection. Repeat steps 2 through 6 for the other electroded surface.

7. Use polyurethane coating to cover the gage for protection.

The silver-filled epoxy used was Dexter Hysol's Type KS0002. The polyurethane coating used was Micro-Measurements' M-Coat A solution.

Another important consideration is the procedure for applying the gage on the concrete surface for shock pressure measurements at the soil-structure interface. The objective is to measure σ_3 from the measured charge P_3 in the following equation:

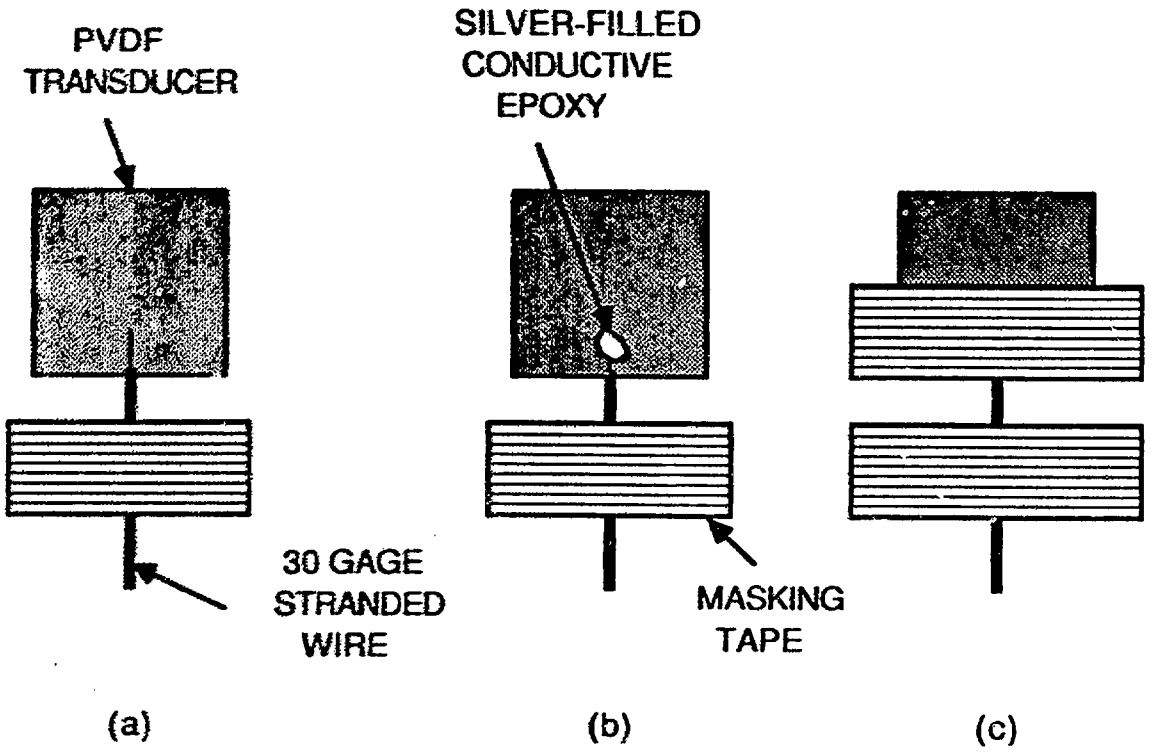

Figure 4.9. Lead-Wire Attachment to PVDF Transducer

$$P_3 = d_{31}\,\sigma_1 + d_{32}\,\sigma_2 + d_{33}\,\sigma_3$$

If the gage were to be glued to the concrete surface, the structural strains in the concrete would result in in-plane strains and stresses in the gage (σ_1 and σ_2) which, in turn, would make unwanted contributions to the measured charge P_3. Therefore, it is essential to decouple the structural strains from the transducer response. This is done by taping, rather than glueing, the gage on the concrete surface. Reinforced nylon strapping tape was used to apply the gages on the concrete surface. Holder et al. (1985) used a similar method of gage application.

As mentioned earlier, the pyroelectric effects must be considered in piezoelectric transducer design. However, Chung et al. (1985) suggest that the temperature rise, for stresses below 2000 psi, in a gage embedded in soil is very small (0.6 °F) and, therefore, temperature correction is not required.

4.2.2.4 Electronic Circuits For Piezoelectric Transducers

There are two general ways for measuring the electrical response of piezoelectric transducers. One is based on voltage sensitivity and the other is based on charge sensitivity. In this section these two methods are discussed and compared. Also, the electronic circuitry designed for the tests reported here is described in detail.

4.2.2.5 Voltage Measurements

A simplified electronic representation of a piezoelectric transducer is shown in Figure 4.10(a) (Dove and Adams, 1964, Endevco 101, 1986). The transducer acts as a capacitor (C_p) which generates electrical charge when subjected to pressure. The open-circuit voltage output (V_o) is related to the generated charge q, and the internal capacitance of the transducer, C_p through the following equation:

$$V_o = \frac{q}{C_p}$$

When this transducer is connected to a voltage measuring instrument (Figure 4.10b), the capacitance of the connecting cables and the input capacitance of the measuring instrument introduce additional external capacitance C_e, to the circuit. Therefore, the voltage output V_o is a function of the total capacitance $C_p + C_e$:

$$V_o = \frac{q}{C_p + C_e}$$

The above equation indicates that the voltage output varies as a function of the external capacitance, and is therefore dependent on such factors as the length and type of cable used between the transducer and the instrument. This is not an ideal situation because each measurement would require an accurate knowledge of the total

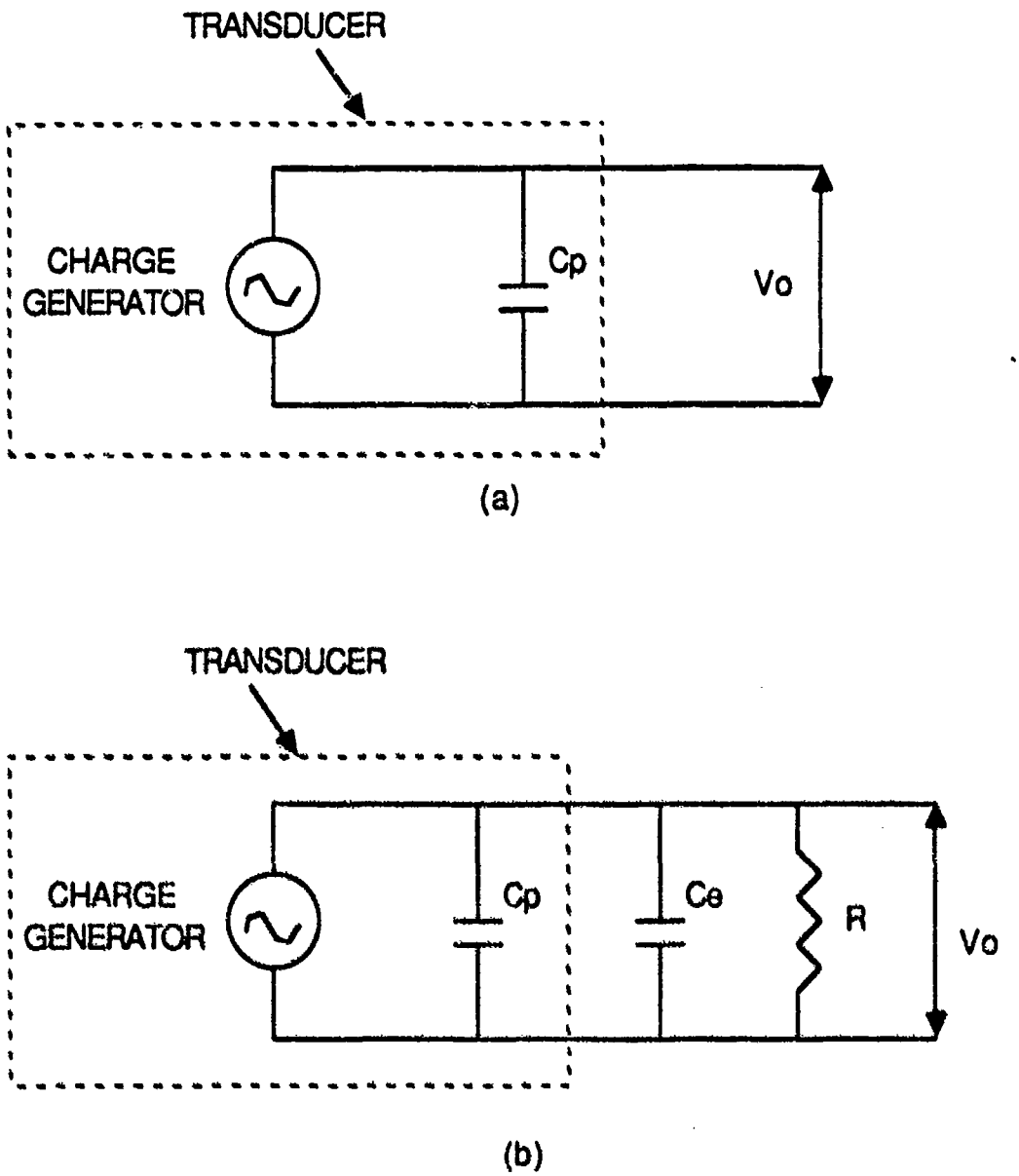

Figure 4.10. Voltage Measuring Method

capacitance. This problem can be eliminated by using the charge measurement method as explained in the next section.

Another consideration is the low frequency response of the transducer. The time constant of the circuit, which is the product of the input resistance of the instrument R and the total capacitance $C_p + C_e$, determines the cut-off point for the low frequency response of this system. The system filters out signal frequencies below the cut-off frequency (f)

$$f = \frac{1}{2\pi R (C_p + C_e)}$$

Gurtin (1961) presents a study of the effect of low-frequency response on transient measurements. Figure 4.11 shows the effect of variations in the time constant of the circuit RC, on the accuracy of response to transient signals. It is clear that as RC is decreased, the accuracy of the response is decreased. This is equivalent to the loss of low-frequency component of the signal. In the limit, when RC approches zero, the response approaches the differentiated form of the actual signal. It is necessary to use devices with very high input impedances (10^{12} to 10^{14} ohms) to accurately measure transient pulses. The high frequency response of the transducer is a function of its mechanical characteristics (Endevco 101, 1986).

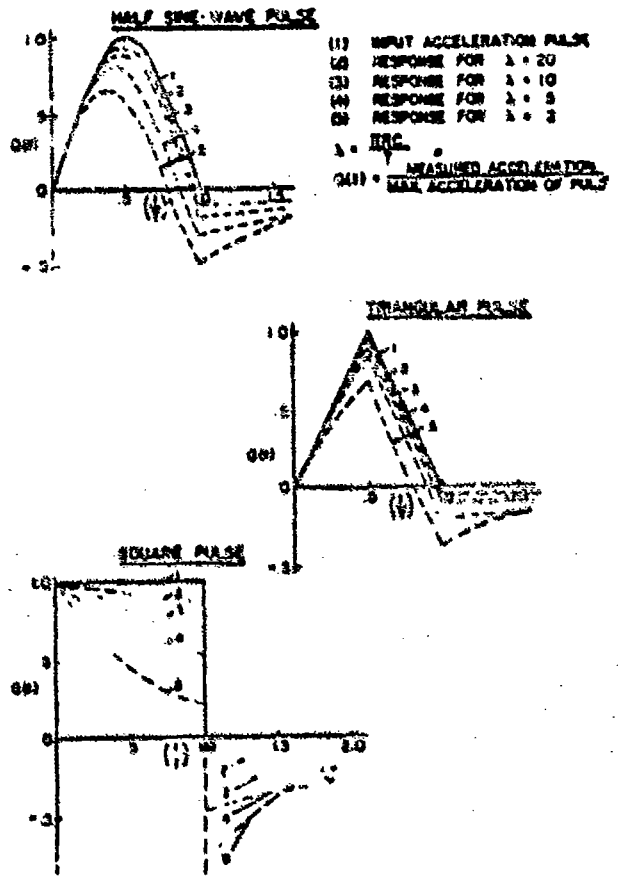

Figure 4.11. Effect of Time Constant on Signals (Gurtin, 1961) (Reprinted by Permission of the Society for Experimental Mechanics).

4.2.2.6 Charge Amplifiers

In this method, all the charge generated by the transducer due to applied pressure is transfered to, and deposited on, a capacitor with a known capacitance. The voltage across this known capacitor is then measured and the charge q is calculated from equation:

$$q = C\ V$$

In this case, C is fixed and is independent of cable capacitance. This is the major advantage of this method over the voltage sensing method explained earlier. The basic electronic circuit is shown in Figure 4.12 (Endevco General Catalog, 1986). The major elements of the circuit are an operational amplifier and a feedback capacitor C_f. This arrangment is called a charge amplifier. The operational amplifier, through its feedback loop, maintains point S at virtual common. The charges on the transducer appear and accumulate on the feedback capacitor C_f as they are generated. Since point S is at virtual common, the output voltage of the operational amplifier V_o is, at any time, equal to the voltage across C_f (Malmstadt et al., 1981). The charge q, calculated from the following equation, is the total accumulated charge by the transducer at any time, and is proportional to the applied pressure on the transducer.

$$q = C_f\ V_o$$

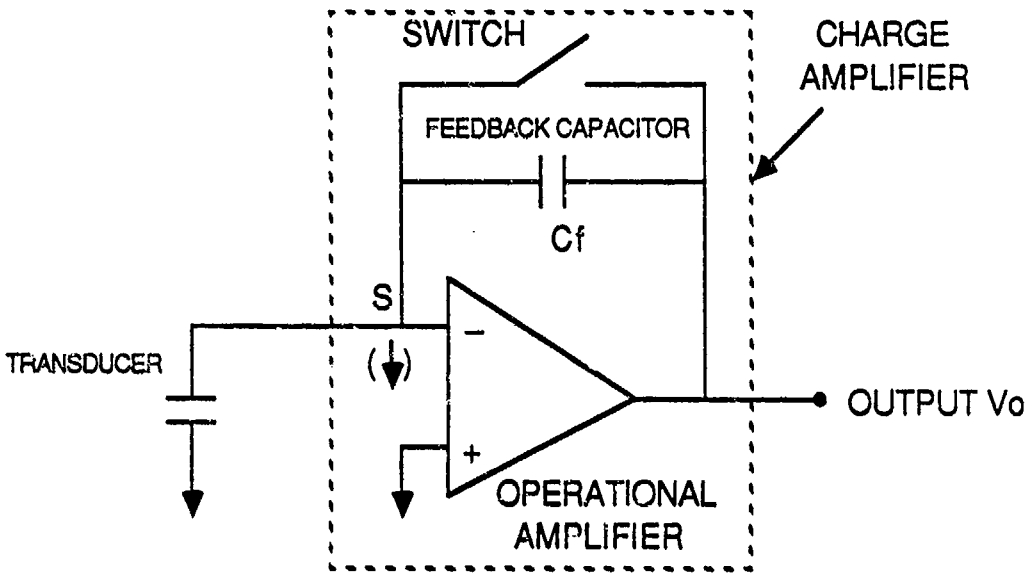

Figure 4.12. Basic Charge Amplifier

An electronic switch placed across the feedback capacitor is used to discharge the capacitor and reset the charge amplifier. This prevents the gradual drift in the output due to long-term integration of low-level leakage currents (Malmstadt et al., 1981).

Although the voltage output V_o is not a function of the length of cables connecting the transducer to the charge amplifier, long cables can increase the noise level and therefore should be avoided when possible (Endevco, 1986, Dove and Adams, 1964). The low frequency response of the charge amplifier is dependent on the low-frequency response of the amplifier (Endevco 101, 1986) and on the time constant R_fC_f, where R_f is the off-resistance of the electronic switch, and C_f is the feedback capacitor (Dove and Adams, 1964). The high frequency response of charge amplifier is a function of the input capacitance (transducer plus cable) and any resistance in the cable connecting the transducer to point S.

A very important consideration for noise reductions in high impedance piezoelectric transducers is the type of cable used to connect the transducer to the charge amplifier. Coaxial cables or shielded twisted-pair cables are recommended (Endevco, 1986). However, when coaxial cables are subjected to mechanical distortions such as vibrations, a separation of the cable dielectric and the outer shield can occur and thereby create low frequency "triboelectric" noise signals (Endevco 101, 1986). Therefore, it is

important to reduce the cable length and to prevent the flexing and vibration of the cable which could be significant in an explosive test. Specially treated cables can also be used to minimize this effect (Endevco 101, 1986).

4.2.2.7 Shock Pressure Measurements in a Centrifuge

On-board signal conditioning is recommended for piezoelectric pressure transducers in a centrifuge based on two main reasons. First, the reduction in the length of cable between the transducer and the charge amplifier reduces the noise level and improves the high frequency response (Dove and Adams, 1964). Second, such an arrangement would prevent the integration of noise signals from the slip rings. In addition to multiple charge amplifiers, electronic switches are required on-board to discharge the feedback capacitors.

Figure 4.13 shows a block diagram of the pressure transducer set-up in the centrifuge. Charge amplifiers and electronic switches are shown in an instrumentation box inside the centrifuge. Upon pressing the "fire" knob on the detonator control unit, a trigger signal is released 2 to 10 microseconds prior to the explosion. A voltage comparator is used to reduce the rise time of this trigger signal to less than 10 nanoseconds. This signal is then used to trigger the oscilloscopes. The relatively fast rise time of the signal insures that, regardless of the trigger levels set on individual oscilloscopes, the difference in

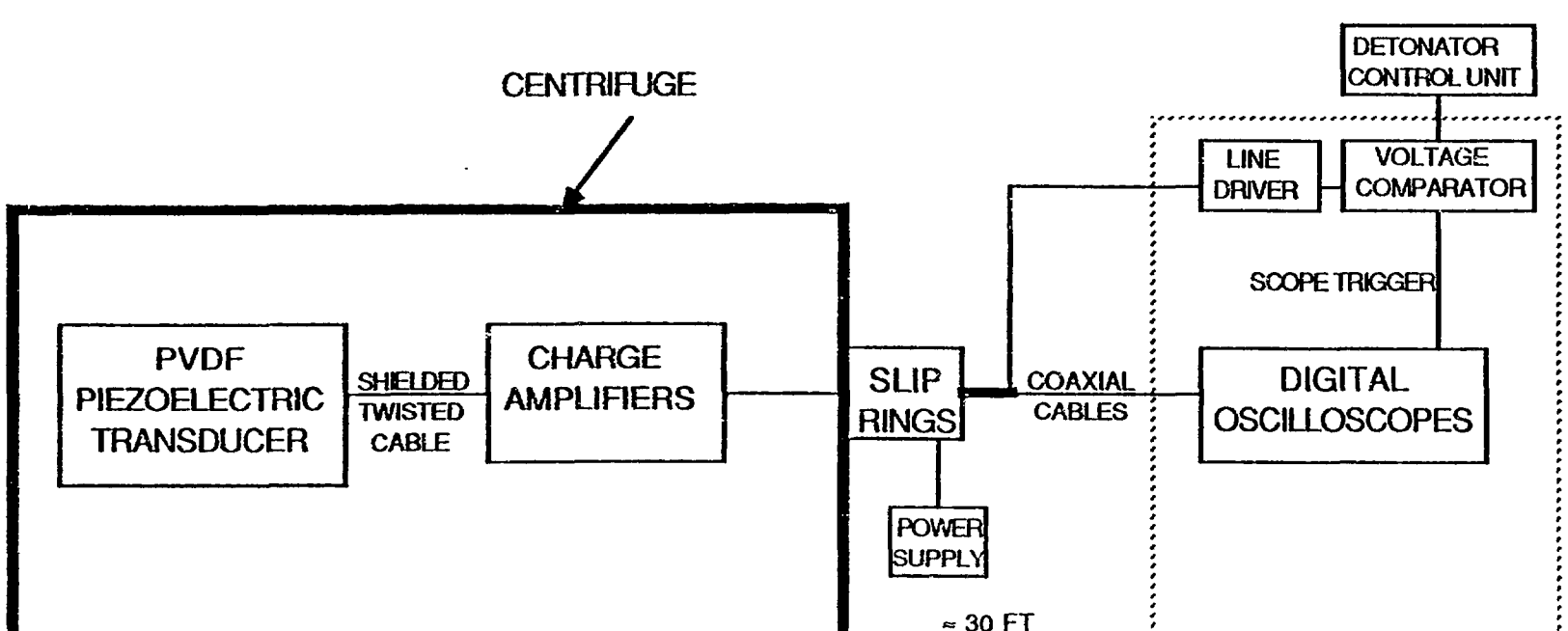

Figure 4.13. Block Diagram for Shock Pressure Transducers

trigger times on different oscilloscopes would be negligible (less than 10 ns). Therefore, all instrumentation channels on the oscilloscopes will have a common time base.

The output of the comparator is also used to activate the electronic switches inside the instrumentation box. However, because of the relatively long distance (approximately 30 feet) that this high frequency signal has to travel, it is important to use a line driver to prevent the distortion of the signal.

Figure 4.14 shows the electronic circuitry for the scope trigger and the line driver. The trigger signal from the detonator control unit has an amplitude of 30 volts. This amplitude is first reduced by using a voltage divider (30V X 1.1 KΩ/ 5.6 KΩ = 5.9 V). The noise floor for the comparator, beyond which the comparator (LM 361) output goes to the limit (5 Volts), is set at 0.5 Volts by using another voltage divider (12 V X 2KΩ/51 KΩ = 0.5 Volts). The comparator is a very high-gain amplifier with well-balanced difference inputs and controlled output limits (Malmstadt et al., 1981). If a signal larger than the noise floor (0.5 V) appears at pin 3, the comparator outputs a 5 volt signal with a very fast rise time.

A capacitor (0.68 μF) is used for filtering the reference voltage and two capacitors (1 μF) on the power supply are also used as noise filters. The comparator output is then used to trigger the oscilloscopes located

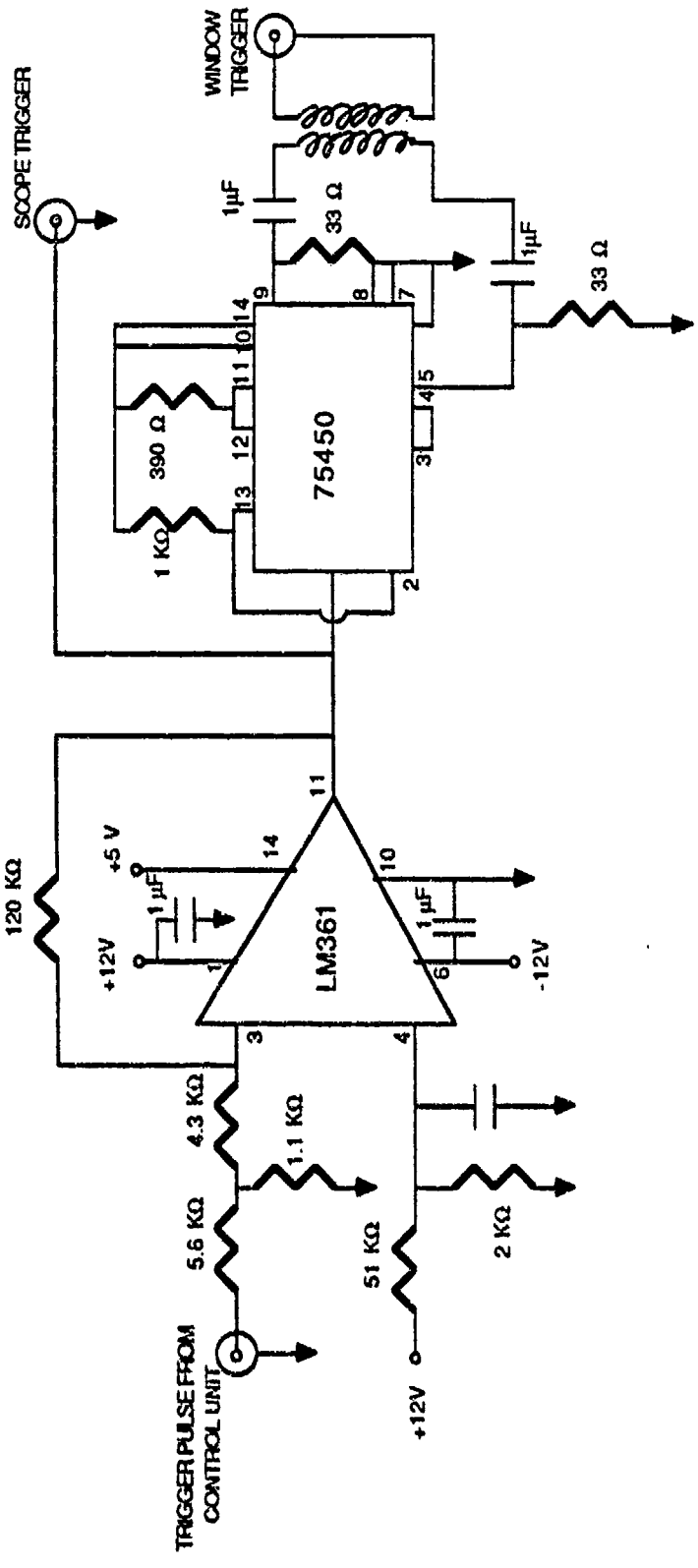

Figure 4.14. Scope Trigger and Line Driver

nearby. A line driver (DS 75450) is used to preserve the high frequency components of the comparator output over a distance of 30 feet to the centrifuge. An insolation transformer is used to float the cable: that is to disconnect the ground of this circuit from the ground in the instrumentation box in the centrifuge.

Figure 4.15 shows the charge amplifiers and other electronic circuitry on-board the centrifuge. A monostable multivibrator or one-shot (1/2 74221) is used to provide a window in which to accept data. This window is the time frame during which the electronic switches are activated and the feedback capacitors are not discharged. This time is a function of the external capacitance and resistors and can be changed by adjusting a variable resistor (10 KΩ). For the tests reported here, the window was set to exceed the time covered by the oscilloscope screens. DS 1488 is an interface driver and is used as a level shifter to interface two families of logic: CMOS and TTL.

Each charge amplifier has an analog switch (4066) which is placed across a feedback capacitor (1000 pF). Another switch (IH 5011) may be used instead in order to obtain better performance. AD 515 is a very high impedance electrometer operational amplifier. Information on all commercial electronic components used in the circuits explained here are given in Appendix A. A total of eight charge amplifiers were built and placed in the instrumentation box on board the centrifuge.

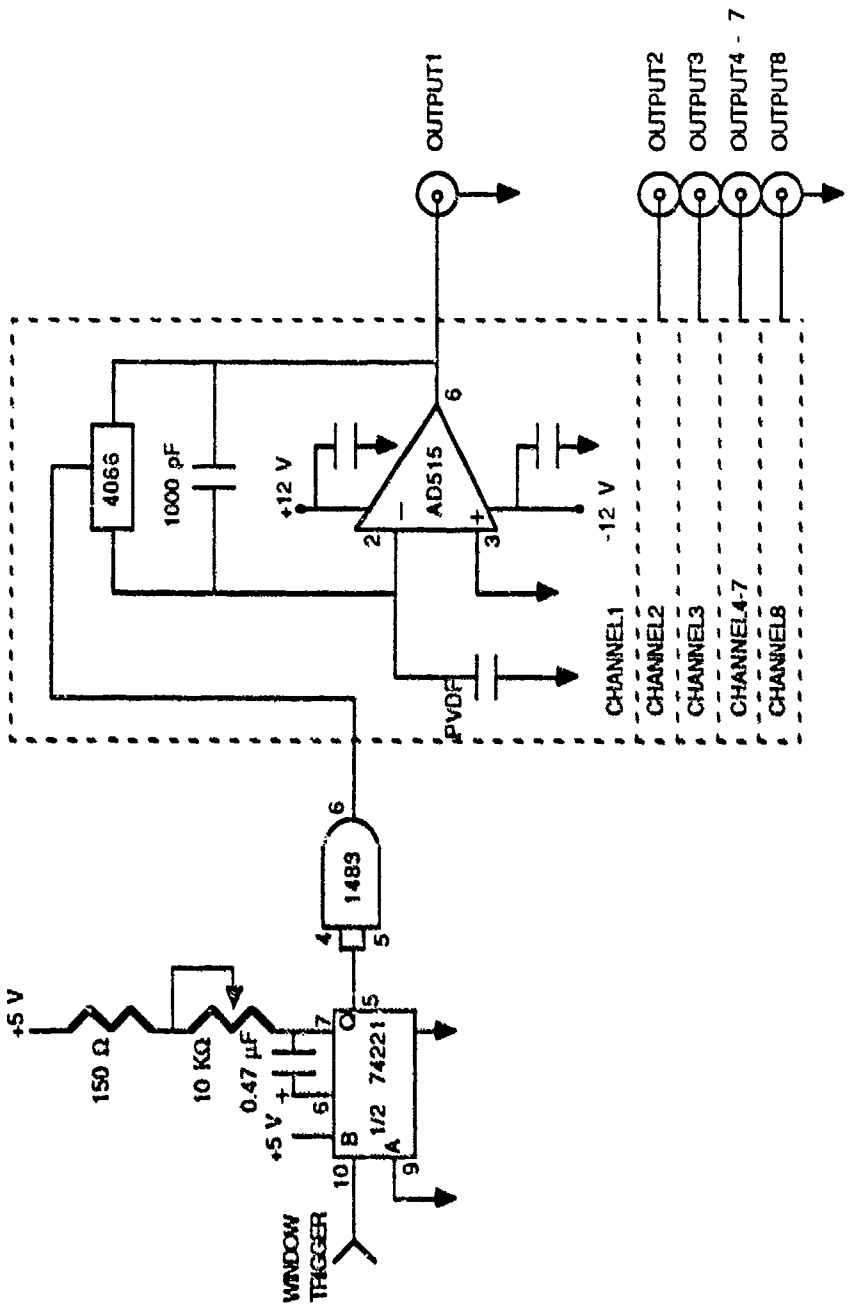

Figure 4.15. Charge Amplifier Circuits

4.2.2.8 Calibration of PVDF Pressure Transducers

In general, the output voltage of the charge amplifier can be related to the applied pressure as follows:

$$V_o = \frac{Q}{C_f} = \frac{A\ d\ \sigma}{C_f} \qquad \text{Equation 4.13}$$

where,

V_o = Output voltage of the charge amplifier

Q = Charge on the feedback capacitor

C_f = Capacitance of the feedback capacitor

A = Surface area of the pressure transducer

d = Piezoelectric constant

σ = Applied pressure

When A, d, and C_f are known, output voltage and stress can be directly related:

$$V_o = K\ \sigma \qquad \text{Equation 4.14}$$

Where,

$$K = \frac{A\ d}{C_f} \qquad \text{Equation 4.15}$$

The piezoelectric coefficient d_{33} given in Table 4.2 can not be used here for pressure measurements at the soil-structure interface, even though the stress direction is essentially perpendicular to the gage surface (direction 3). The reason is that the confining effect of concrete and soil creates a more complex state of stress in the gage resulting in a different apparent piezoelectric coefficient (Dragnich

and Calder, 1973). Therefore, it is essential that the calibration of transducers be conducted under conditions similar to the actual test.

A special test arrangement was designed for this calibration. A 1 inch-thick circular micro-concrete slab (3 inch diameter) was built. Three 1/4 in X 1/4 in PVDF gages were taped on the slab as shown in Figure 4.16. A cardboard cylinder with an inside diameter of 3 inches was placed around the slab such that it extended 1/4 inch above the top of the slab. A 1/4 inch-thick layer of sand was placed on top of the slab. The test specimen was then placed in an MTS testing machine to be subjected to cyclic loads. A 1 inch-thick circular steel plate and a load cell were placed on the specimen as shown in Figure 4.17.

Sinusoidal loads were applied on the specimen with varying frequencies of up to 50 hertz. Only one level of peak stress (162 psi) was tested because of an equipment malfunction after the first series of tests were completed. However, because of the relatively low stress levels (less than 2000 psi), the gage response is expected to be linear (Meeks and Ting, 1983).

The charge amplifiers and other electronic circuits used for the actual tests were also utilized for these calibration tests. The sequence of events was as follows: first, the load was applied on the specimen. second, the control unit of the detonator was used to send a trigger signal (no explosion) to activate the switches and trigger

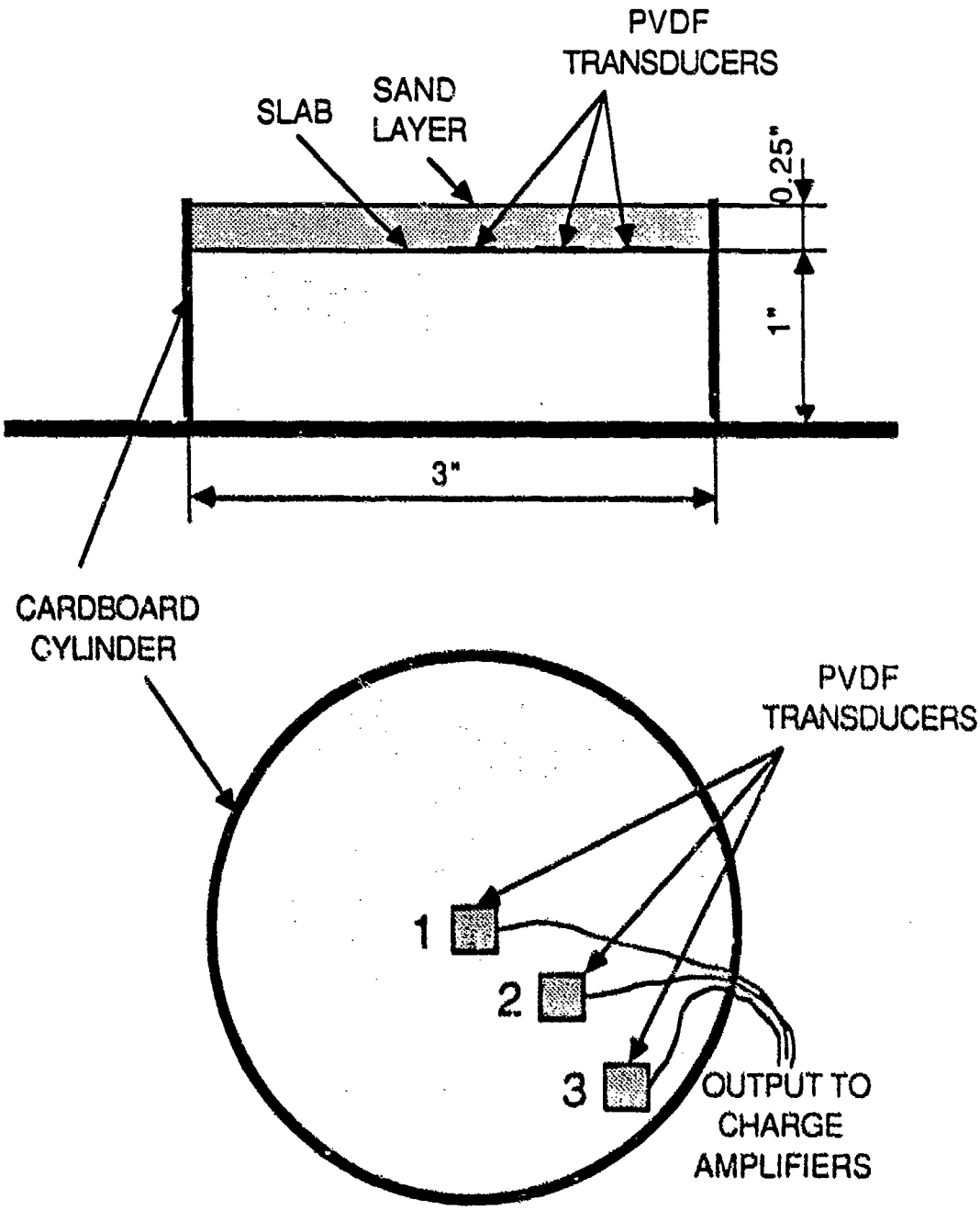

Figure 4.16. Test Specimen for Calibrating Pressure Gages

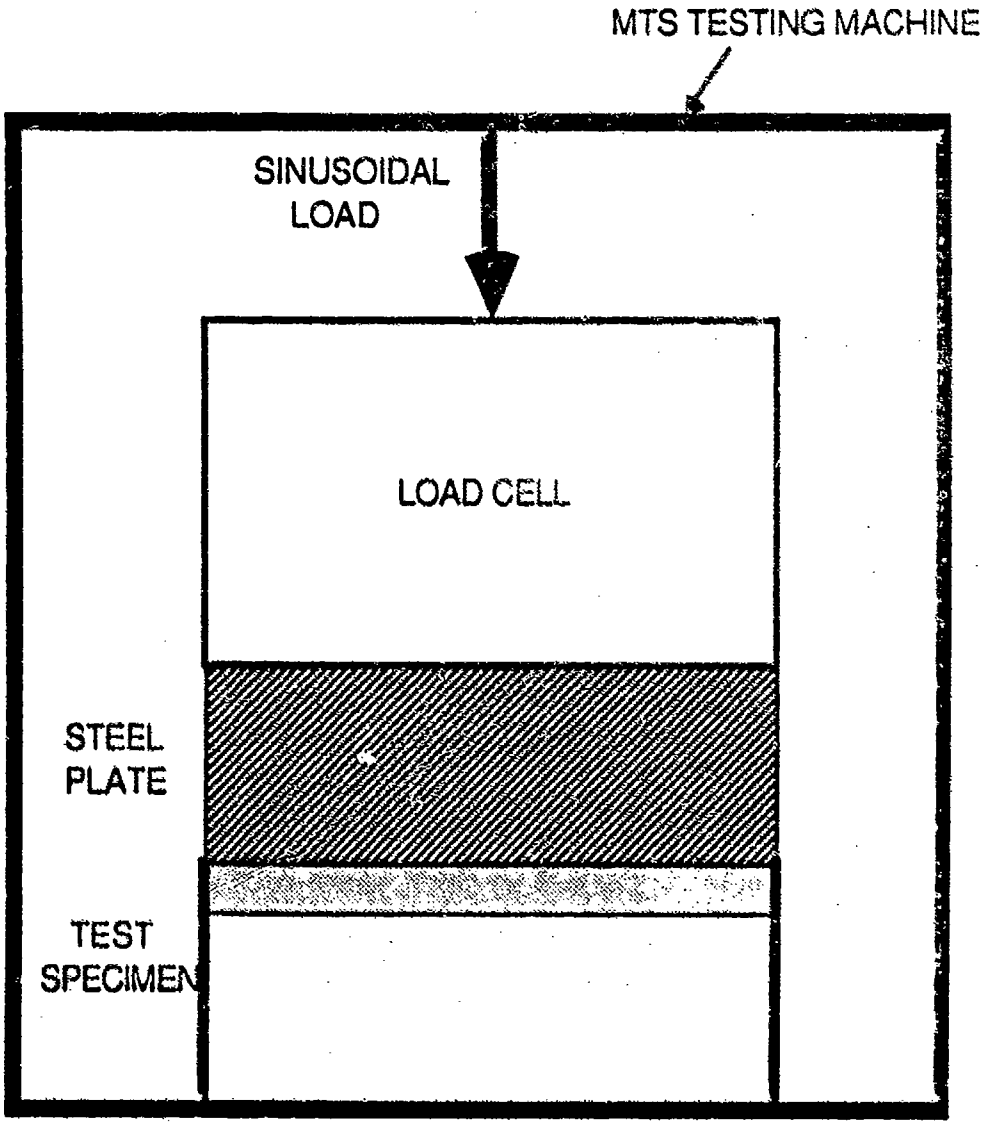

Figure 4.17. Test Setup for Calibrating Pressure Gages

the oscilloscope which, in turn, recorded the outputs of the load cell and the three charge amplifiers for the pressure transducers.

Figures 4.18 to 4.21 show the applied load and pressure gage response curves for different frequencies of up to 50 hertz. These figures indicate that, in all cases, the pressure gage response is sinusoidal and corresponds to the applied load. It is interesting to note that some pressure transducers show negative responses. This is due to the fact that, when the trigger signal is released, the pressure at that time is shown as zero on the output. Therefore, any pressure less than the pressure at trigger time appears as negative in the output. Thus, calibration is based on the ratio of peak-to-peak amplitudes of applied load and gage outputs rather than absolute peaks.

The amplitude of response for the gage closest to the edge of the slab (cardboard cylinder) is consistantly lower than the other two gages which exhibit similar responses. The reason for lack of uniformity of pressure near the edge of the slab is believed to be due to transfer of some of the load in that immediate area to the cylinder. The response of the gage located in that area is omitted from the calculation of calibration factor. Table 4.3 summarizes the calibration test results. These results indicate that frequency variations (up to 50 Hz) do not have a major influence on the calibration values.

The calibration factor (369 psi/volt) can be related to

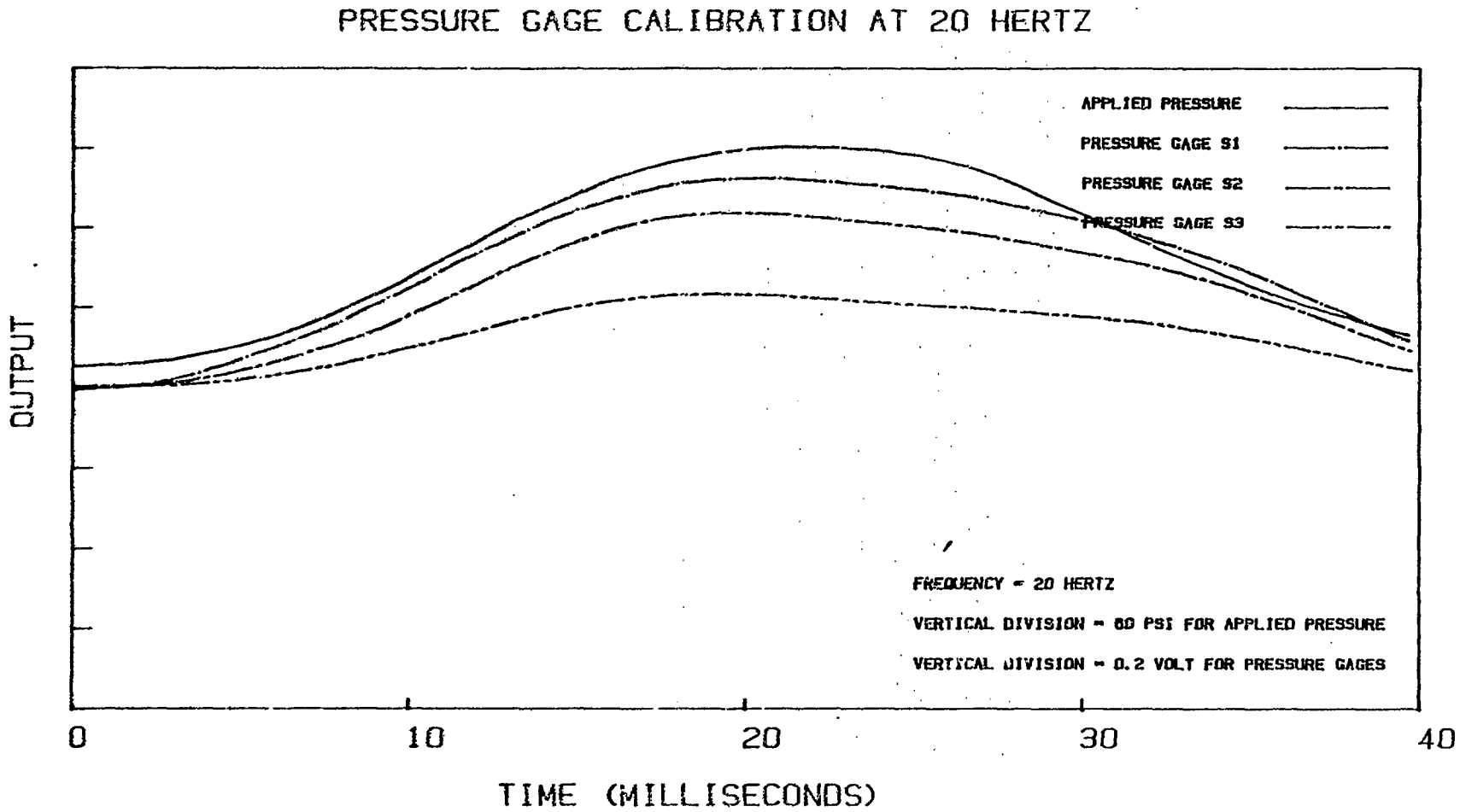

Figure 4.18. Pressure Gage Calibration at 20 Hertz

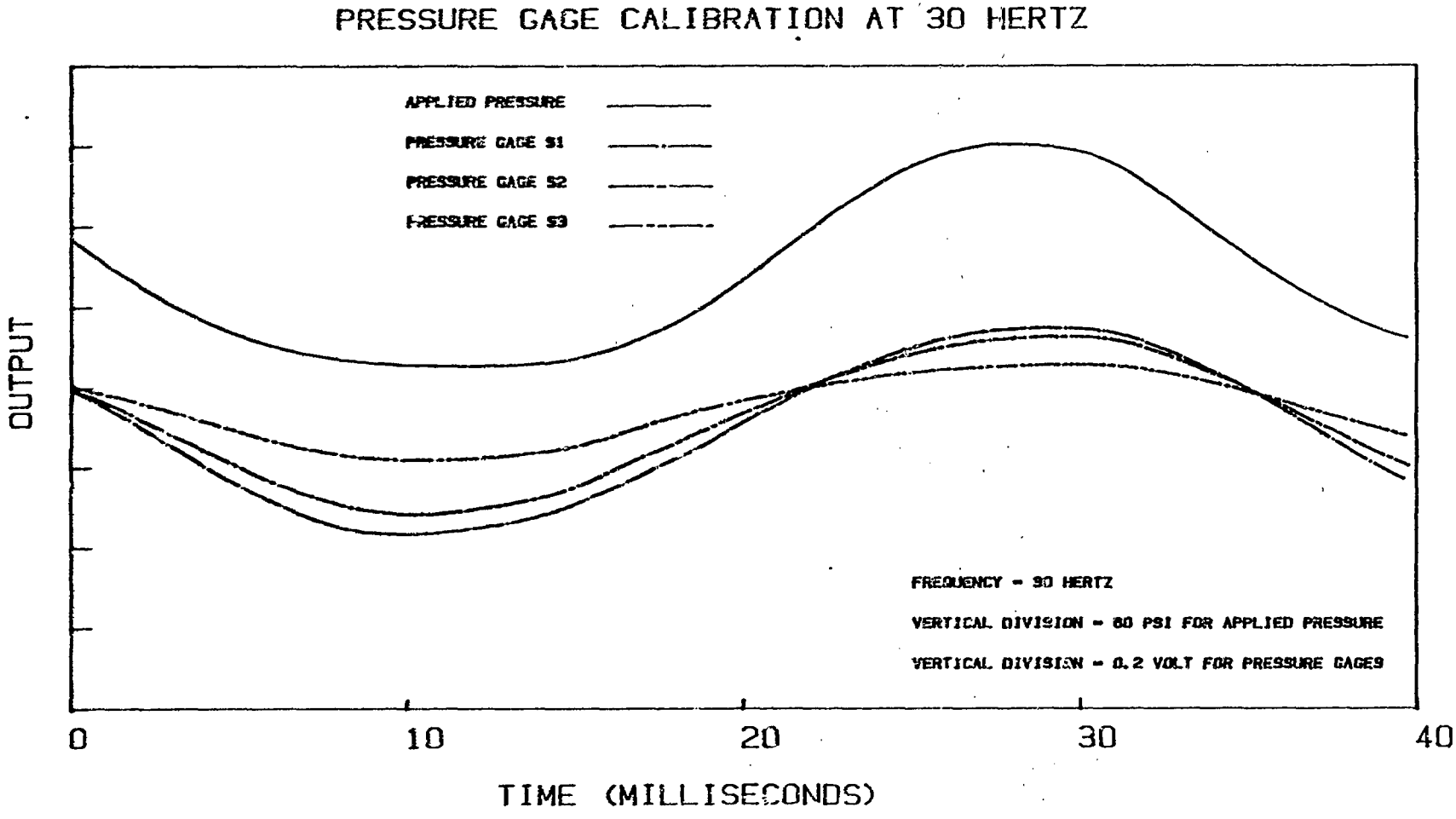

Figure 4.19. Pressure Gage Calibration at 30 Hertz

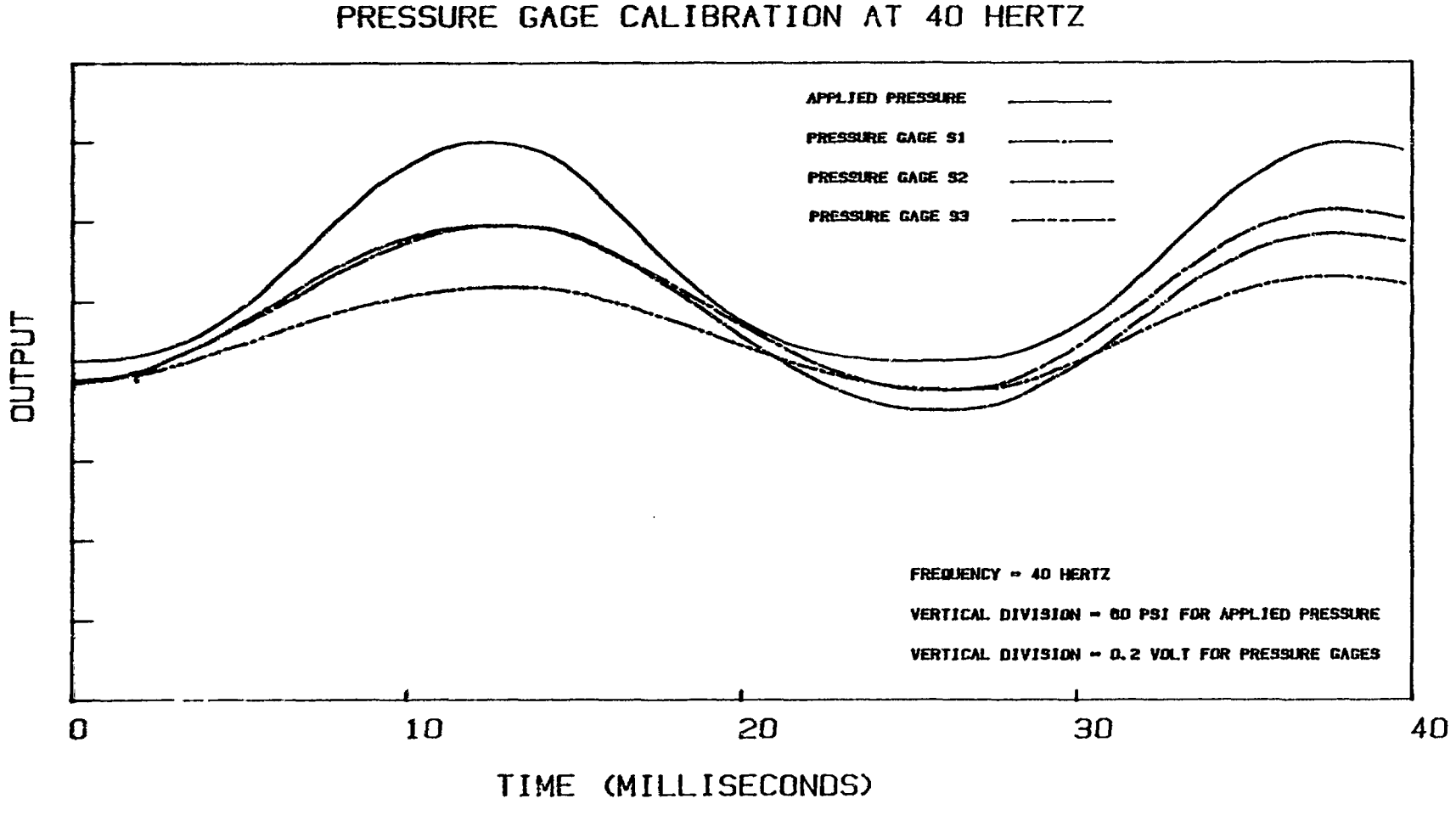

Figure 4.20. Pressure Gage Calibration at 40 Hertz

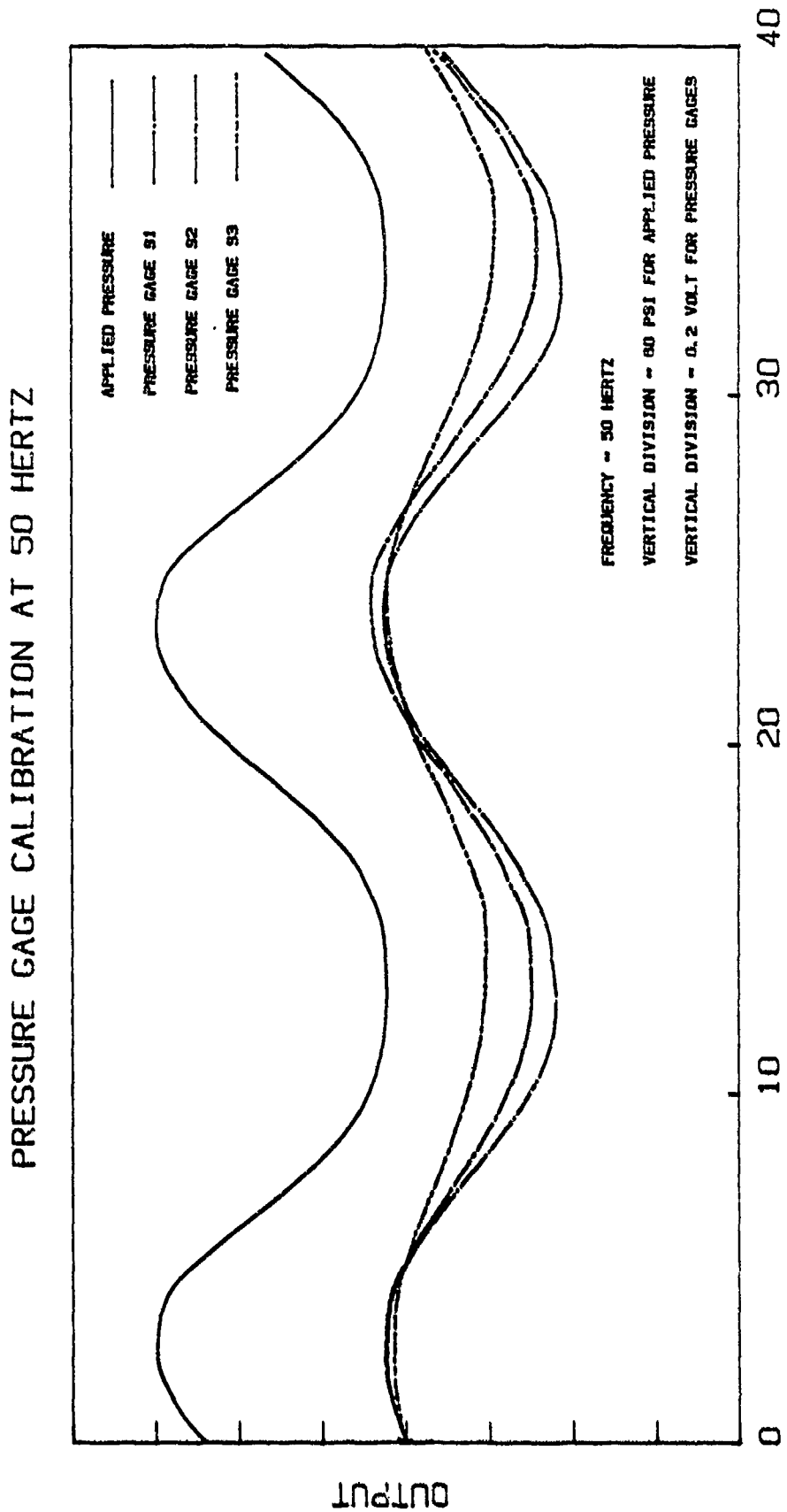

Figure 4.21. Pressure Gage Calibration at 50 Hertz

piezoelectric coefficient d through Equations 4.14 and 4.15.

Thus:

$$\frac{1}{K} = 369 \text{ psi/volt}$$

$$d = \frac{K\, C_f}{A} = \frac{1000 \text{ pF}}{(369 \text{ psi/volt})(1/16 \text{ in}^2)(4.488 \text{ N/lb})} = 9.66 \text{ pC/N}$$

Table 4.3

Calibration of Pressure Transducers

	Frequency (Hertz)			
	20	30	40	50
Load (lb)	1090	1100	1100	1100
Pressure (psi)	161	162	162	162
Gage 1 (volt)	.472	.512	.468	.414
Gage 2 (volt)	.418	.440	.414	.382
Gage 3 (volt)	.208	.238	.260	.236
Average G1 & G2	.445	.476	.441	.398
Calib. (psi/v)	362	340	367	407

Average Calibration Value = 369 psi/volt

4.2.2.9 Pressure Gage Setup on the Test Structure

A total of six PVDF pressure transducers (1/4 in X 1/4 in) were used on each structure. Their locations are shown in Figure 4.22. The gages were distributed around the structure in order to determine pressure distributions on the top slab and the side wall.

4.3 Piezoelectric Accelerometers

In this study, accelerometers were used to measure accelerations on the top slab and the side wall. Piezoelectric accelerometers are essentially spring-mass systems (Endevco, 1986) in which the mass exerts a force on the spring (piezoelectric material) when the base is subjected to accelerations. The amount of generated charge on the piezoelectric material is then related to acceleration. In small scale model tests, it is important that the mass and size of the accelerometer be as small as possible to prevent distortions in the structure response. Miniature accelerometers are commercially available which can be suitable for blast tests on small scale models. Baird (1984) presents an evaluation of different commercially available accelerometers for such tests.

4.3.1 Coriolis Accelerations

Acceleration measurements in a centrifuge may include unwanted components due to the nature of a rotating

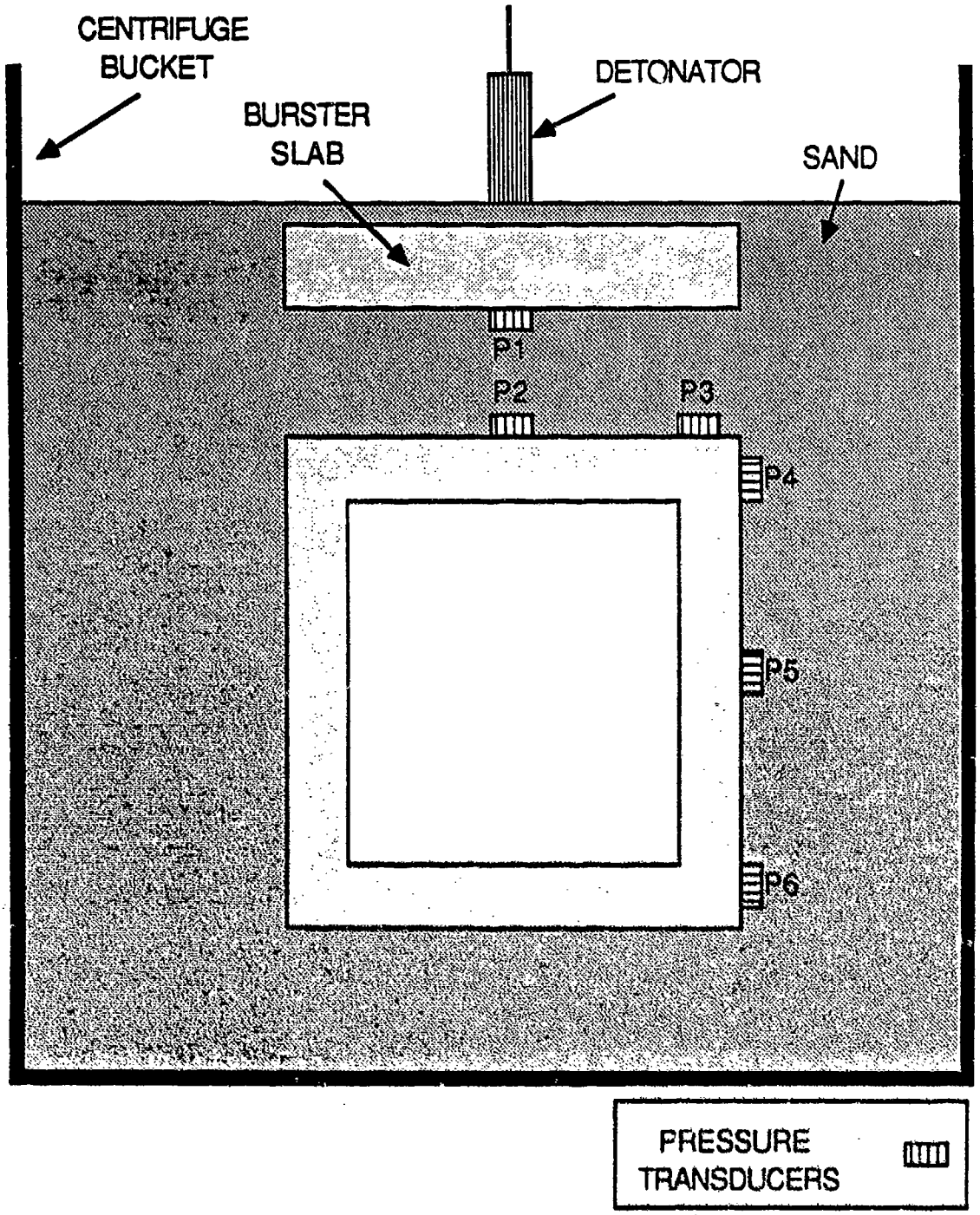

Figure 4.22. Pressure Gage Locations on the Model

coordinate system. Figure 4.23 shows an inertial coordinate system X Y Z and a coordinate system X'Y'Z' which moves and rotates with respect to X Y Z. The following equation relates the acceleration of point P in the two coordinate systems (D'Souza and Garg, 1984 and Baird, 1984):

$$\underline{a} = \underline{a}' + \ddot{\underline{r}} + 2\underline{w}x\dot{\underline{r}} + \dot{\underline{w}}x\underline{r} + \underline{w}x(\underline{w}x\underline{r}) \qquad \text{Equation 4.16}$$

where,

$\underline{a}$ = Acceleration vector for point P with respect to X Y Z (absolute acceleration)

$\underline{a}'$ = Acceleration vector for point O' with respect to X Y Z

$\underline{r}$ = Position vector for point P with respect to X'Y'Z'

$\dot{\underline{r}}$ = Velocity vector for point P with respect to X'Y'Z'

$\ddot{\underline{r}}$ = Acceleration vector for point P with respect to X'Y'Z'

$\underline{w}$ = Angular velocity vector for X'Y'Z'

$\dot{\underline{w}}$ = Angular acceleration vector for X'Y'Z'

In a centrifuge test, the angular velocity $\underline{w}$ is constant. Therefore,

$\dot{\underline{w}} = 0$ and $\underline{a}' = 0$

Therefore, for centrifuge tests equation 4.16 can be rewritten in the following form

$$\underline{a} = \ddot{\underline{r}} + 2\underline{w}x\dot{\underline{r}} + \underline{w}x(\underline{w}x\underline{r})$$

where $\underline{w}$ X ($\underline{w}$ X $\underline{r}$) is the centripetal acceleration and $2\underline{w}$ X $\dot{\underline{r}}$ is the coriolis acceleration. The magnitude of coriolis acceleration is proportional to the angular velocity of the centrifuge and the particle velocity in the rotating coordinate system. The direction of the coriolis

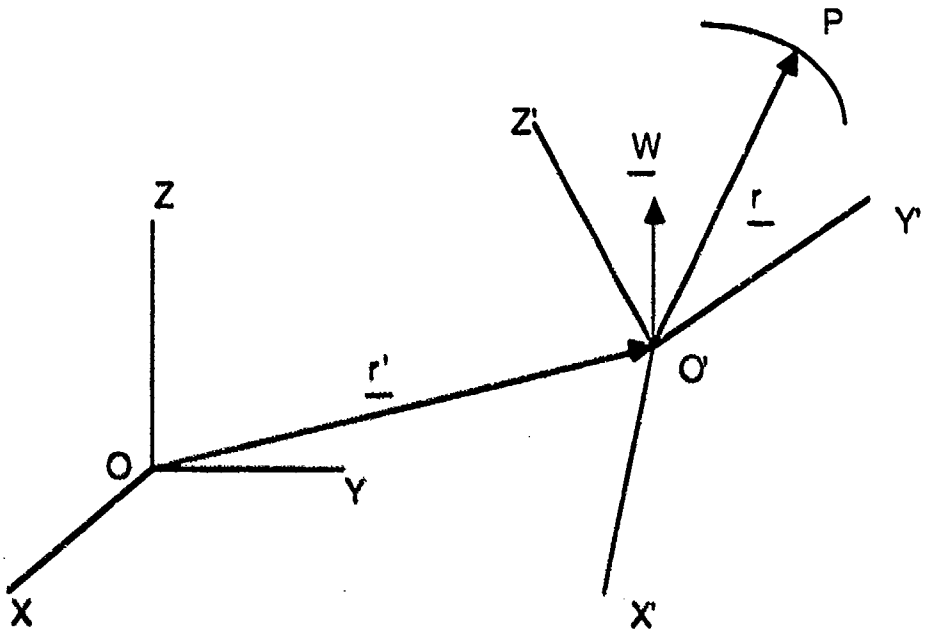

Figure 4.23. Inertial and Rotating Coordinate Systems

acceleration is perpendicular to both the particle velocity and the angular velocity vectors.

Accelerometer measurements indicate the component of the absolute acceleration (inertial coordinate system) along the sensitive axis of the accelerometer. In the tests reported here the velocity and acceleration vectors have the same directions (on the top slab and the side wall where accelerometers are located). Therefore, the coriolis acceleration is perpendicular to the sensitive axis of the accelerometer which is in the same direction as the acceleration and velocity vectors. Thus, in this case, the effect of coriolis acceleration on the accelerometer readings is limited to the transverse sensitivity of accelerometer.

4.3.2 Accelerometer Setup on the Test Structure

Two Endevco (model 2255A) accelerometers were attached to the structure as shown in Figure 4.24. Characteristics of these accelerometers which have integral electronics are illustrated in Table 4.4. The accelerometers were screwed on a nut and then epoxied on the structure. A sealant was used on the threads to prevent relative motion between the accelerometer and the nut. Figure 4.25 shows the block diagram for acceleration measurements in the centrifuge.

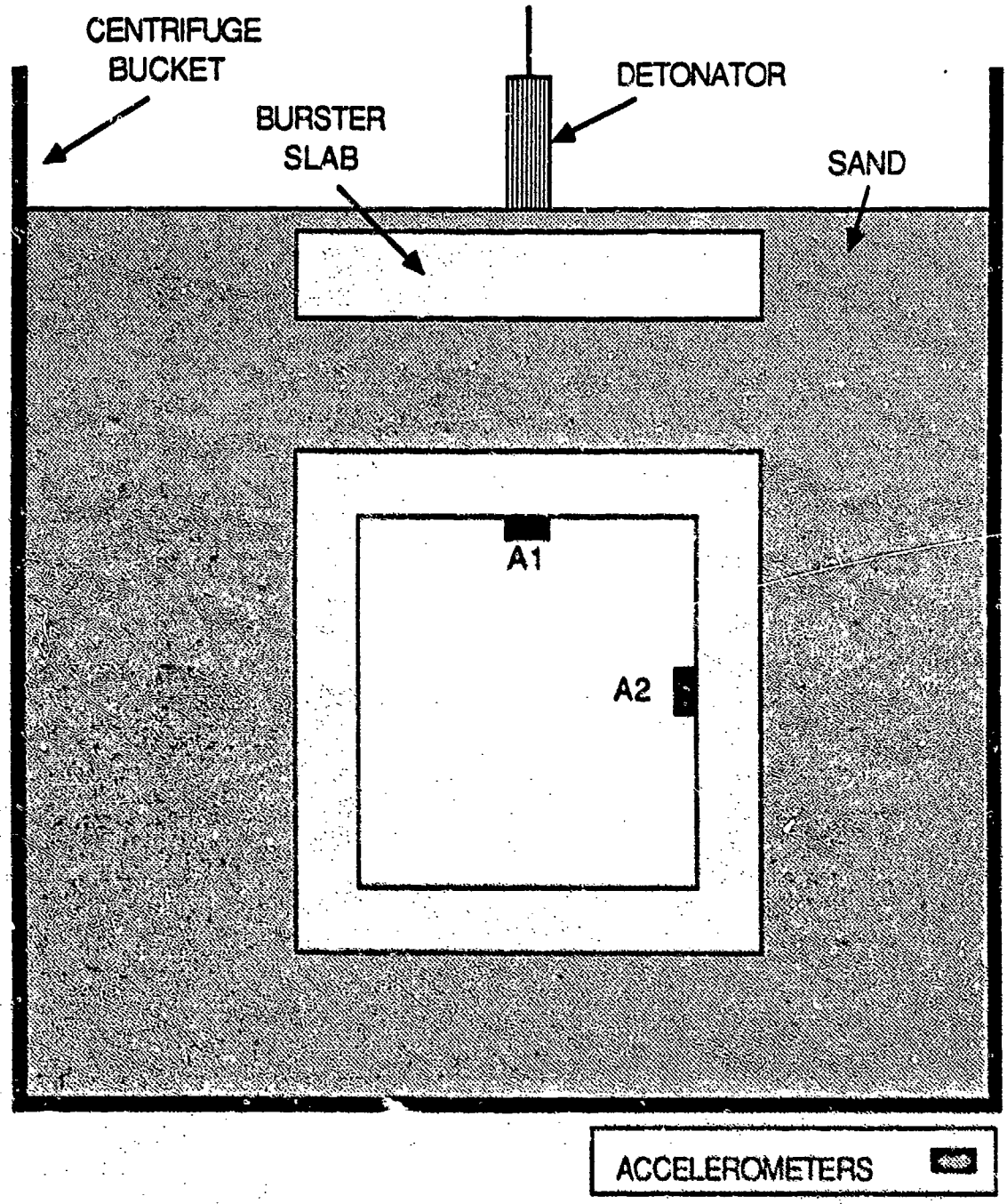

Figure 4.24. Accelerometer Locations on the Model

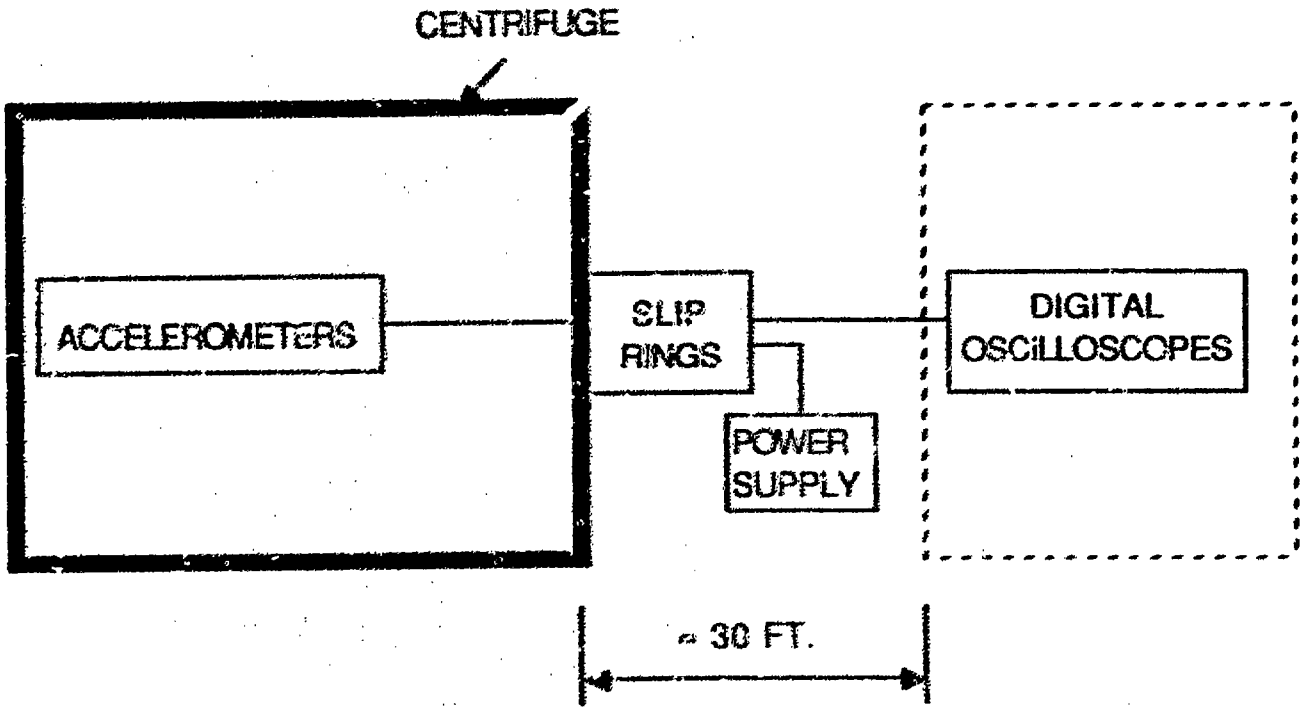

Figure 4.25. Block Diagram for Accelerometer Arrangements in the Centrifuge

Table 4.4

Characteristics of Endevco Model 2255A Accelerometers

Sensitivity	0.1 mV/g
Range, Full Scale	50000 g
Frequency Response	50 KHz
Mounted Resonant Frequency	270 KHz
Transverse Sensitivity	5 %
Weight	1.6 grams

4.4 Detonators

Based on the similitude requirements for modelling a 500 lb bomb (explained in Section 2.2) and the availability of commercial detonators to meet those requirements at 60 and 82 g's, Reynolds Industries' Standard and Modified RP-83 detonators are used. Figure 4.26 shows the standard RP-83 detonator. It consists of an exploding bridge wire, a low density pressing of Pentaerythritol (PETN), a high density Cyclotrimethyleretrinitramine (RDX) initiator, and a high density output charge. All of these charges are contained in a .007-inch thick aluminum cup. Each of the four RDX pressings weigh 0.200 grams and the composite RDX-PETN initiator weighs 0.125 grams (Nielson, 1983, and Gill, 1985). The modified RP-83 used in these tests contains only one pressing of RDX. The exploding bridgewire (EBW) type detonators resist explosion when subjected to heat, friction, and low voltages because of the exclusive use of

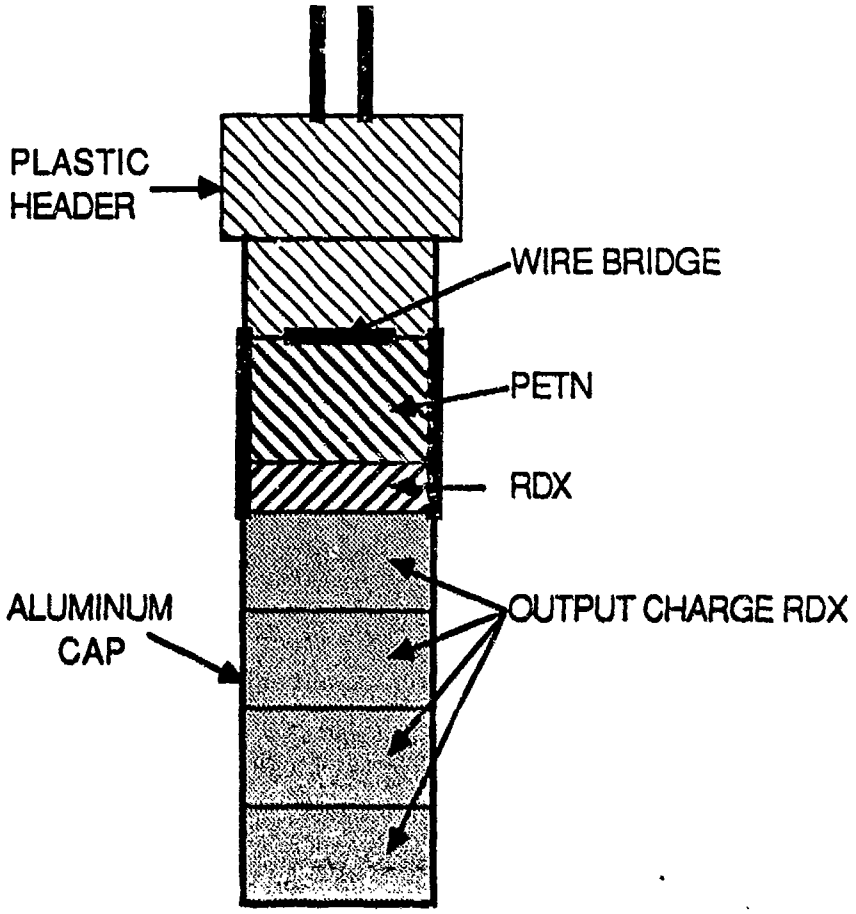

Figure 4.26. Reynolds Industries' RP-83 Detonator (Nielsen, 1984)

secondary explosives (FS10 Operating Manual, 1981).

Reynolds Industries' FS-10 firing system is designed to fire EBW detonators. This system consists of a control unit and a firing module. The control unit provides low voltage (32-40 volts) electrical energy to the firing module which is accumulated on a capacitor. When the capacitor voltage reaches 4000 volts, the system is armed and ready to fire. The signal to release the 4000 volt signal to explode the detonator is released from the control unit by the operator. when the operator presses the "fire" switch, another signal (30 volts) to be used to trigger scopes is also released which precedes the explosion by approximately 2 to 10 microseconds.

Figure 4.27 shows a block diagram for the detonator and firing system arrangements in the centrifuge. The firing module is located inside the centrifuge (on the arm) in order to avoid transmitting 4000-volt signals through slip rings. The firing module and the high-voltage cables were at least 10 inches away from the instrumentation wires and equipment at all times to minimize interference.

4.5 Overall Instrumentation and Data Acquisition

Figure 4.28 illustrates a block diagram of overall instrumentation and data acquisition for centrifuge testing of small scale models subjected to blast loading. Figure 4.29 shows the instrumentation box attached to the centrifuge arm.

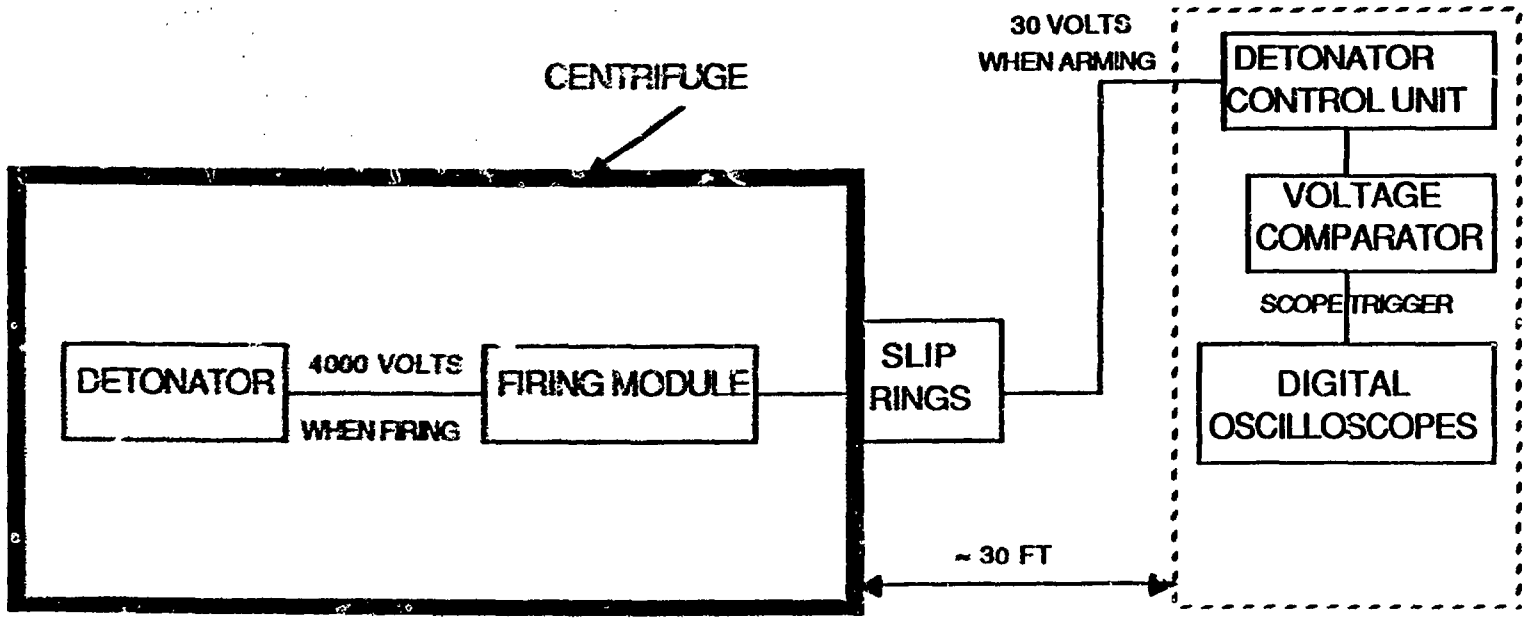

Figure 4.27. Block Diagram for Detonator Arrangements in the Centrifuge

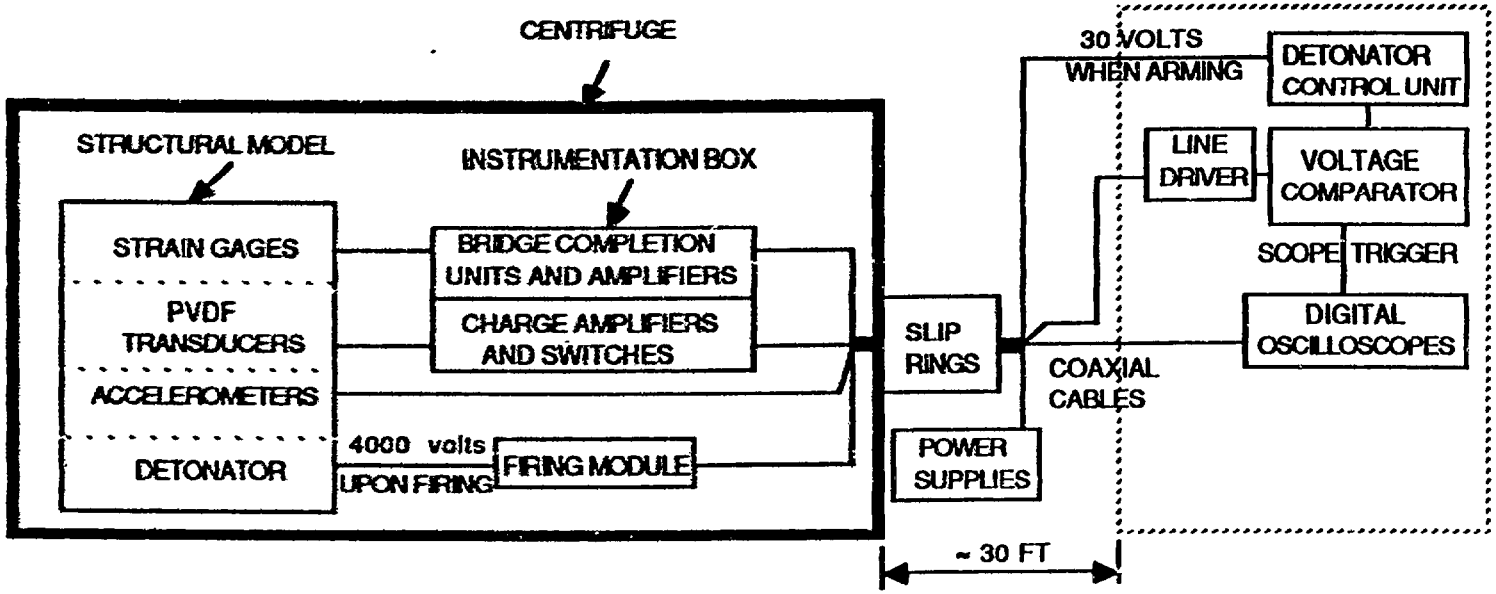

Figure 4.28. Overall Block Diagram for Instrumentation and Data Acquisition

A number of digital oscilloscopes (16 channels) were used to record the signals from the transducers (Figure 4.30). These oscilloscopes were Nicolet models 4094 and 2090. The oscilloscope digitizing rate was selected to be 1MHz for pressure transducers and 200 KHz for strain gages and accelerometers (12-bit resolution). The output signals were recorded on 5 1/4 inch diskettes. The waveforms were also transferred to an HP 9816 computer for further analysis and plotting on a digital plotter. Appendix B contains programs written on the HP computer for the transfer of waveforms, plotting on a plotter, and analysis of data.

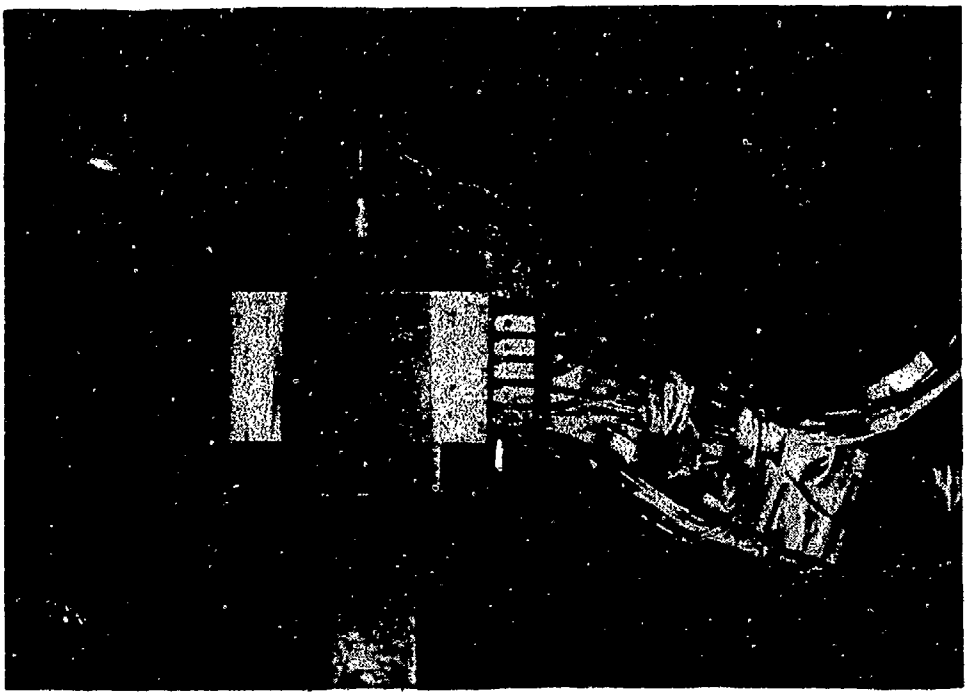

Figure 4.29. Instrumentation Box on the Centrifuge Arm

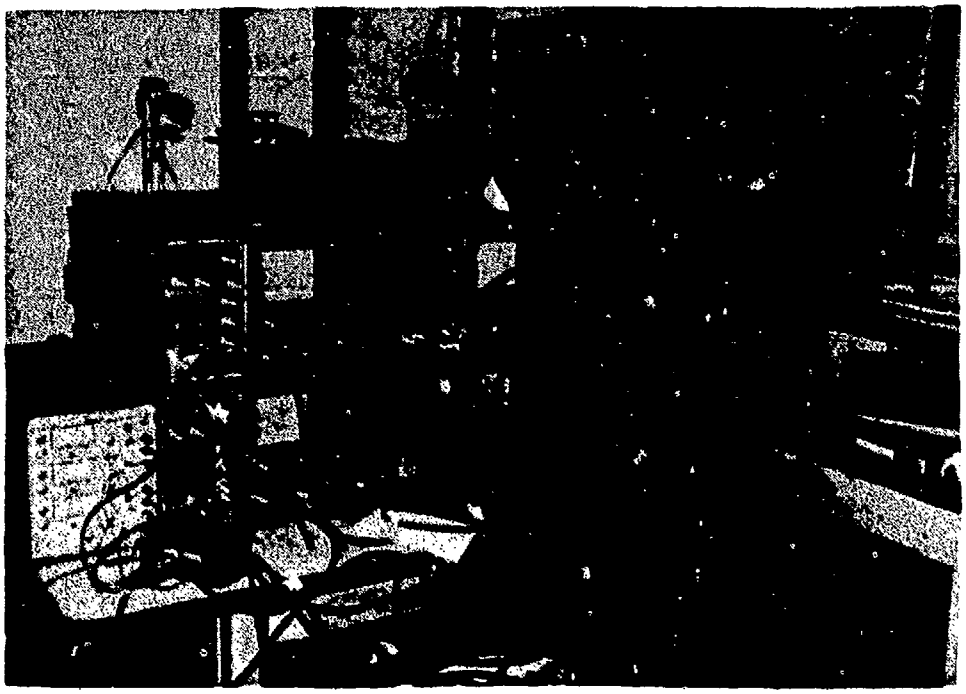

Figure 4.30. Nicolet Digital Oscilloscopes

CHAPTER 5
TESTING PROCEDURES

The following is a step-by-step account of the preparations made and the procedures followed in carrying out experiments on the test specimens. Detailed information on the geometry of the test specimens is given in Chapter 3.

Small styrofoam panels were used to cover the two open sides of the structural model in order to prevent sand from entering the box structure. Fiberboard panels were used to line the walls and floor of the centrifuge bucket in order to dampen shock wave reflections.

The next step was the placement of the structural model and sand inside the bucket. First, a 1-inch layer of dry sand was placed on the bottom of the bucket (Figure 5.1). In all cases, sand was dropped from a height of approximately 10 inches in order to obtain a uniform density distribution. Density of sand was measured by placing a small container inside the bucket when sand was being dropped. The weight and volume of the sand in the container was measured after removing it from the bucket. An average density of 89 pcf was obtained.

The box structure was then placed on the bottom sand layer. Great attention was given to the placement of the

structure at the exact center of the bucket. A PVC pipe located at a corner of the bucket was used to shield the instrumentation wires from damage due to explosion (Figure 5.2). More sand was then placed all around the structure (Figure 5.3).

The box structure was subsequently covered with 7 scaled feet of sand (1.4" in 1/60-scale and 1.0" in 1/82-scale models). The exact height of sand above the top of the structure was verified by dipping a metal ruler (marked at the desired height) into the sand.

The next step was to place the burster slab on top of the sand and at the exact center of the bucket (Figure 5.4). The burster slab was then covered with 2 scaled feet of sand (0.4" in 1/60-scale and 0.3" in 1/82-scale models) as shown in Figure 5.5. A wooden frame was used to hold the detonator in the exact position on top of the burster slab (Figure 5.6). The detonator was attached to the bottom of the bolt located at the center of the wooden frame. The distance between the bottom of the detonator and the top of the burster slab (standoff distance) varied between 2 scaled feet to zero feet (direct contact between detonator and burster slab) in different tests.

The next step was to connect the instrumentation wires from the structure to the instrumentation box on the centrifuge arm using RS-232 type connectors.
Output wires from the instrumentation box were connected to binding posts for slip rings. Outside the centrifuge, the

Figure 5.1. A Layer of Sand on the Bottom of the Bucket

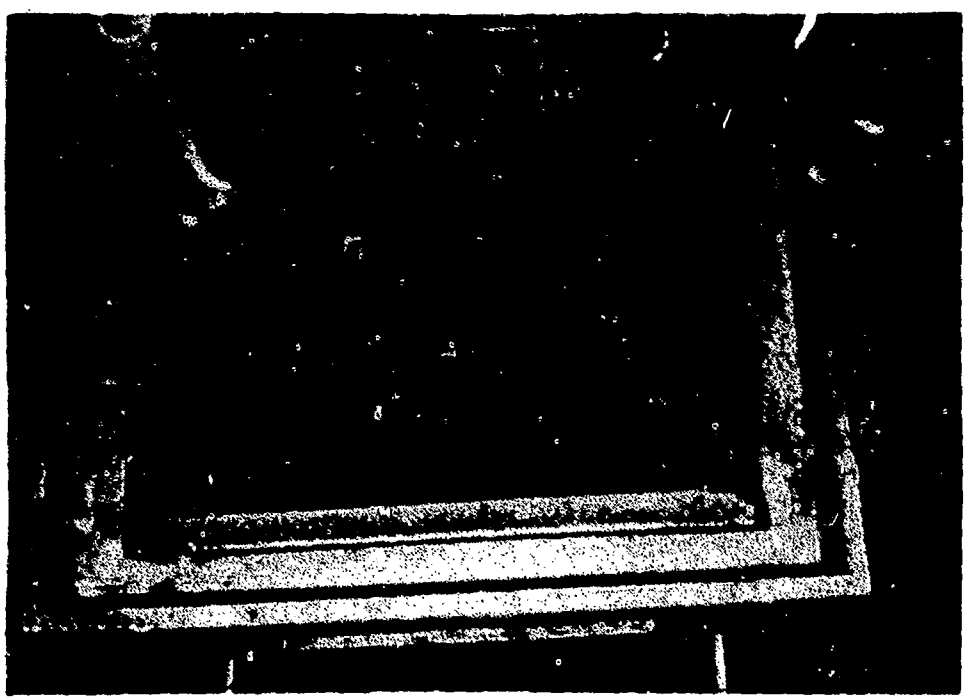

Figure 5.2. Structural Model Placed Inside the Bucket

Figure 5.3. Sand Placed Around the Model

Figure 5.4. Burster Slab in Place

Figure 5.5. Sand Placed on Top of the Burster Slab

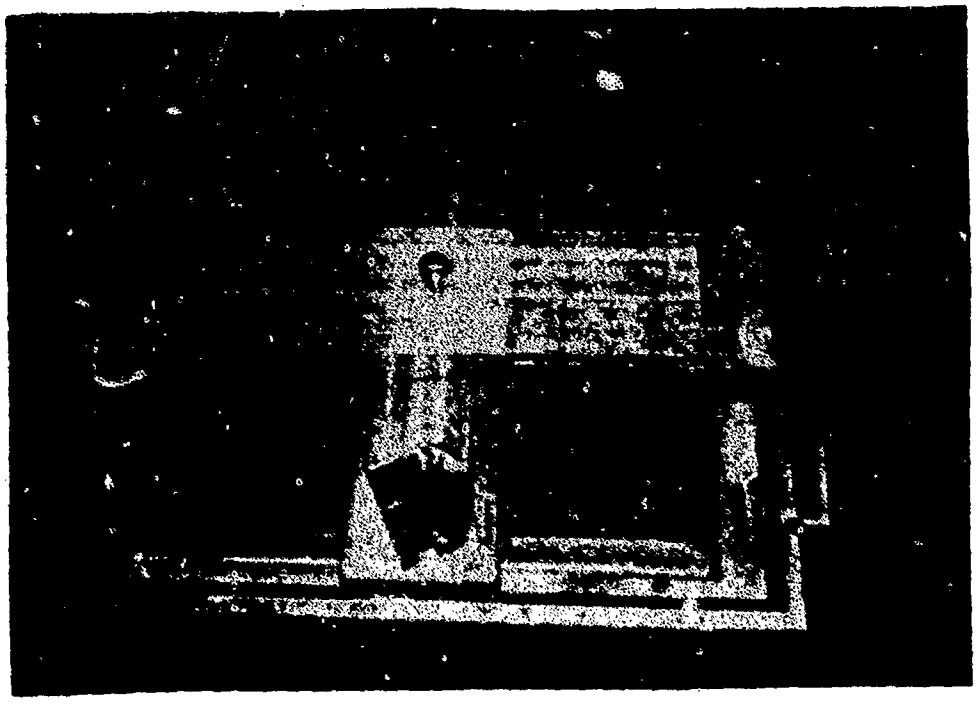

Figure 5.6. Wooden Frame to Support the Detonator

output of each instrumentation channel was connected to a digital storage oscilloscope through a 30-foot long coaxial cable.

A complete check of the wiring systems, electronic components, mechanical connections, oscilloscopes, power supplies, and detonator control systems was then performed. Necessary measures were taken to insure safety at all times. An explosives expert was in charge of storage, handling, safety, and operation of explosives and associated equipment.

Upon completion of the equipment and safety checks, the system was ready for performing experiments. At this point, for tests at 1g, the explosive charge was put in place and the charge was exploded when the signal to detonate was given to the operator. For tests at 60 or 82 g's, the explosive charge was put in place and the centrifuge was spun until it reached the desired speed (242 rpm for 60 g's and 276 rpm for 82 g's). The signal to detonate was then given and the charge was exploded. The resulting waveforms displayed on the oscilloscope screens were then stored on diskettes so that the waveforms could be recalled at a later time for transfer to, and analysis on a computer (Hewlett Packard model 9816).

Although some variations existed for some model tests, the general testing sequence for each test specimen was as follows. First, a test was performed at 1g at a standoff distance of 2 scaled feet. Next, the same test was repeated

but at 60 or 82 g's depending on the scale of the model. Subsequently, another test was performed on the same structure at 1g but at a standoff distance of zero. Finally, a test with a standoff distance of zero was performed at 60 or 82 g's. Table 5.1 illustrates the characteristics of the various tests performed on different models.

Table 5.1

Tests Performed on Structural Models

	1/60 scale							1/82 scale				
Test No.	A1	A2	A3	A4	A5	A6	A7	B1	B2	B3	B4	B5
Model No.	1	1	1	1	2	2	2	3	3	3	4	4
Standoff (scaled ft)	2	2	0	0	2	2	0	2	2	0	2	0
Gravity (g's)	1	60	1	60	1	60	60	1	82	82	82	82

In tests A1 and A3 (1/60 scale), the centrifuge was spun to 60 g's before tests at 1g were performed. Therefore, the density of sand for these tests at 1g were expected to be higher than if the centrifuge had not been spun before the tests. In tests A5 (1/60 scale) and B1 (1/82 scale), the centrifuge was not spun before the test.

All structures and burster slabs were reinforced, except for the burster slab in model No. 2 which was unreinforced. There were no tests performed on models no. 2, 3 and 4 at 1g

with a standoff distance of zero. The reason is that tests at zero standoff result in cratering and cracking on the burster slab which render it useless for further tests. Therefore, it was decided to perform the tests at zero standoff for models 2, 3 and 4 only at 60 and 82 g's and not at 1g.

CHAPTER 6
EVALUATION OF TEST RESULTS

In this chapter the test results are presented and evaluated in such a manner as to help answer the questions raised in this research effort. Therefore, the main focus of this chapter is on evaluating the significance of increased gravity (centrifuge) rather than studying the performance and survivability of underground structures subjected to blast loading. Measurements of pressures, accelerations and strains on the models in tests at 1 g and 60 or 82 g's are compared. Also, the scaling relationships are evaluated by comparing tests at 60 and 82 g's. Table 5.1 lists the characteristics of the various tests performed on different models.

6.1 Pressures

Locations of various pressure gages attached to the structural model and the burster slab are shown in Figure 4.21. In this section, the pressure-time histories at each gage location in different tests are compared and studied. Explosive tests generally have spurious effects on transducer responses. This can be seen in most of the pressure responses during the first few microseconds.

6.1.1 Pressure Gage P1

Pressure gage P1 is located on the bottom of the burster slab. Because of the close proximity of this gage to the explosive, the pressure gage (P1) responses in some tests were not satisfactory. Figure 6.1 is one such example. It shows the pressure response from gage P1 in tests A1 and A2. The slow rise of the signal after the passage of the main shock wave may be attributed to a severe vibration of the cable which could be significant in piezoelectric transducers (see Chapter 4). There were some tests that yielded reasonable responses for Gage P1. Figure 6.2 shows the response of pressure gage P1 in test A4 (0' standoff, 60 g's). The first peak of the response exceeded the range set on the oscilloscope at approximately 1500 psi. The signal shows a second peak of magnitude 1060 psi at a time of 294 μseconds. This second peak is believed to be a reflection of the main shock wave on the top slab of the box structure. In this case, the average speed of the shock wave in soil is approximately 930 ft/sec.

Figure 6.3 shows the pressure response P1 for test A7 (0' standoff, 60 g's). This test is similar to test A4 (Figure 6.2) with one important difference. The burster slab in test A4 was already damaged and cracked during test A3 while test A7 was performed using an intact burster slab. It is not clear wheather the first sharp peak in the response in the A7 test is due to the effects of explosion

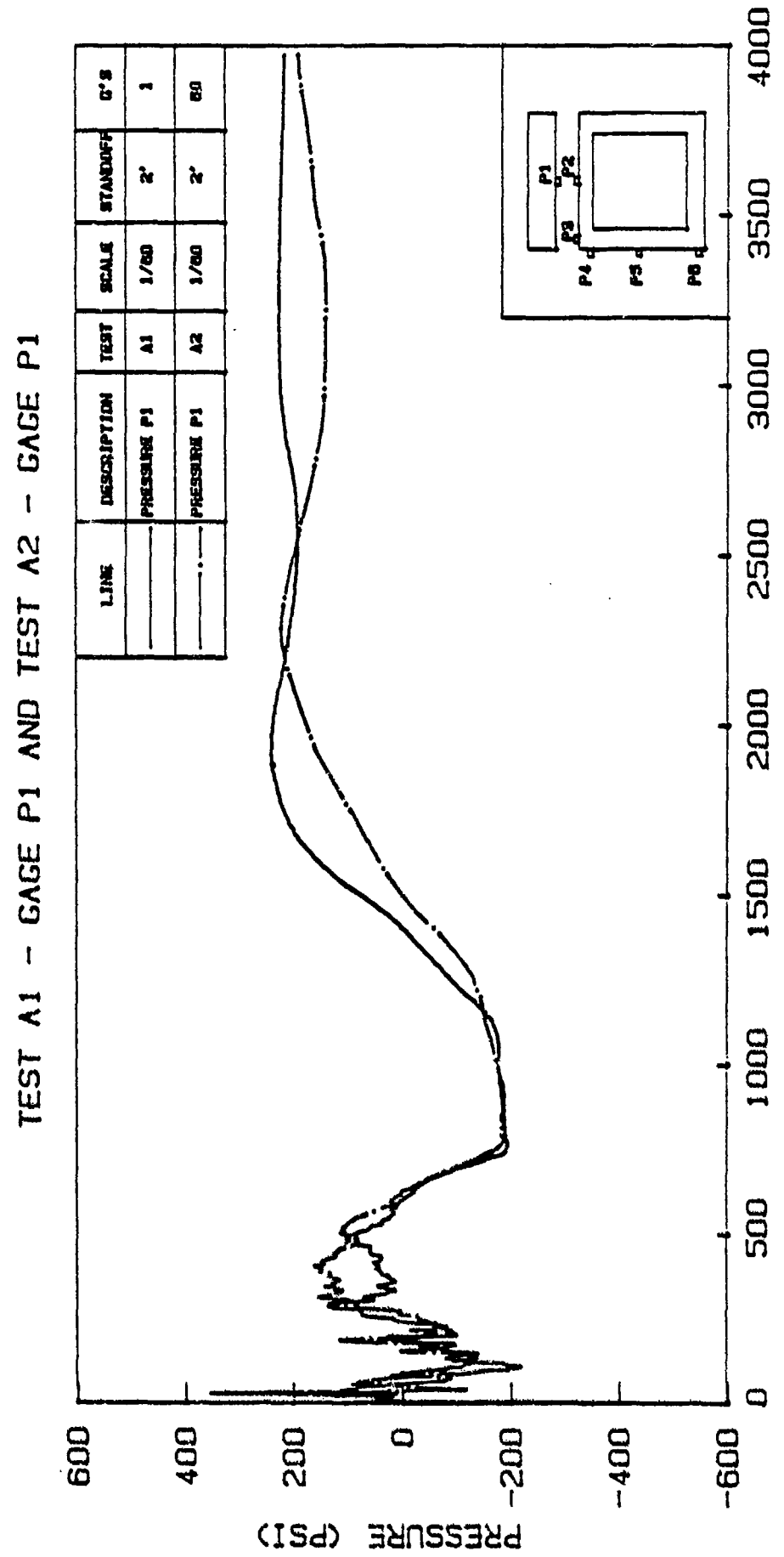

Figure 6.1. Response of Pressure Gage P1 in Tests A1 and A2

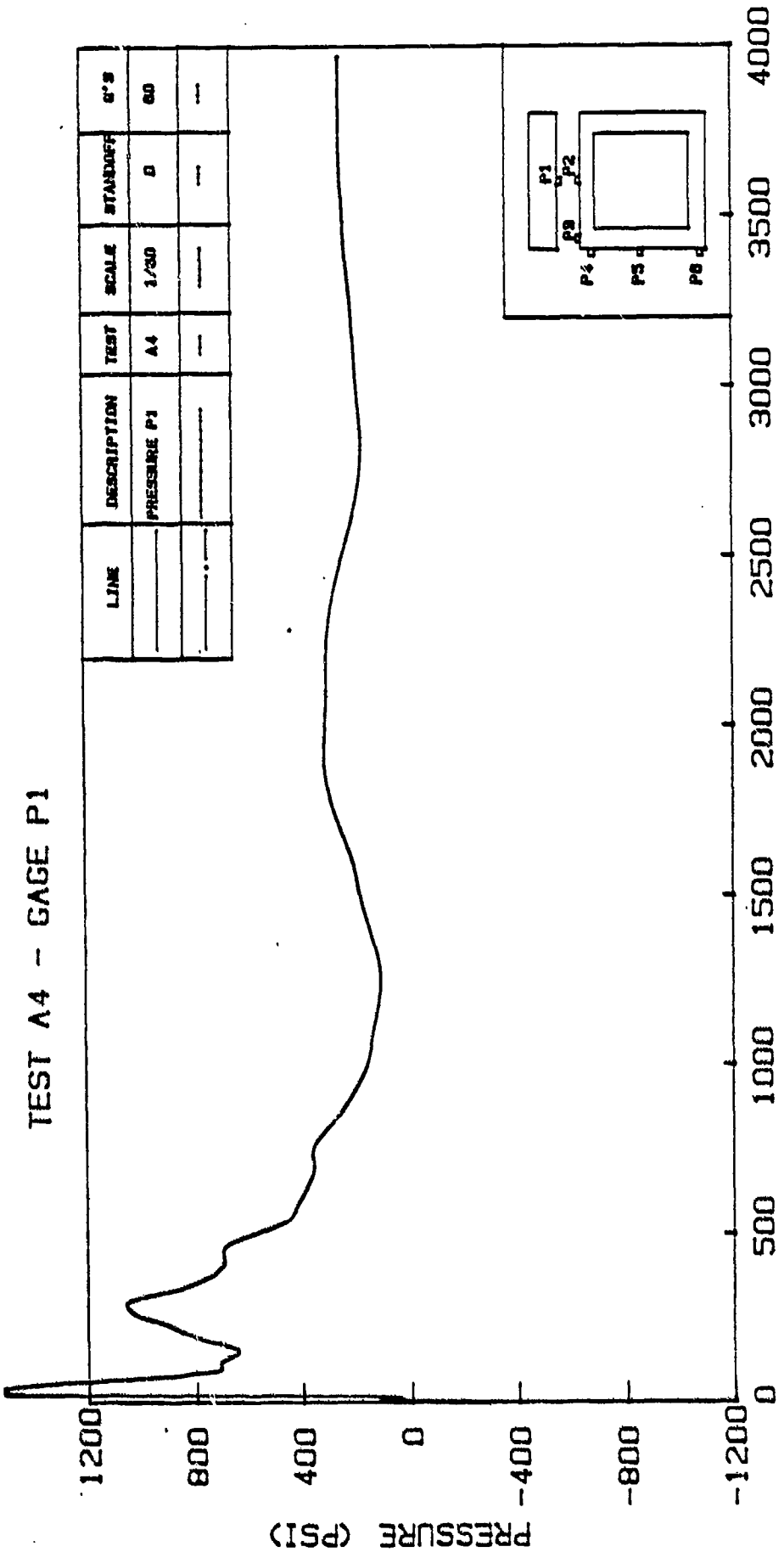

Figure 6.2. Response of Pressure Gage P1 in Test A4

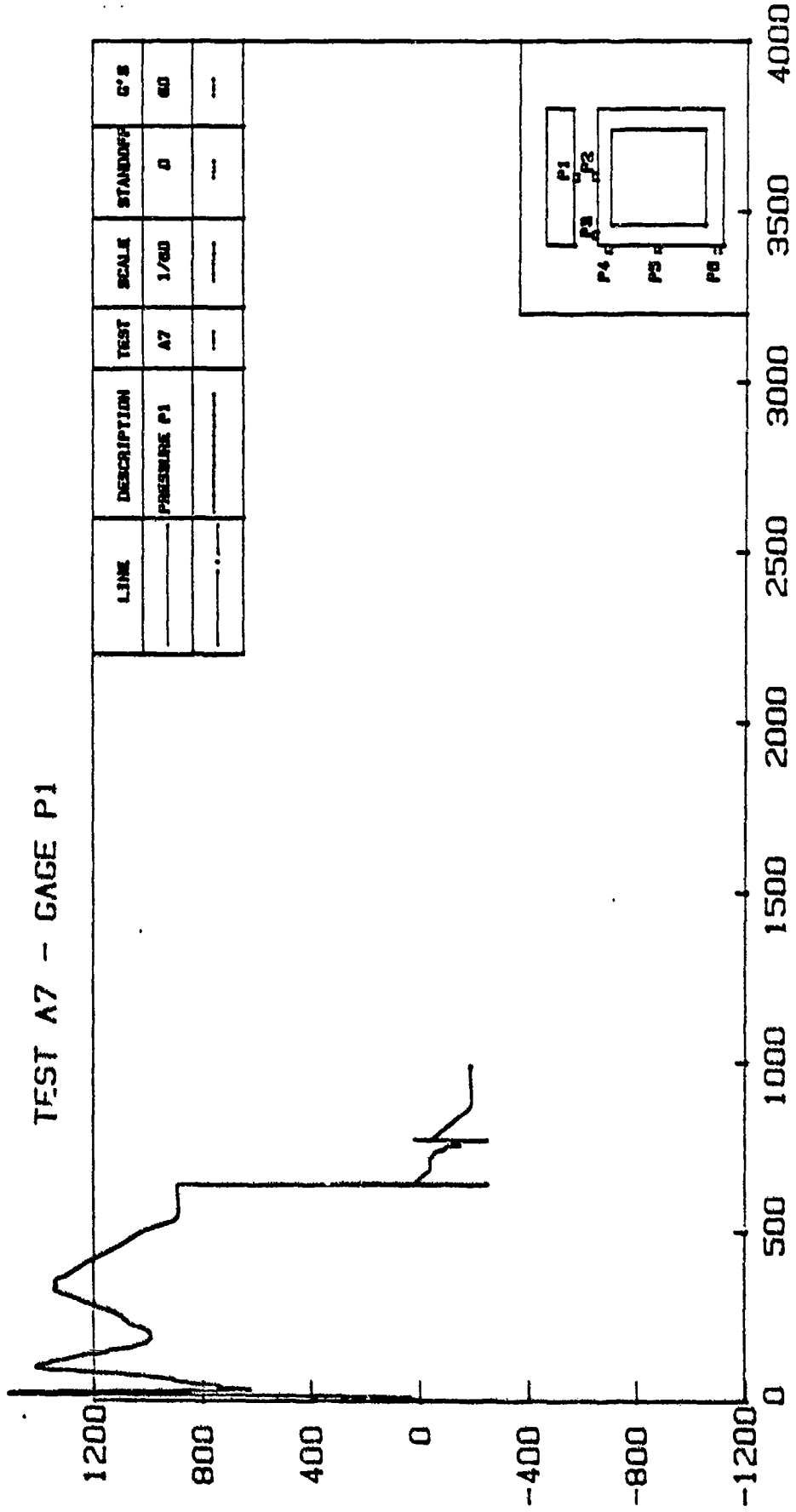

Figure 6.3. Response of Pressure Gage P1 in Test A7

on instrumentation or a precursor wave front. This effect is observed in almost all of the pressure gage responses. The second peak is considered to be the main shock front and the third peak is believed to be a reflection of the main wave on the top slab of the box structure. It can be seen that at 640 μseconds the wire connection to the gage was cut and the rest of the signal was lost. The main shock front is estimated to have a rise time (the time it takes for the signal to rise from 10% to 90% of its peak) of approximately 65 μseconds with a peak pressure of 1400 psi which is slightly smaller than the corresponding pressure in test A4 (1500 psi). However, the reflected pressure in test A7 is approximately 1345 psi which is higher than the second peak in test A4 by 27%. The wave speed in soil is calculated to be 1003 ft/sec which is close to the value obtained from test A4. The accuracy of this speed is verified by checking the time of arrival for pressure gage P2 in tests A4 and A7 which yield very similar results.

Figure 6.4 shows the pressure response P1 for test B3 (0' standoff, 82 g's). According to the scaling relationships (Chapter 2), the peak pressures in this test should be the same as in tests A4 and A7 (Figure 6.2 and 6.3). In addition, the arrival times in test B3 should be less than the corresponding arrival times in tests A4 and A7 by a factor of 60/82. The first peak in test B3 exceeded 1500 psi (similar to test A4). However, the second pressure peak in test B3 (662 psi) was less than the second peak in

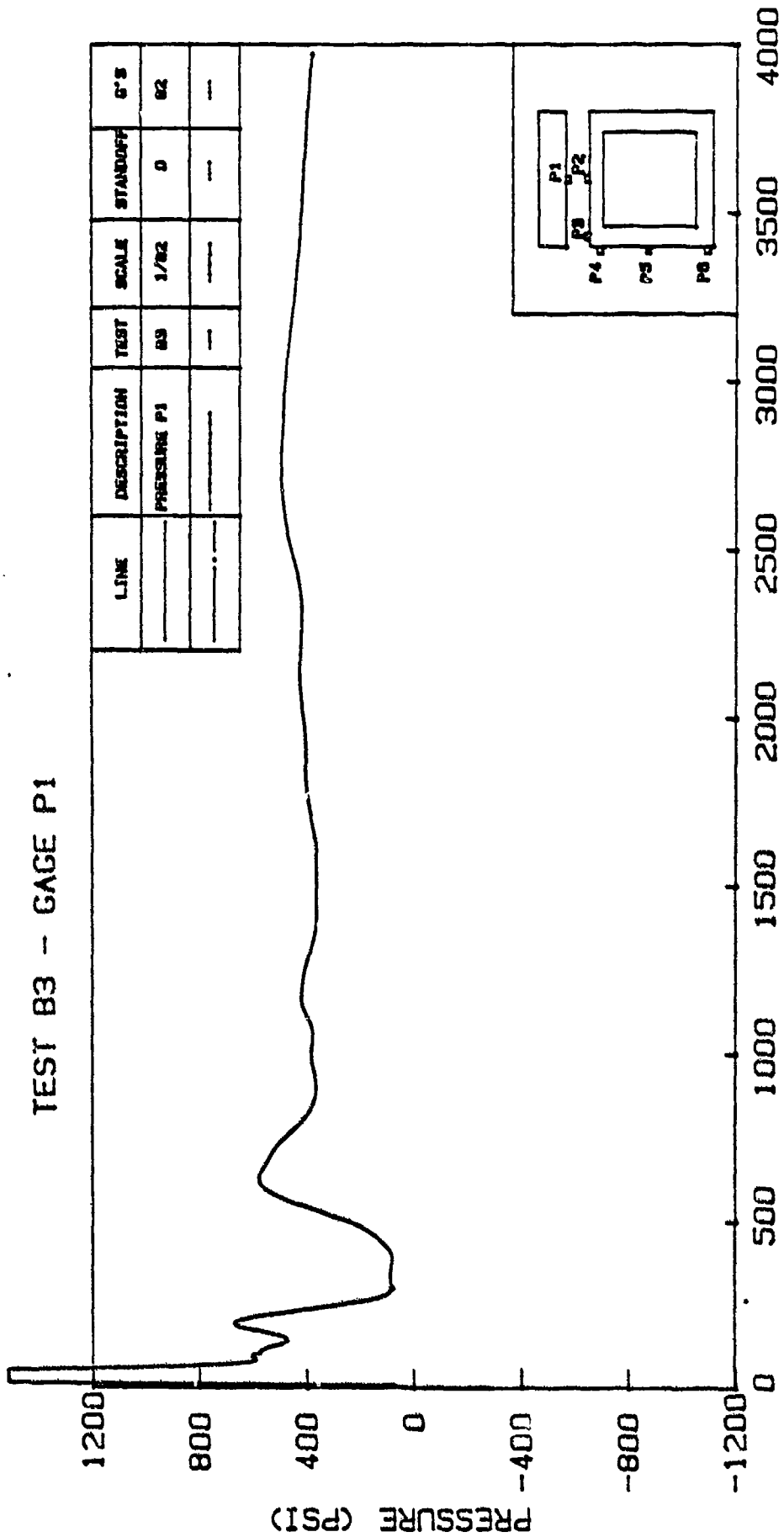

Figure 6.4. Response of Pressure Gage P1 in Test B3

test A4 (1060 psi) by approximately 37%. The arrival time of the second peak in test B3 was 191 μseconds which is equivalent to 261 μseconds on a 1/60 scale model (191 X 82/60 = 261). The actual arrival time in test A4 was about 10% higher (294 μseconds). Again, the residual observed pressure in test B3 is believed to be due to the vibration of the cable (triboelectric effect) explained in Chapter 4.

Figure 6.5 shows the pressure gage response P1 for test B2 (2' standoff, 82 g's). The arrival time for the peak of the main wave is 103 microseconds. It should be noted that this arrival time is the same as the arrival time in test A7, even though the standoff distances in the two tests are different and the model scales (and therefore the time relationships) are different. If the standoff distances had been the same in both tests, the theoretical arrival time for test B2 (based on scaling laws) would have been 60/82 times the arrival time in test A7 or 75 μseconds. However, since the standoff distance in test B2 is 0.29 inches (2 scaled ft) compared to zero inches in test A7, the wave front has to travel a longer distance (40% longer). Assuming equal wave speeds in soil and microconcrete, the arrival time should be 40% longer than 75 μseconds (105 μseconds), which is very close to the arrival time observed in test B2.

The rise time of the main signal is about 60 μseconds but the pressure is much smaller (564 psi) than the A4, A7 or B3 tests because of the larger standoff distance in test

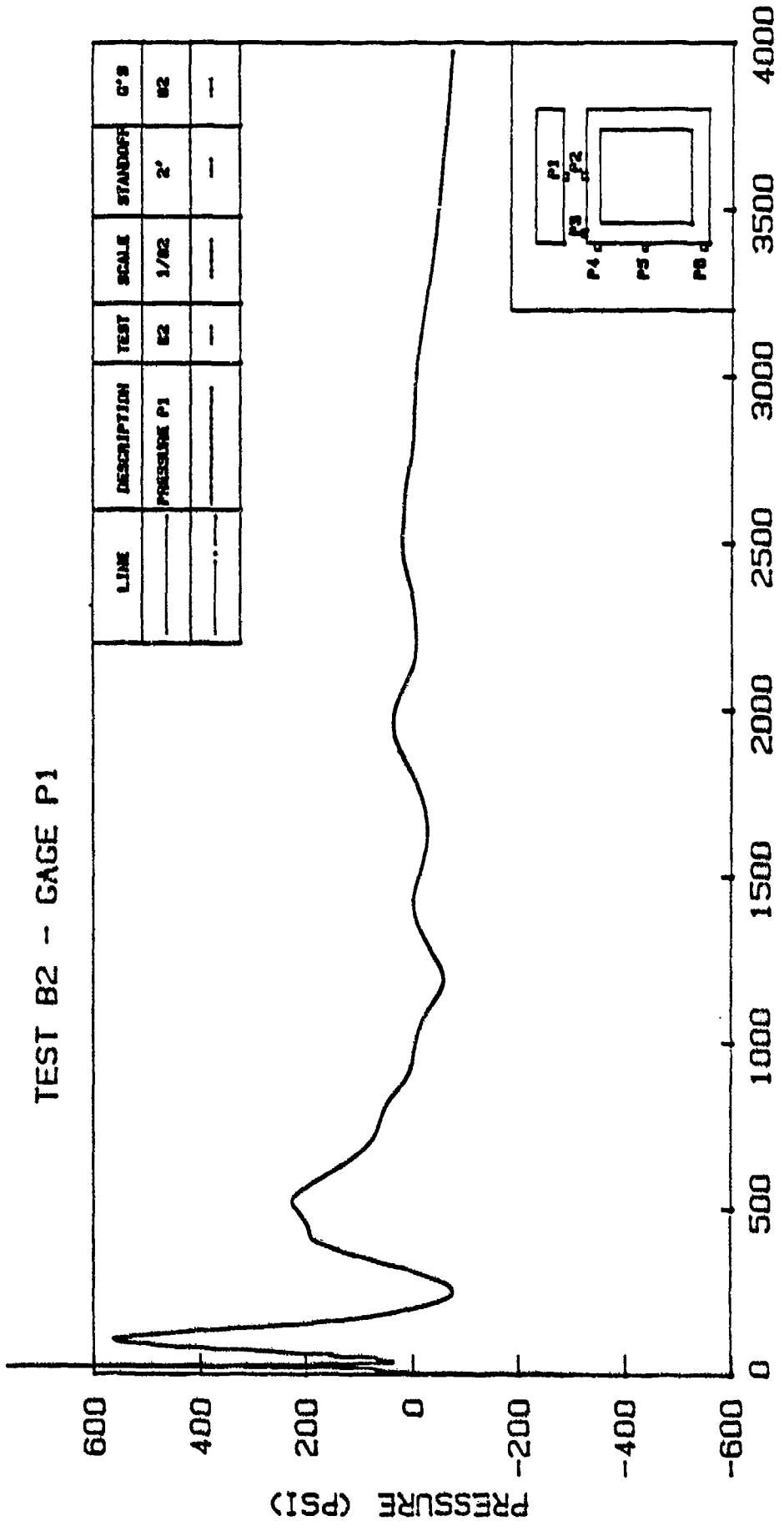

Figure 6.5. Response of Pressure Gage P1 in Test B2

B2. The wave speed in soil is calculated by dividing the distance between the bottom of the burster slab and top of the structure by the time difference between the peaks in P1 and P2 for test B2. A speed of 918 ft/sec is obtained which is similar to the value obtained in other tests. The second peak on the P1 response has a delay and therefore a lower speed compared to the other tests.

Figure 6.6 shows the pressure response P1 in test B1 (2' standoff, 1g). The arrival time of the main peak is the same as in test B2. Test B2 is similar to test B1 except that the test is performed at 82 g's. Equal arrival times for the main peak pressure in P1 are expected because gravity mainly affects wave speed in soil but not concrete. The peak pressure in test B2 (564 psi) is larger than the peak pressure in B1 (430 psi) by about 31%. This is because of a larger soil stiffness (under the burster slab) due to greater confinement stresses at higher gravities. The speed of shock wave in soil (test B1) is calculated to be 688 ft/sec by observing the arrival time of the main wave on the top of the structure. The wave speed in test B2 is higher than speed in test B1 by approximately 33%.

Although the number of satisfactory pressure responses on the bottom of the burster slab are limited, the results indicate generally repeatable responses in similar tests and larger peak pressure in the test at 82 g's (2' standoff) as compared to the test at 1g (2' standoff).

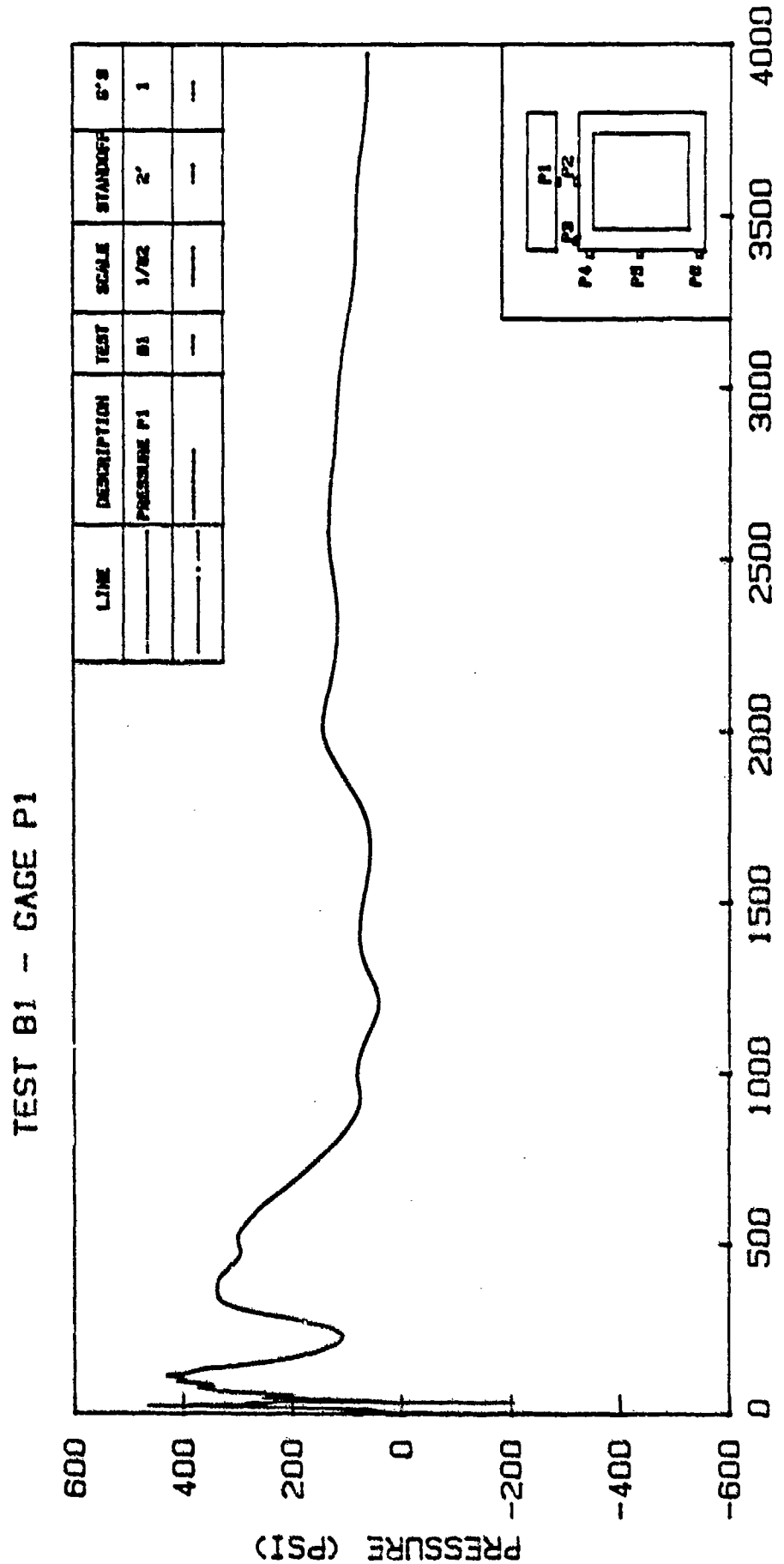

Figure 6.6. Response of Pressure Gage P1 in Test B1

6.1.2 Pressure Gage P2

Pressure Gage P2 is located on top of, and at the center of the top slab of the box structure (Figure 4.21). Figure 6.7 shows the pressure gage P2 response for tests A1 (2' standoff, 1g) and A2 (2' standoff, 60 g's). The centrifuge was spun to 60 g's before the test at 1g (A1) was performed. Therefore, the density of sand in both tests were equal and the only difference was the effect of gravity.

It can be seen that the shock wave arrives faster in the 60g test and has a slightly larger peak pressure. The two pressure responses show ripple effects before the arrival of the main wave. As mentioned earlier, this effect is seen in almost all the pressure gage responses and it is not clear wheather this is a side effect of explosion on instrumentation or a precursor wave.

The exact wave speed in soil can not be determined in this case because of a lack of precise information on the arrival time of the shock wave on the bottom of the burster slab (Pressure Gage P1 in tests A1 and A2 did not function properly). The arrival time of the first peak of the shock wave in test A1 is 393 μseconds which is larger than the corresponding arrival time for test A2 (264 μseconds) by 50%. Also, the arrival time for the second peak in test A1 (561 μseconds) is larger than the corresponding arrival time for test A2 (460 μseconds) by about 22%. The rise time of the signal in test A1 is 96 μseconds while the rise time

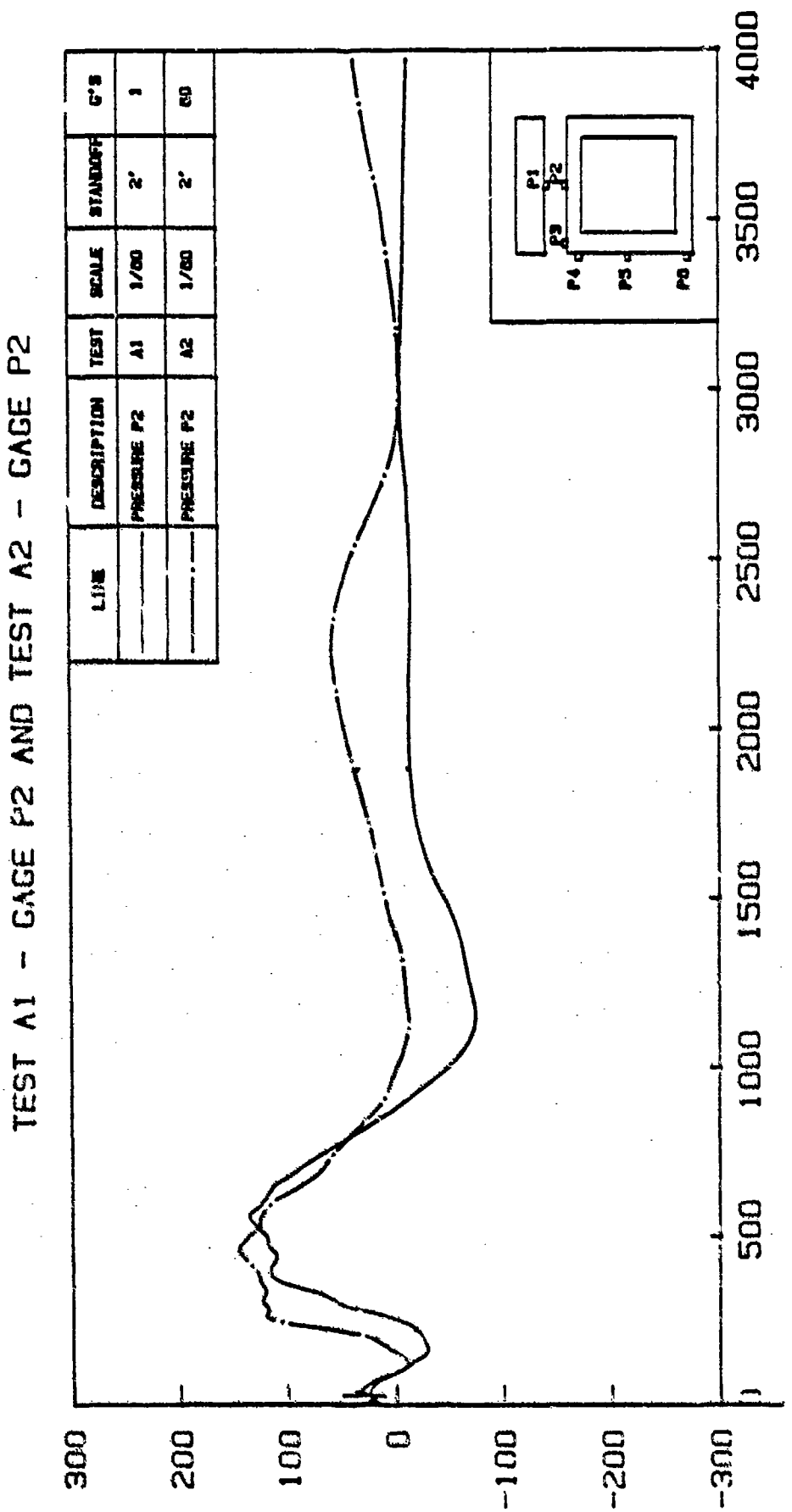

Figure 6.7. Response of Pressure Gage P2 in Tests A1 and A2

in test A2 is 68 μseconds which is a reduction of about 30%. The first peak pressure in test A1 is 120 psi which is slightly smaller than the first peak pressure in test A2 (123 psi). However, the second peak pressure in test A2 (148 psi) is larger than the corresponding peak pressure in test A1 (139 psi) by about 7%. These differences can be explained by considering the fact that the stiffness of sand is a function of gravity stresses. Therefore, in tests at high gravities, the soil stiffness is higher and thus the shock wave arrival times are smaller and the peak pressures are higher. The shape of the pressure response curve is a complex function of the reflections on the burster slab and the structural motion of the box structure in response to the load. Wong and Weidlinger (1983) suggest that the motion of an underground structure and the loading acting on the structure are closely coupled.

Figure 6.8 shows the impulse (area under the pressure - time curve) for pressure gage P2 at 1 and 60 g's. The peak impulse (at zero pressure) in test A2 is larger than the peak impulse in test A1 by about 28%.

Figure 6.9 shows the Pressure Gage P2 responses in tests A5 (2' standoff, 1g) and A6 (2' standoff, 60 g's). These two tests are similar to tests A1 and A2 respectively, except that the centrifuge was not spun to 60 g's before test A5 (at 1g) was performed. Therefore, in addition to the difference in gravities between tests A5 and A6, the sand densities were not equal either.

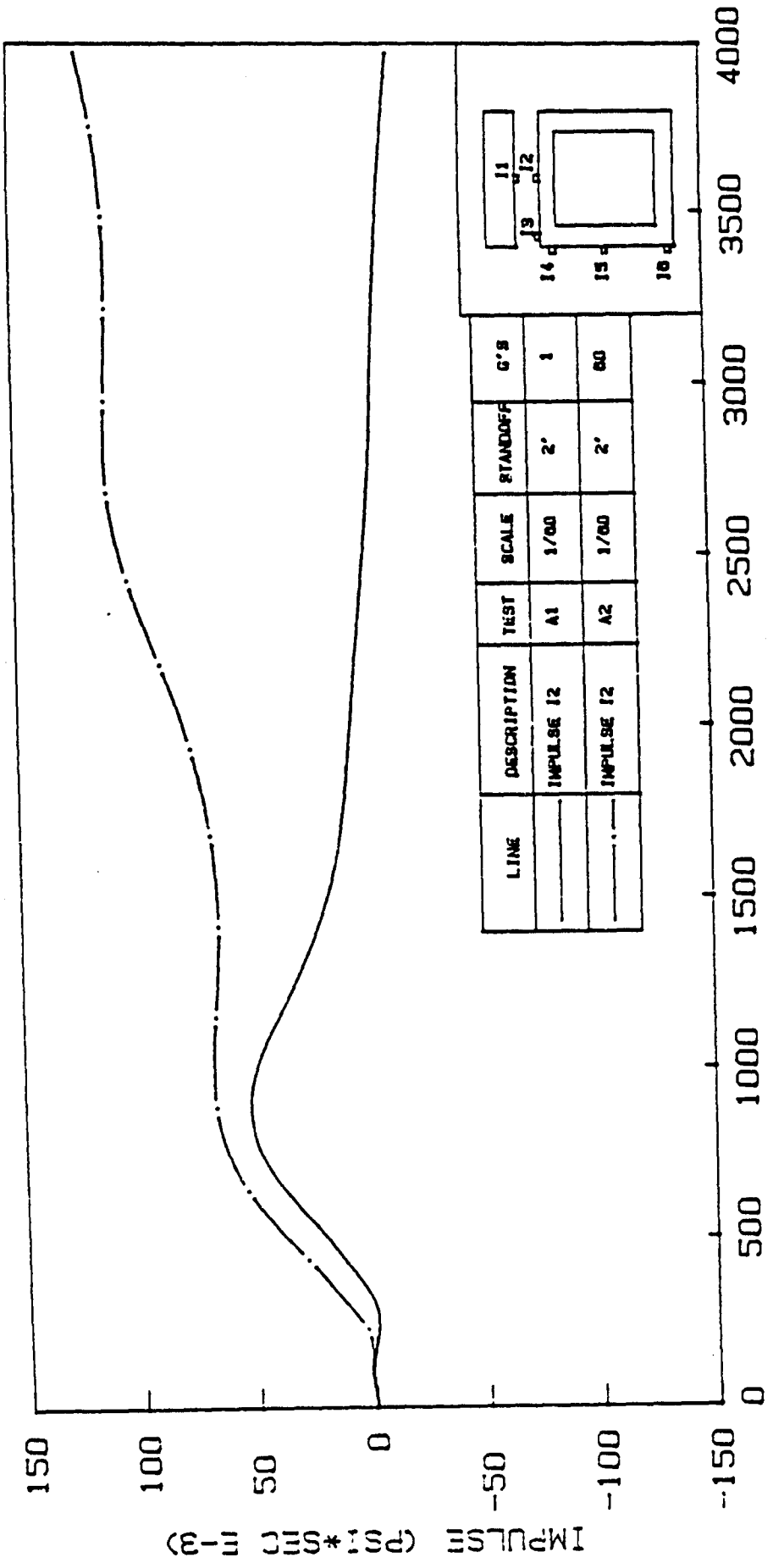

Figure 6.8. Impulse Curves (I2) in Tests A1 and A2

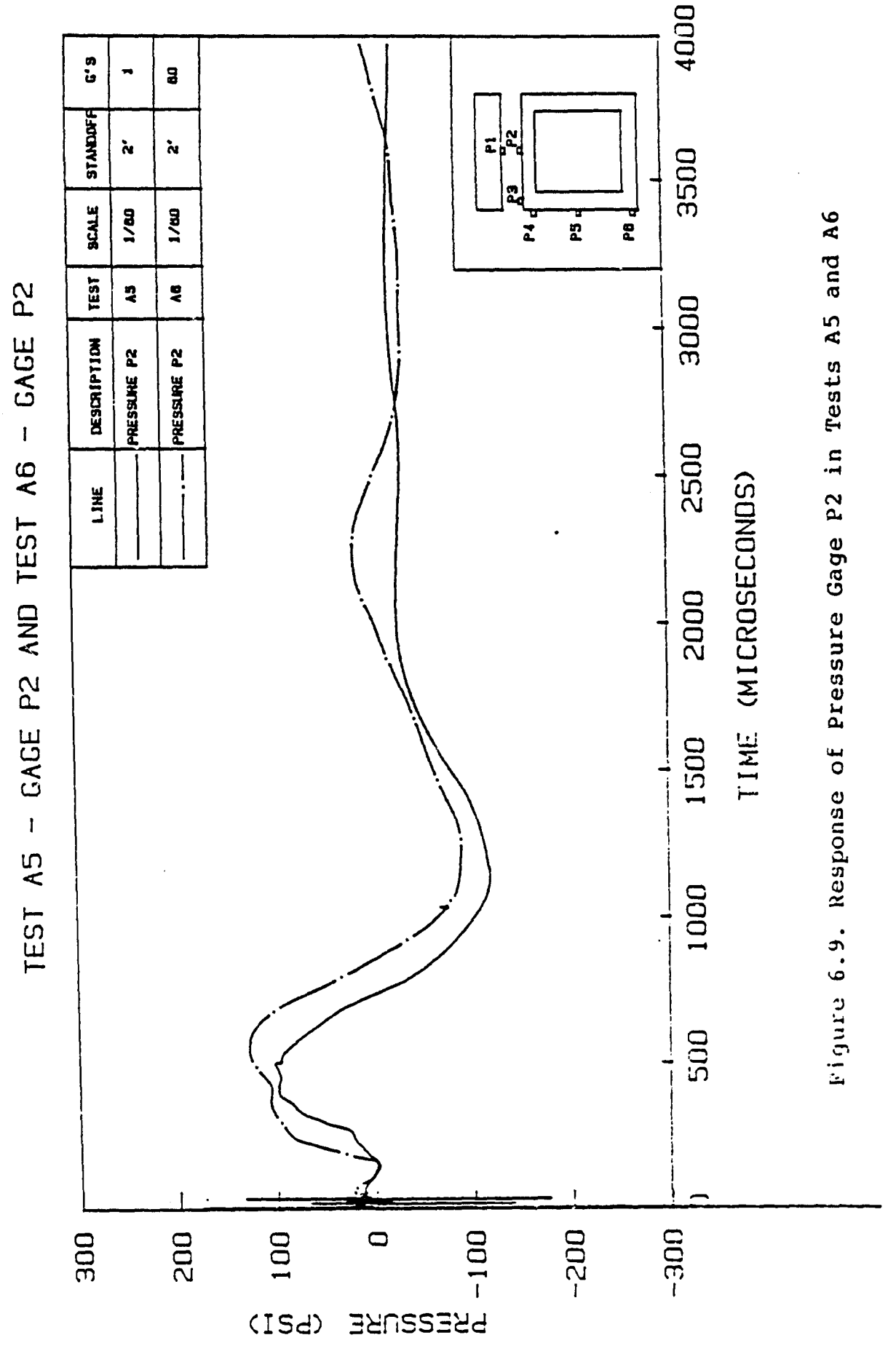

Figure 6.9. Response of Pressure Gage P2 in Tests A5 and A6

The arrival time of the first peak in test A5 is 408 μseconds which is larger than the corresponding arrival time for test A6 (361 μseconds) by about 13%. The arrival time for the second peak in test A5 (500 μseconds) is 8% smaller than the corresponding arrival time for test A6 (541 μseconds).

The rise time of the signal in test A5 (137 μseconds) is much larger than the rise time in test A6 (61 μseconds). The first peak pressure in test A6 is 108 psi which is higher than the corresponding peak pressure in test A5 (99 psi) by about 9%. However, the difference in second peak pressures in these two tests is larger. Test A6 has a second peak of 129 psi which is larger than the second peak in test A5 (105 psi) by 23%.

Figure 6.10 illustrates the difference in impulse curves between tests A5 and A6. The peak impulse in test A6 is larger than the peak impulse in test A5 by about 73%.

In order to evaluate the repeatability of tests conducted under similar conditions, tests A1 and A2 are compared with tests A5 and A6 respectively. It should be noted that the densities of sand in tests A1 and A5 were not equal. Table 6.1 summarizes the results for Pressure Gage P2. For tests A1 and A5, the difference in the amplitude of the first and second peaks are 21% and 32% respectively. Larger values in test A1 can be attributed to a larger density. The arrival time for the first peak in tests A1 and A5 are fairly close (4% difference). The

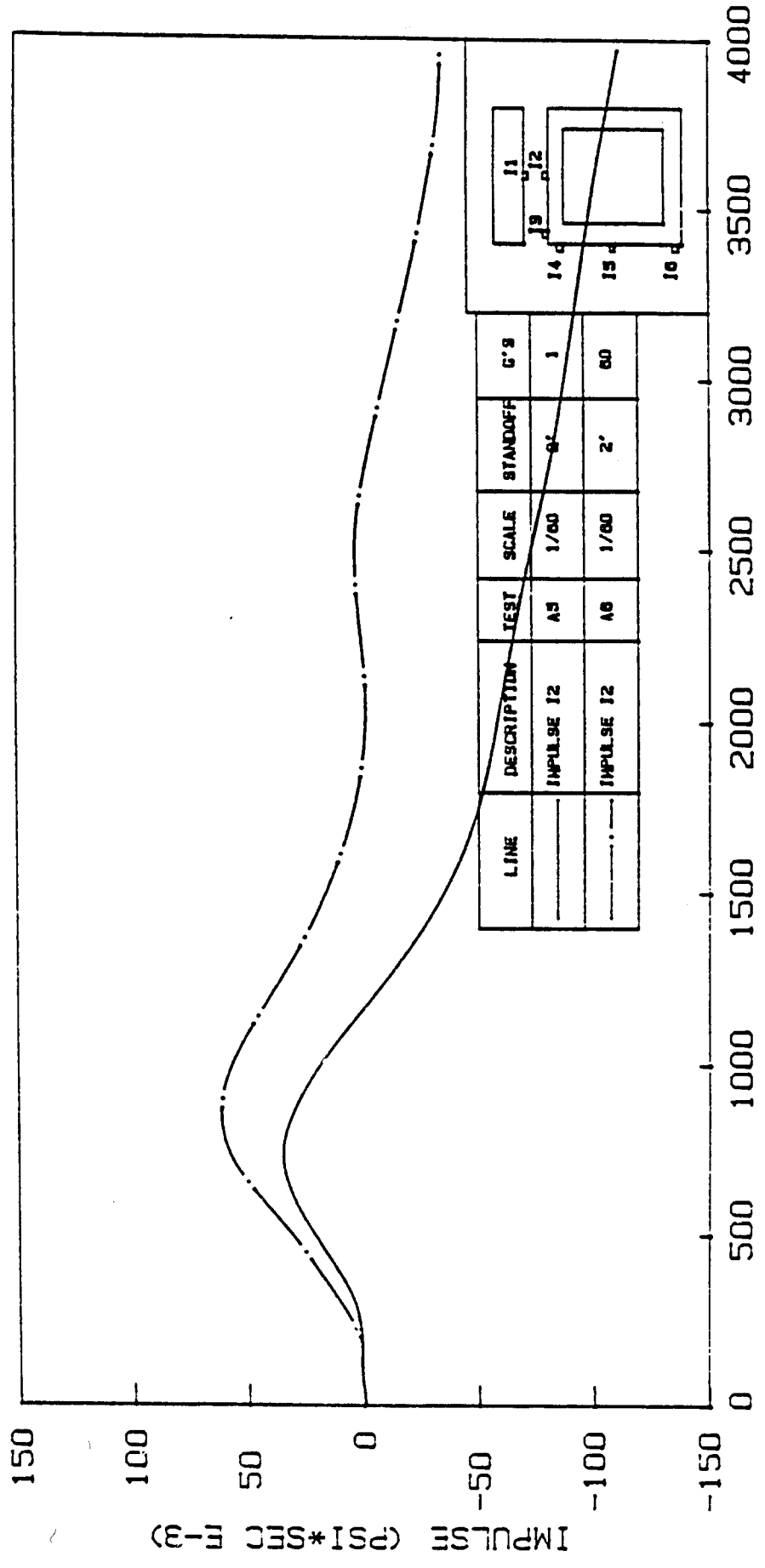

Figure 6.10. Impulse Curves (I2) in Tests A5 and A6

Table 6.1

Summary of Pressure Gage P2 Responses

Standoff	0' Standoff						2' Standoff						
Gravity	1g		60 g's		82 g's		1g			60 g's		82 g's	
Model Scale	1/60	1/82	1/60		1/82		1/60		1/82	1/60		1/82	
Test Number	A3	None	A4	A7	B3	B5	A1	A5	B1	A2	A6	B2	B4
Maximum Pressure 1st Peak (psi)	277	----	163	169	313	404	120	99	133	123	108	142	113
Arrival Time* (Microseconds)	231	----	255	231	148	204	393	408	279	264	361	251	259
Maximum Pressure 2nd Peak (psi)	221	----	151	10	240	337	139	105	163	148	129	168	180
Arrival time* (Microseconds)	516	----	510	694	377	357	561	500	488	460	541	641	454

* For 1/82 scale tests, the actual arrival time is multiplied by 82/60 to obtain an arrival time equivalent to 1/60-scale tests

arrival time for the second peak in test A1 is higher the corresponding arrival time in test A5 by 11%. The differences in magnitudes of the first and second peaks in tests A2 and A6 are slightly smaller. Both peaks in test A2 are larger than the corresponding peaks in test A6 by about 14%. However, the difference in arrival times are relatively larger than in tests A1 and A5. It should be noted that the selection of the first peak in test A6 may be arbitrary because of a lack of a clear first peak. The comparison of the impulse curves for tests A1 and A5 indicate a noticeable difference in the peak impulse between the two tests. However, this difference is much smaller in tests A2 and A6.

Figure 6.11 shows Pressure Gage P2 responses for tests B1 (2' standoff, 1g) and B2 (2' standoff, 82 g's). The centrifuge was not spun to 82 g's before test B1 was performed. These two tests are similar to the two sets of tests explained earlier (A1, A2 and A5, A6) in that the standoff distance is 2 scaled feet. However, tests B1 and B2 are conducted on 1/82-scale models rather than 1/60-scale models. It is clear that the arrival time of the main wave in test B2 is faster and the peaks are higher than in test B1. Table 6.1 includes the results from these two tests. It should be noted that all arrival times for tests on 1/82-scale models as listed in table 6.1 have been multiplied by 82/60 for the purpose of comparing these arrival times with the corresponding arrival times in tests

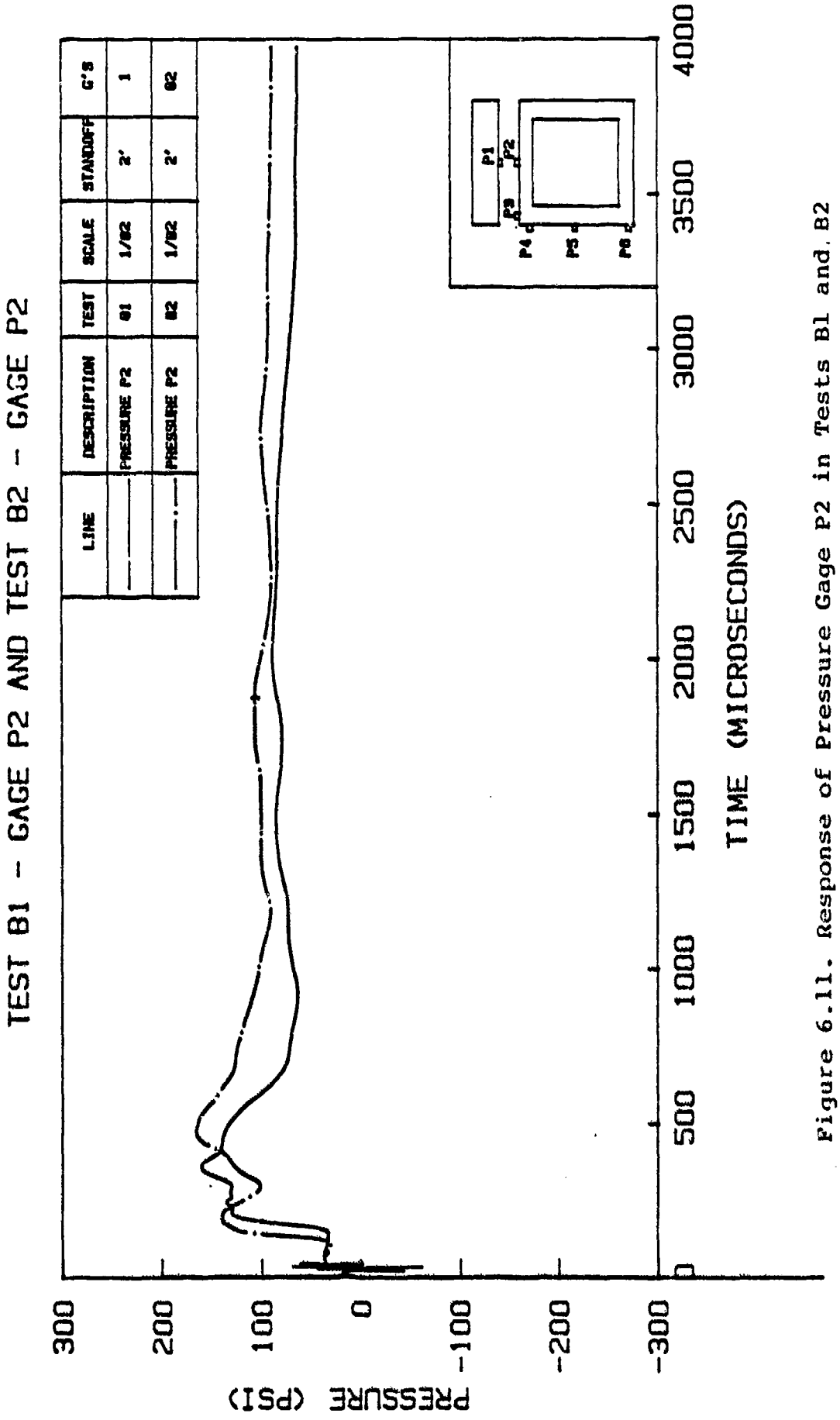

Figure 6.11. Response of Pressure Gage P2 in Tests B1 and B2

on 1/60-scale models. The arrival time for the first peak in test B1 is larger than the first peak arrival time in test B2 by 11%. However, the arrival time of the second peak in test B1 is smaller than the corresponding arrival time in test B2 by 24%.

The first peak pressure in test B2 (142 psi) is higher than the first peak pressure in test B1 (133 psi) by 7%. The second peak pressure in test B2 (168 psi) is larger than the corresponding pressure in test B1 (163 psi) by 3%. Both pressure responses show residual apparent pressures after the main shock wave has passed. This is believed to be due to the vibration and flexing of the cable. Figure 6.12 illustrates the impulse curves for tests B1 and B2 which show very slight differences.

According to the laws of similitude and, assuming that the structure and the explosive charge are scaled properly, the magnitudes of pressures and arrival times (including adjustments for different scale models) should be the same in tests at 2' standoff on 1/60- and 1/82-scale models. However, although in selecting the explosive charge the total mass of explosive was scaled properly, the distribution of the mass in the detonator, the relative size of the detonator, thickness of the case, etc. were not taken into account because of limitations with regard to availability of commercial detonators. Therefore, slight differences in pressures and arrival times are to be expected. The first peak pressure in test B1 (133 psi) is

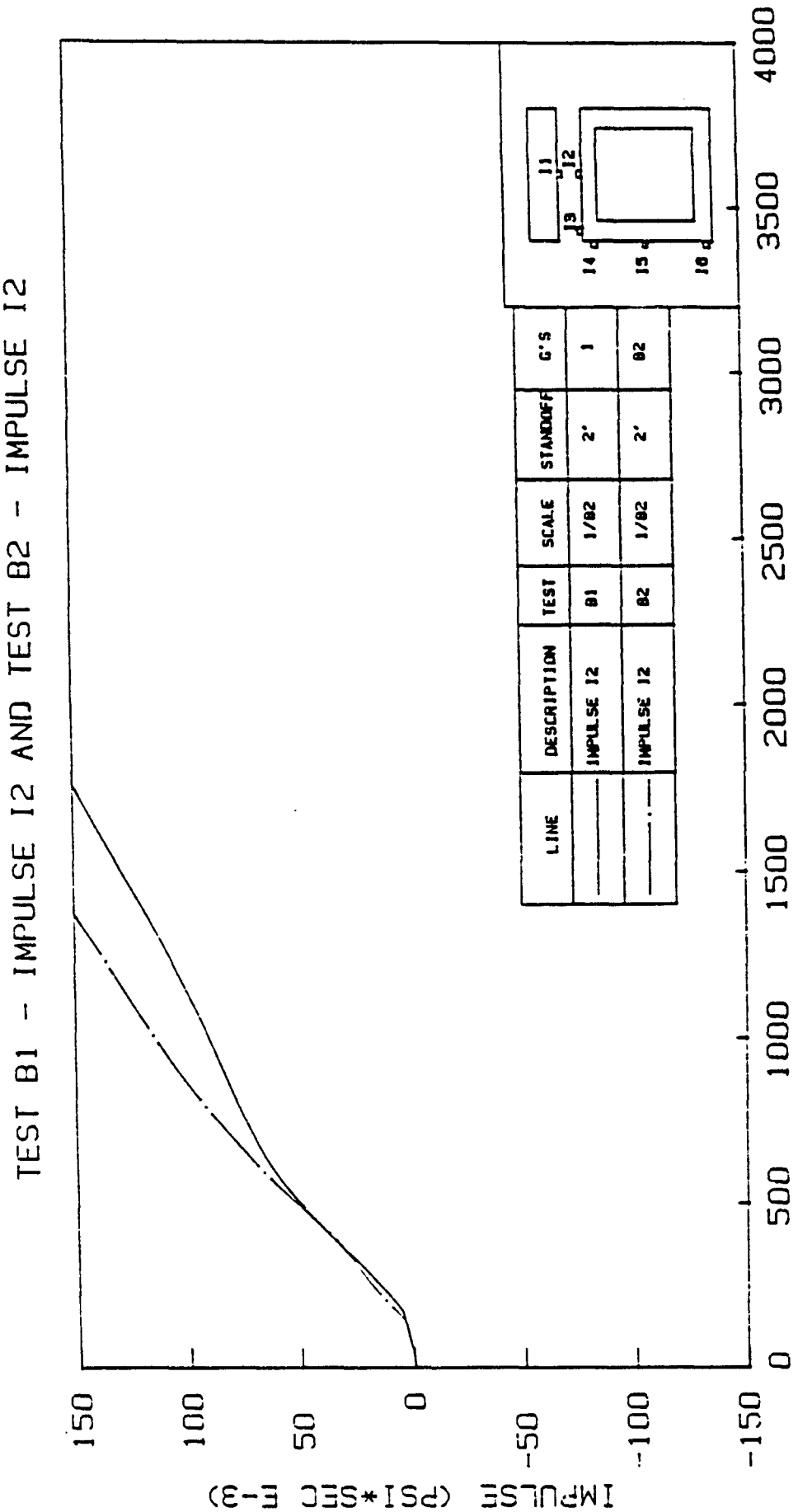

Figure 6.12. Impulse Curves (I2) in Tests B1 and B2

larger than the average of the first peak pressures in tests A1 and A5 (110 psi) by 21% (see Table 6.1). Similarly, the second peak pressure in test B1 (163 psi) is larger than the average second peak pressure for tests A1 and A5 (122 psi) by 34%. The arrival time (adjusted) of the first peak in test B1 (279 μseconds) is smaller than the corresponding average time in tests A1 and A5 (400 μseconds) by 30%. The arrival time (adjusted) of the second peak in test B1 (488 μseconds) is smaller than the average arrival time for tests A1 and A5 (531 μseconds) by 8%.

Figure 6.13 shows the Pressure Gage (P2) response for tests B2 (2' standoff, 82 g's) and B4 (2' standoff, 82 g's). These two tests are conducted under similar conditions and should yield similar results. Table 6.1 indicates that the arrival times for the first peak in both tests are very close (251 and 259 μseconds). However, the first peak in test B2 (142 psi) is larger than the first peak in test B4 (113 psi) by 26%. This situation is reversed for the second peak where the pressure in test B4 (180 psi) is larger than the second peak in test B2 (168 psi) by 7%. Figure 6.14 shows that impulse curves in tests B2 and B4 are very close.

The next step is to evaluate tests at zero standoff distance. Only one test (A3) was performed at 1g and at zero standoff distance. The reason for this was that any test at zero standoff destroys the burster slab and further tests on such a slab may not provide accurate information.

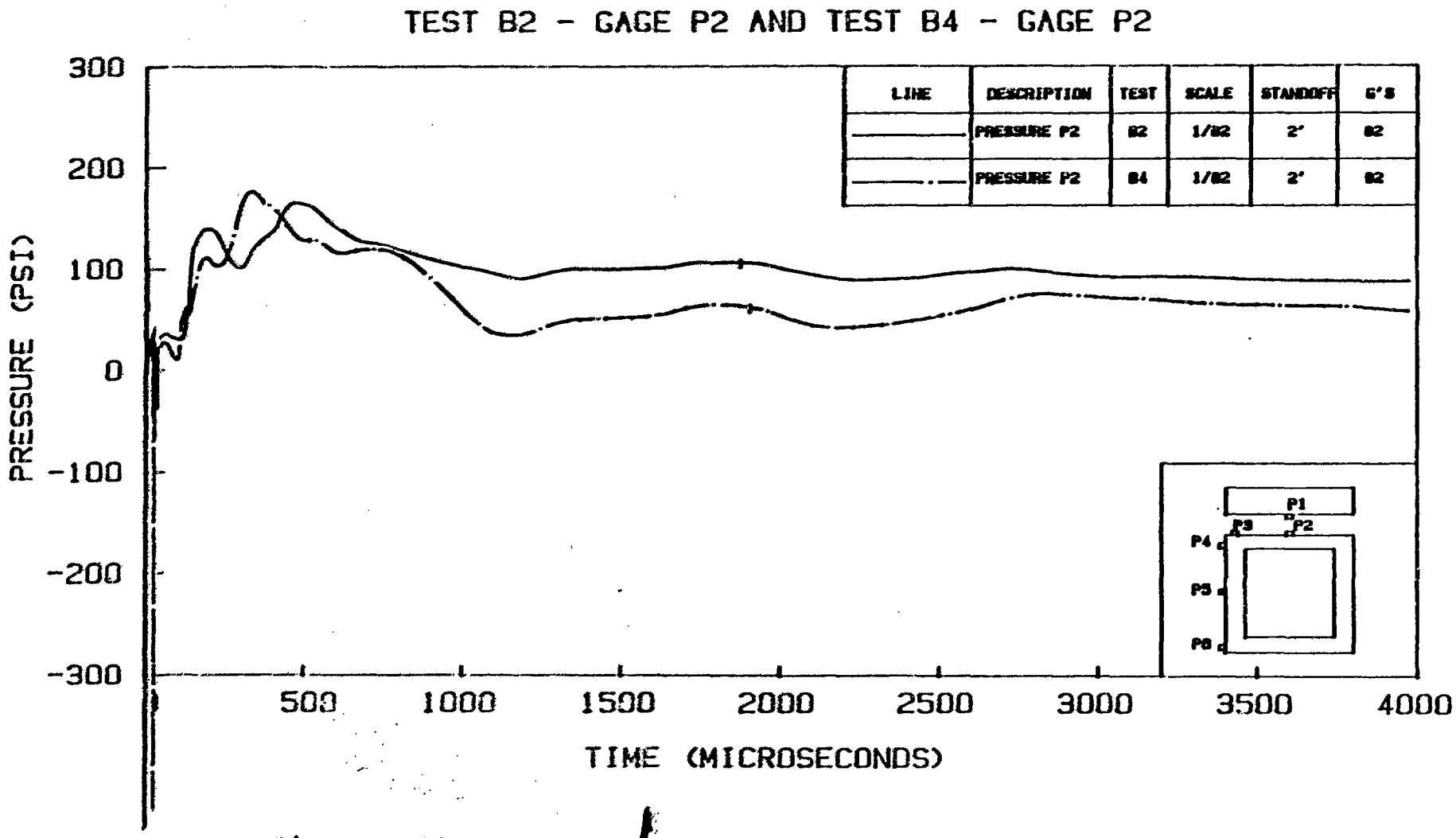

Figure 6.13. Response of Pressure Gage P2 in Tests B2 and B4

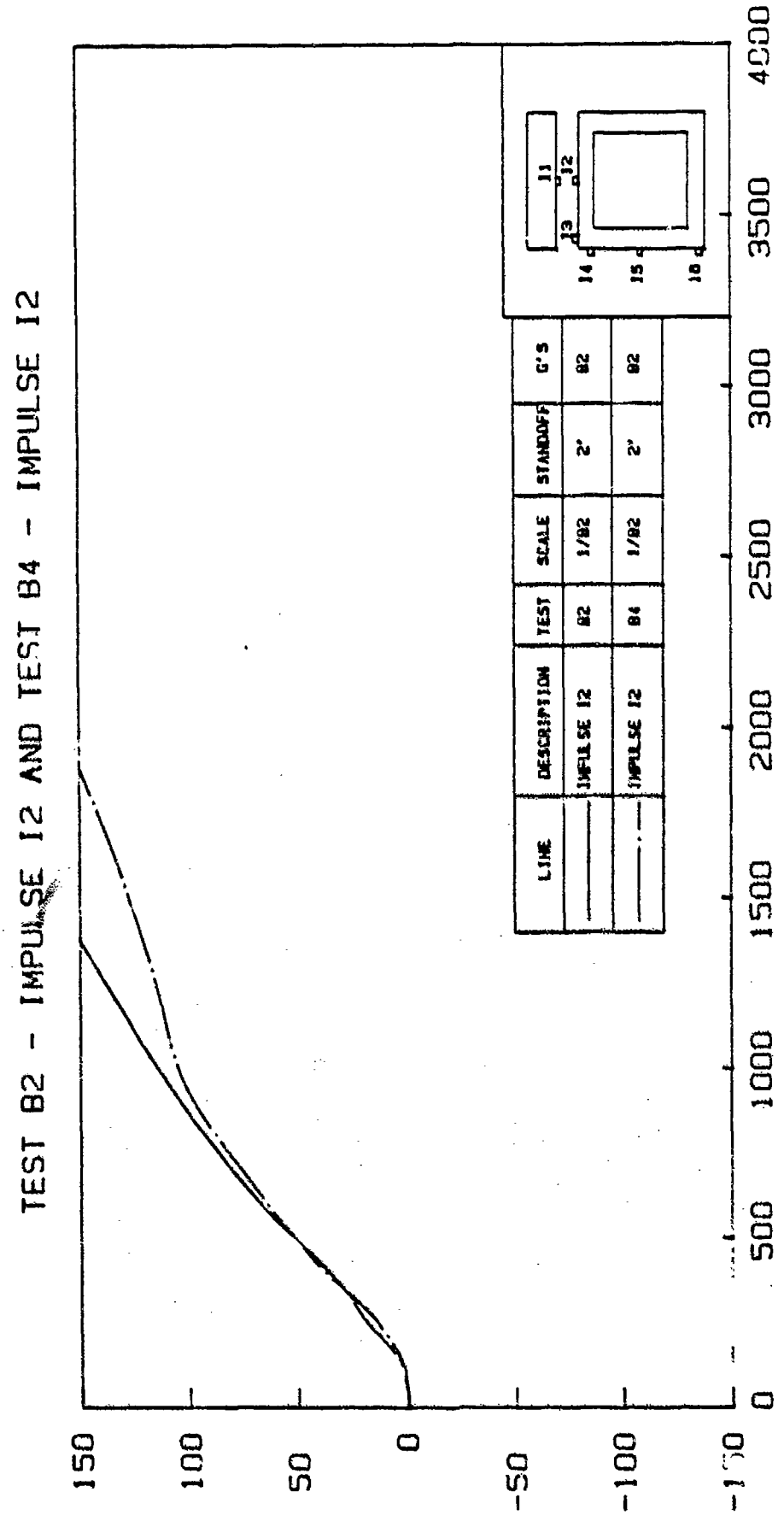

Figure 6.14. Impulse Curves (I2) in Tests B2 and B4

Figure 6.15 shows the Pressure Gage (P2) responses in tests A3 (0' standoff, 1g) and A4 (0' standoff, 60 g's). Test A4 was performed using a burster slab which had a crater and some cracks which appeared during test A3. Test A3 exhibits an unusual response considering the observed responses in tests at 2' standoff explained earlier. The peak pressure in test A3 (277 psi) is higher than the peak pressure in test A4 (163 psi) by 70%. This phenomenon may be explained by considering several factors. First, in tests at zero standoff, the explosive charge rests on the top surface of the burster slab and most of the pressure is expected to transfer to the soil at a point directly beneath the charge. If there is increased soil stiffness (60-g test), the pressure is expected to distribute more evenly on top of the box structure. Second, a part of the total energy of explosion is expended in crater excavation. Crater formation in soils is shown to be a function of gravity (Schmidt and Holsapple, 1980 and Kutter et al., 1985). Assuming that the same holds true for crater formations in concrete, a larger portion of the total energy is used in crater formations at high-gravity environments. Therefore, a smaller portion of the total energy is transmitted to the structure or soil as shock wave. Third, there is a slight possibility that the placement of the model or the explosive may not have been precise in the only test performed at 1g with a standoff distance of zero (test A3).

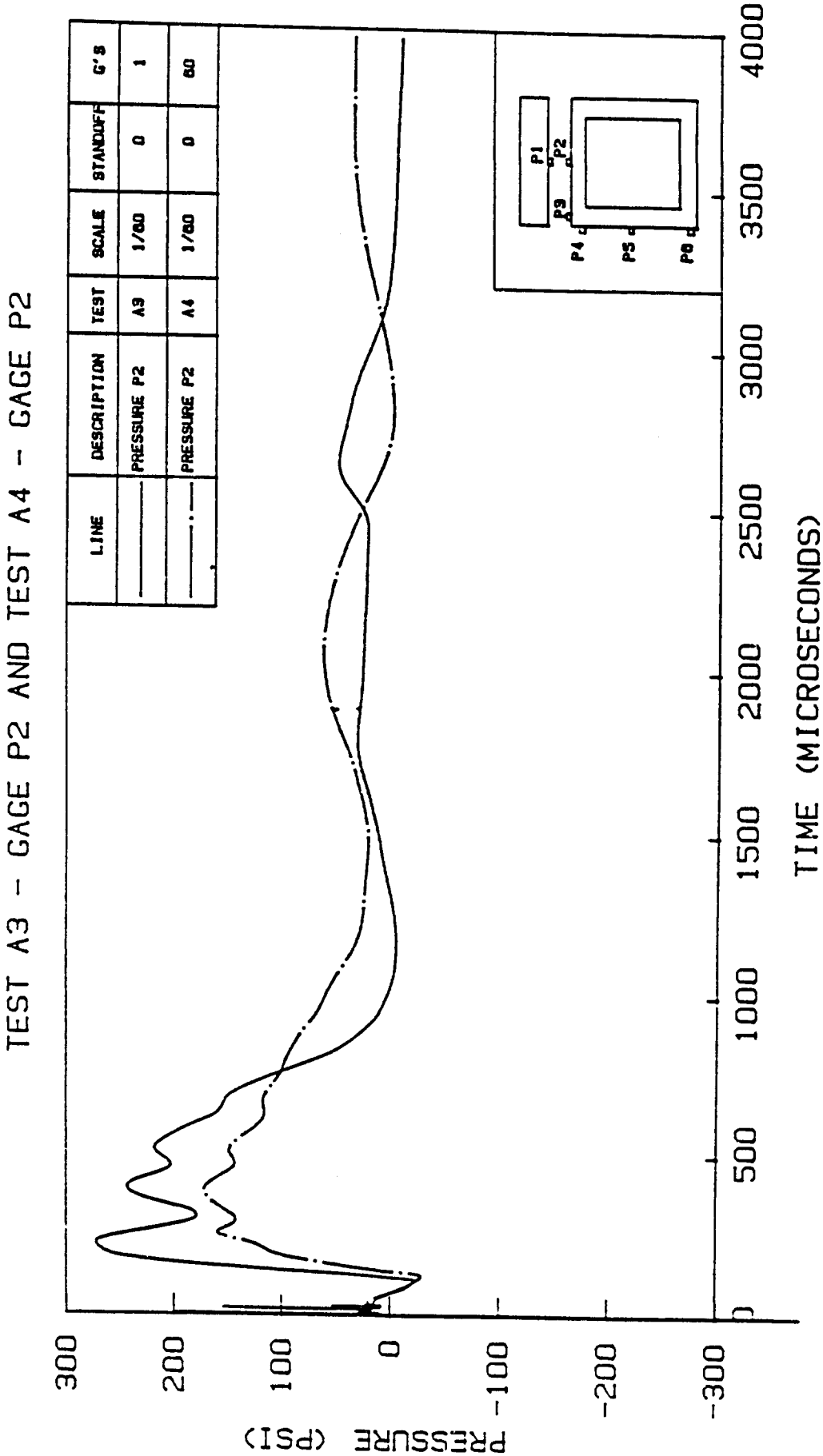

Figure 6.15. Response of Pressure Gage P2 in Tests A3 and A4

Figure 6.16 shows the impulse curves for tests A3 and A4. The peak impulse (impulse at zero pressure) in test A3 is 23% larger than the peak impulse in test A4.

Figure 6.17 compares the Pressure Gage (P2) responses in tests A3 (0' standoff, 1g) and A7 (0' standoff, 60 g's). In this case, the burster slab used in test A7 was intact before the test. Again, the pressure peak in test A3 (277 psi) is larger than the peak in test A7 (169 psi) by 64%.

Table 6.1 shows the two similar tests (A4 and A7) with very good agreement with respect to the magnitude and the arrival time of the first peak but the values of the second peak have large differences. Figure 6.18 shows a considerably larger impulse values for test A3 compared to test A7.

Figure 6.19 shows the Pressure Gage (P2) response curves for tests B3 (0' standoff, 82 g's) and B5 (0' standoff, 82 g's). These two tests are similar. However, even though the arrival time of the shock waves are very close, the peak pressures in test B5 (404 psi and 337 psi) are higher than in test B3 (313 psi and 240 psi) by 29% and 40% respectively. Figure 6.20 shows large impulse values for test B5 compared to test B3. Table 6.1 shows that the first peak pressures in tests on 1/82-scale models at zero standoff are higher than the pressures in tests on 1/60-scale models.

In summary, Table 6.1 shows that for tests at 2' standoff, the arrival times of the first peak pressure in

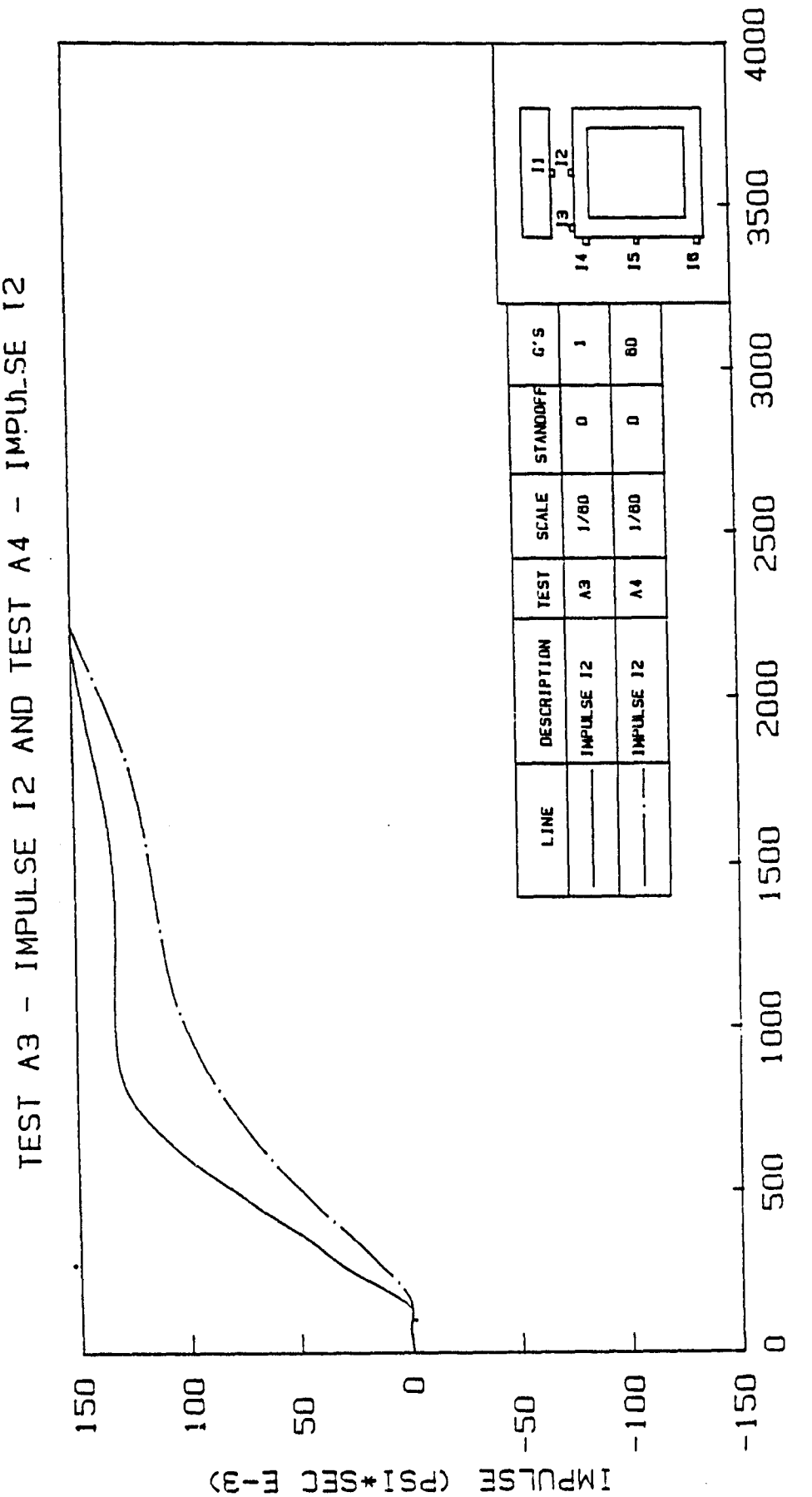

Figure 6.16. Impulse Curves (I2) in Tests A3 and A4

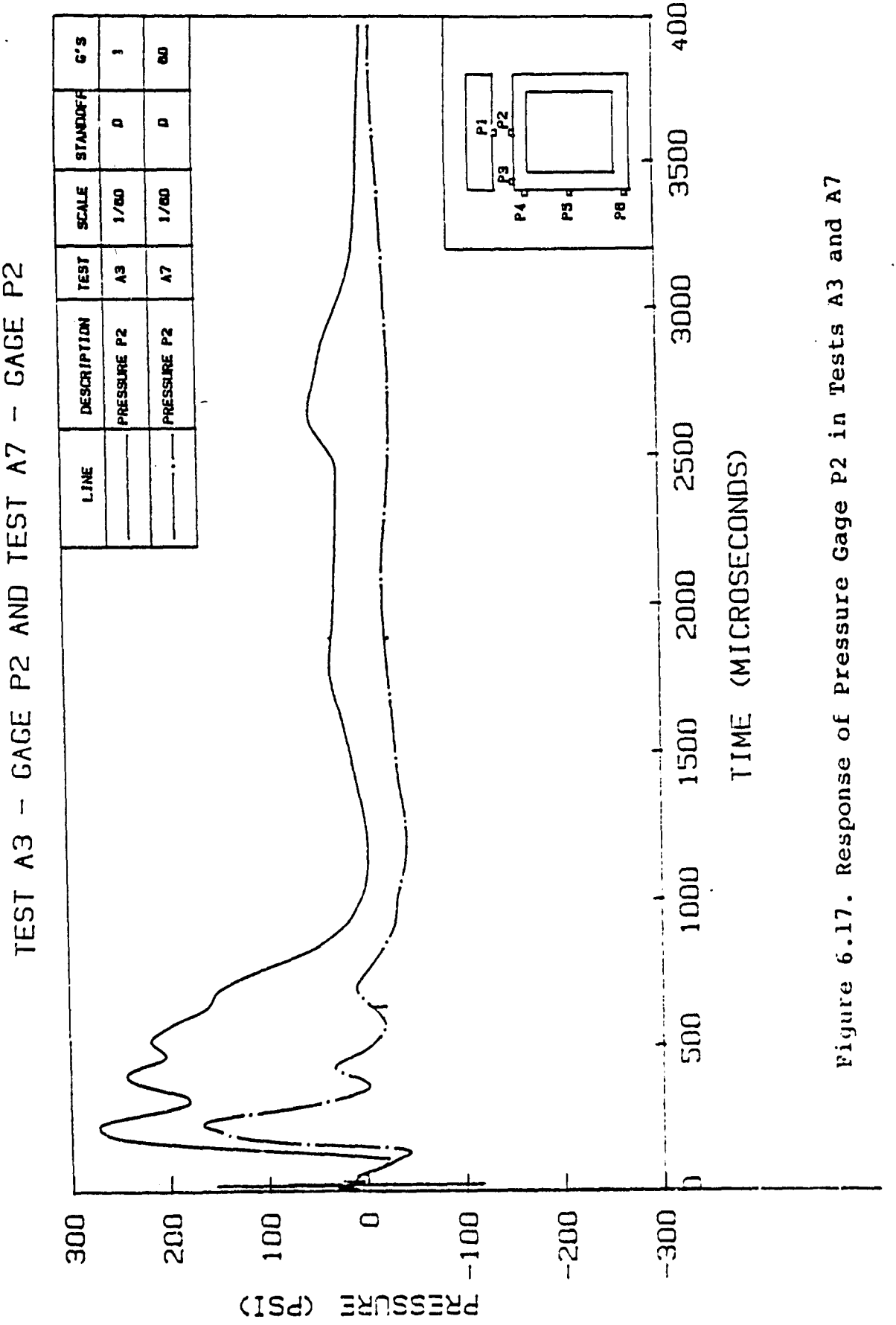

Figure 6.17. Response of Pressure Gage P2 in Tests A3 and A7

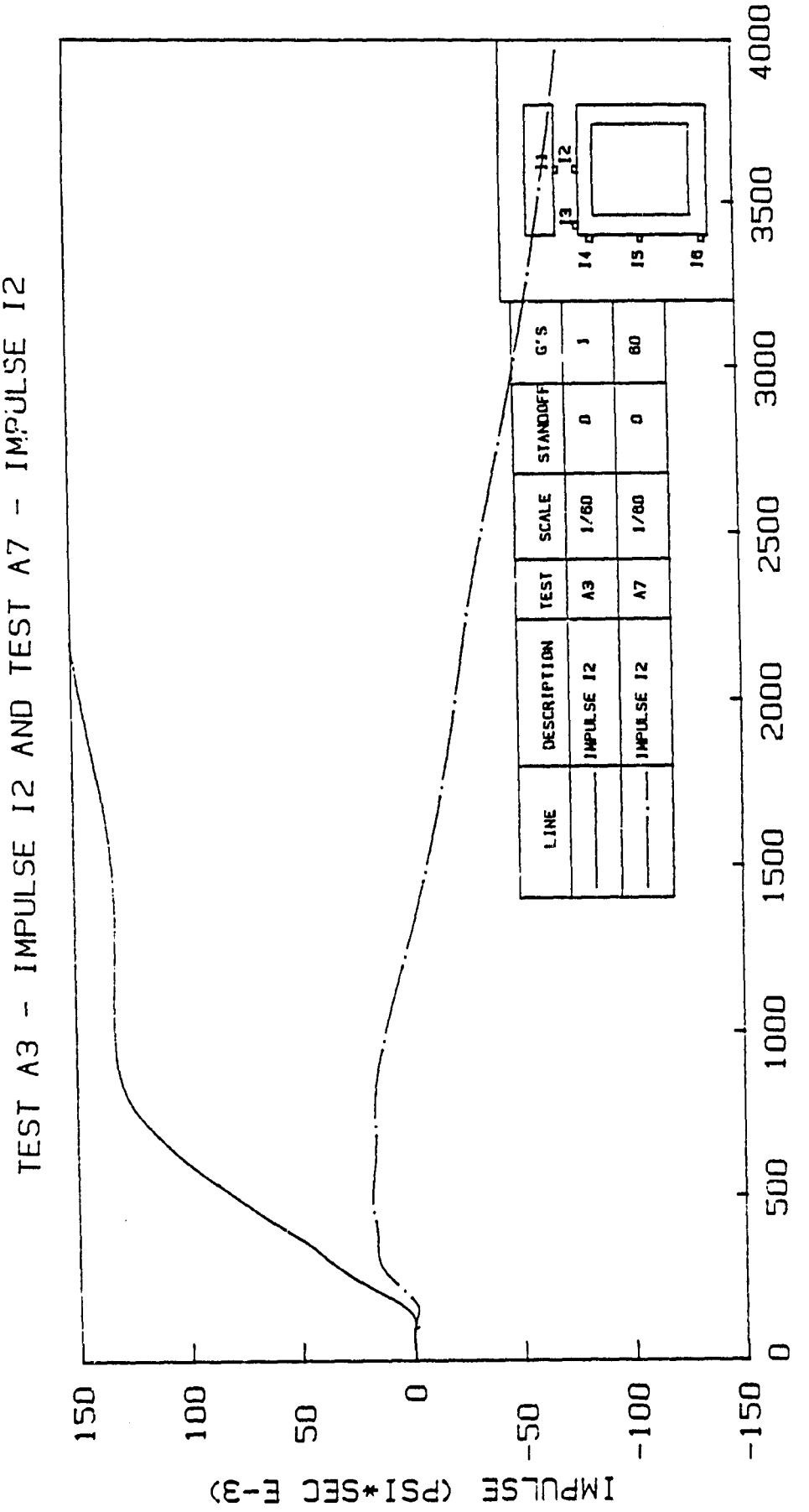

Figure 6.18. Impulse Curves (I2) in Tests A3 and A7

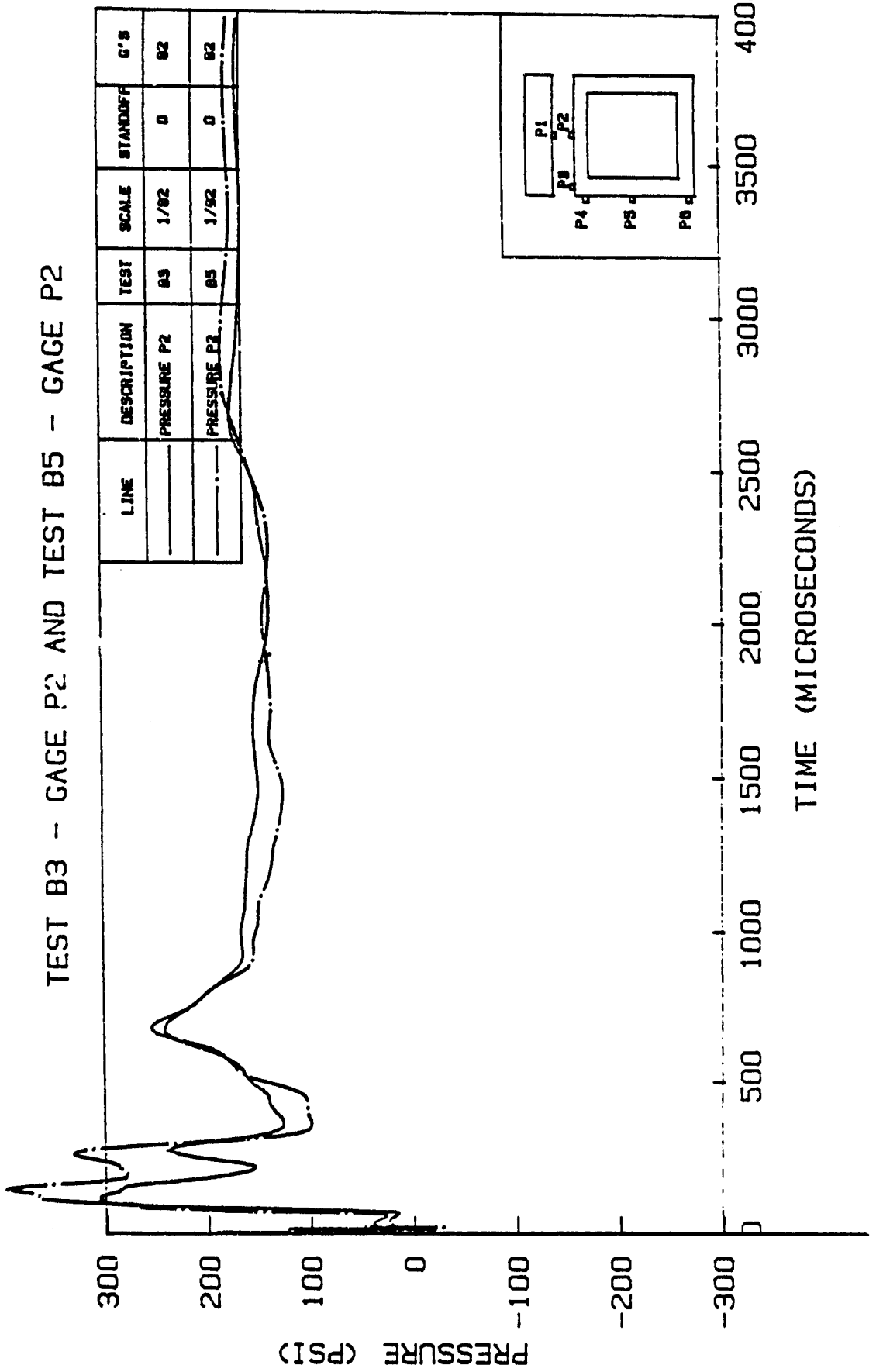

Figure 6.19. Response of Pressure Gage P2 in Tests B3 and B5

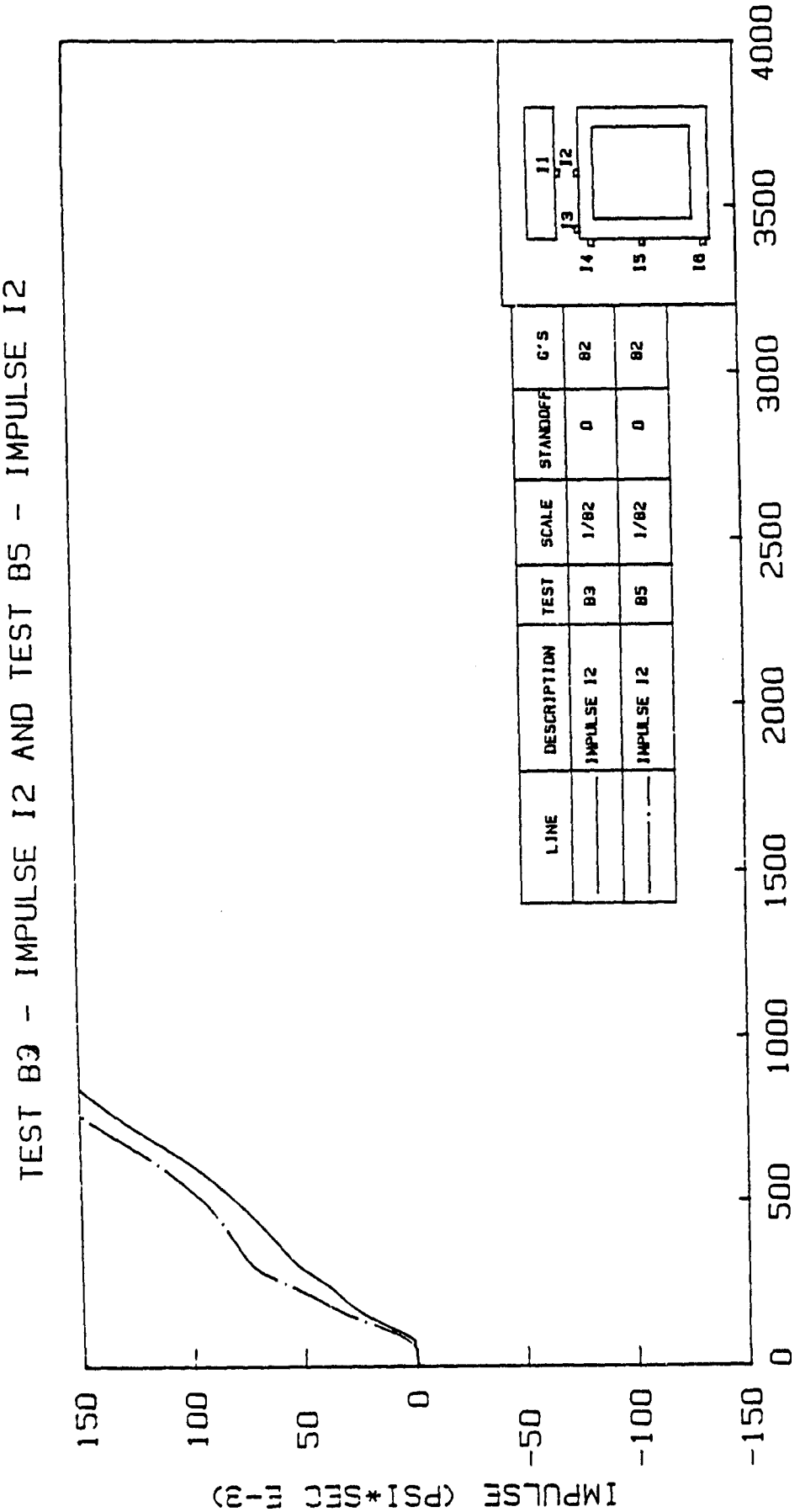

Figure 6.20. Impulse Curves (I2) in Tests B3 and B5

1g tests are consistently and substantially higher than the corresponding arrival times in 60 or 82g tests. Moreover, the impulse curves show larger values in high-gravity tests at 2' standoff. The peak pressures in tests at 60 g's are slightly higher than tests at 1g. For tests at 0 standoff distance, the only test performed at 1g shows larger pressures and impulses as compared to high-gravity tests. These facts indicate the importance of properly accounting for the effect of gravity stresses through centrifuge testing. Comparisons of tests on 1/60 and 1/82-scale models indicate slight variations from the theoretical scaling relationships. This can be attributed to inaccurate scaling of the geometry and mass distribution of the explosive charge in 1/82-scale tests.

6.1.3 Pressure Gage P3

Pressure Gage P3 is located on top of the box structure and directly over the side wall (see Figure 4.21). In this section, only the largest peak pressure is used as a basis for comparisons between different tests because, in most cases, only one significant peak appeared in the response of Pressure Gage P3. Figure 6.21 shows the Pressure Gage (P3) responses in tests A1 (2' standoff, 1g) and A2 (2' standoff, 60 g's). The peak pressure in the 60-g test (58 psi) is much larger than the peak in test A1 (7 psi). Also, the arrival time of the peak in test A1 (548 μseconds) is larger than the corresponding arrival time in test A2 (482

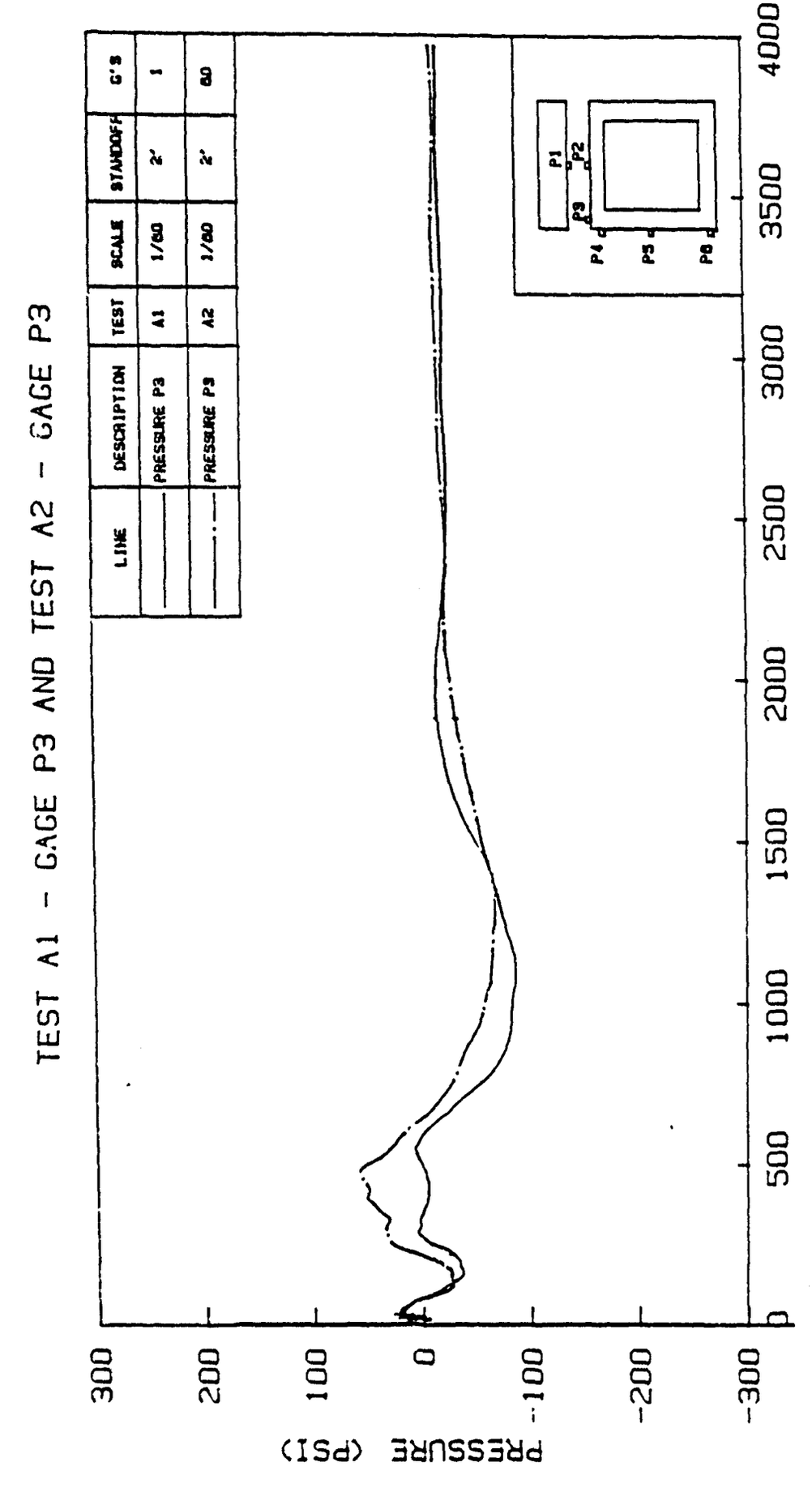

Figure 6.21. Response of Pressure Gage P3 in Tests A1 and A2

μseconds) by 14%. Figure 6.22 shows the impulse curves for the two pressure curves in Figure 6.21.

Figure 6.23 shows the Pressure Gage (P3) response in tests A5 (2' standoff, 1g) and A6 (2' standoff, 60 g's). It is clear that the peak pressure in the 60-g test (194 psi) is much larger than the peak pressure in the 1-g test (69 psi) by 181%. Although the arrival time of the peak in test A6 is larger than the arrival time in A5 by 12%, the arrival time of the shock front is clearly smaller in test A6.

Comparisons of tests A1 and A2 with A5 and A6 respectively indicate that there are wide variations in magnitudes of pressures in similar tests even though the arrival times are close. The reason may be due to an incorrect placement of the burster slab which resulted in the burster slab not being precisely over the box structure in tests A1 and A2. Also, variations in soil density at different locations may be a contributing factor. Figure 6.24 shows much larger impulse for test A6 as compared to A5.

Figure 6.25 shows pressure responses in tests B1 (2' standoff, 1g) and B2 (2' standoff, 82 g's) on 1/82-scale models. Test B1 exhibits a very well-defined pressure response. This type of response is expected for Pressure Gage P3 because of its location on top of the side wall. Gage P3 is subjected to much smaller structural deformations and wave reflections than Gage P2. The arrival

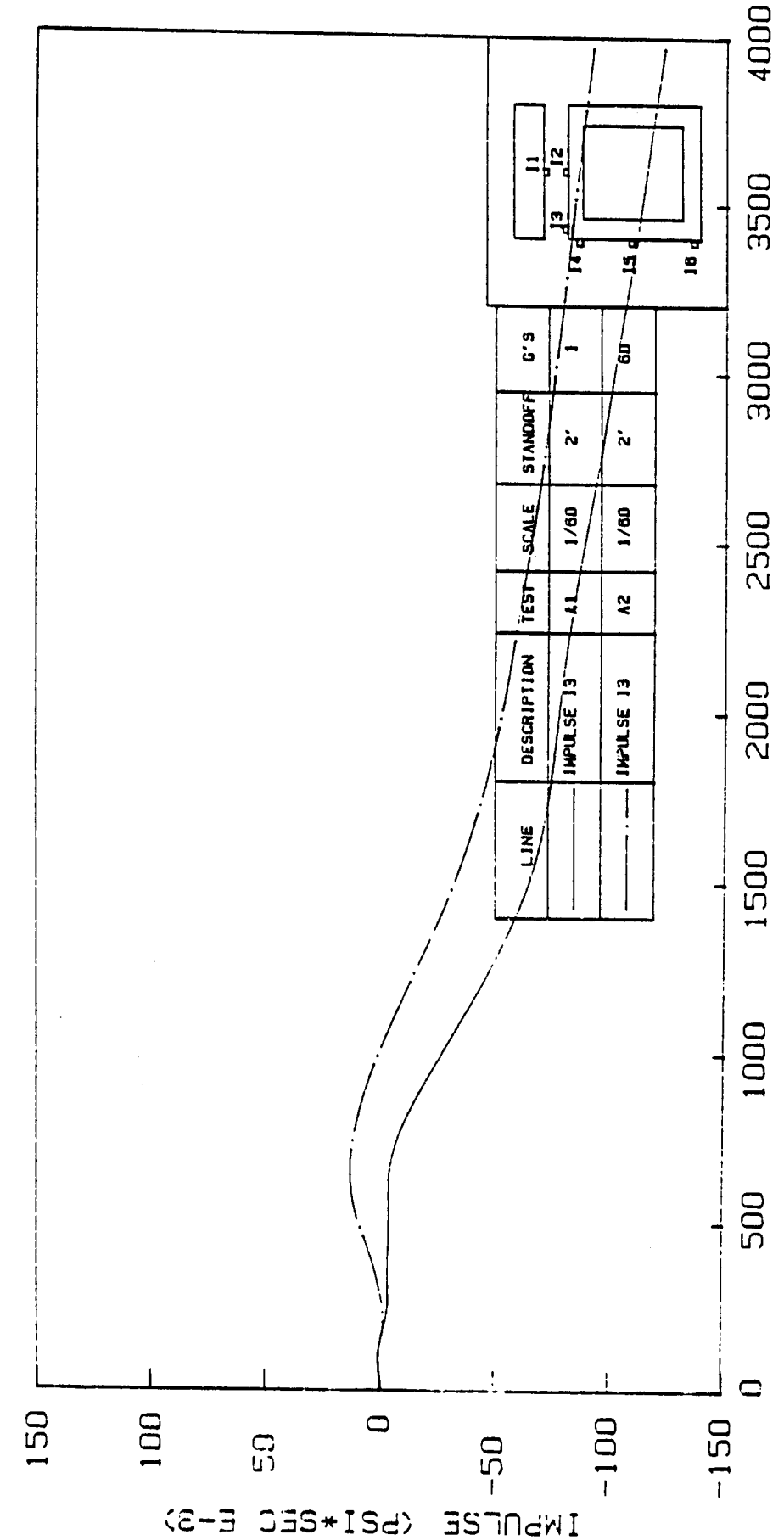

Figure 6.22. Impulse Curves (I3) in Tests A1 and A2

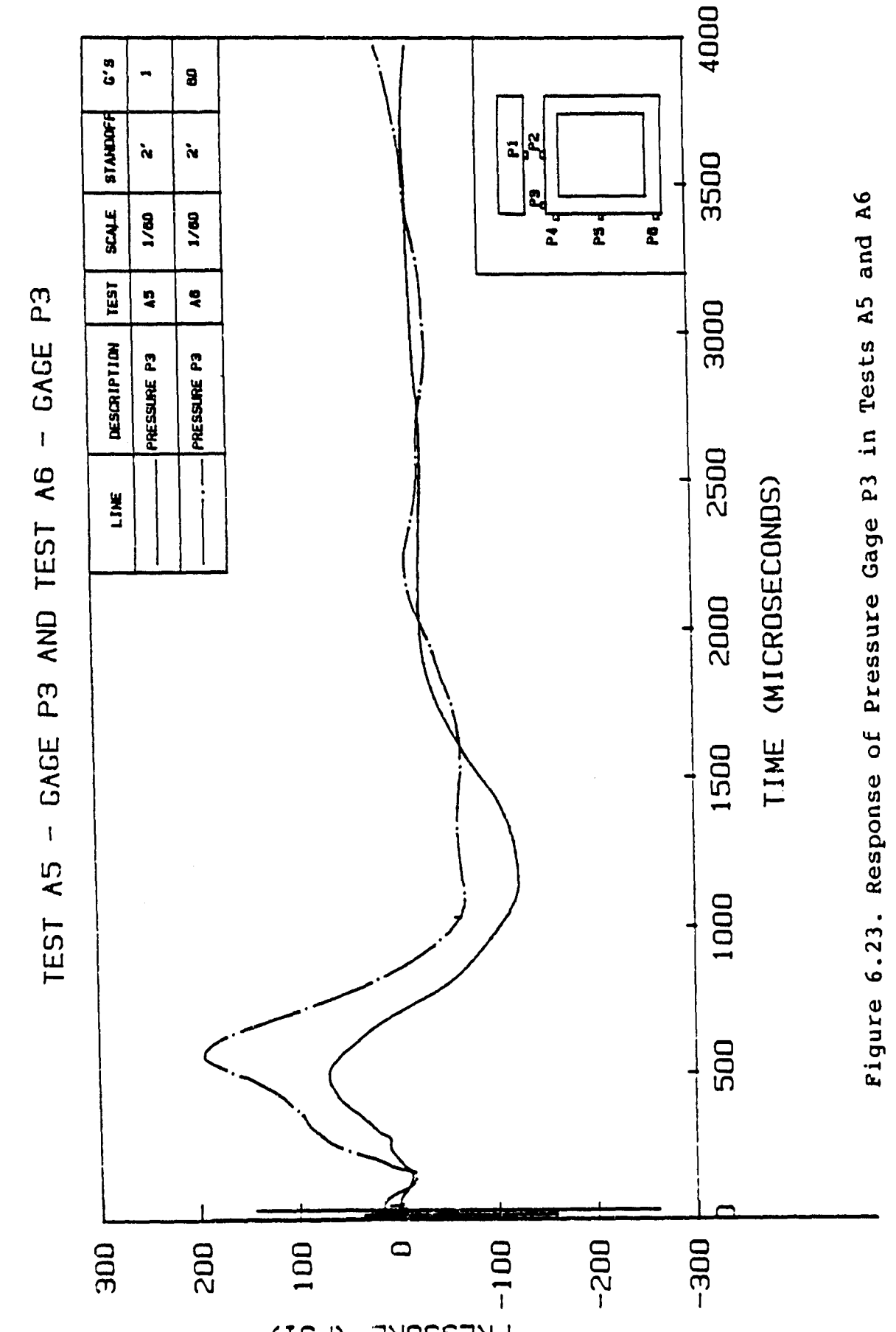

Figure 6.23. Response of Pressure Gage P3 in Tests A5 and A6

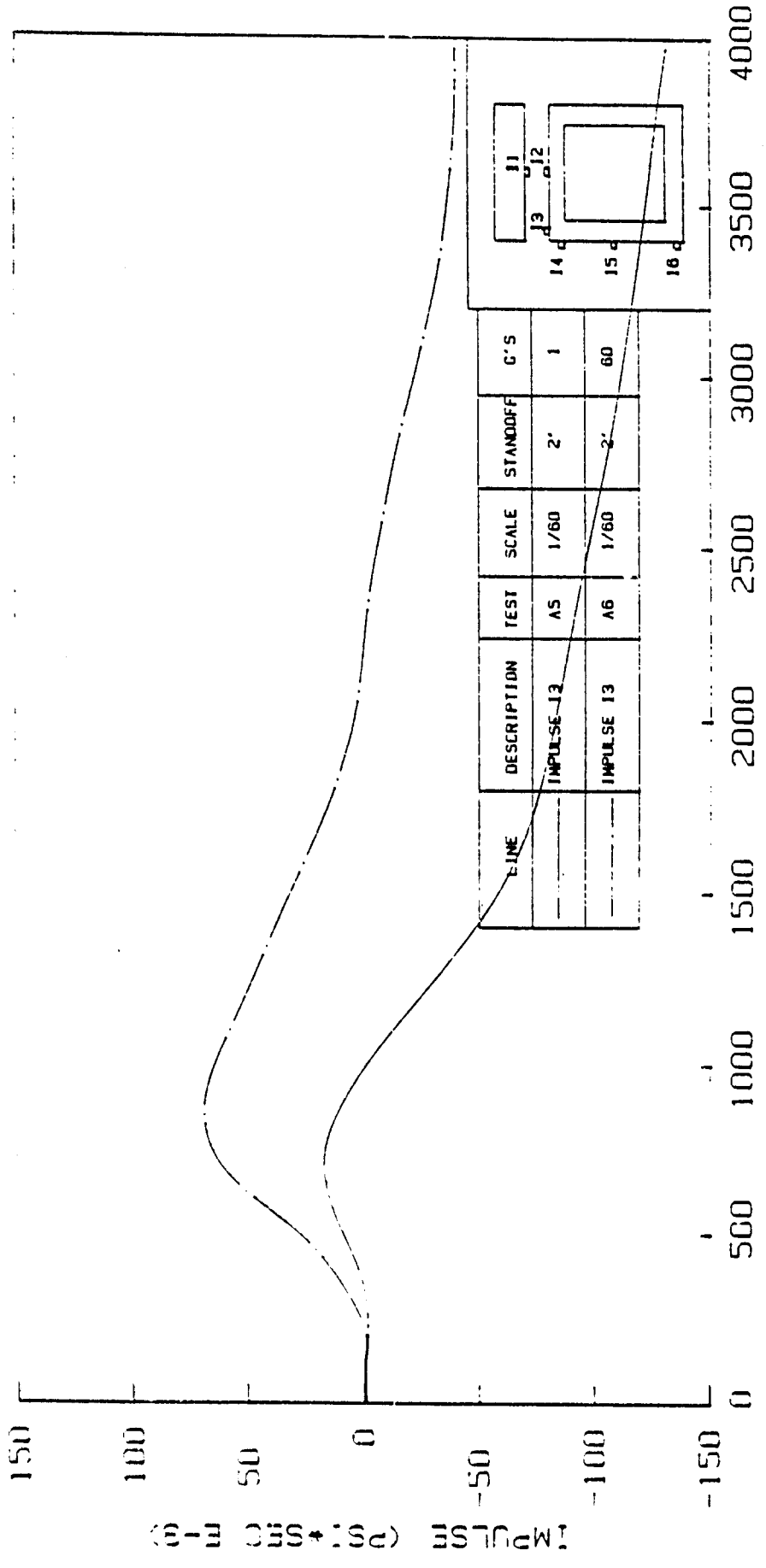

Figure 6.24. Impulse Curves (I3) in Tests A5 and A6

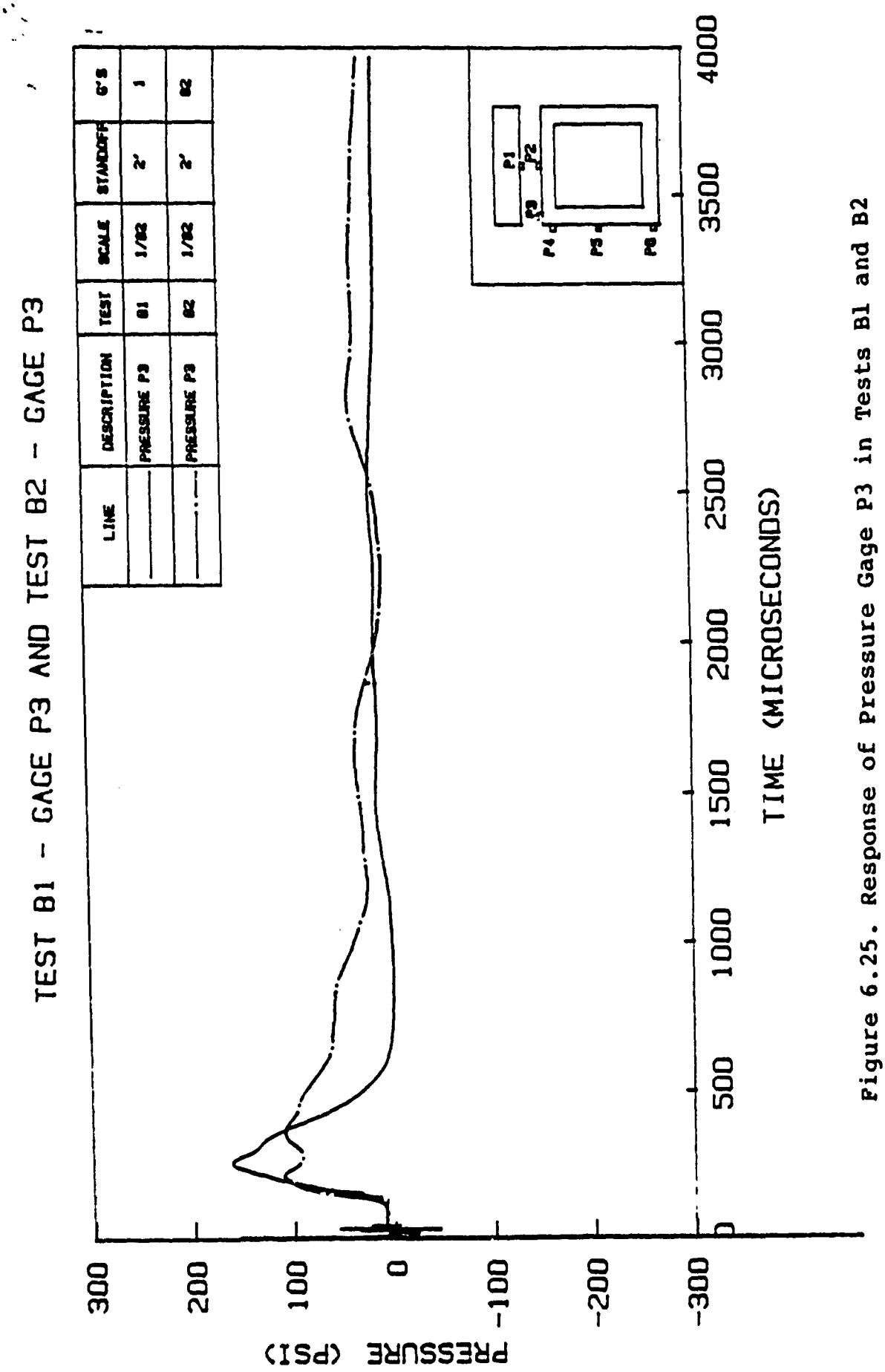

Figure 6.25. Response of Pressure Gage P3 in Tests B1 and B2

time of the shock front in test B2 is slightly smaller (faster) as expected. However, the peak pressure in test B2 is smaller (double-peak) by about 45%. This unusual behavior may be attributed to a rigid-body movement of the structure when subjected to pressure. The duration of the pressure wave in test B2 is longer than in test B1. Figure 6.26 illustrates the difference in impulse curves between these two tests.

A similar-shape response is obtained in tests A3 (0' standoff, 1g) and A4 (0' standoff, 60 g's) as shown in Figure 6.27. The peak pressure in test A3 (135 psi) is larger than the peak pressure in test A4 (108 psi) by 25%. Figure 6.28 shows the impulse curves for these two tests.

Figure 6.29 shows pressure responses in tests A3 (0' standoff, 60 g's) and test A7 (0' standoff, 60 g's). The difference between these two tests and tests A3 and A4 shown in Figure 6.27 is that the burster slab in test A7 was intact before the test was performed while the burster slab in test A4 was damaged during test A3. The peak pressure in test A7 (158 psi) is larger than the peak pressure in test A3 (135 psi) by 17%. The arrival time of the peak in test A7 is also higher by 21%.

Figure 6.30 shows the pressure results for tests B3 (0' standoff, 82 g's) and B5 (0' standoff, 82 g's) which are similar. The arrival time of the shock wave and the peaks are very close (206 and 208 μseconds). However, the magnitude of the peak in test B3 is larger by 31% (see

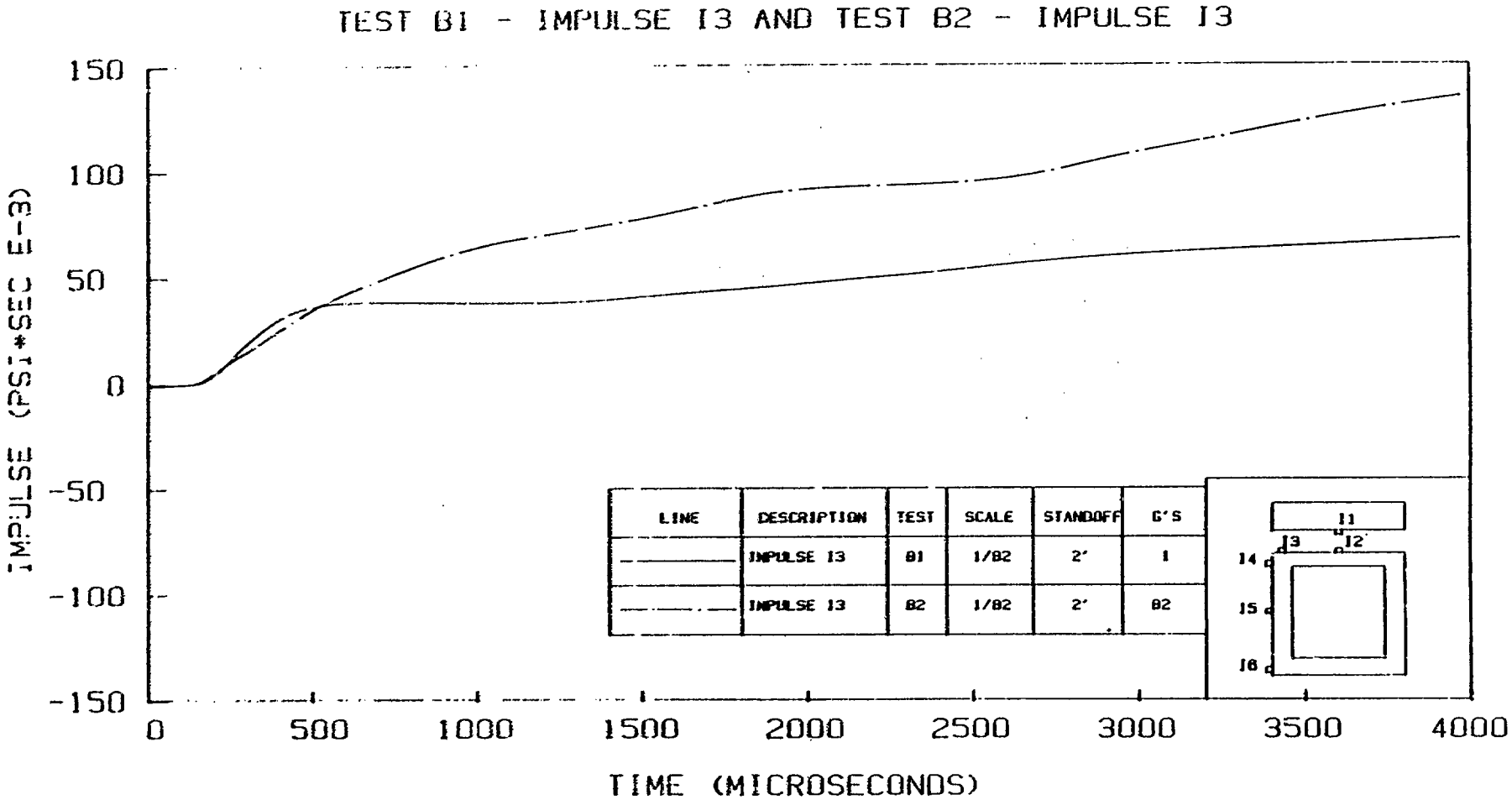

Figure 6.26. Impulse Curves (I3) in Tests B1 and B2

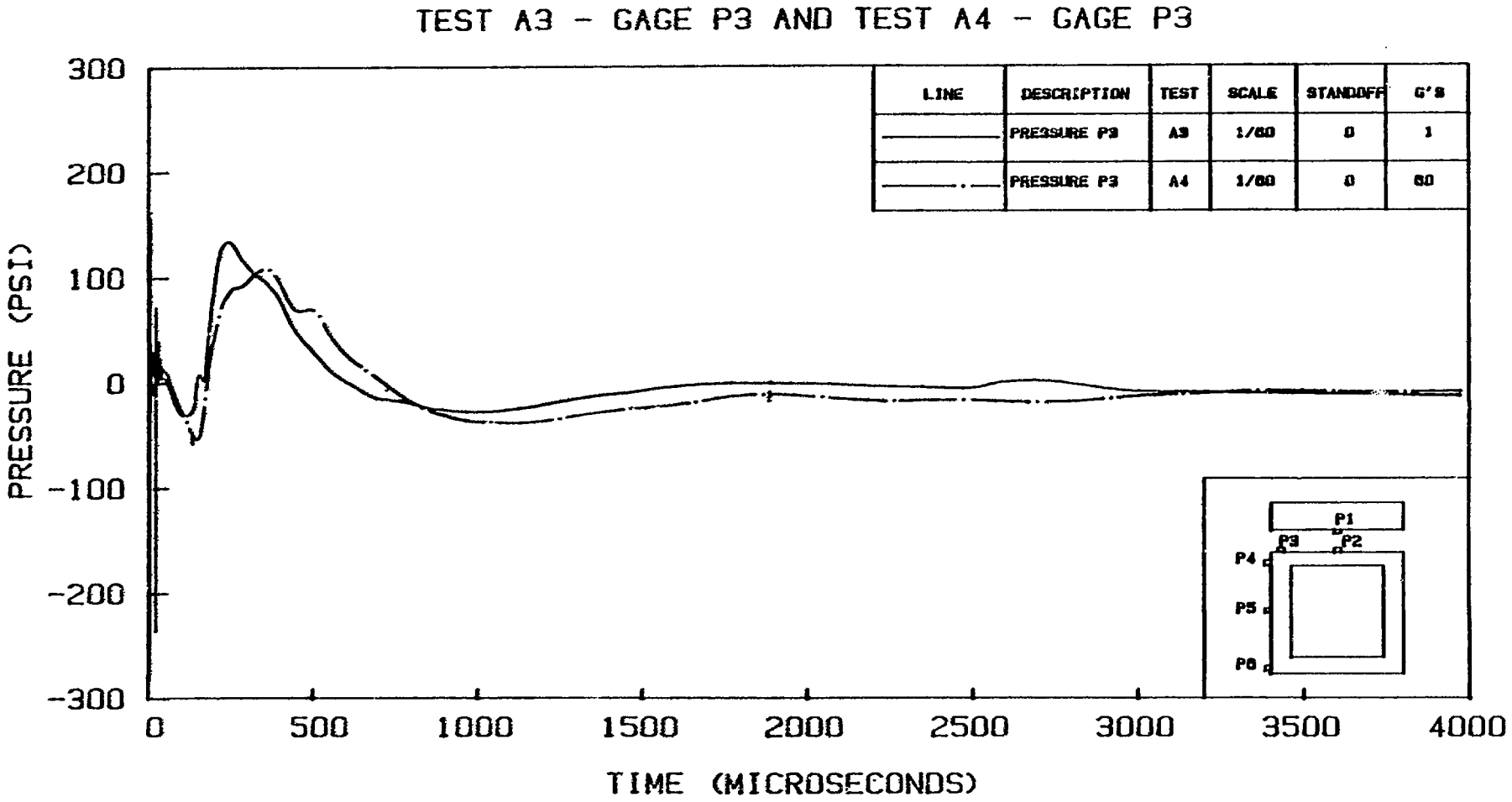

Figure 6.27. Response of Pressure Gage P3 in Tests A3 and A4

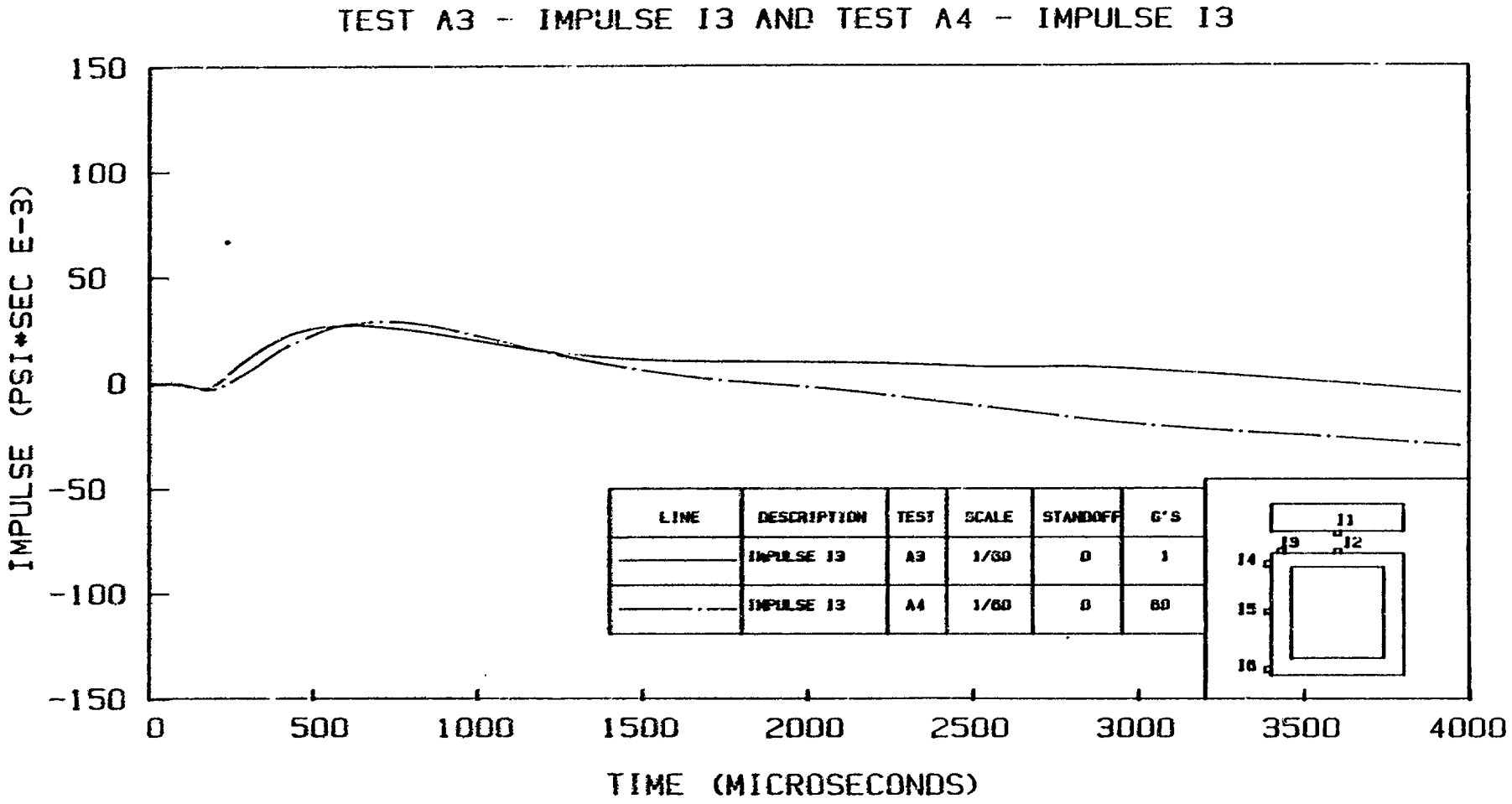

Figure 6.28. Impulse Curves (I3) in Tests A3 and A4

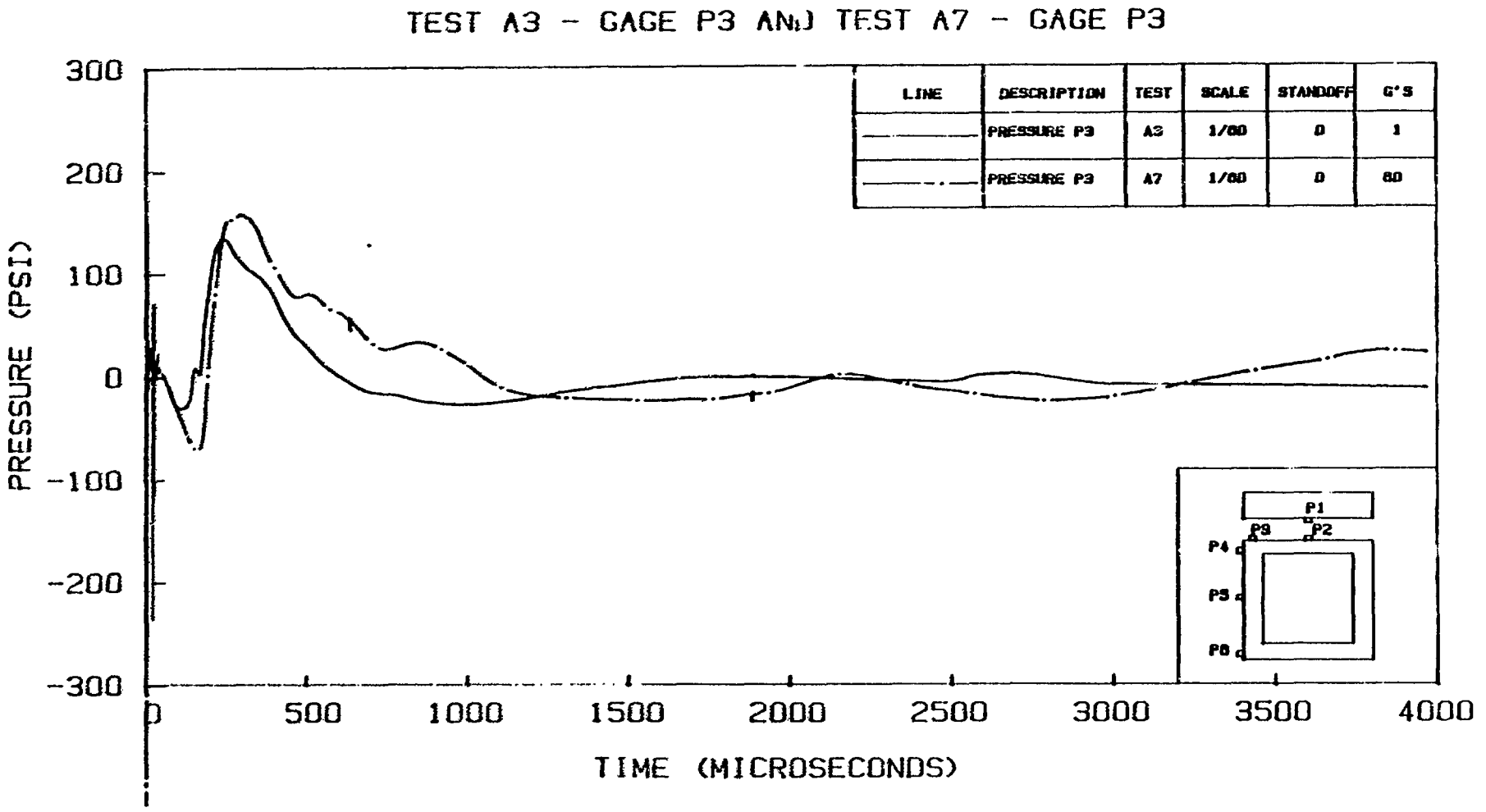

Figure 6.29. Response of Pressure Gage P3 in Tests A3 and A7

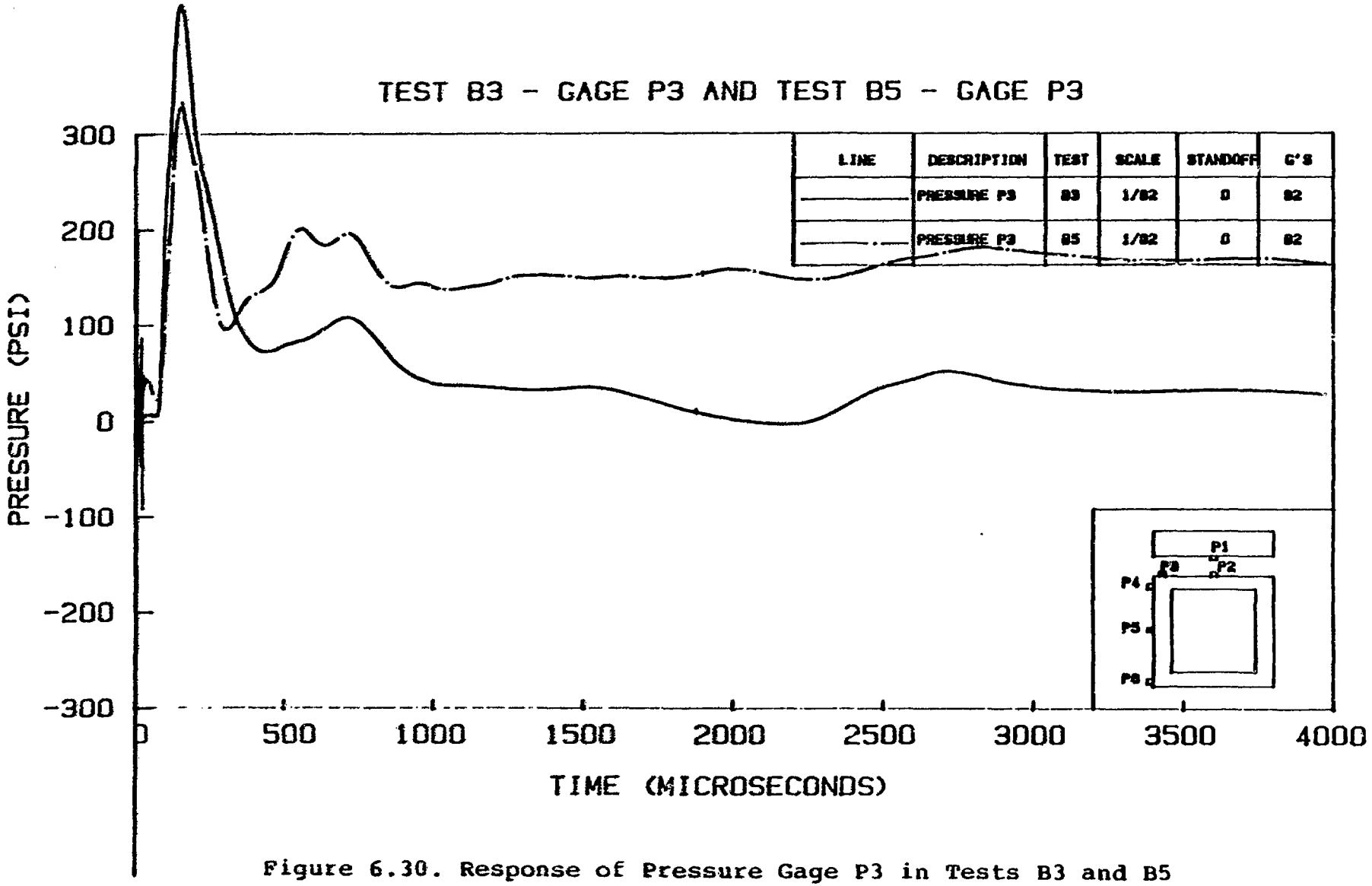

Figure 6.30. Response of Pressure Gage P3 in Tests B3 and B5

Table 6.2). These two tests show larger pressures and smaller arrival times than the corresponding 1/60-scale tests (A4 and A7). Table 6.2 also shows that 1/82- and 1/60-scale tests at high g's have better agreement in tests at 2' standoff.

In summary, the peak pressures (P3) in tests at 60 g's (2' standoff) are substantially larger than the corresponding pressures in tests at 1g. The arrival times of the shock fronts are also faster in the 60g tests. This type of behavior is not observed in tests on 1/82-scale model (B1 and B2) which may be due to a rigid body movement of the structure in test B2. The peak pressure in the 1g test at 0 standoff is higher than the corresponding test at 60 g's.

6.1.4 Pressure Gage P4

Pressure Gage P4 is located on top of the side wall as shown in Figure 4.21. If the sand used in these tests was saturated, then pressure Gage P4 would register relatively high pressures due to a hydrostatic pressure condition. However, the sand used in these tests were dry and therefore very little pressure is expected at the location of Gage P4. Figures 6.31 and 6.32 are two examples of P4 responses which are very close to zero.

Table 6.2

Summary of Pressure Gage P3 Responses

Standoff	0' Standoff						2' Standoff						
Gravity	1g		60 g's		82 g's		1g			60 g's		82 g's	
Model Scale	1/60	1/82	1/60		1/82		1/60		1/82	1/60		1/82	
Test Number	A3	None	A4	A7	B3	B5	A1	A5	B1	A2	A6	B2	B4
Maximum Pressure 1st Peak (psi)	135	----	108	158	437	334	7	69	162	58	194	110	85
Arrival Time* (Microseconds)	242	----	357	294	206	208	548	495	353	482	554	294	467

* For 1/82-scale tests, the actual arrival time is multiplied by 82/60 to obtain an arrival time equivalent to 1/60-scale tests

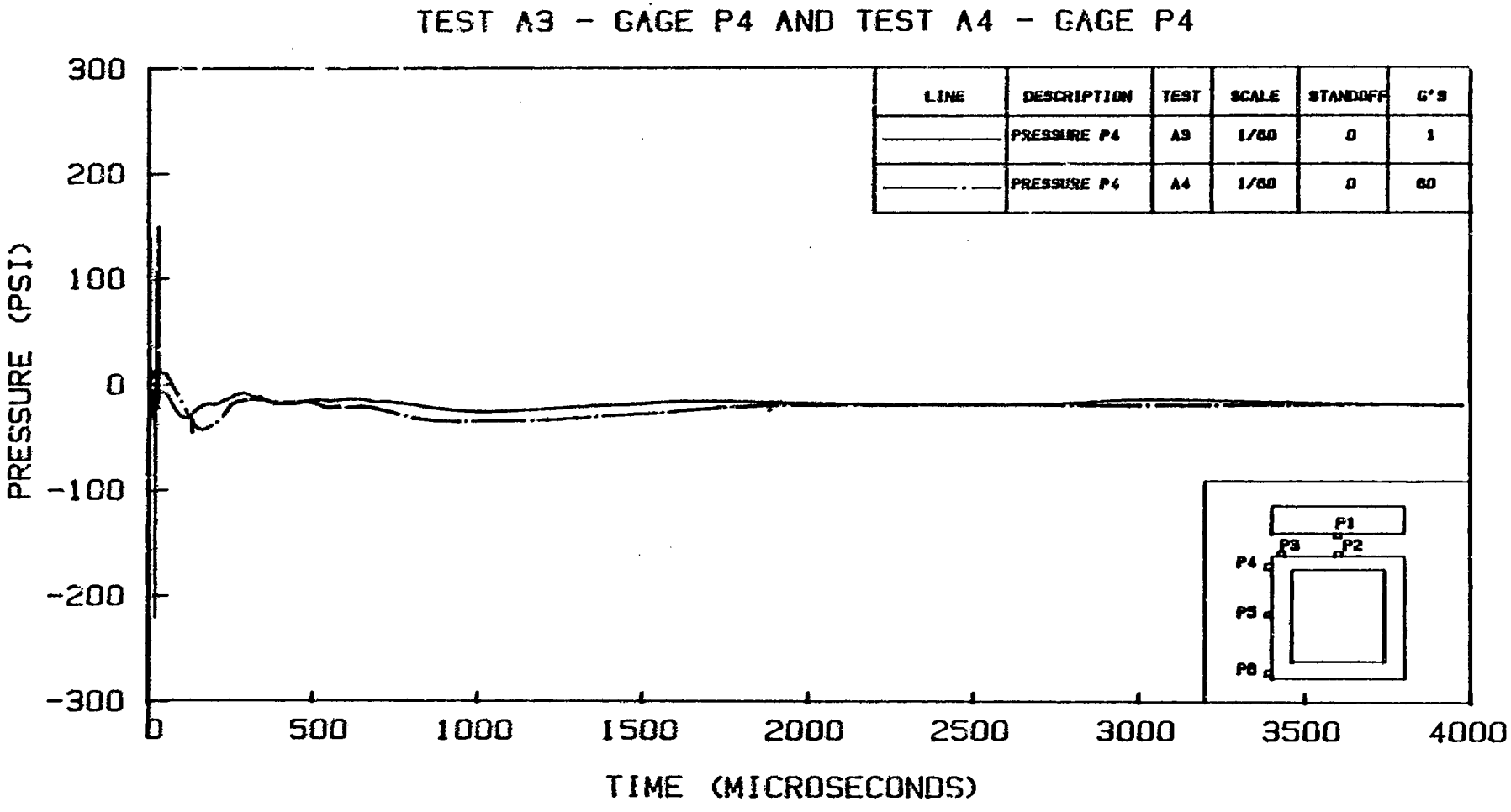

Figure 6.31. Response of Pressure Gage P4 in Tests A3 and A4

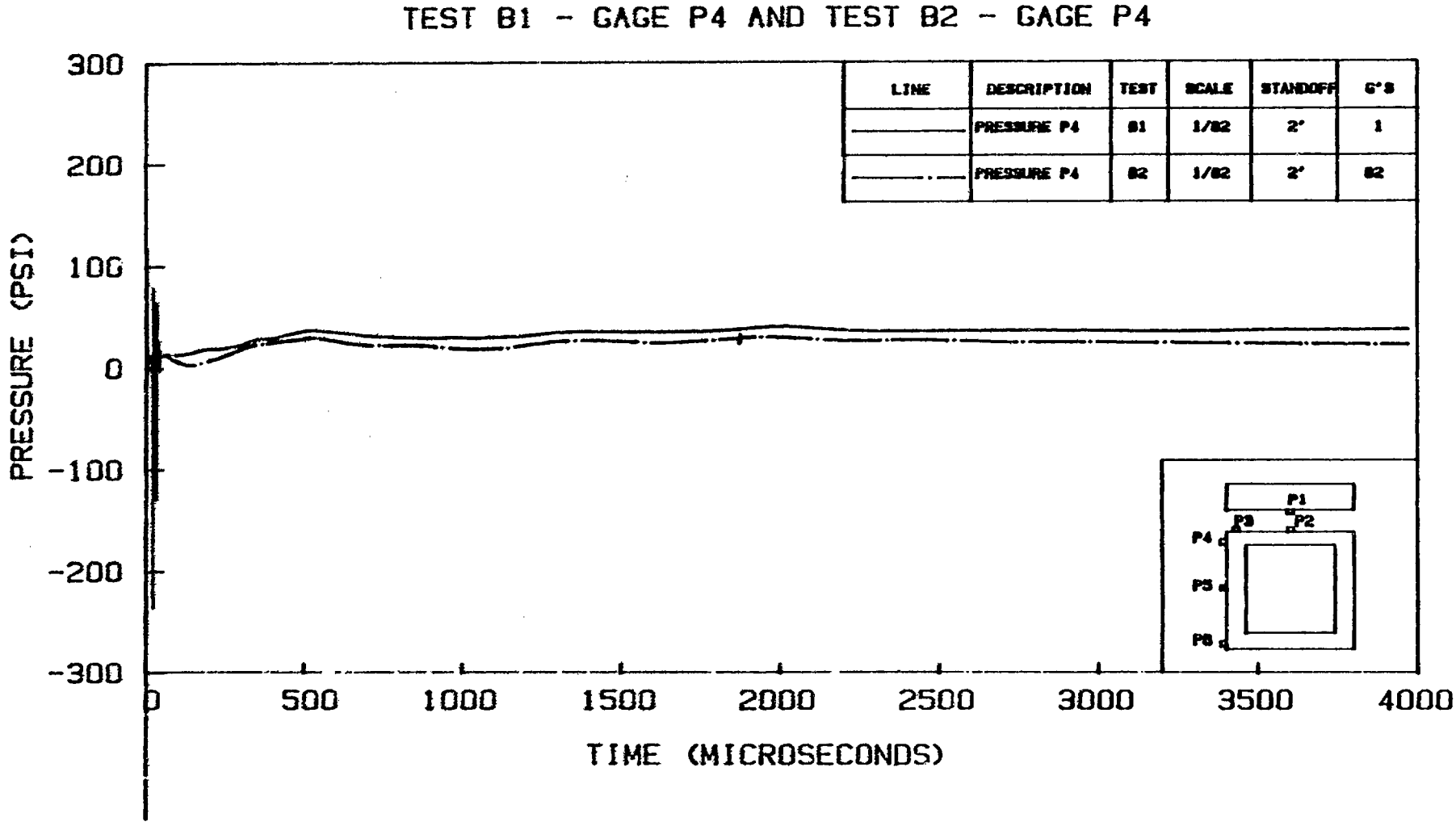

Figure 6.32. Response of Pressure Gage P4 in Tests B1 and B2

6.1.5 Pressure Gage P5

Pressure Gage P5 is located in the middle of the side wall as shown in Figure 4.21. Figure 6.33 shows the Pressure Gage (P5) response in tests A1 (2' standoff, 1g) and A2 (2' standoff, 60 g's). The peak pressure in the 60-g test (32 psi) is larger than the peak pressure in the 1g test (16 psi) by 100%. Figure 6.34 also indicated larger impulse for the 60-g test.

Figure 6.35 shows the pressure responses (P5) for tests A3 (0' standoff, 1g) and A4 (0' standoff, 60 g's). The pressures are very close to zero in both tests. Figure 6.36 shows a similar response for tests A3 and A7. Pressure Gage (P5) did not perform satisfactorily in tests on 1/82-scale models (B series). Therefore, those results are not presented here.

6.1.6 Pressure Gage P6

Pressure Gage P6 is located on the bottom of the side wall as shown in Figure 4.21. This gage also indicates pressures very close to zero in all tests (low and high-gravity tests). Figures 6.37 to 6.40 show the results for Gage P6 in some of the tests.

6.2 Accelerations

Locations of the two accelerometers (A1 and A2) used in the tests reported here are shown in Figure 4.23. In this section, the accelerometer waveforms for different tests

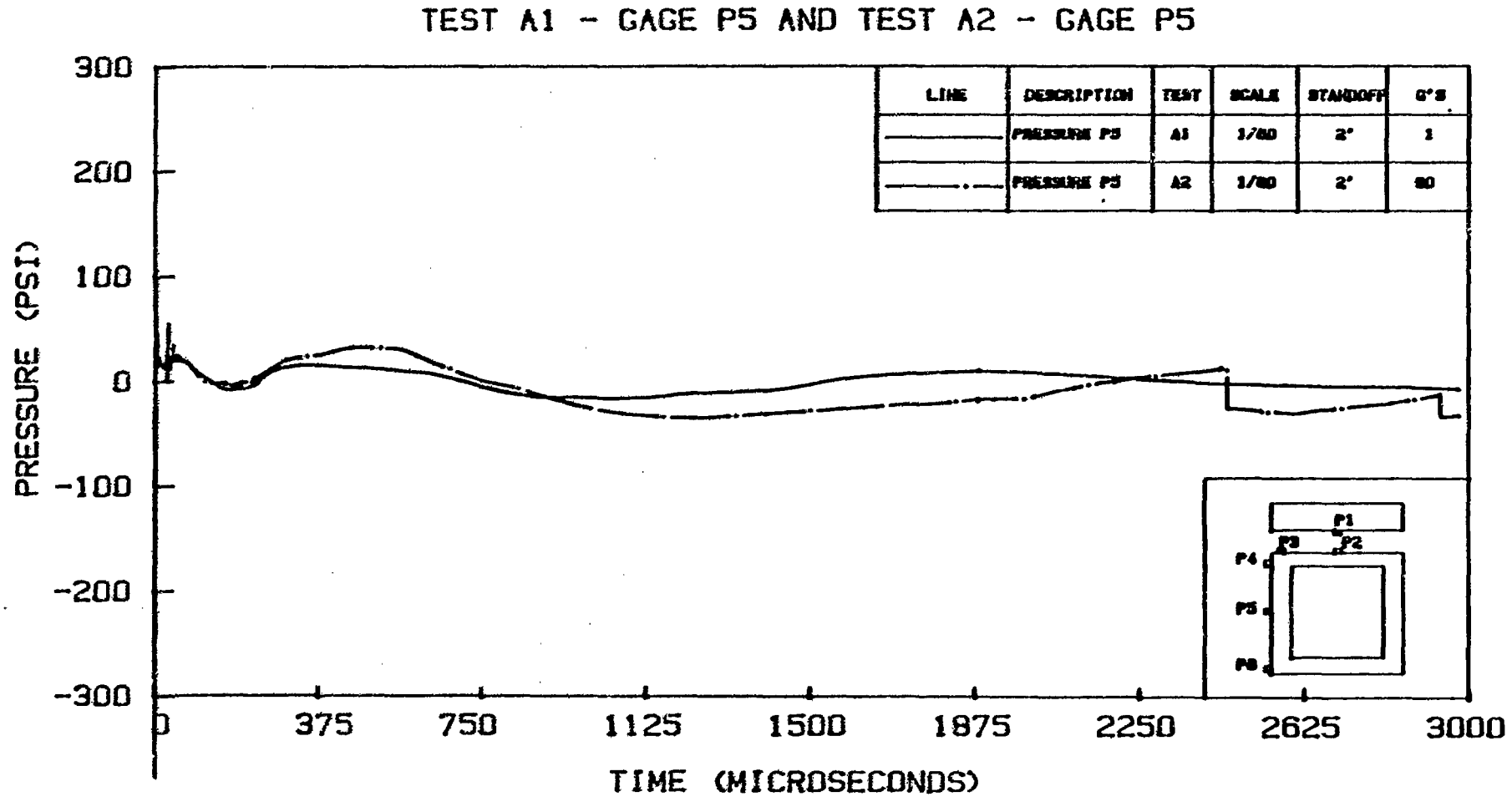

Figure 6.33. Response of Pressure Gage P5 in Tests A1 and A2

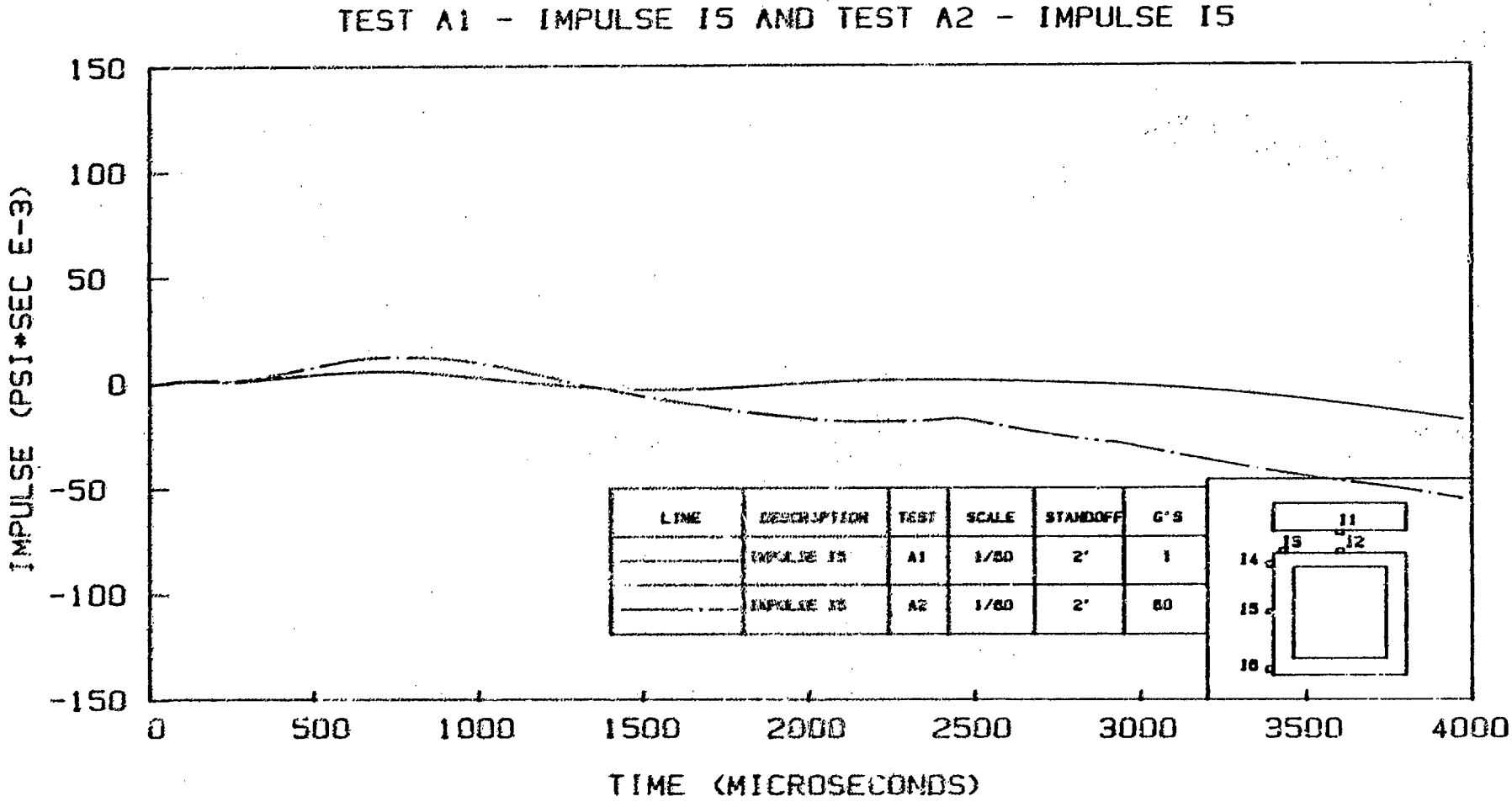

Figure 6.34. Impulse Curves (I5) in Tests A1 and A2

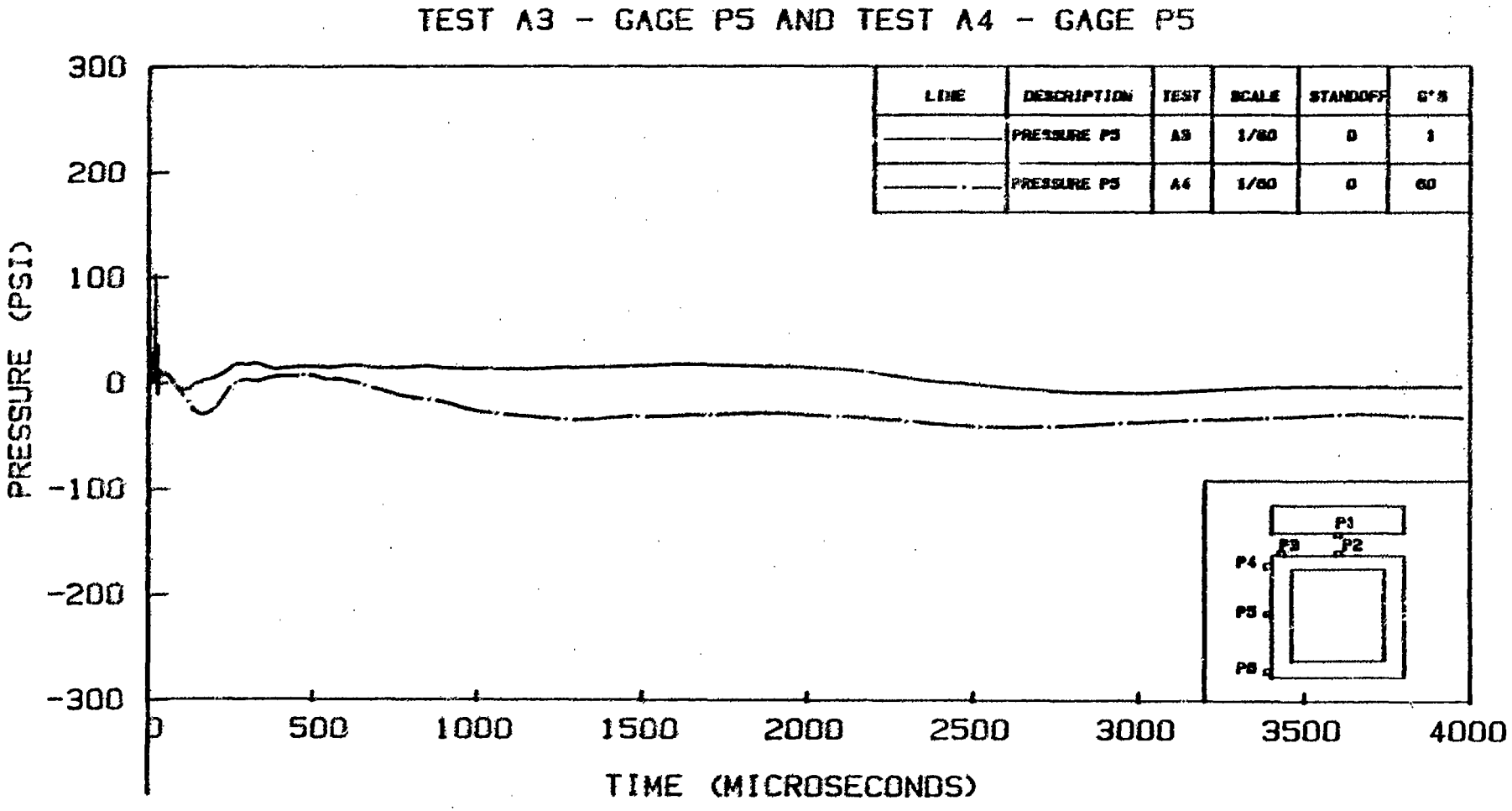

Figure 6.35. Response of Pressure Gage P5 in Tests A3 and A4

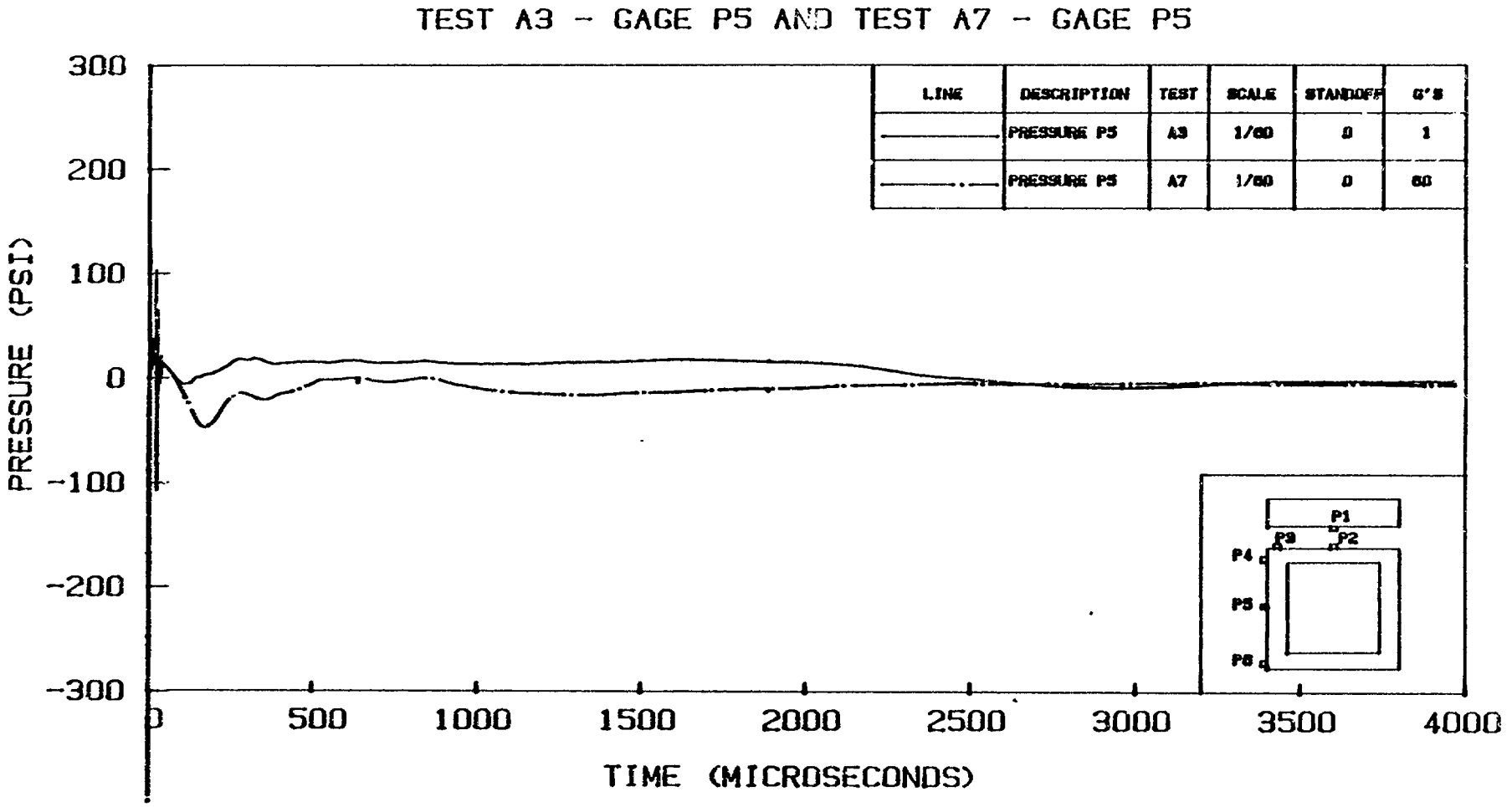

Figure 6.36. Response of Pressure Gage P5 in Tests A3 and A7

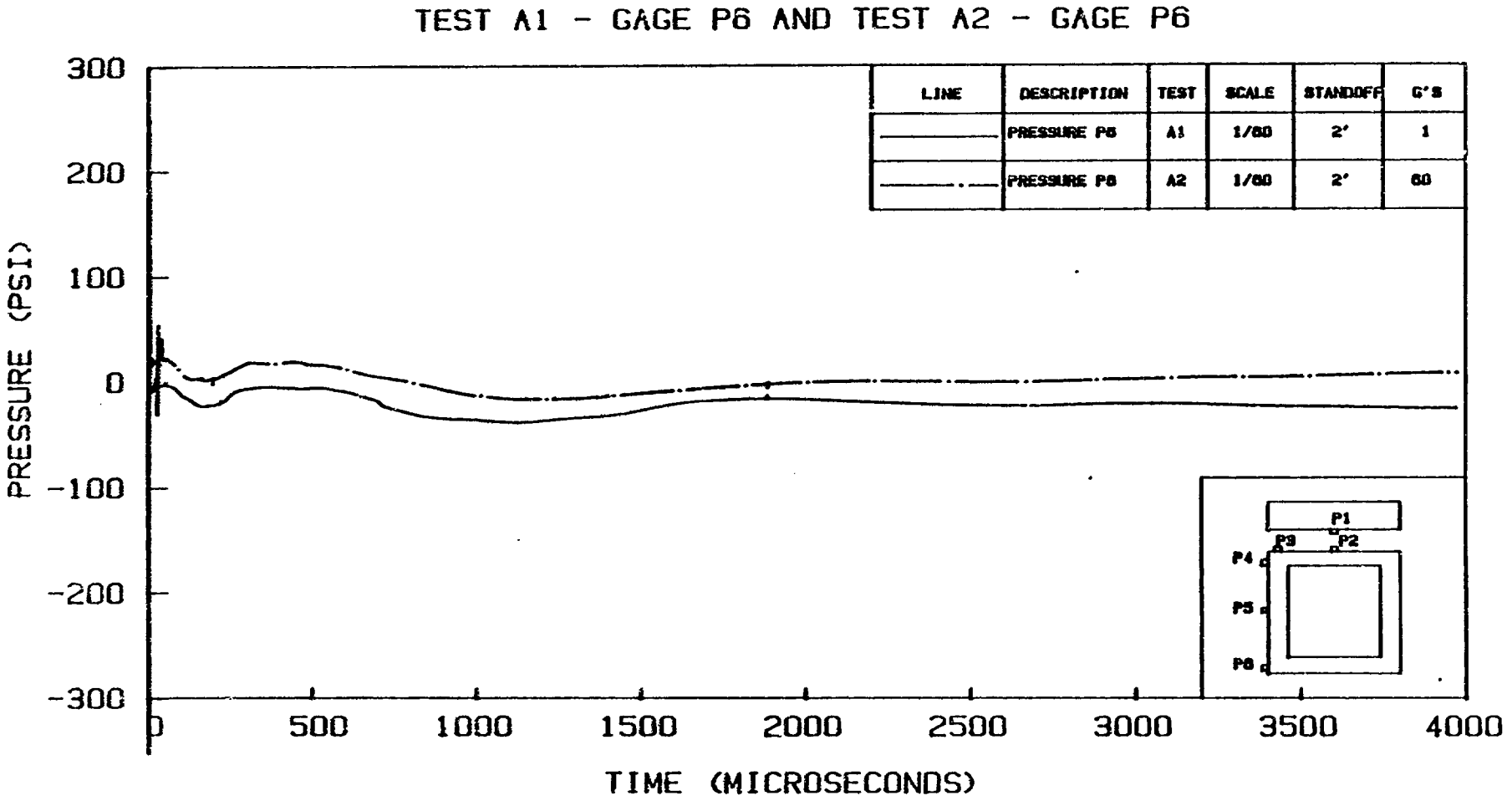

Figure 6.37. Response of Pressure Gage P6 in Tests A1 and A2

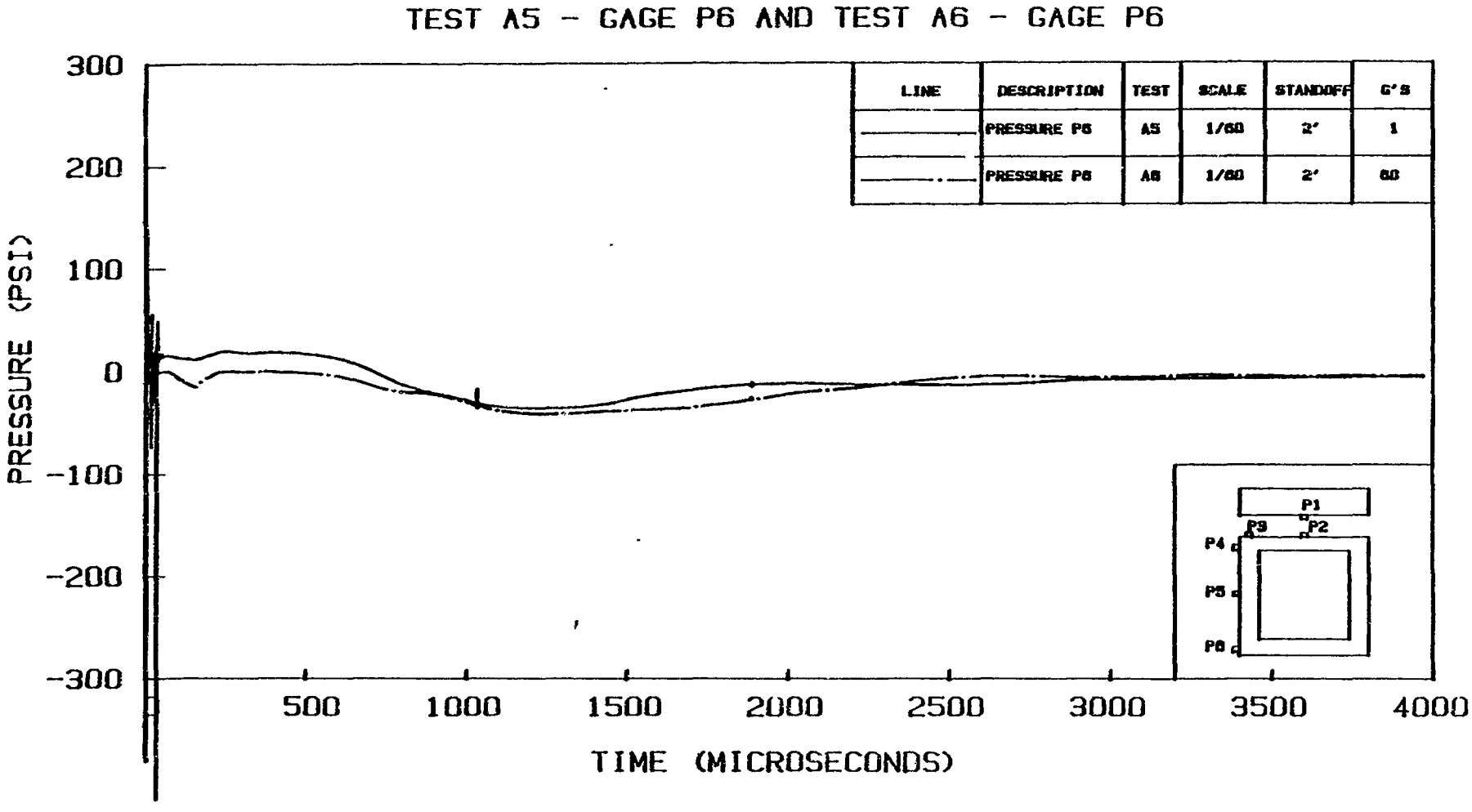

Figure 6.38. Response of Pressure Gage P6 in Tests A5 and A6

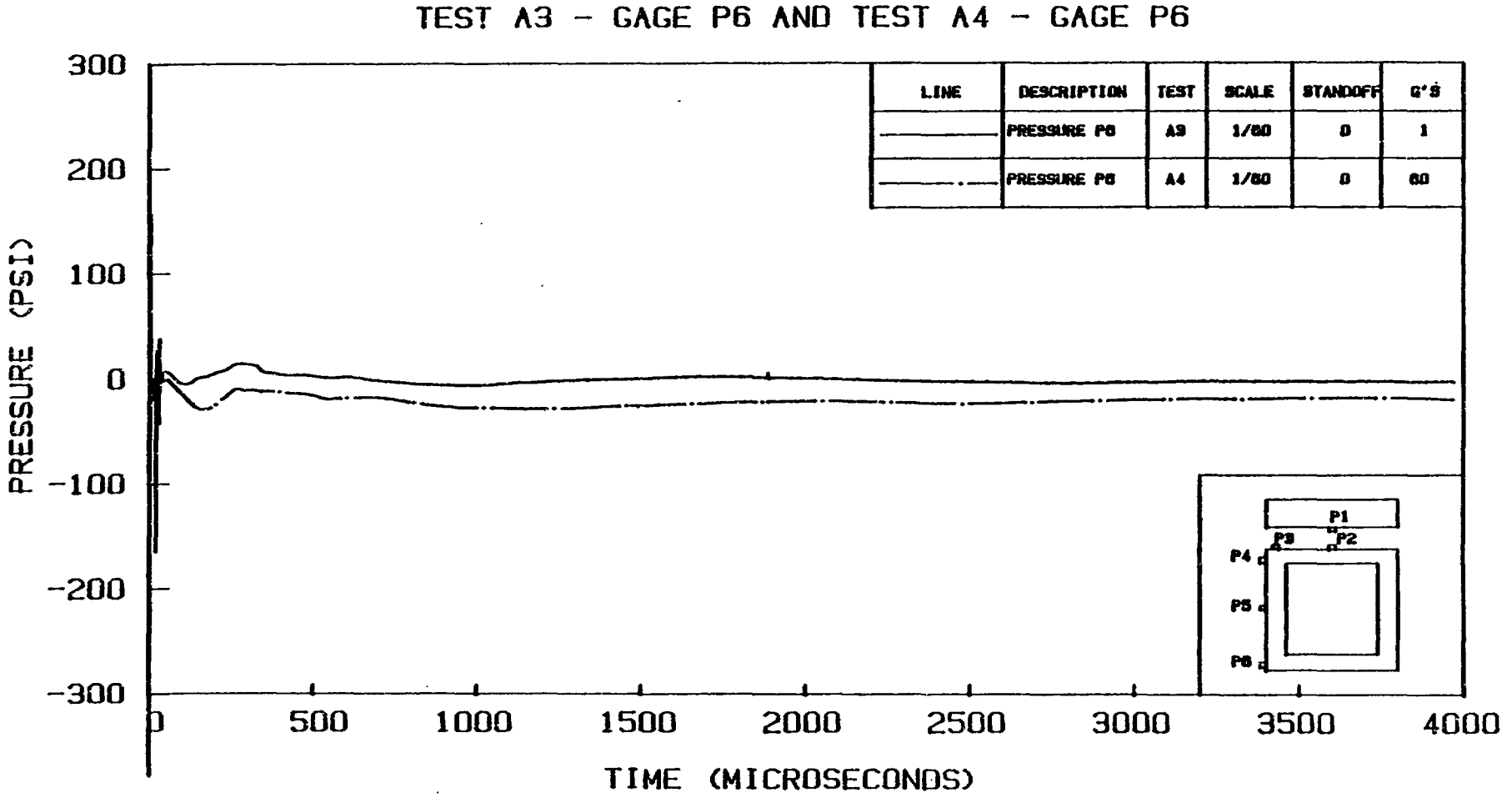

Figure 6.39. Response of Pressure Gage P6 in Tests A3 and A4

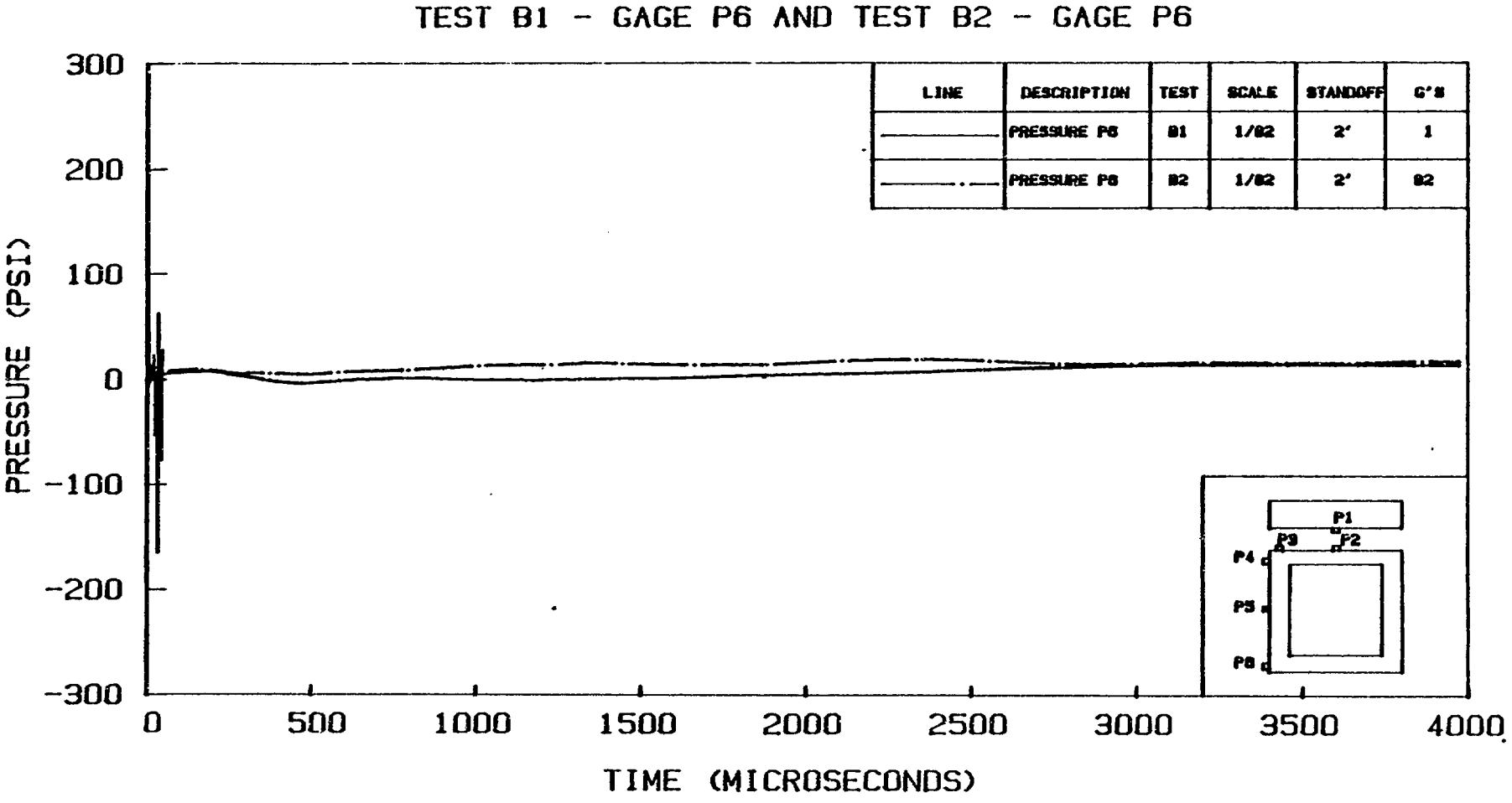

Figure 6.40. Response of Pressure Gage P6 in Tests B1 and B2

are compared to evaluate the significance of gravity effects in the response of an underground structural model subjected to blast loading.

As explained in Chapter 4, the outputs of piezoelectric accelerometers generally drift with time. Prior to conducting each test, the output of each accelerometer was adjusted to zero on the oscilloscope, and the oscilloscopes were then set to trigger when the explosion occurred. During the time period between the adjustment and explosion, the accelerometer output may have a slight drift. Therefore, digital zero on the oscilloscope may not indicate zero acceleration and the absolute acceleration values should be calculated by including the amount of drift in the calculation. The values of accelerations given here in the text and tables are adjusted for the amount of drift. Also, in a way similar to other transducers, explosions have spurious effects on the accelerometer response in the time span of a few microseconds. This effect can be seen in all accelerometer responses presented here.

Positive acceleration is directed away from the base. Therefore, for accelerometer A1, positive acceleration is directed downward and for accelerometer A2, positive acceleration is directed to the right.

6.2.1 Accelerometer A1

Accelerometer A1 is located in the bottom and at the middle of the top slab of the box structure (Figure 4.23). Figure 6.41 shows accelerometer response A1 in test A1 (2' standoff, 1g). The main accelerometer response occurs at 250 μseconds which is slightly later than the time shock wave hits the top slab (see Pressure Gage P2). The first peak has a magnitude of 447 g's and occurs at 285 μseconds (see Table 6.3). Figure 6.42 shows accelerometer response (A1) in test A2 (2' standoff, 60 g's). Comparing Figures 6.41 and 6.42 shows that the peaks in test A2 are larger and the arrival times of the peaks are faster. Table 6.3 shows that the first peak in test A2 (519 g's) is larger than the first peak in test A1 (447 g's) by 16%. The difference in the second peak (negative) is as much as 300%. The arrival time for the first peak in test A1 (285 μseconds) is larger than the corresponding arrival time in test A2 (225 μseconds) by 27%. The difference in the arrival times of the second peak for these two tests is 18%.

Figures 6.43 and 6.44 show accelerometer (A1) responses in tests A5 and A6. These two tests are similar to tests A1 and A2, respectively, except for the density variations explained earlier. Table 6.3 shows that the magnitude and arrival times of the first peak in test A1 and A5 are very close (447 and 453 g's, 285 and 280 μseconds). The second

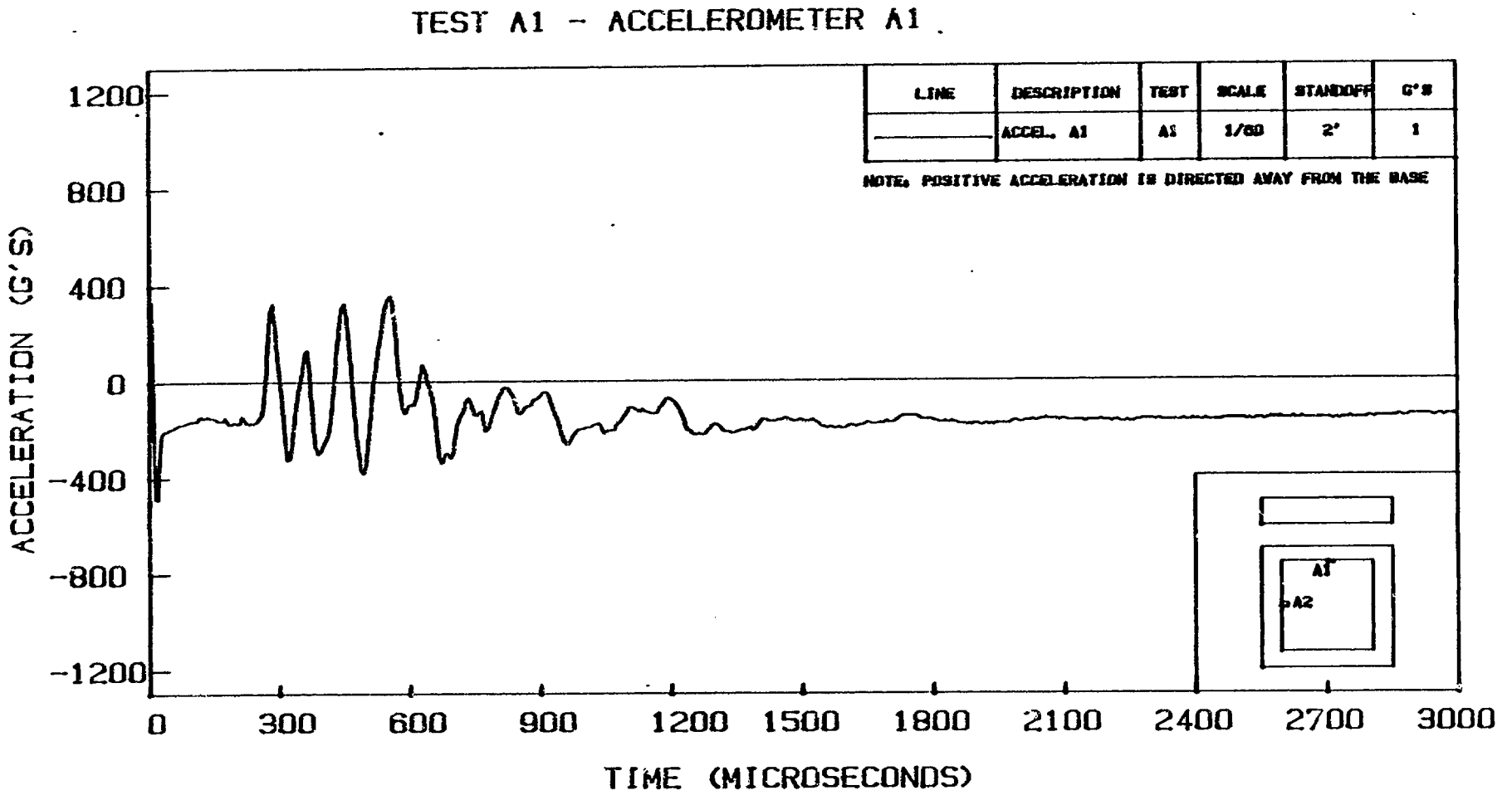

Figure 6.41. Accelerometer Response A1 in Test A1

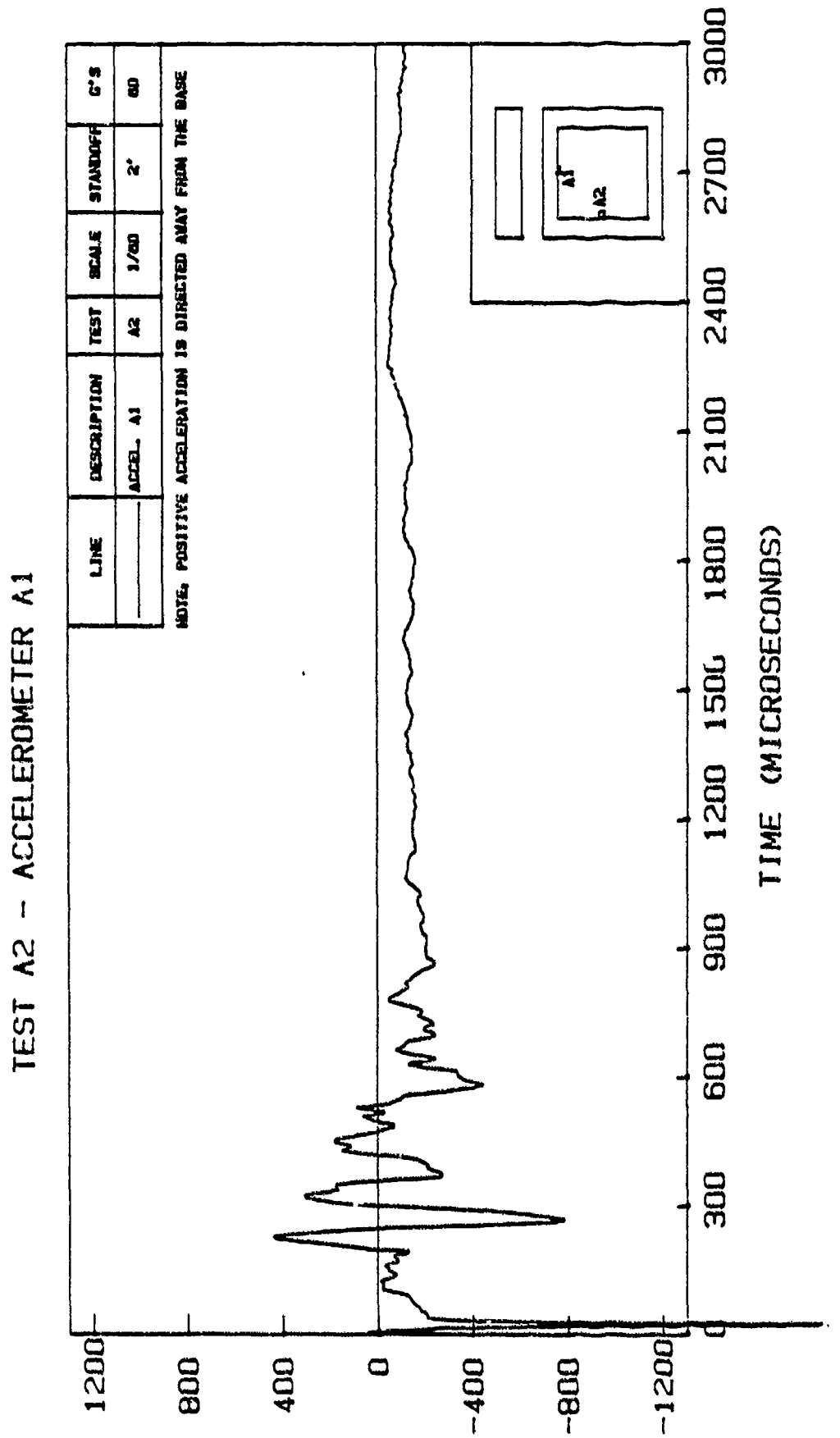

Figure 6.42. Accelerometer Response A1 in Test A2

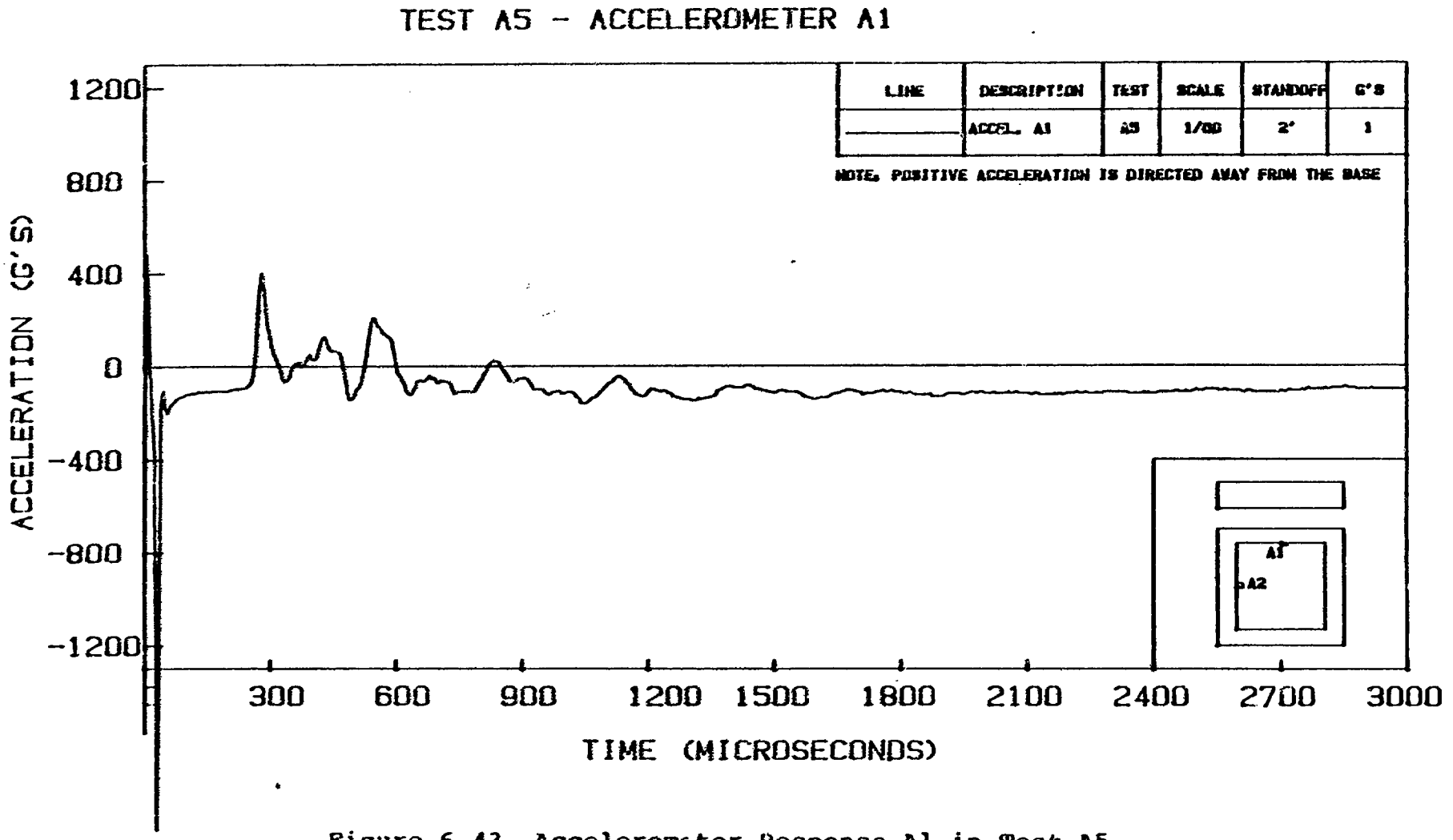

Figure 6.43. Accelerometer Response A1 in Test A5

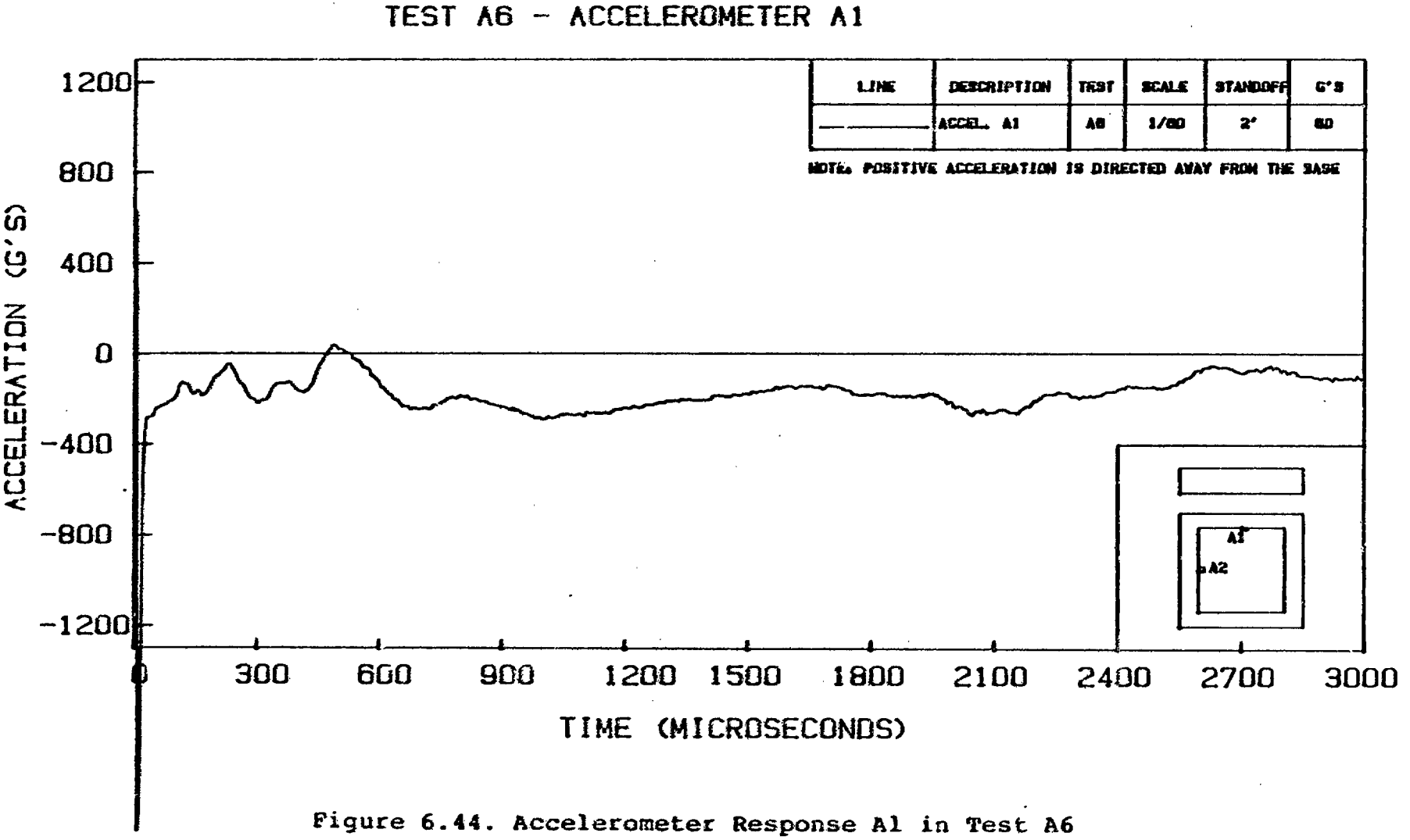

Figure 6.44. Accelerometer Response A1 in Test A6

Table 6.3

Summary of Accelerometer A1 Responses*

Standoff	0' Standoff						2' Standoff						
Gravity	1g		60 g's		82 g's		1g			60 g's		82 g's	
Model Scale	1/60	1/82	1/60		1/82		1/60		1/82	1/60		1/82	
Test Number	A3	None	A4	A7	B3	B5	A1	A5	B1	A2	A6	B2	B4
First Response (Microseconds)	115	----	90	95	82	82	250	240	185	195	170	96	89
Maximum Accel. 1st Peak (g's)	1605	----	1038	1163	2790	3938	447	453	786	519	131	677	886
Arrival Time (Microseconds)	140	----	144	170	123	109	285	280	226	225	230	198	157
Maximum Accel. 2nd Peak (g's)	-1247	----	-501	-728	-847	-2196	-149	24	-437	-603	-30	-362	-100
Arrival time (Microseconds)	190	----	190	210	157	150	320	335	280	270	300	267	198

* For 1/82-scale tests, the actual arrival time is multiplied by 82/60 to obtain an arrival time equivalent to 1/60-scale tests. Also, acceleration values are multiplied by 60/82 in 'B' tests.

peaks vary substantially in magnitude but are very close with respect to arrival times.

Tests A2 and A6 show agreement with respect to arrival times of the first and second peaks. However, the magnitudes of those peaks are substantially smaller in test A6. This may have been due to a possible problem with the connection of the accelerometer to the surface of the microconcrete.

The values presented in Tables 6.3 and 6.4 and discussed here for magnitudes and arrival times of peak accelerations in tests on 1/82-scale models are multiplied by 60/82 and 82/60 respectively to adjust for scaling size differences in 1/60- and 1/82-scale models and thereby have a common basis for comparisons.

Figures 6.45 and 6.46 show accelerometer (A1) responses in tests B1 and B2 (1/82-scale model). Both the magnitude and the arrival time of the first peak in test B1 (786 g's, 226 μseconds) are larger than the corresponding values in test B2 (677 g's, 198 μseconds) by about 15% (see Table 6.2). The second peak in test B1 (-437 g's) is also larger than the second peak in test B2 (-362 g's) by 21% while the arrival time for the second peak in test B1 (280 μseconds) is larger than the corresponding arrival time in test B2 (267 μseconds) by 5%.

Figure 6.47 shows the Accelerometer (A1) response in test B4 (2' standoff, 82 g's). This test is similar to test B2. However, the first peak response in test B4 (886 g's)

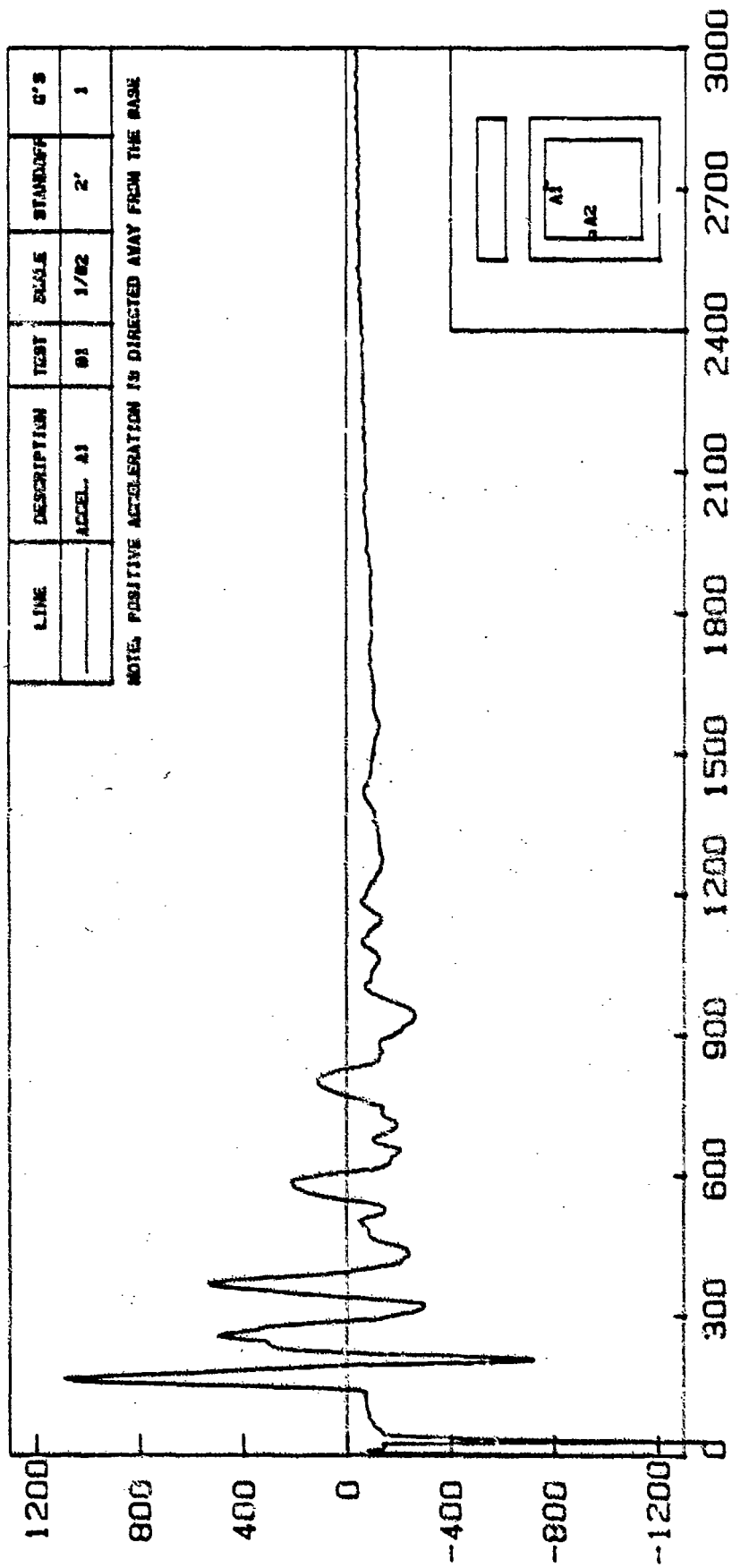

Figure 6.45. Accelerometer Response A1 in Test B1

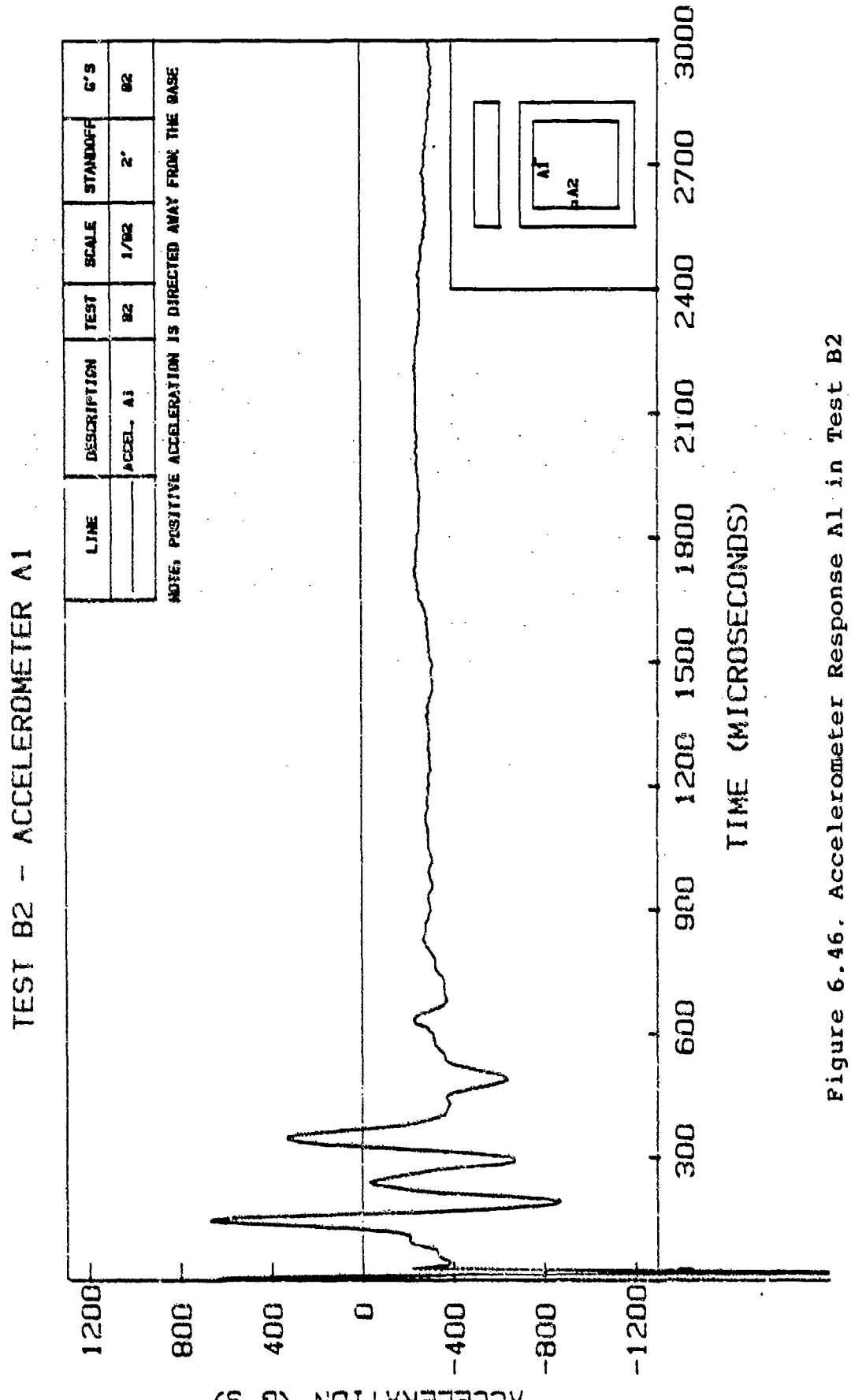

Figure 6.46. Accelerometer Response A1 in Test B2

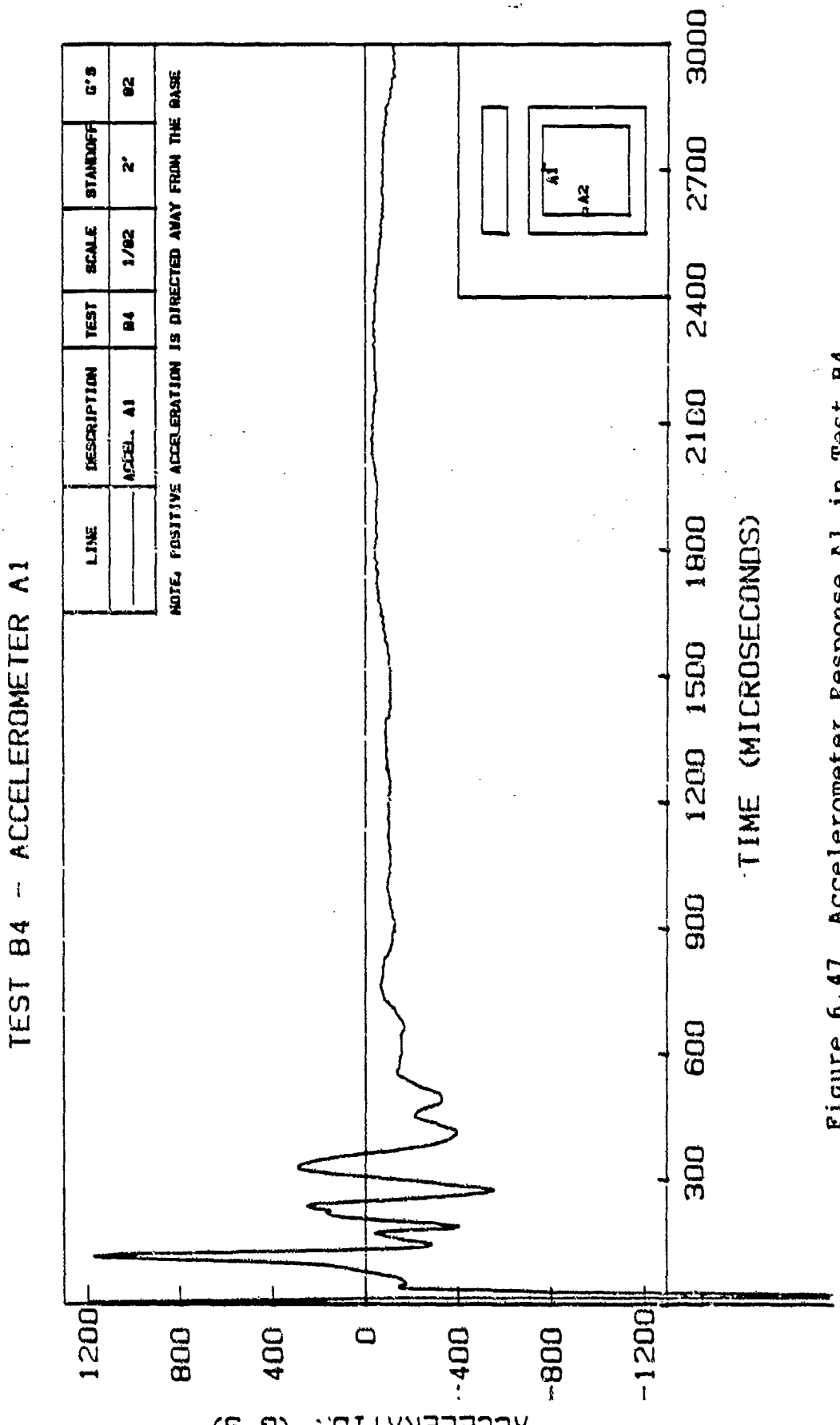

Figure 6.47. Accelerometer Response A1 in Test B4

is higher than the first peak response in test B2 (677 g's) by 31% while the second peak in test B4 (-100 g's) is smaller than the second peak in B2 (-362 g's) by 72%. The arrival time of the first peak in B2 (198 μseconds) is larger than the corresponding arrival time in test B4 (157 μseconds) by 26%.

In summary, acceleration responses in tests at 2' standoff on 1/60-scale models show larger peaks and faster arrival times at 60 g's as compared to tests at 1g. The average first peak acceleration in tests on 1/82-scale models (B2 and B4) is very close to the peak in test B1 while the average second peak is smaller in tests B2 and B4 as compared to test B1. However, the arrival times in 82-g tests are faster compared to 1g tests on 1/82-scale models. Comparable tests on different scale models (1/60 and 1/82) show larger first peaks and faster arrival times for 1/82-scale models. This may be attributed to an improper scaling of the explosive, not in terms of total mass which was properly accounted for, but rather in terms of mass distribution and charge geometry. Also, dimensional tolerances with regard to the placement of structural model in the centrifuge bucket may be harder to maintain in 1/82-scale models.

Figures 6.48 and 6.49 show accelerometer (A1) responses in tests A3 (0' standoff, 1g) and A4 (0' standoff, 60 g's). The adjusted first acceleration peak (see Table 6.3) in test A3 (1605 g's) is larger than the first acceleration

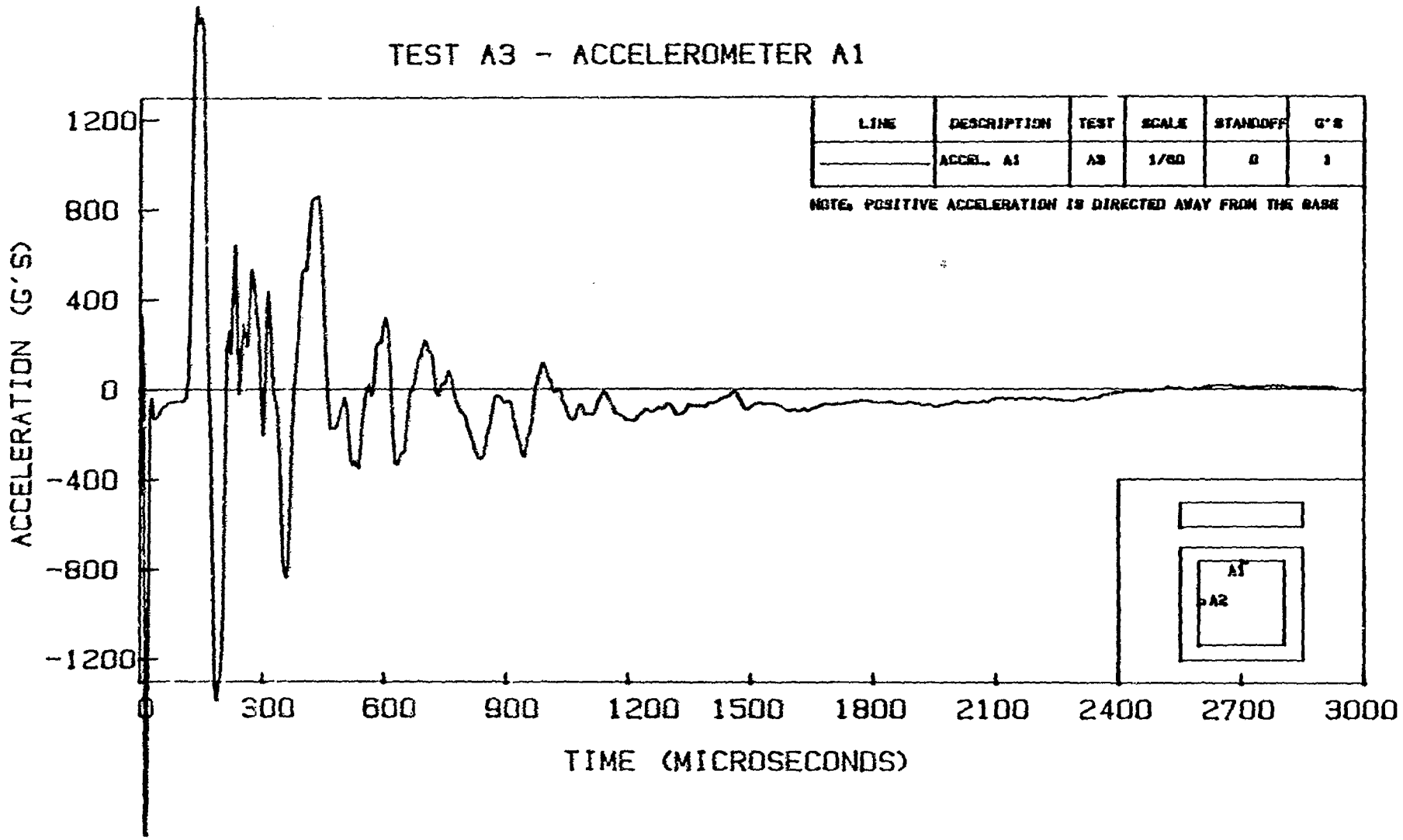

Figure 6.48. Accelerometer Response A1 in Test A3

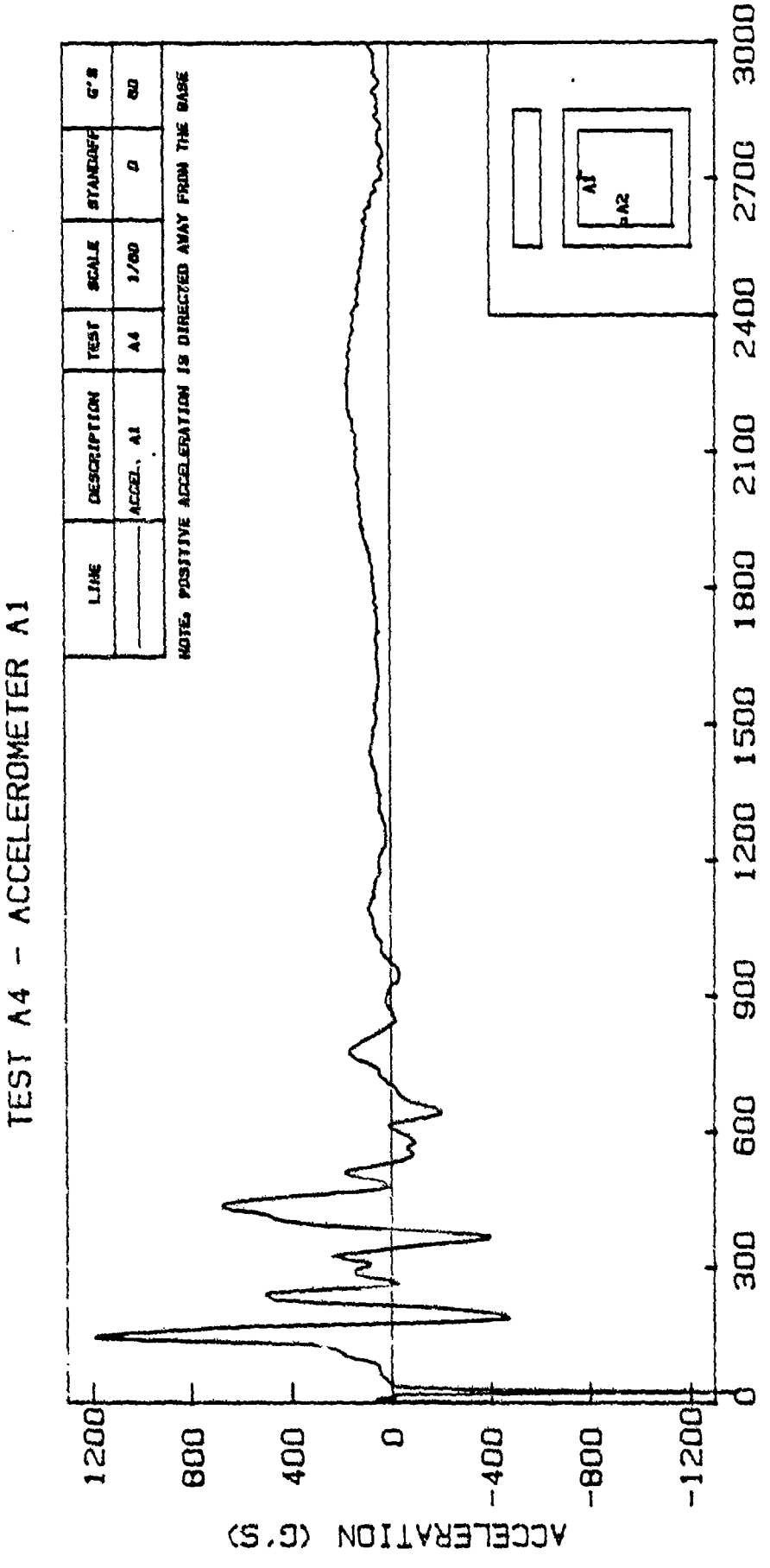

Figure 6.49. Accelerometer Response A1 in Test A4

peak in test A4 (1038 g's) by 55%. The second peak in test A3 (-1247 g's) is also higher than the second peak in test A4 (-501 g's) by 149%. The arrival times for the first and second peaks however, are very close (140 and 144 μseconds and 190 and 190 μseconds). The higher peak accelerations in the 1g test (A3) is expected here because of an observed higher pressure P2 (see Figure 6.15).

Figure 6.50 shows accelerometer (A1) response in test A7 (0' standoff, 60 g's). This test is similar to test A4 except for the damaged and cracked burster slab used in test A4. Test A7 shows higher first peak accelerations than in test A4 (1163 g's compared to 1038 g's) by 12%. The second peak in test A7 (-728 g's) is also higher than the second peak in test A4 (-501 g's) by 45%. The arrival times for the first and second peaks in test A7 (170 and 210 μseconds) are higher than the corresponding arrival times in test A4 (144 and 190 μseconds) by 18% and 11% respectively.

Figures 6.51 and 6.52 show Accelerometer (A1) responses in tests B3 (0' standoff, 82 g's) and B5 (0' standoff, 82 g's). These two tests are conducted under similar conditions. Test B5 shows a higher adjusted first peak (3938 g's) as compared to test B3 (2790 g's) by 41%. The second peak in test B5 (-2196 g's) is higher than the second peak in test B3 (-847 g's) by 159%. The arrival times for the first and second peaks in test B3 (123 and 157 μseconds) are larger than the corresponding arrival

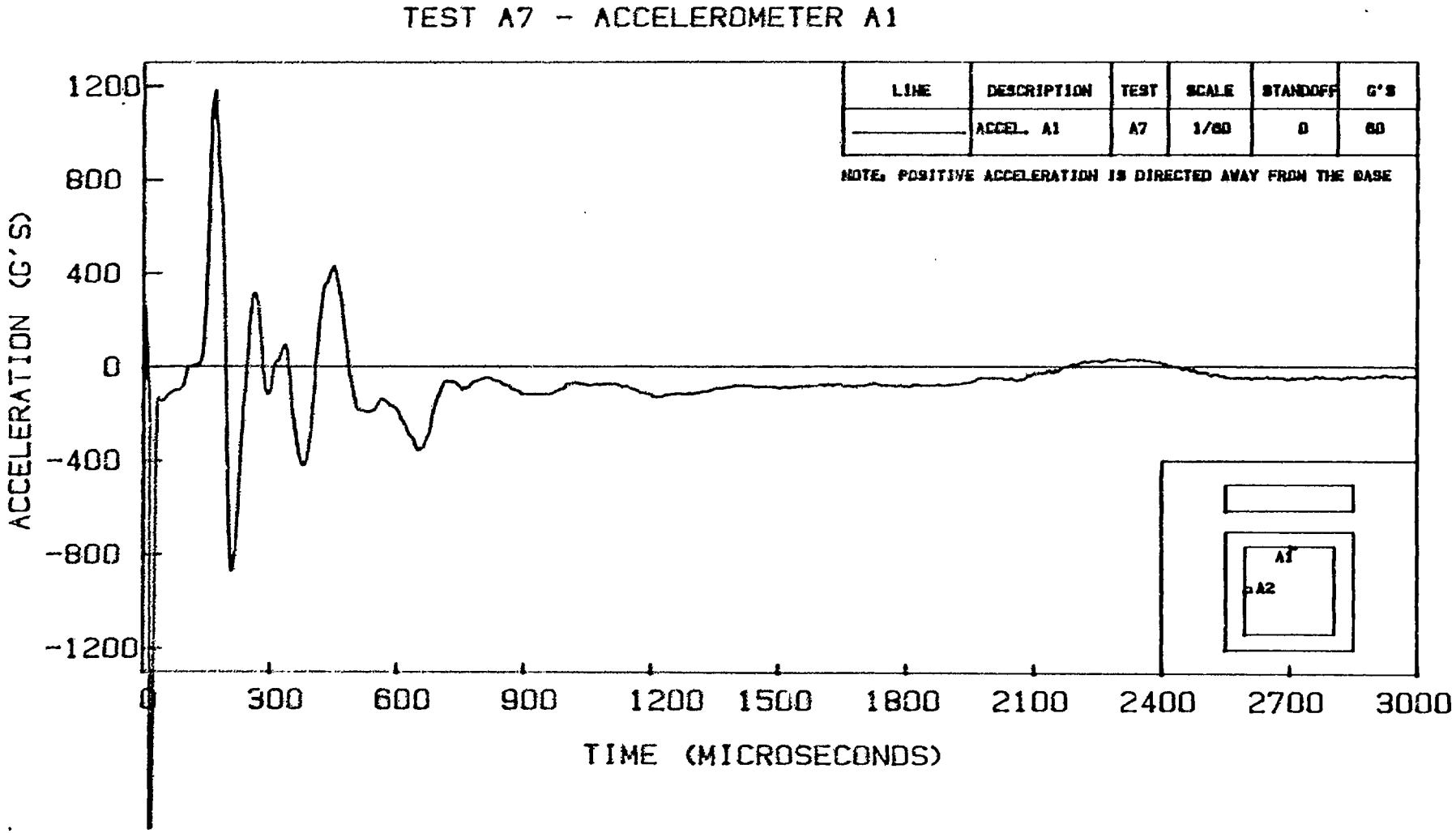

Figure 6.50. Accelerometer Response A1 in Test A7

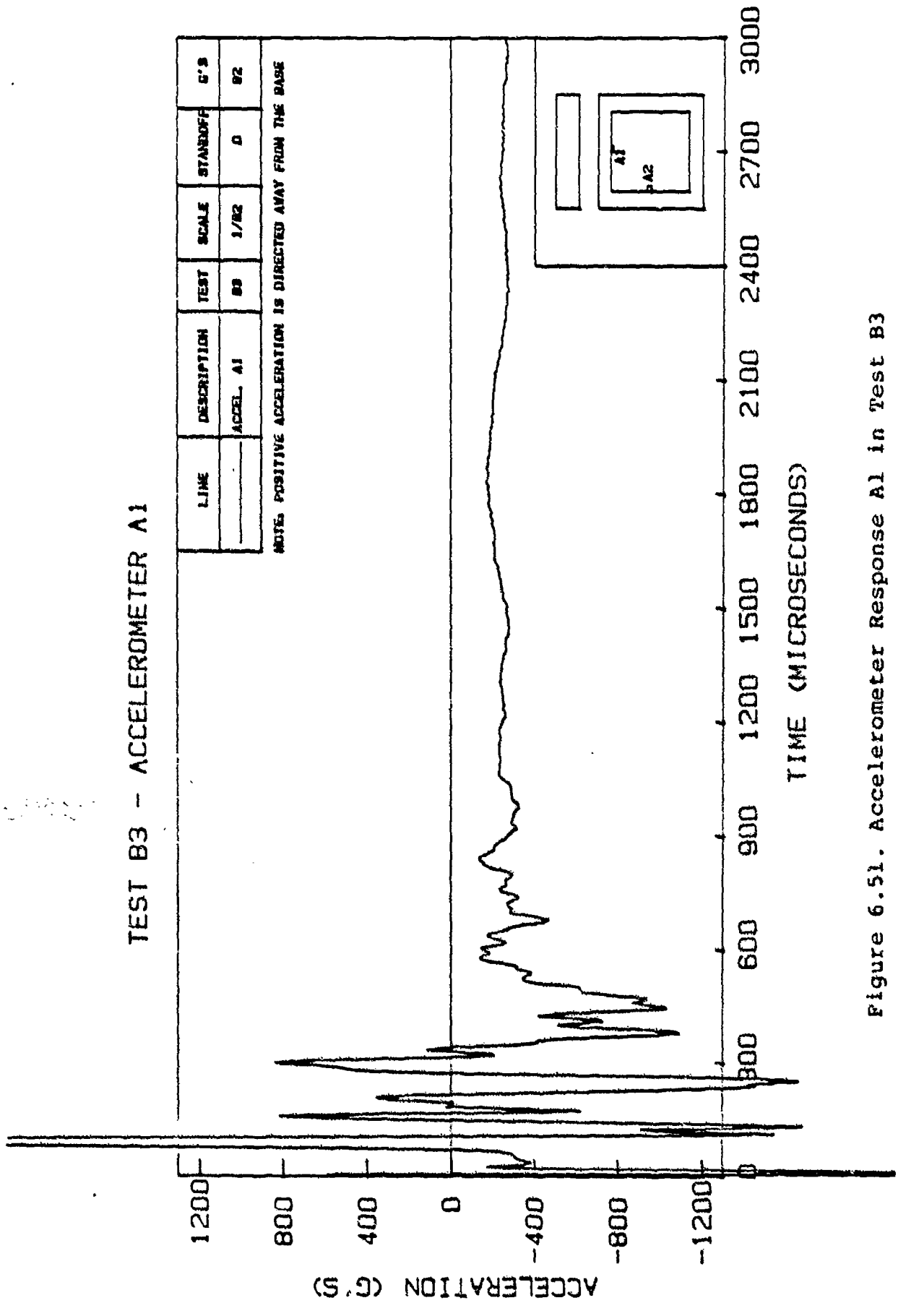

Figure 6.51. Accelerometer Response A1 in Test B3

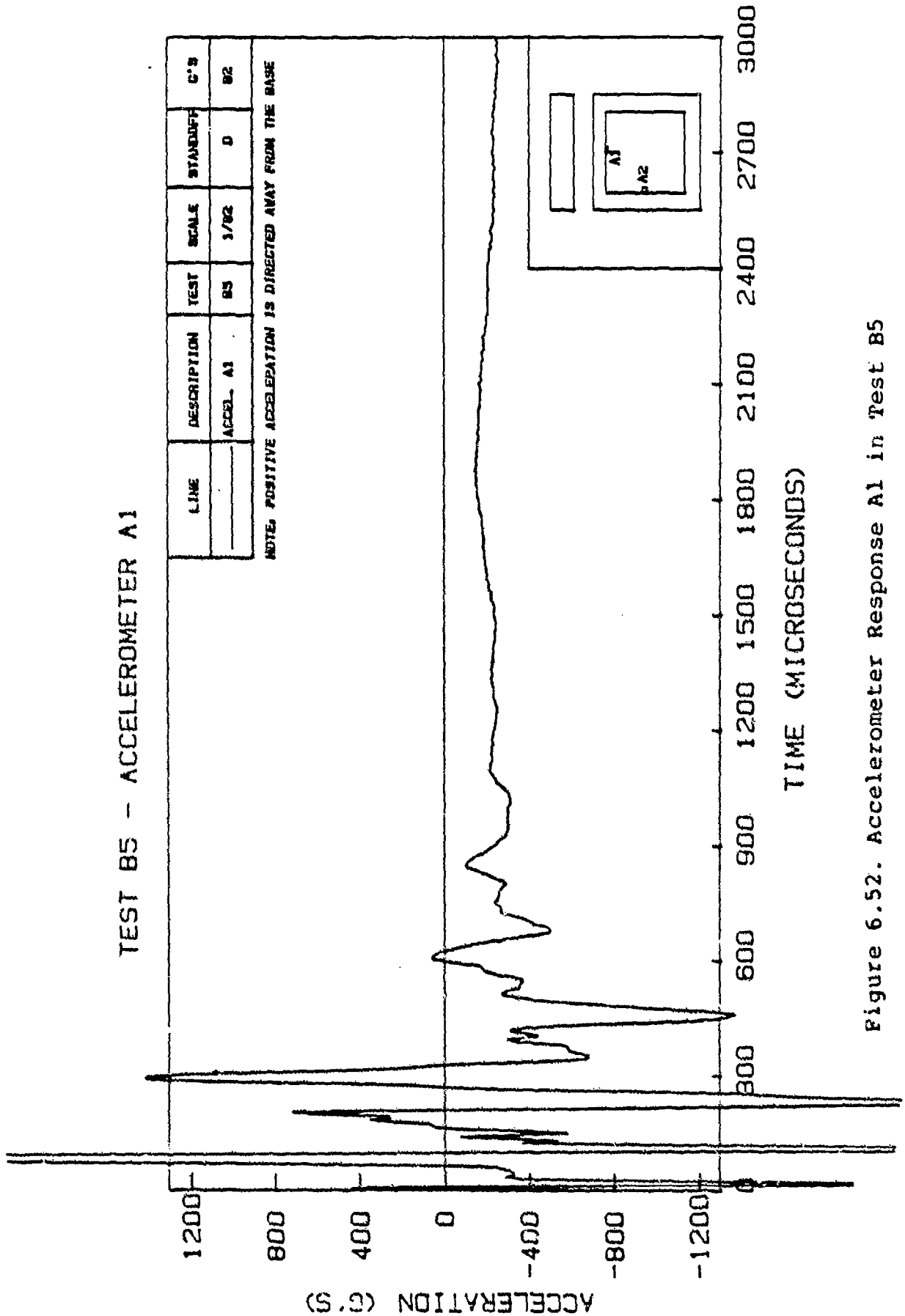

Figure 6.52. Accelerometer Response A1 in Test B5

times in test B5 (109 and 150 μseconds) by 13% and 5%, respectively.

In summary, acceleration responses in tests at zero standoff on 1/60-scale models at 60 g's result in smaller peak accelerations compared to the test at 1g. The arrival times for the peaks in tests at 60 g's are, on the average, higher than in 1g tests. High-g tests on 1/60- and 1/82-scale models show different responses. 82-g tests (B series) show larger adjusted peak accelerations and faster arrival times as compared to 60-g tests (Table 6.3). As explained earlier, this is believed to be due to an incorrect scaling in terms of the distribution of explosive mass and the geometry of the detonator.

6.2.2 Accelerometer A2

Accelerometer A2 is located on the inside and the middle of the side wall as shown in Figure 4.23. Figures 6.53 and 6.54 show Accelerometer (A2) responses in tests A1 (2' standoff, 1g) and A2 (2' standoff, 60 g's). The first response time of Accelerometer A2 in test A1 (290 μseconds) has a delay of 40 μseconds compared to the first response time of Accelerometer A1 in test A1 (250 μseconds). The negative first peak acceleration in these tests indicate an outward direction (on the side wall) for the first acceleration peak. The first peak in test A2 (-121 g's) is higher than the first peak in test A1 (-94 g's) by 29% (Table 6.4). The second peak in test A2 (231 g's) is

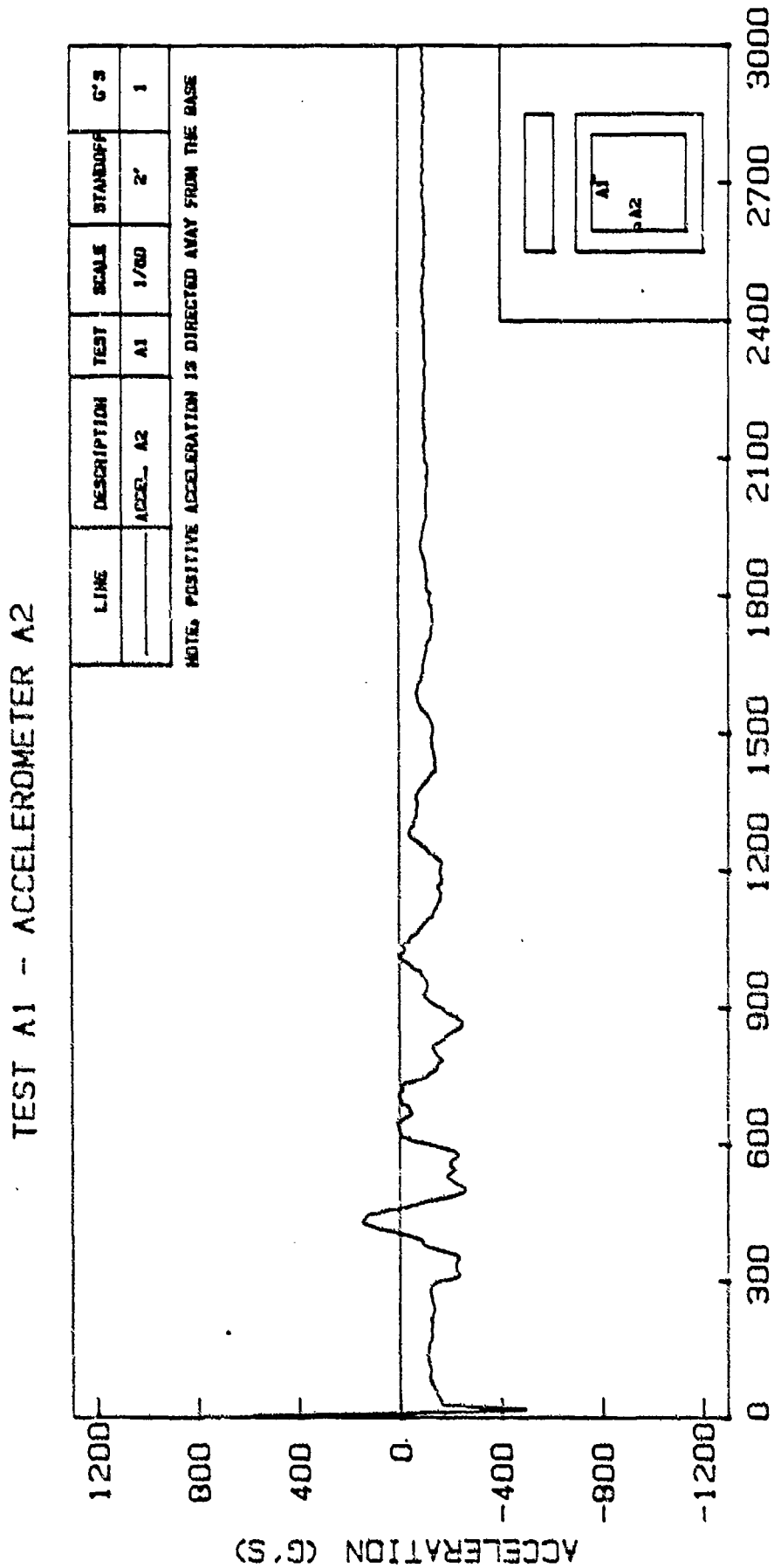

Figure 6.53. Accelerometer Response A2 in Test A1

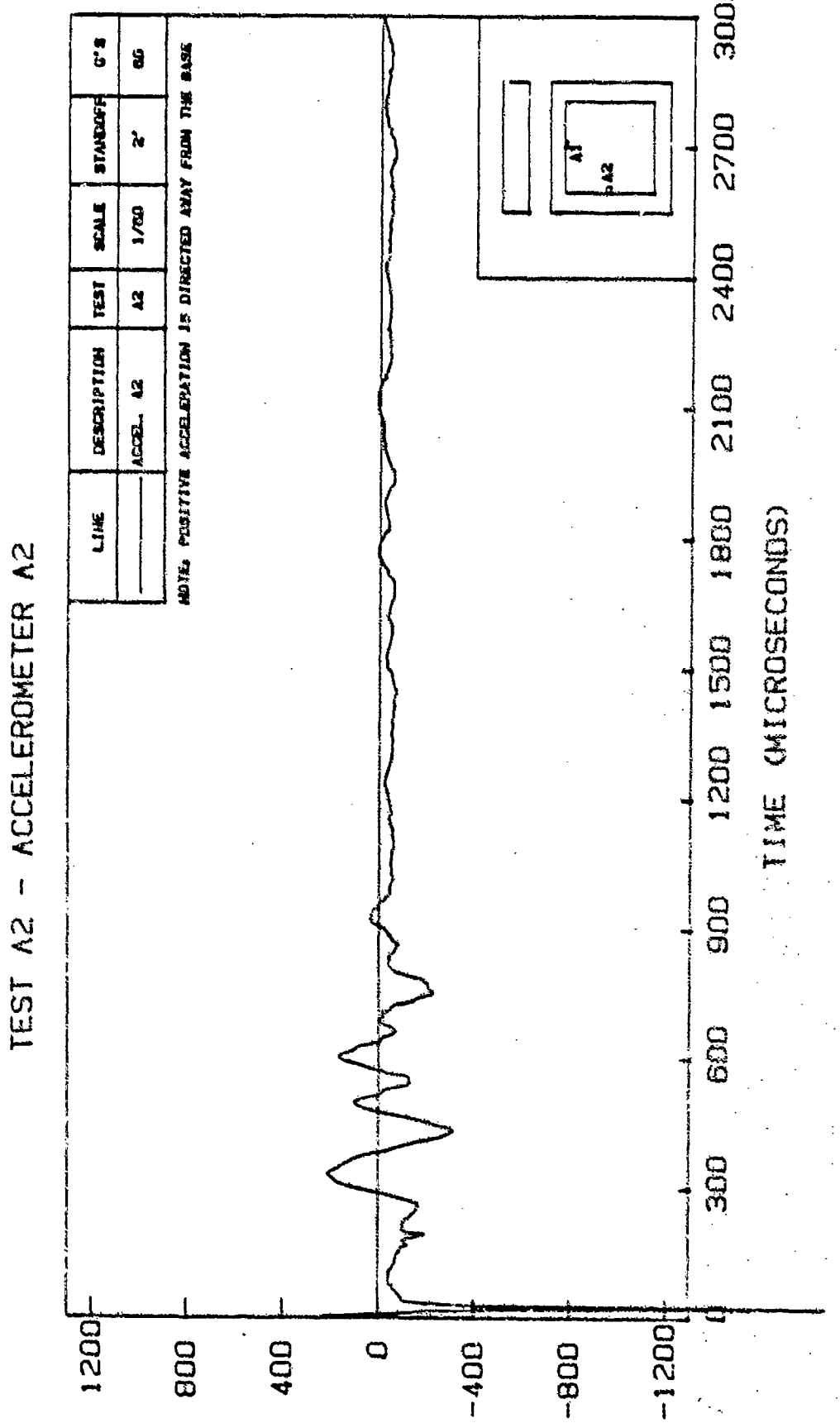

Figure 6.54. Accelerometer Response A2 in Test A2

Table 6.4

Summary of Accelerometer A2 Responses*

Standoff	0' Standoff						2' Standoff						
Gravity	1g		60 g's		82 g's		1g			60 g's		82 g's	
Model Scale	1/60	1/82	1/60		1/82		1/60		1/82	1/60		1/82	
Test Number	A3	None	A4	A7	B3	B5	A1	A5	B1	A2	A6	B2	B4
First Response (Microseconds)	150	----	145	165	123	116	290	285	212	254	240	171	144
Maximum Accel. 1st Peak (g's)	-424	----	-281	-369	-769	-845	-94	-138	-205	-121	-22	-173	-165
Arrival Time (Microseconds)	165	----	175	200	144	137	310	320	246	260	270	239	178
Maximum Accel. 2nd Peak (g's)	902	----	594	638	1332	1533	253	248	503	231	127	475	503
Arrival time (Microseconds)	285	----	290	315	253	246	430	420	355	335	355	335	301

* For 1/82-scale tests, the actual arrival time is multiplied by 82/60 to obtain an arrival time equivalent to 1/60-scale tests. Also, acceleration values are multiplied by 60/82 in 'B' tests.

smaller than the second peak in test A1 (248 g's) by 7%. The arrival times for the first and second peaks in test A1 (310 and 430 μseconds) are larger than the corresponding arrival times in test A2 (260 and 335 μseconds) by 19% and 28% respectively.

Figure 6.55 and 6.56 show Accelerometer (A2) responses in tests A5 (2' standoff, 1g) and A6 (2' standoff, 60 g's). Tests A5 and A6 are similar to tests A1 and A2 respectively except for the difference in soil density between tests A1 and A5 explained earlier. The first response time of Accelerometer A2 in test A5 (285 μseconds) is 45 μseconds larger than the first response time of Accelerometer A1 in test A5 (240 μseconds). Test A6 shows smaller peak accelerations as compared to test A5. A similar response was obtained from the Accelerometer A1 results. The first peak in test A5 (-138 g's) is higher than the first peak in test A1 (-94 g's) by 47%. However, the second peak in test A5 (248 g's) is slightly smaller than the second peak in test A1 (253 g's). The arrival times for the first and second peaks in test A5 (320 and 420 μseconds) and A1 (310 and 430 μseconds) are very close.

Although the magnitudes of the first and second peaks in tests A6 and A5 vary substantially, the arrival times for the peaks in these tests are relatively close (270 and 355 μseconds in A5 and 260 and 335 μseconds in A6).

Figures 6.57 and 6.58 show Accelerometer (A2) responses in tests B1 (2' standoff, 1g) and B2 (2' standoff, 82 g's)

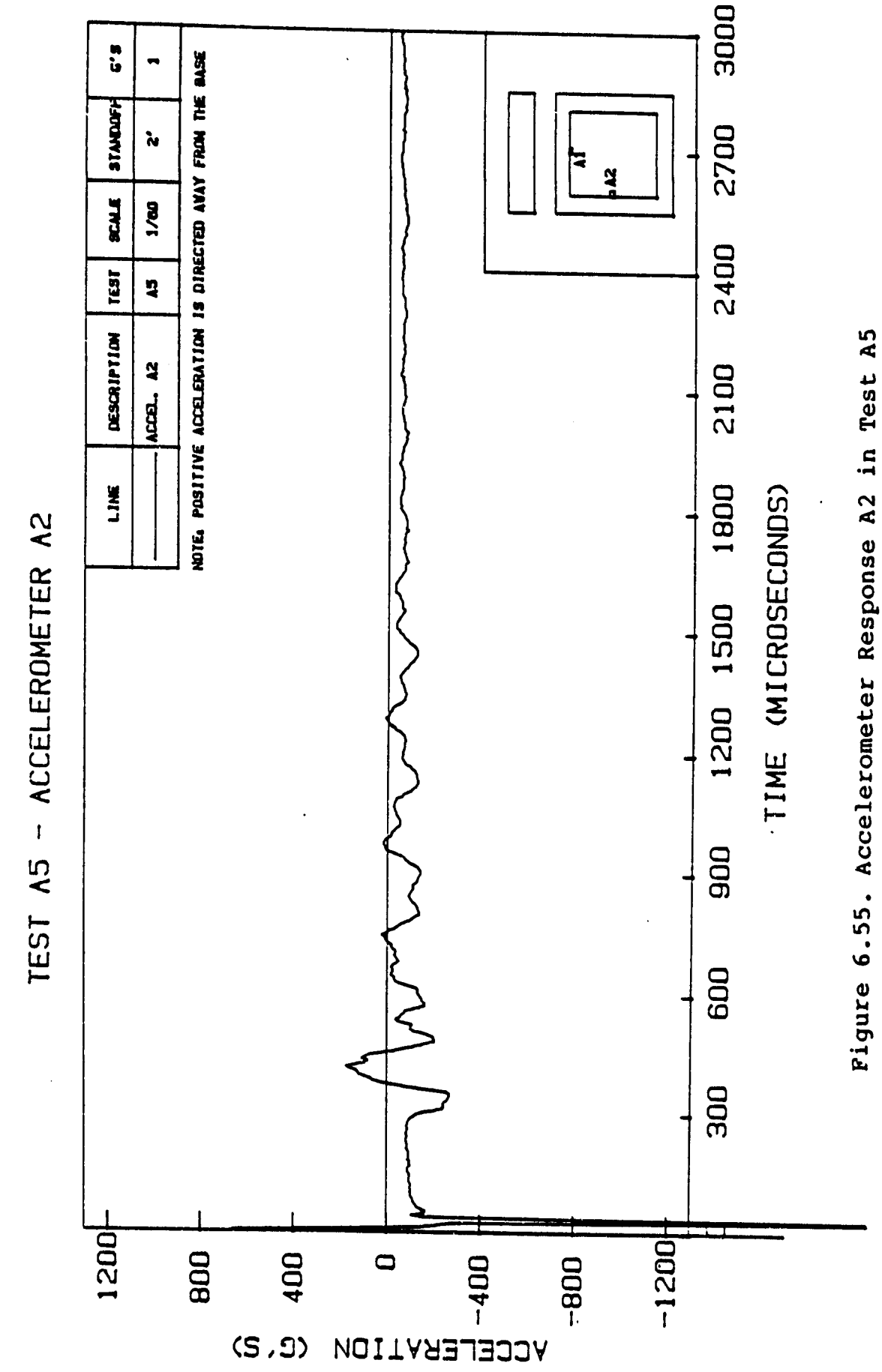

Figure 6.55. Accelerometer Response A2 in Test A5

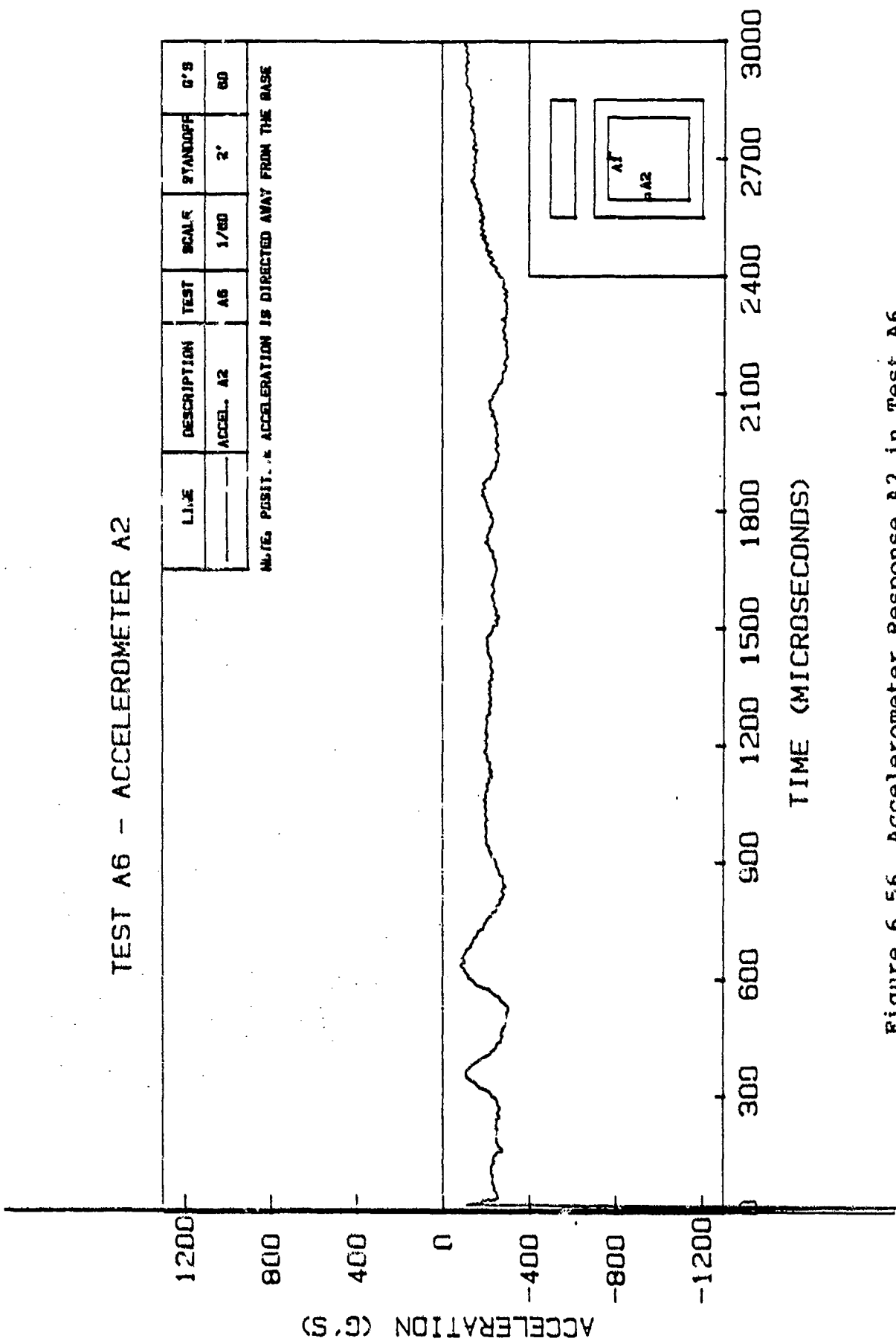

Figure 6.56. Accelerometer Response A2 in Test A6

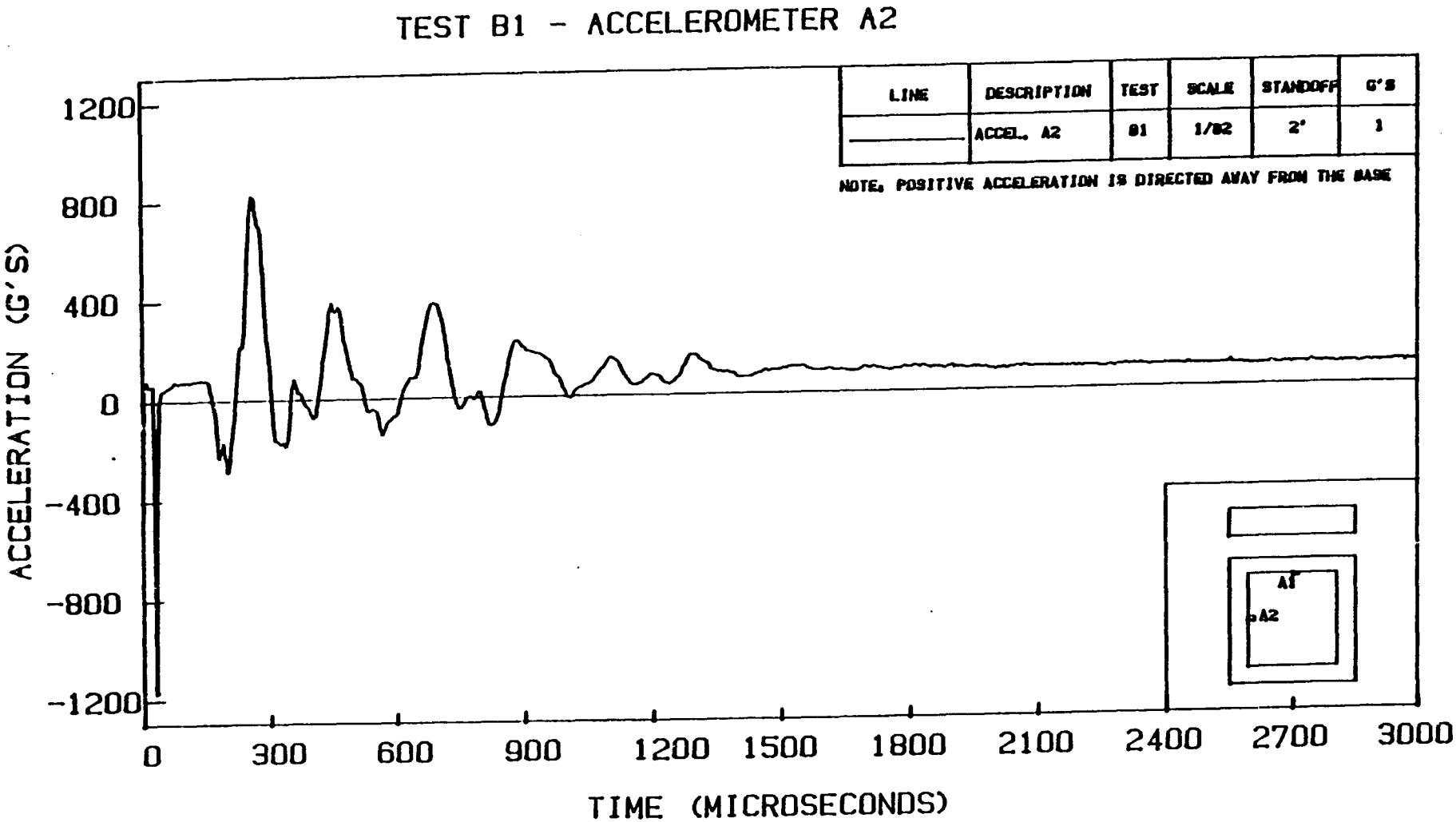

Figure 6.57. Accelerometer Response A2 in Test B1

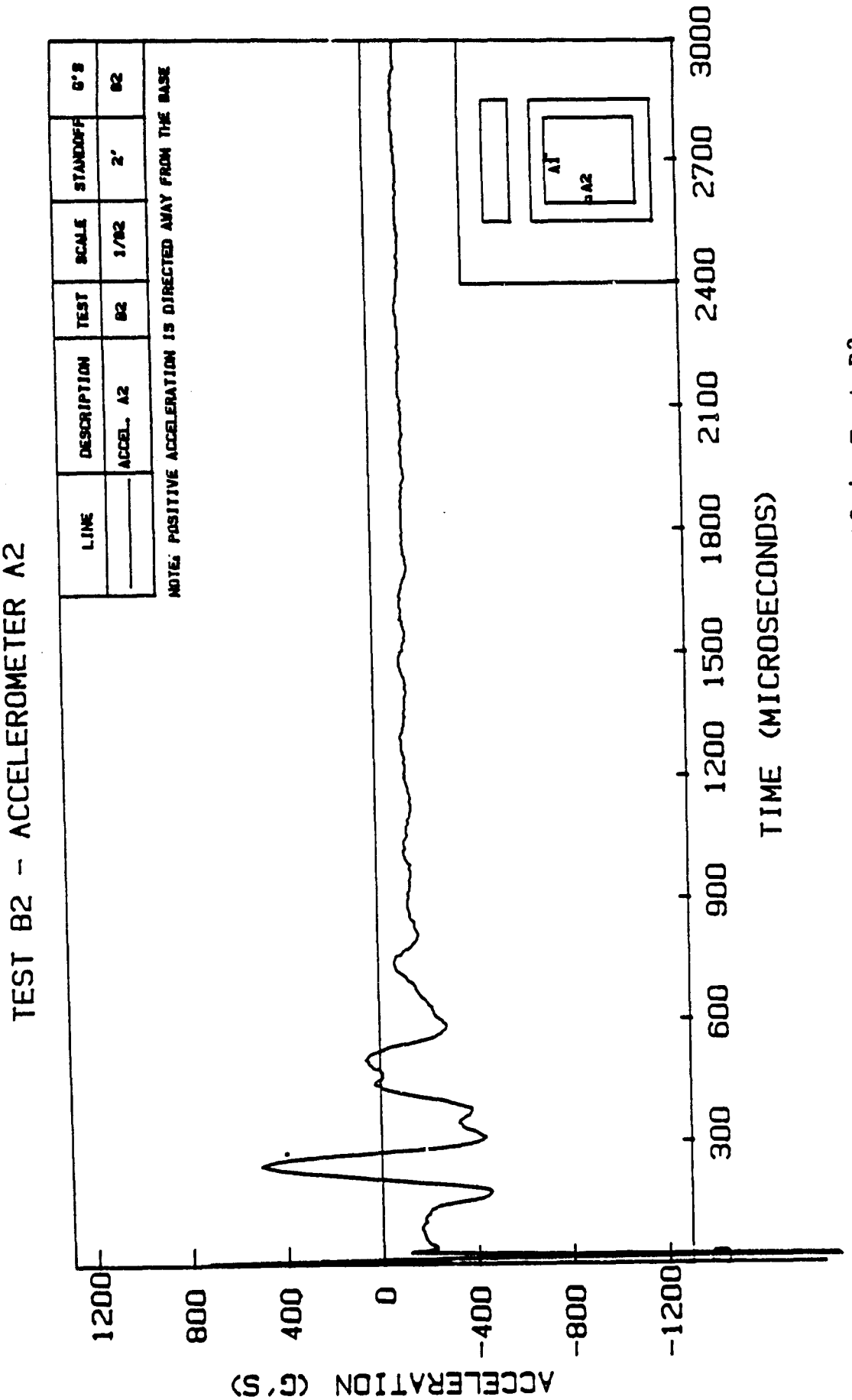

Figure 6.58. Accelerometer Response A2 in Test B2

on 1/82-scale models. The adjusted first and second peaks in test B2 (-173 g's and 475 g's) are smaller than the corresponding peak accelerations in test B1 (-205 and 503 g's) by 16% and 6% respectively. The adjusted arrival times for the first and second peaks in test B1 (246 and 355 μseconds) are larger than the corresponding arrival times in test B2 (239 and 335 μseconds) by 3% and 6% respectively. The time at first response for Accelerometer A2 in test B1 (212 μseconds) is 27 μseconds larger than the time at first response for Accelerometer A1 in the same test.

Figure 6.59 shows Accelerometer A2 response in test B4 (2' standoff, 82 g's). This test was conducted under conditions similar to test B2. The first and second acceleration peaks in test B4 (-165 and 503 g's) are relatively close to the first and second peaks in test B2 (-173 and 475 g's), respectively. The arrival time for the first peak in test B2 (239 μseconds) is higher than in test B4 (178 μseconds) by 34%. The arrival times for the second peak in these two tests are close (335 and 301 μseconds).

Figures 6.60 and 6.61 show Accelerometer (A2) responses in tests A3 (0' standoff, 1g) and A4 (0' standoff, 60 g's). Both peak accelerations in test A3 (-424 and 902 g's) are higher than the peak accelerations in test A4 (-281 and 594 g's) by about 51%. The arrival time for the peak accelerations in test A4 (175 and 290 μseconds) are

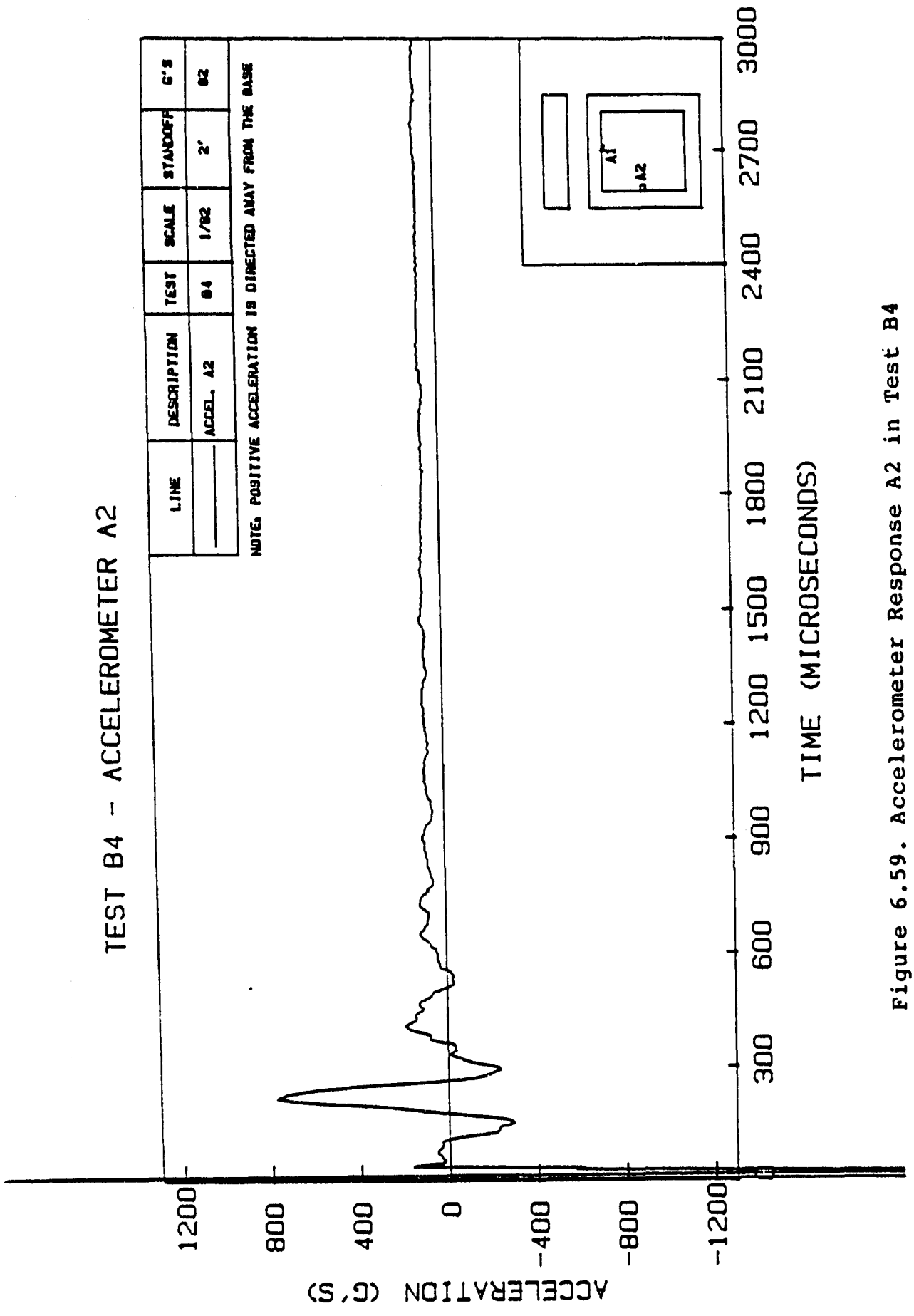

Figure 6.59. Accelerometer Response A2 in Test B4

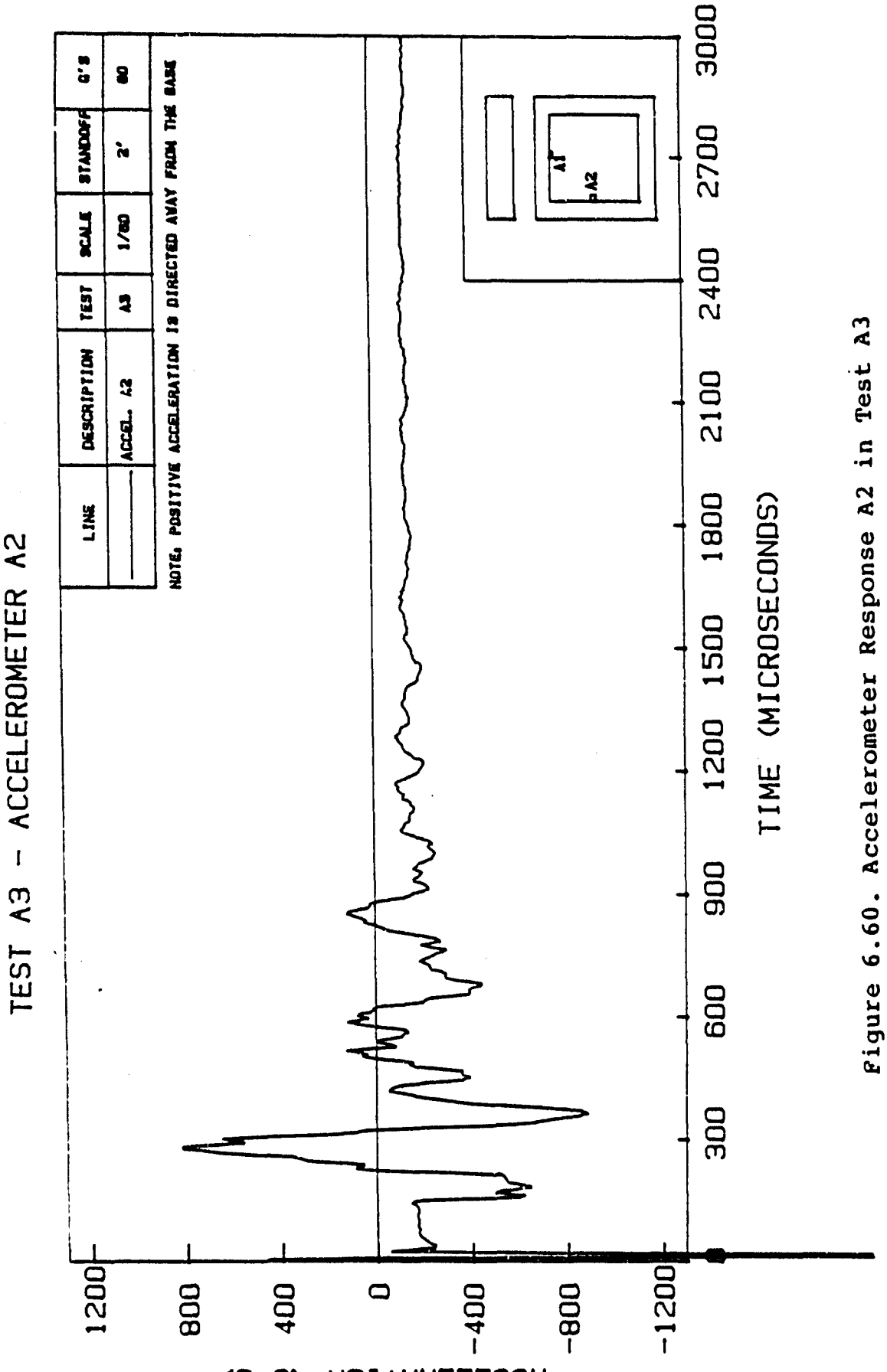

Figure 6.60. Accelerometer Response A2 in Test A3

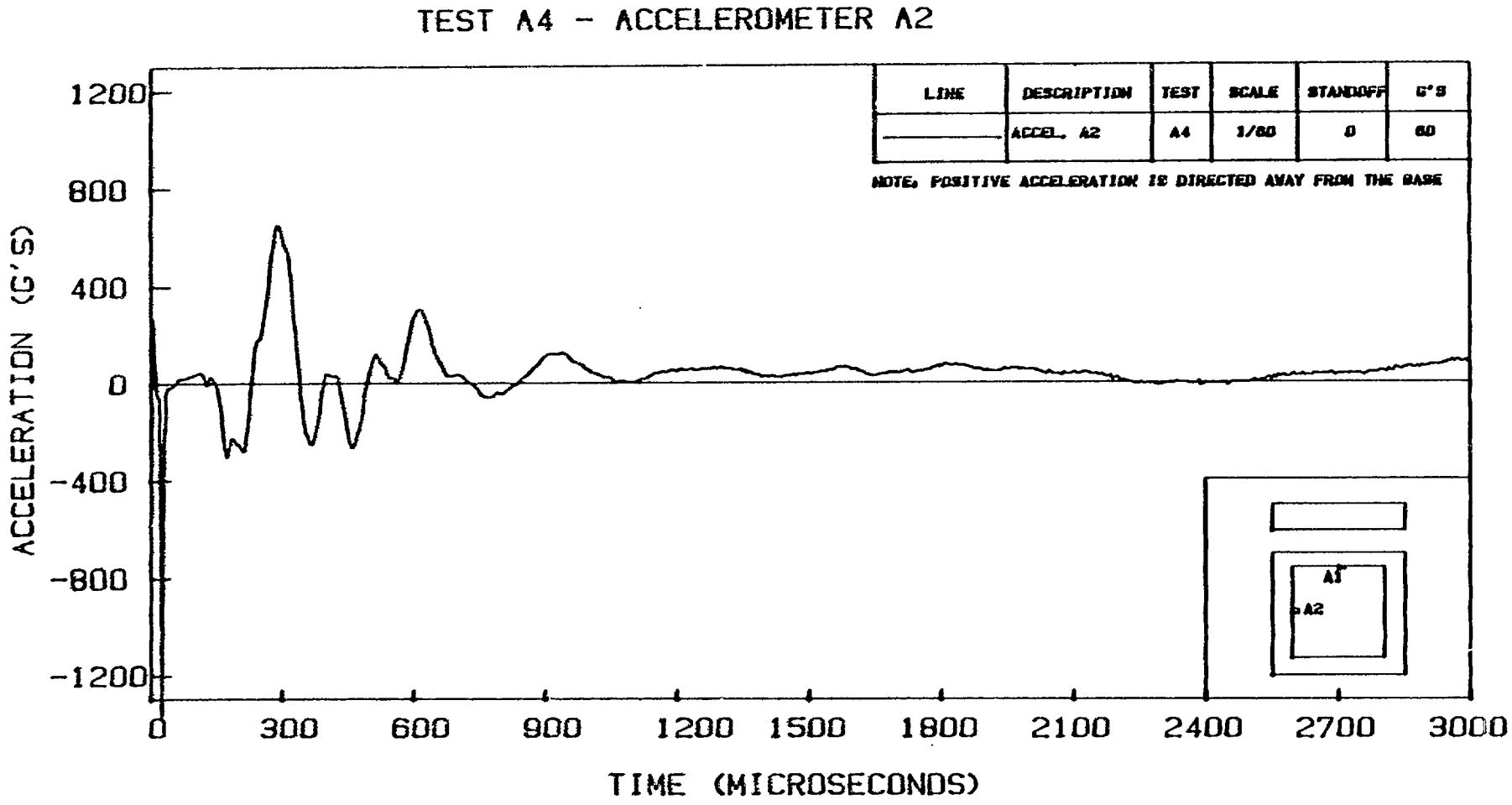

Figure 6.61. Accelerometer Response A2 in Test A4

slightly higher than the corresponding arrival times in test A3 (165 and 285 μseconds).

Figure 6.62 shows Accelerometer (A2) response in test A7. Test A7 was conducted under conditions similar to test A4 except that test A4 was performed using a cracked burster slab. The peak accelerations in test A7 (-369 and 638 g's) are higher than the peak accelerations in test A4 (-281 and 594 g's) by 31% and 7% respectively. The arrival times in test A7 (200 and 315 μseconds) are higher than the corresponding arrival times in test A4 (175 and 290 μseconds) by 14% and 9% respectively.

Figures 6.63 and 6.64 show Accelerometer (A2) responses in test B3 (0' standoff, 82 g's) and B5 (0' standoff, 82 g's). These two tests were performed under similar conditions. The peak accelerations and arrival times are close as shown in Table 6.4.

In summary, blast tests at 2' standoff show consistently faster arrival times for the first and second acceleration peaks (A2) in tests at high gravities as compared to tests at 1g. The only 1g test performed at zero standoff on a 1/60-scale model (A3) shows larger peaks and faster arrival times compared to similar tests at 60 g's. On the other hand, high-g tests on 1/82-scale models at 82 g's show larger adjusted peak accelerations and faster arrival times than tests on 1/60-scale models at both 1g and 60-g tests.

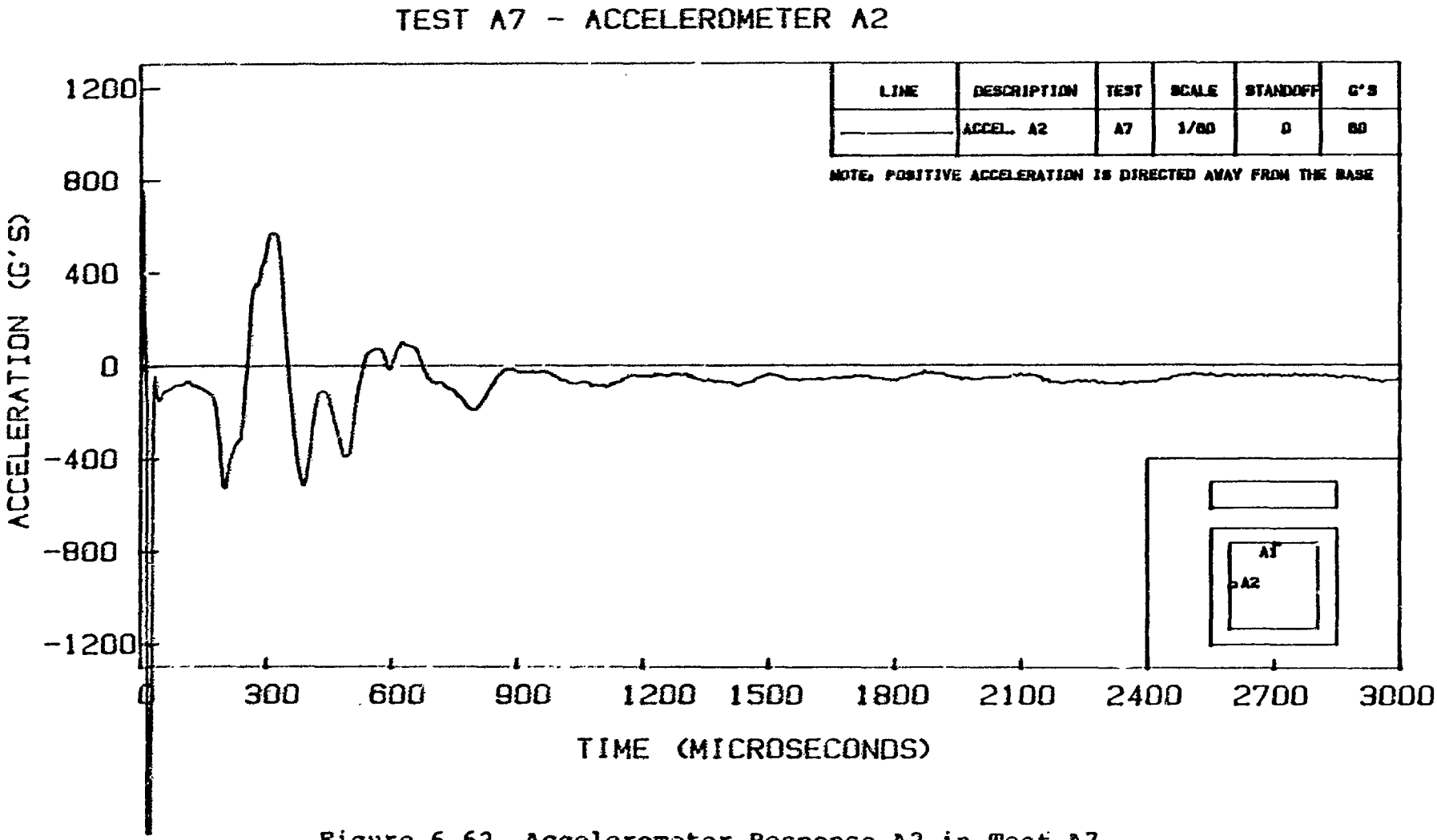

Figure 6.62. Accelerometer Response A2 in Test A7

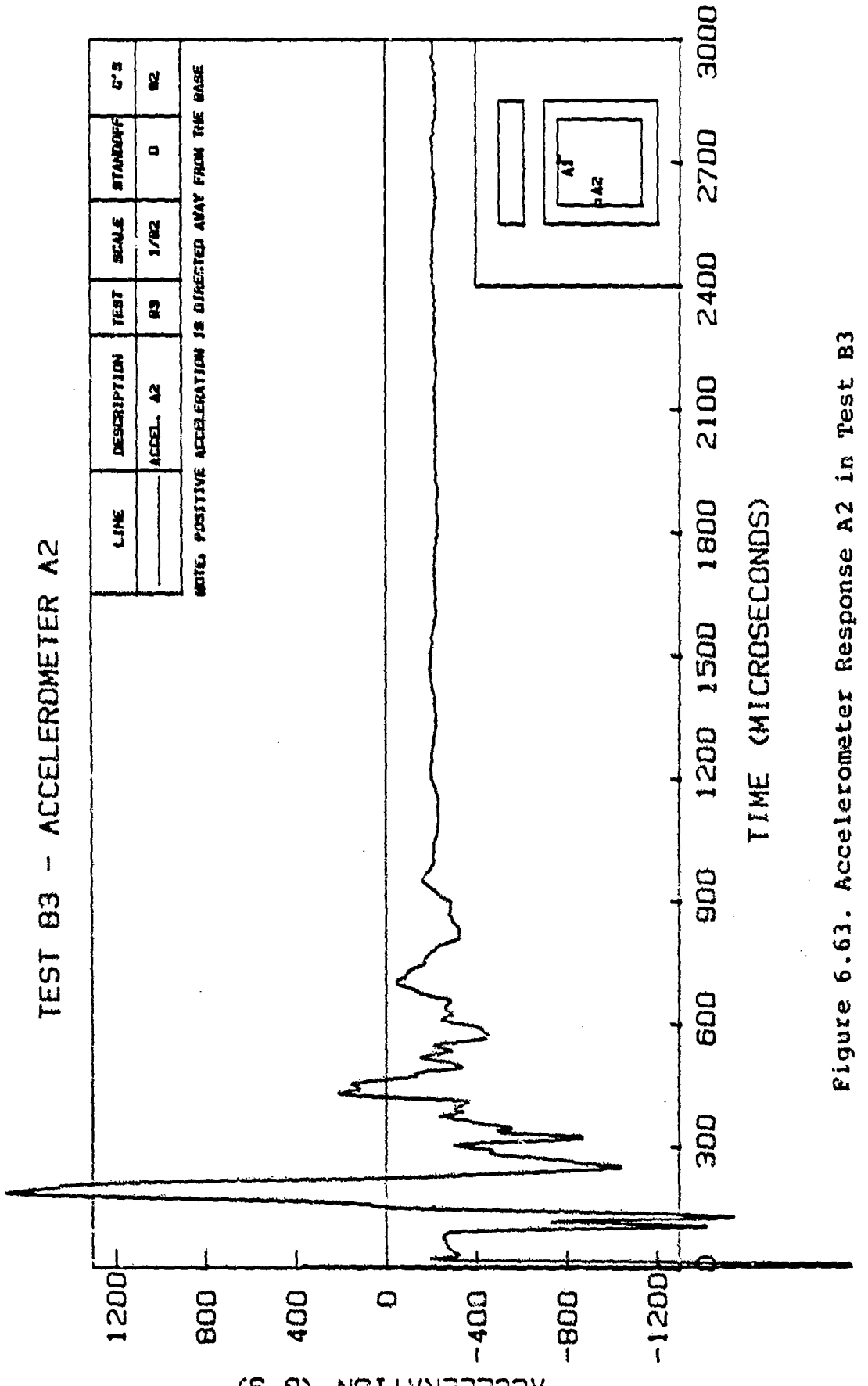

Figure 6.63. Accelerometer Response A2 in Test B3

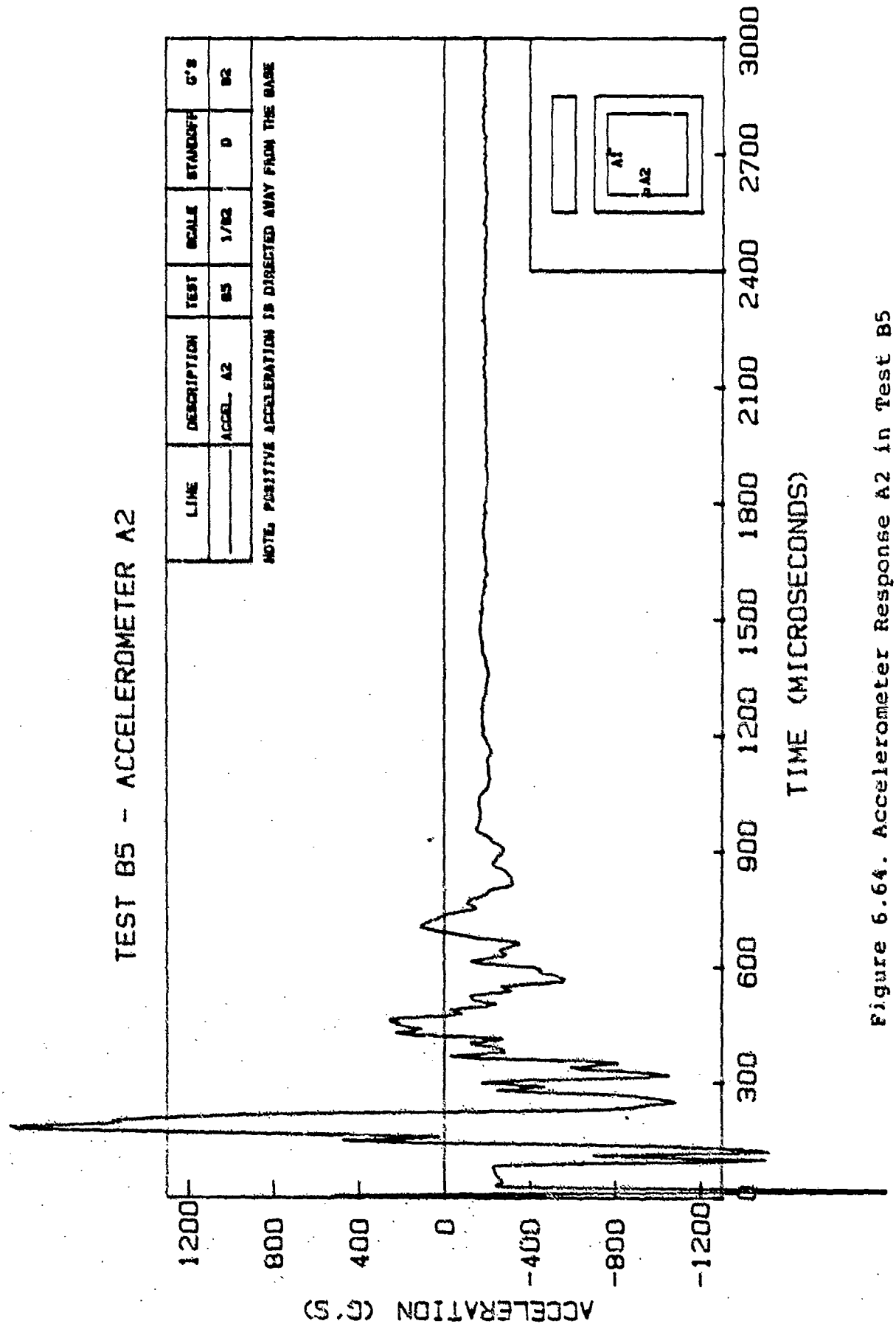

Figure 6.64. Accelerometer Response A2 in Test B5

6.3 Strains

A total of eight (four pairs) strain gages were used on each structure. Locations of these strain gages are shown in Figure 4.6. Because of the unavailability of a sufficient number of digital oscilloscopes with disk storage capabilities, results from strain gages S3 and S4 were only recorded photographically. Therefore, results from these two gages were not transferred to the computer (HP 9816) for reduction and analysis. Results from other strain gages (stored on oscilloscope disks) were transferred to the computer through a direct link between the oscilloscopes and the computer after the completion of all tests.

During tests of the trigger system for the detonator (before actual explosive tests), it appeared that the trigger signal had an influence on the strain gage responses. This interference lasted for a relatively short period of time. This influence was recorded and subsequently subtracted from corresponding strain gage outputs in different blast tests to compensate for that unwanted effect. However, because of possible variability of such an interference in different tests, the first 150 to 200 microseconds of all strain gage data should be viewed and interpreted cautiously and with due consideration of a great possibility of interference.

Fortunately, the main shock wave arrives at the structure just after this time period has passed.

Axial and flexural strains in the slabs and sidewall of each structure in different tests are calculated (on the computer) from the adjusted strain gage data using Equations 4.7 and 4.8 (see Figure 4.7). Strain gages S1 and S2 (top slab) did not function properly in tests on 1/82-scale models (B series).

6.3.1 Strains in Top Slab

In this section, only the results of tests on 1/60-scale models are presented because strain gages S1 and S2 did not work properly in tests on 1/82-scale models. Figure 6.65 shows flexural strains in the top slab for tests A1 (2' standoff, 1g) and A2 (2' standoff, 60 g's). As mentioned earlier, the response in the first 150 μseconds should be considered as influenced by interference from the trigger system and the explosion. In these discussions, only the time frame during which the shock wave is applied on the structure is considered.

It is clear that the compressive flexural strains (on top of the top slab), which appear in the same time frame as the applied pressure P2, are substantially larger in the 60g test (93% difference in peak strains). Figure 6.66 shows flexural strains (in top slab) for tests A5 (2' standoff, 1g) and A6 (2' standoff, 60 g's). These two tests are conducted under conditions similar to tests A1 and A2

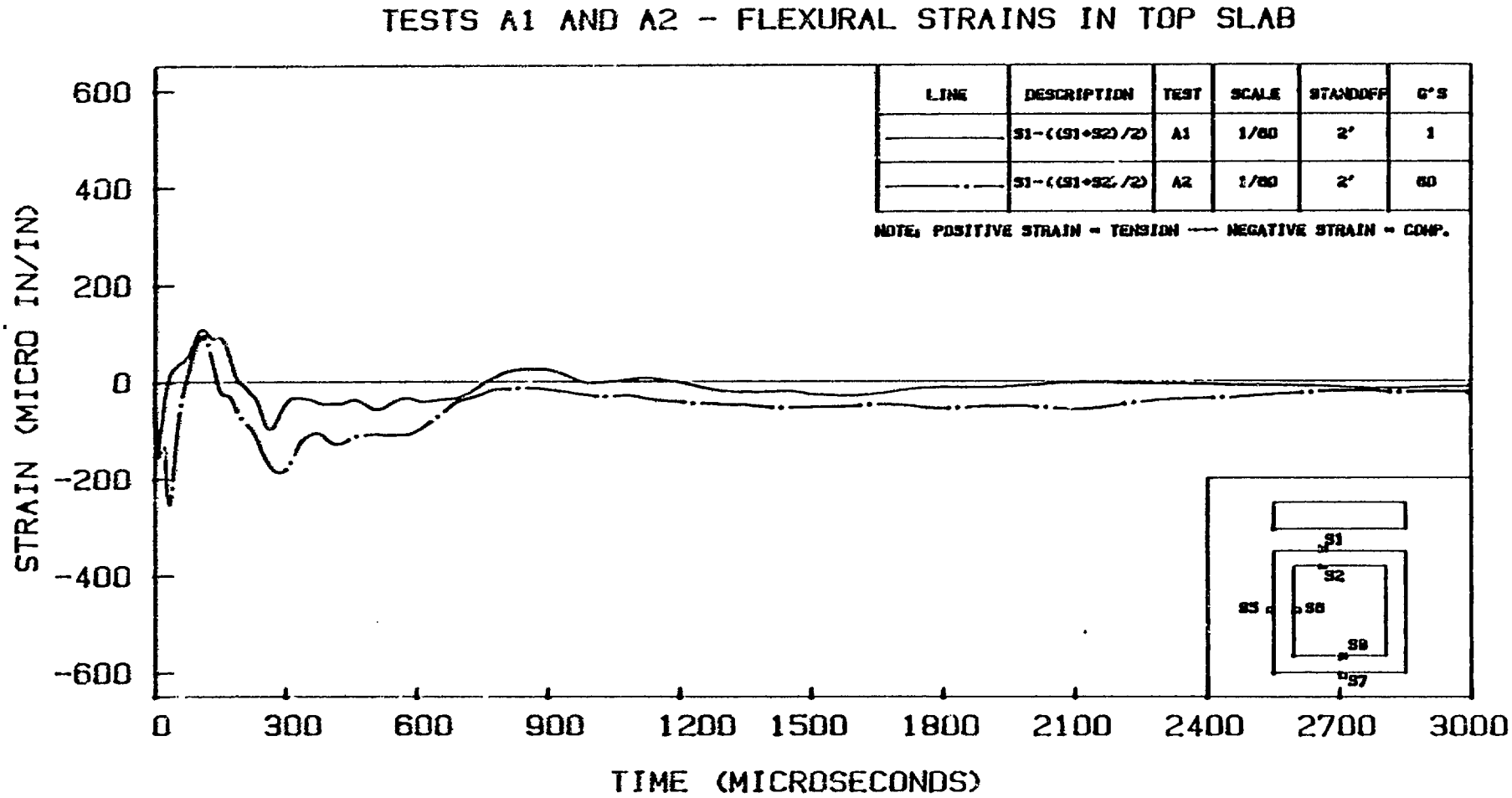

Figure 6.65. Flexural Strains in the Top Slab for Tests A1 and A2

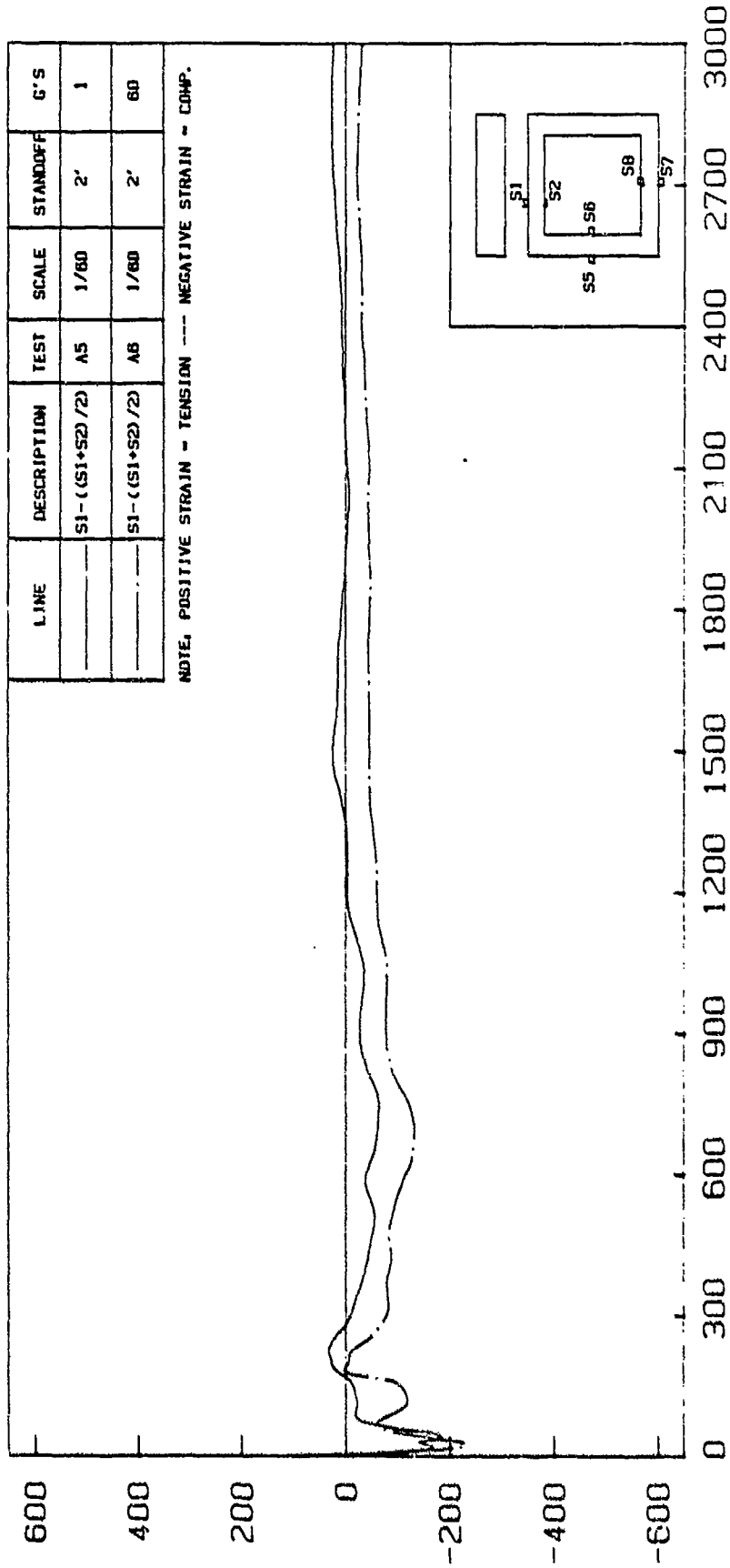

Figure 6.66. Flexural Strains in the Top Slab for Tests A5 and A6

except for a difference in soil density as explained earlier. Again, the flexural strain curves show larger compressive strains in the 60g test (A6) compared to the 1g test (A5). The peak compressive strain in test A6 is larger than the peak strain in test A5 by 100%. However, these flexural strains are smaller than the corresponding flexural strains in tests A1 and A2.

Figure 6.67 shows flexural strains for test A3 (0' standoff, 1g) and A4 (0' standoff, 60 g's). As explained earlier, test A4 was performed on a cracked burster slab. It is clear that the 60g test results are not much larger than the 1g test results. In fact, flexural strains in test A3 (1g) show slightly larger values at the beginning. This effect can be better seen in Figure 6.68 which shows flexural strains for tests A3 and A7 (0' standoff, 60 g's). Tests A4 and A7 are similar except for the condition of burster slab which was intact in test A7. Flexural strains in the 1g test (A3) are larger than strains in the 60g test (A7). This effect can be explained by considering the fact that Pressure Gage P2 also recorded higher pressures in test A3.

Figure 6.69 shows axial strains in the top slab for tests A1 and A2. It appears that, at smaller deflections (times), there is compressive axial strain in the slab and as the deflection (time) increases, the axial strain becomes tensile due to rigidity of the sidewalls. Test A2 shows smaller compressive strains than test A1. Of course,

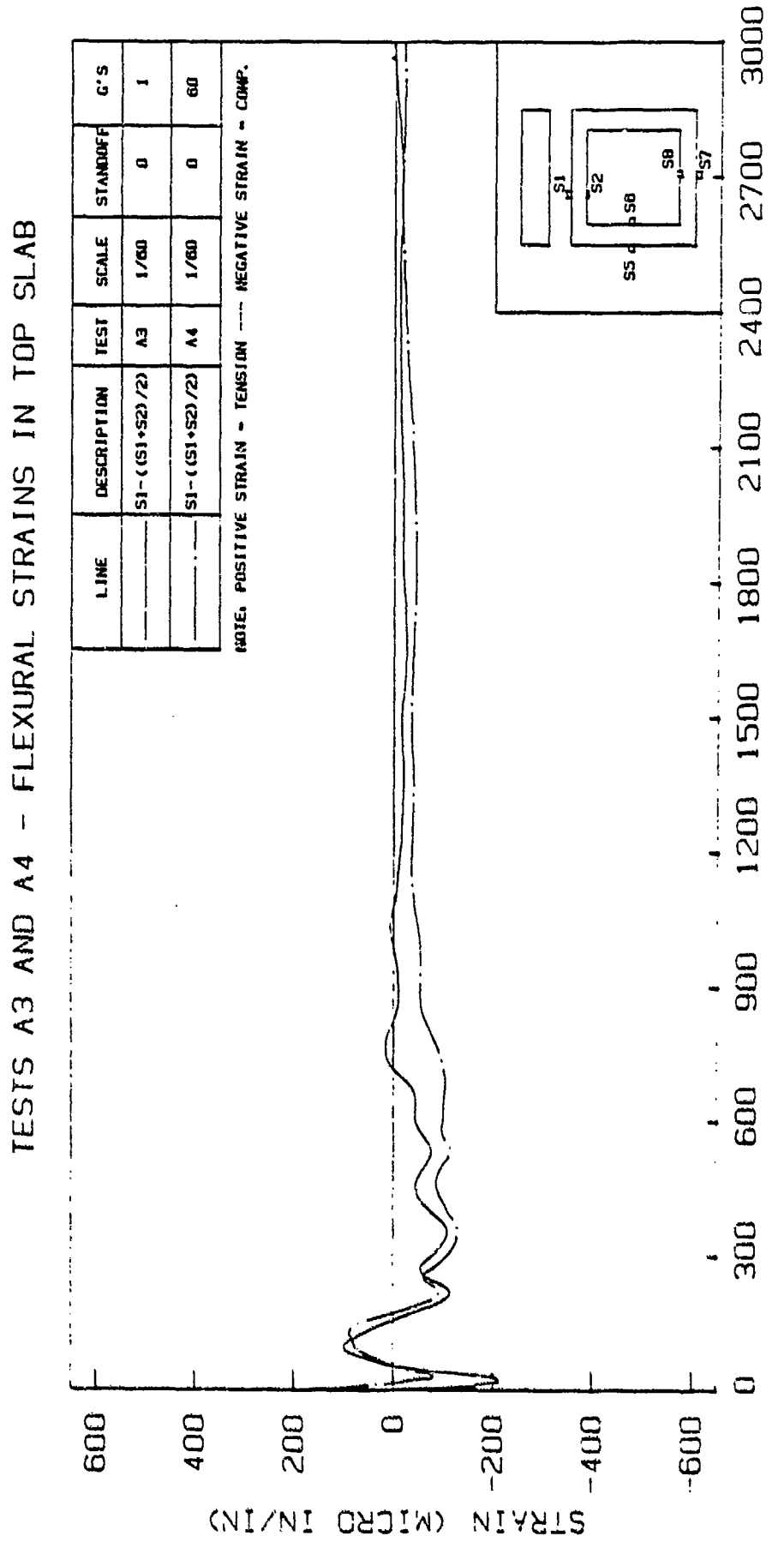

Figure 6.67. Flexural Strains in the top Slab for Tests A3 and A4

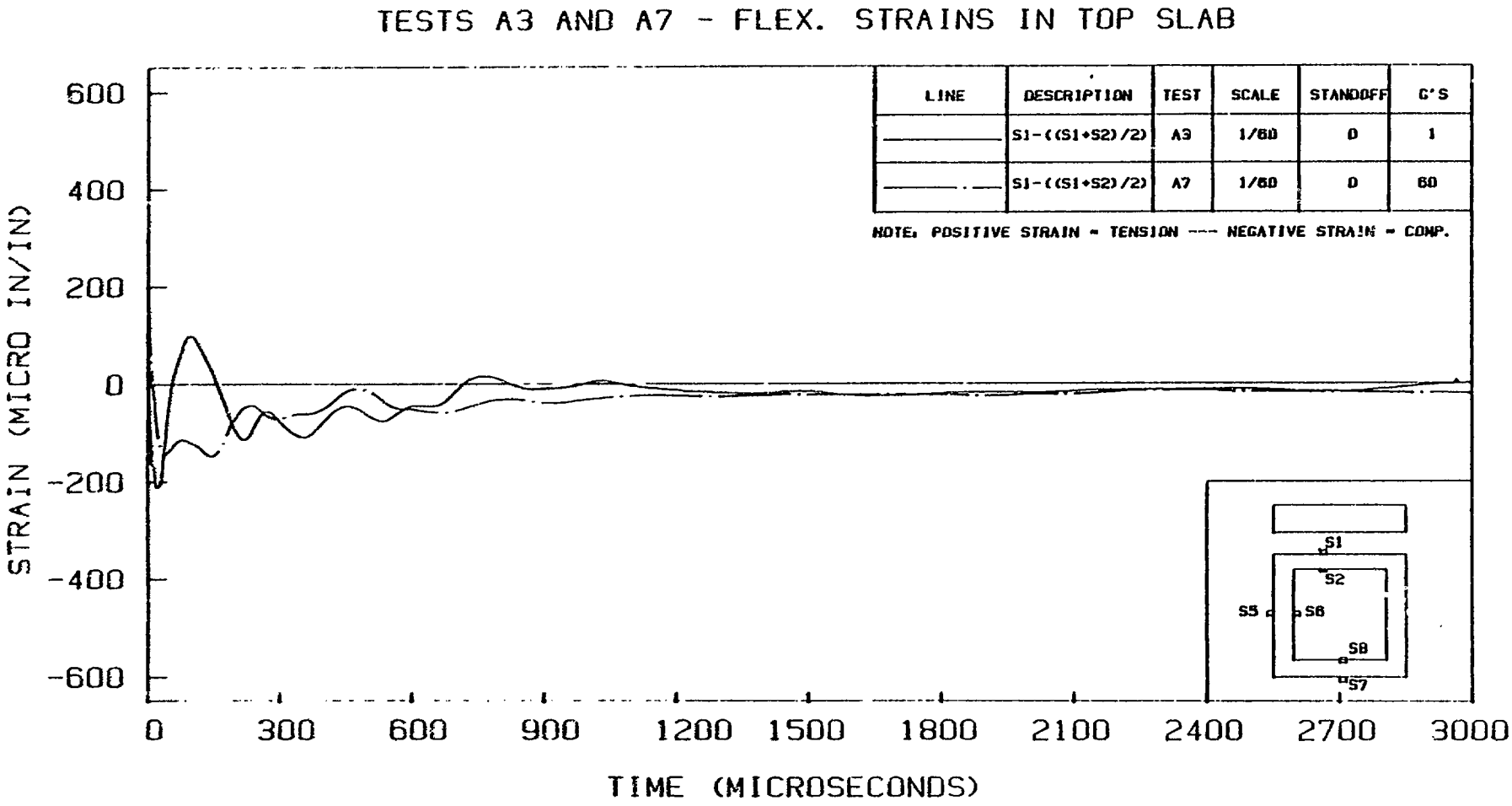

Figure 6.68. Flexural Strains in the Top Slab for Tests A3 and A7

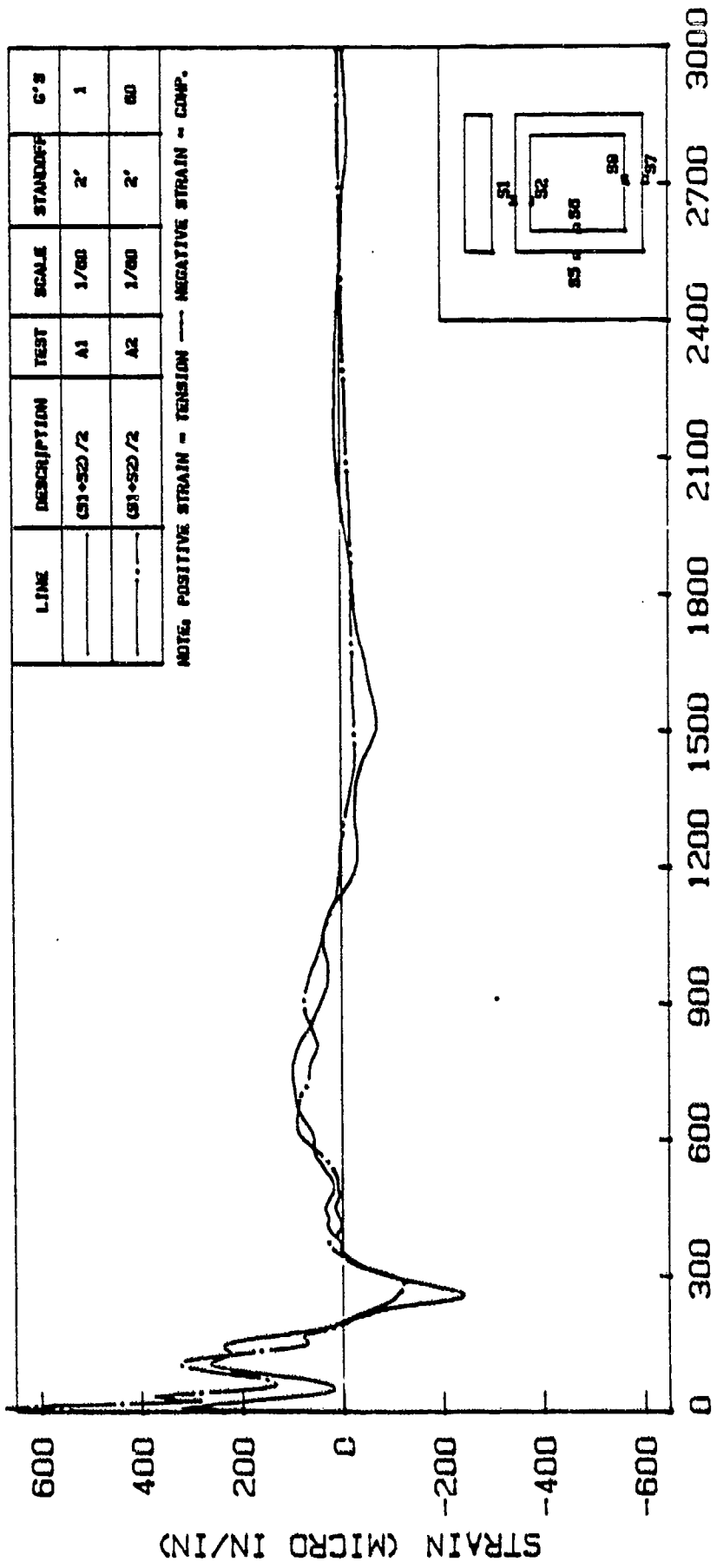

Figure 6.69. Axial Strains in the Top Slab for Tests A1 and A2

compressive axial strains (stresses) help with ultimate flexural strength of slabs subjected to dynamic loads (Krauthammer, 1984). Figure 6.70 shows axial strains in tests A5 and A6. In this case, test A6 shows larger compressive strains than test A5 in the beginning, but then they both show tensile axial strains.

Figure 6.71 shows axial strains in tests A3 and A4. Test A4 shows larger tensile strains than test A3. A similar type response is observed in Figure 6.72 for tests A3 and A7.

6.3.2 Strains in the Side Wall

Figure 6.73 shows flexural strains in the side wall for tests A1 and A2. The large tensile strains in test A2 are due to existance of larger pressures on the top slab of the structure in test A2 as compared to test A1. Flexural strain in test A1 (on the side wall) fluctuate between compression and tension.

Figure 6.74 shows flexural strains in test A5 and A6. Again, there are larger flexural tensile strains on the outside of the side wall in the 60g test (A6) compared to the 1g test (A5). However, the magnitudes of strains are smaller than in tests A1 and A2.

Figure 6.75 shows flexural strains in tests B1 (2' standoff, 1g) and B2 (2' standoff, 82 g's) performed on 1/82-scale models. Larger tensile strains appear in the 82g test (B2) compared to the 1g test (B1). The magnitudes and

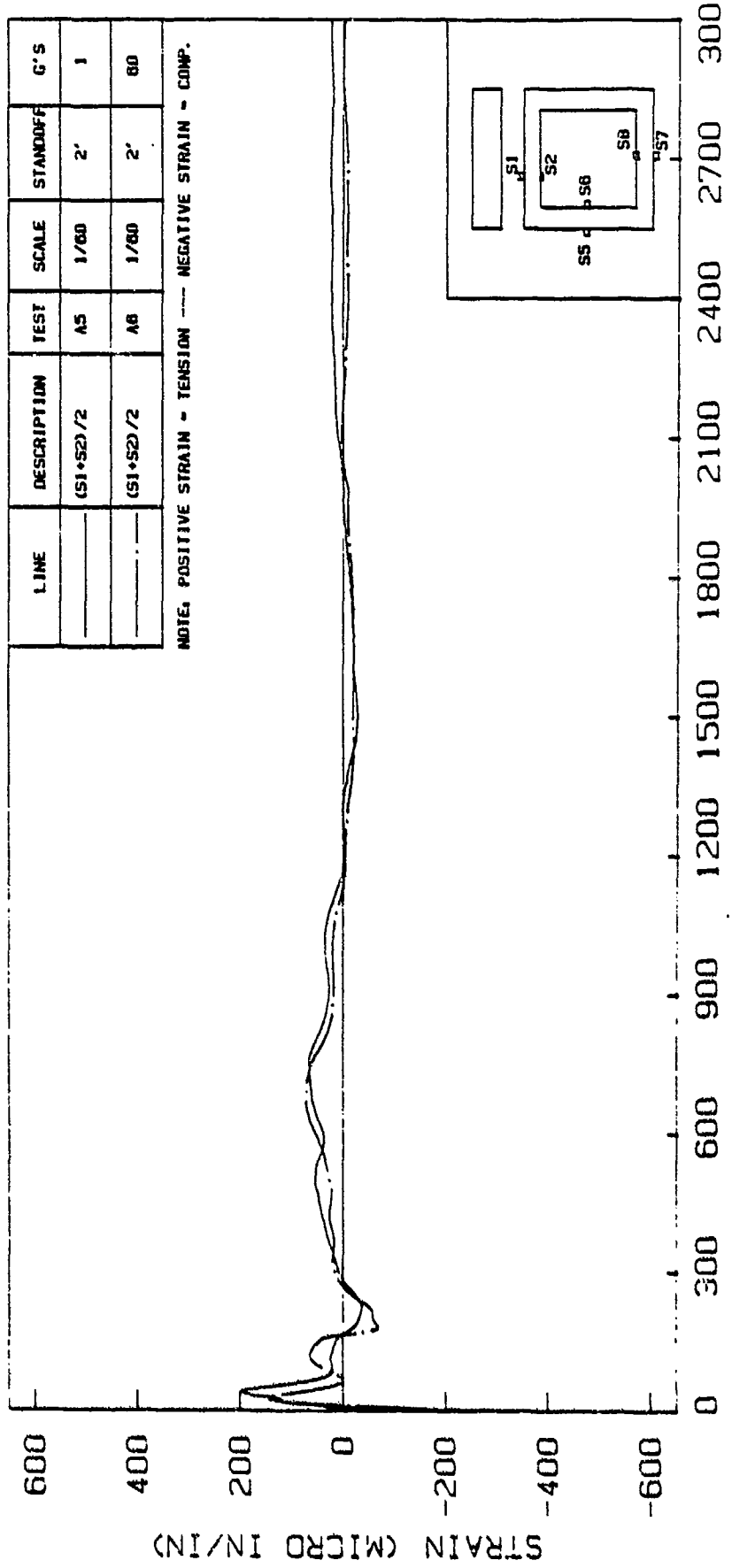

Figure 6.70. Axial Strains in the Top Slab for Tests A5 and A6

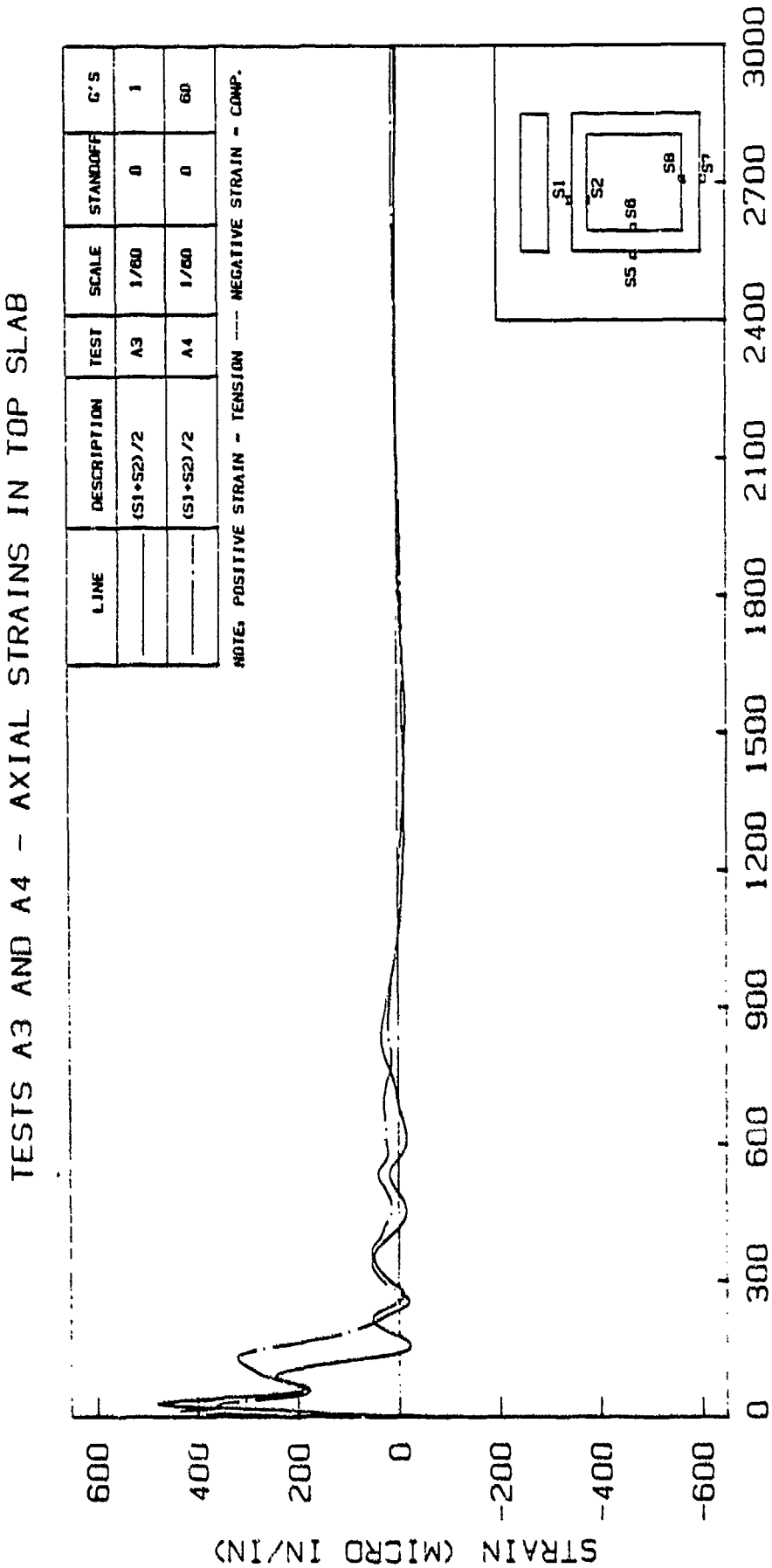

Figure 6.71. Axial Strains in the Top Slab for Tests A3 and A4

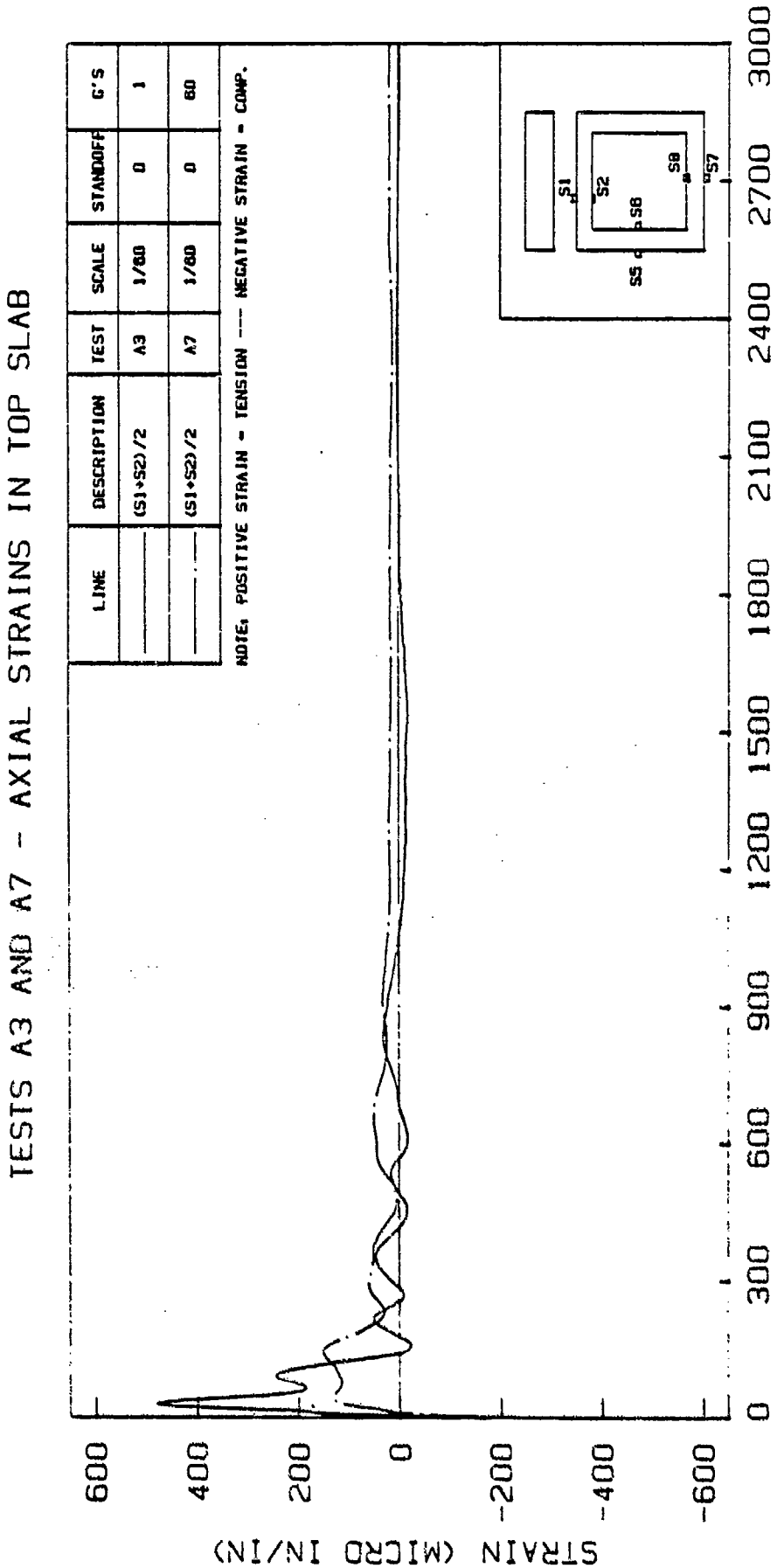

Figure 6.72. Axial Strains in the Top Slab for Tests A3 and A7

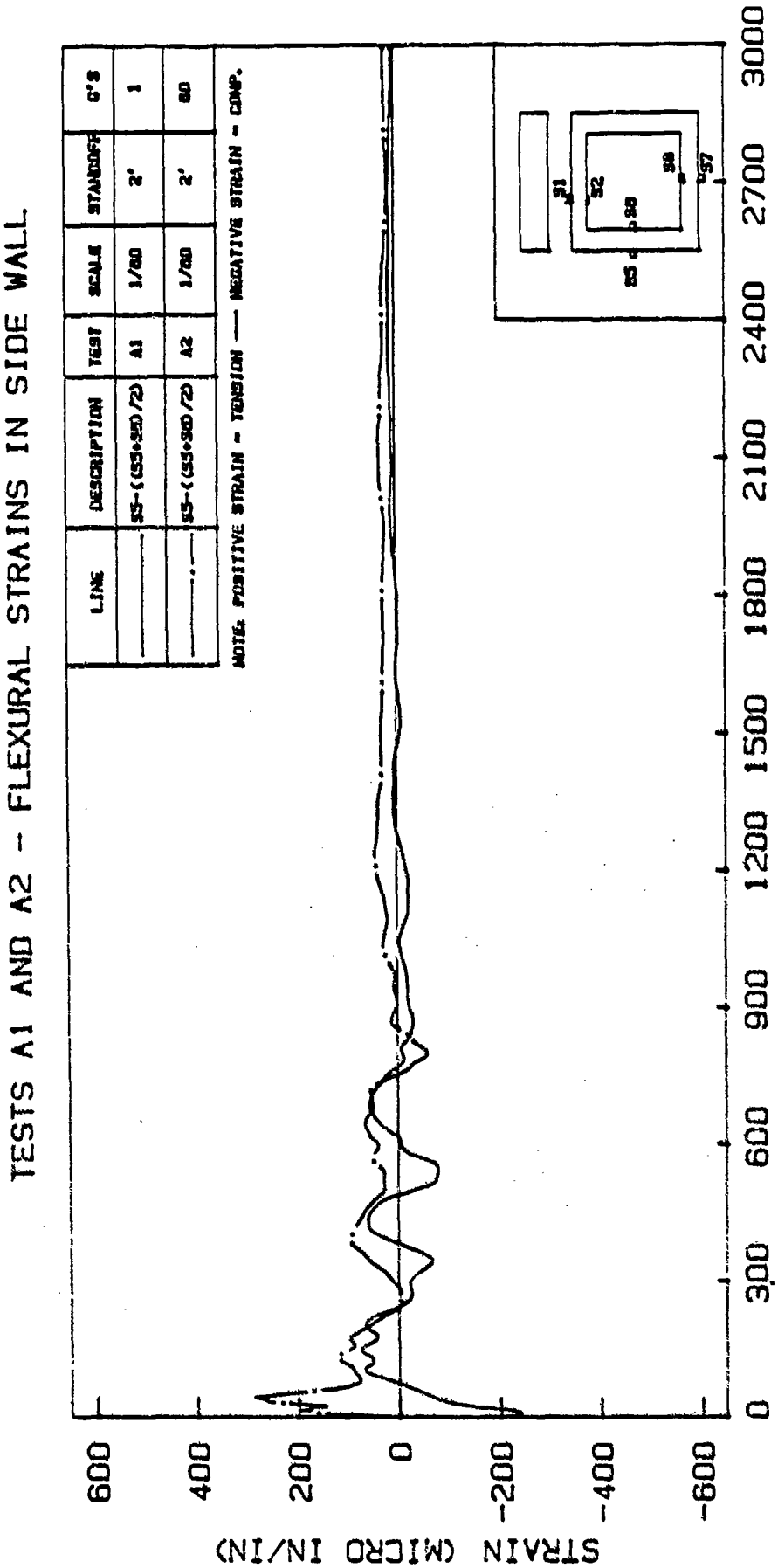

Figure 6.73. Flexural Strains in the Side Wall for Tests A1 and A2

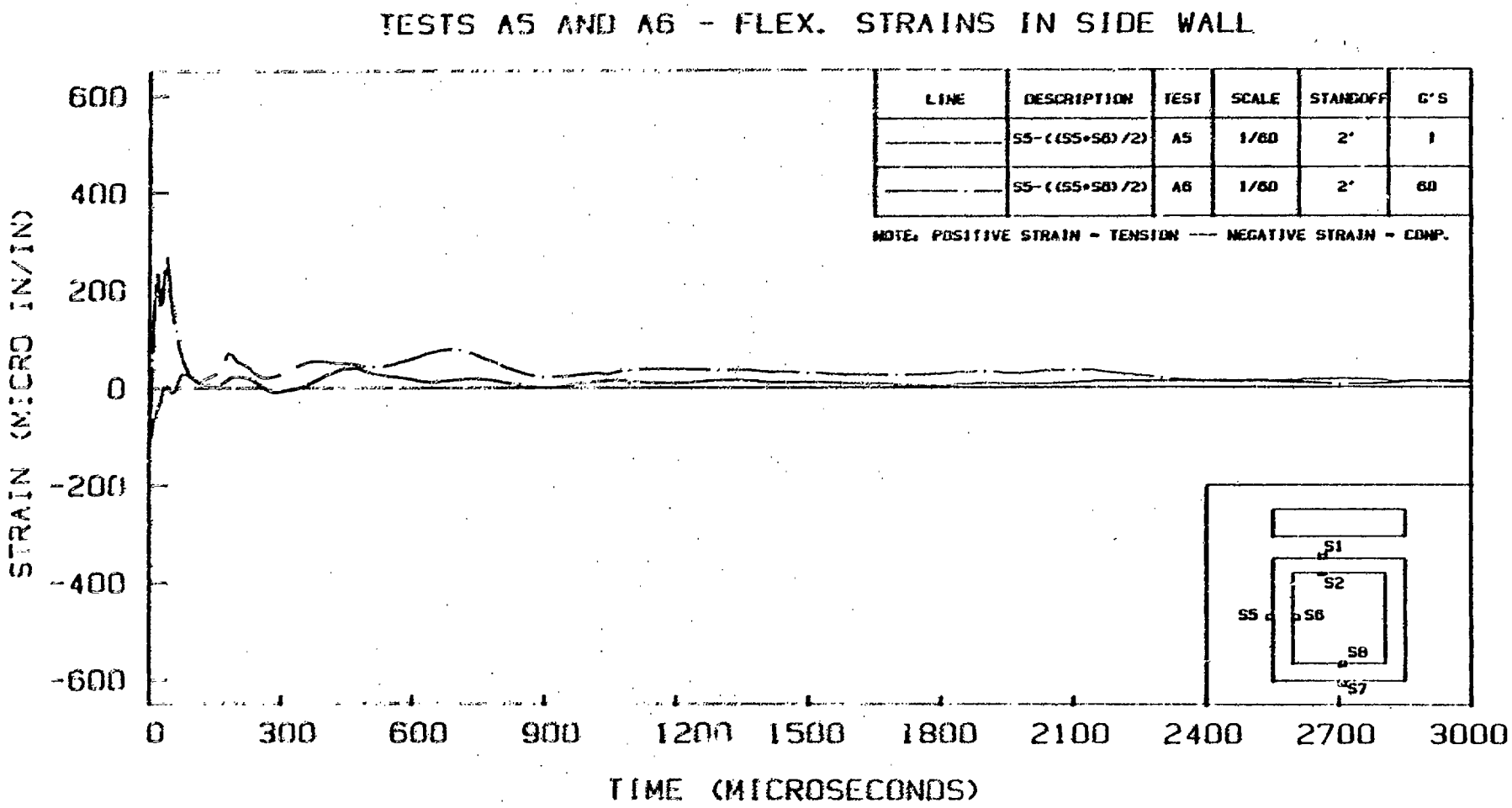

Figure 6.74. Flexural Strains in the Side Wall for Tests A5 and A6

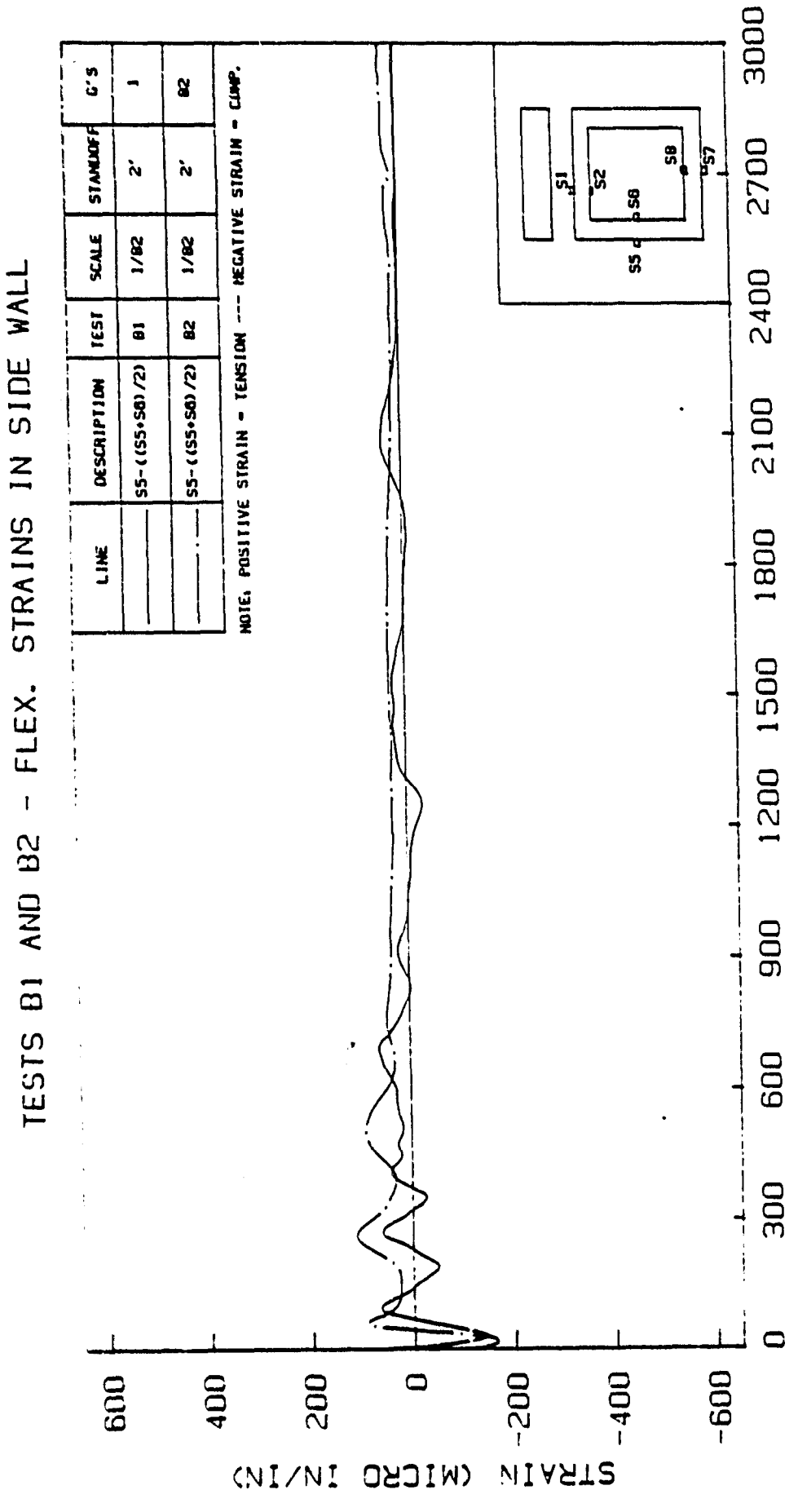

Figure 6.75. Flexural Strains in the Side Wall for Tests B1 and B2

shapes of the strain response curves in tests B1 and B2 are similar to the curves in tests A1 and A2 (Figure 6.73). In fact, the arrival time for the first tensile peak in test B2 (during the time the shock wave is applied on structure) is almost exactly 60/82 times smaller than the first comparable peak in test A2. Figure 6.76 shows flexural strains in tests B2 and B4 (2' standoff, 82 g's). These two tests are similar and they show equal magnitudes for the first tensile peak. The arrival times of this peak are also close.

Flexural strains in tests A3 and A4 (Figure 6.77) show equal peak magnitudes of tensile strain on the outside of the side wall. A similar type of response is obtained from tests A3 and A7 (Figure 6.78). Figure 6.79 shows flexural strains in the side wall for test B3 (0' standoff, 82 g's) and B5 (0' standoff, 82 g's). These two tests show very different responses even though they are essentially the same tests. It appears that test B5 presents a more valid response considering the similarity of this response to the results obtained in test A7.

Figure 6.80 shows axial strains in the side wall for tests A1 and A2. It appears that the compressive strains in tests A1 and A2 are almost equal even though a larger compressive strain was expected in test A2 considering larger pressures applied on the top slab in this test. This may be explained by pointing out that the increased confinement by the soil on the structure could result in a

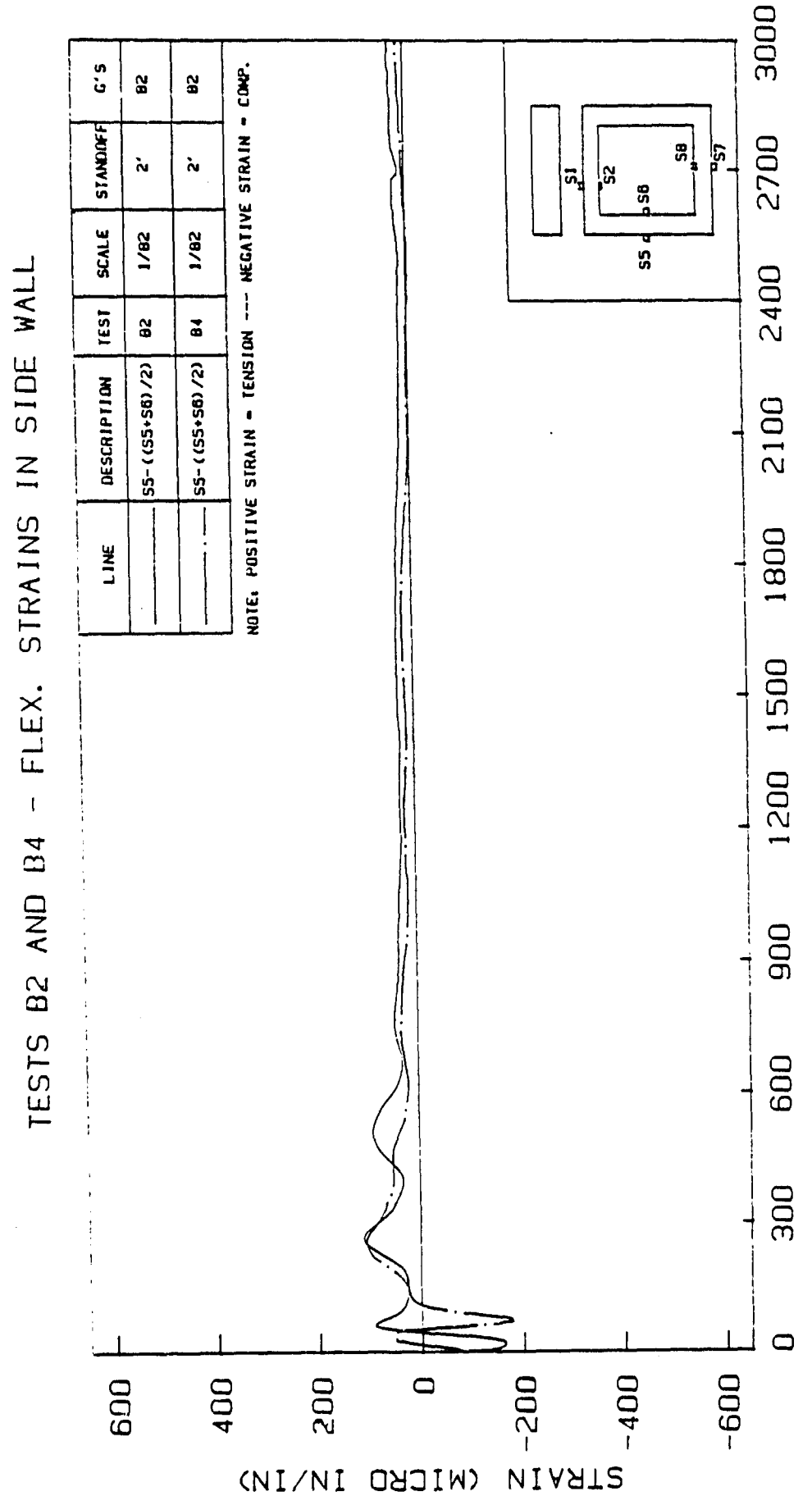

Figure 6.76. Flexural Strains in the Side Wall for Tests B2 and B4

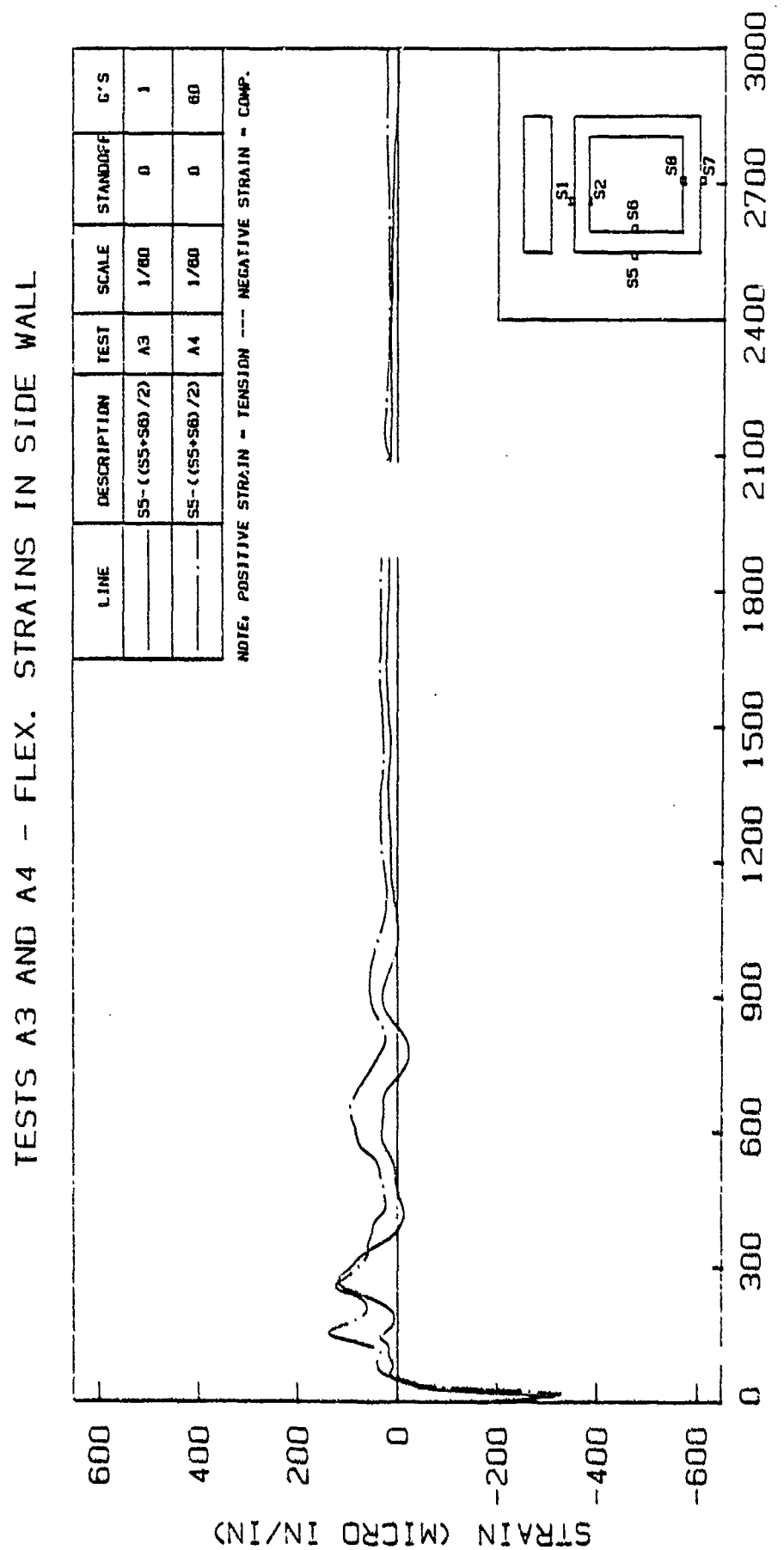

Figure 6.77. Flexural Strains in the Side Wall for Tests A3 and A4

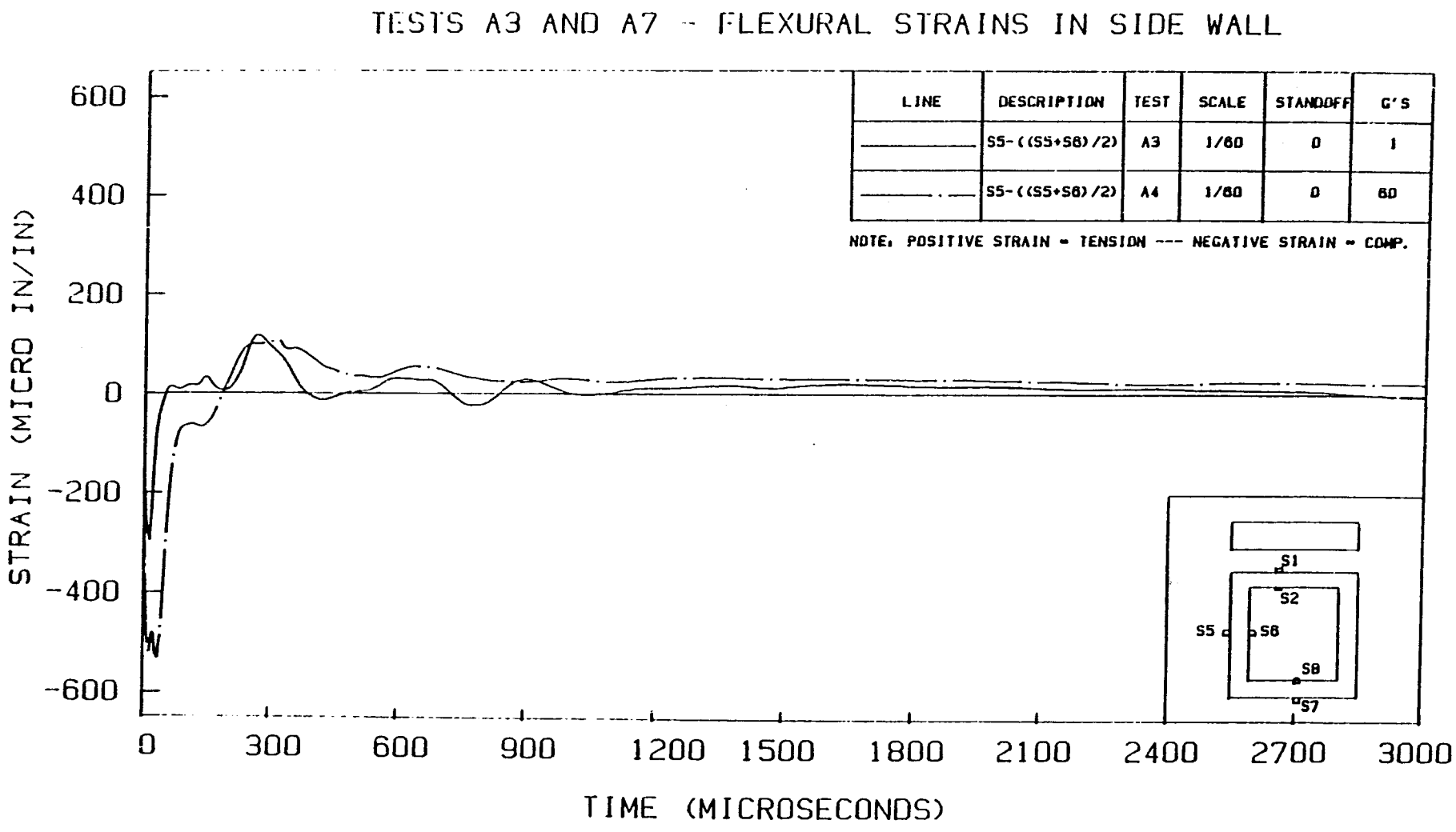

Figure 6.78. Flexural Strains in the Side Wall for Tests A3 and A7

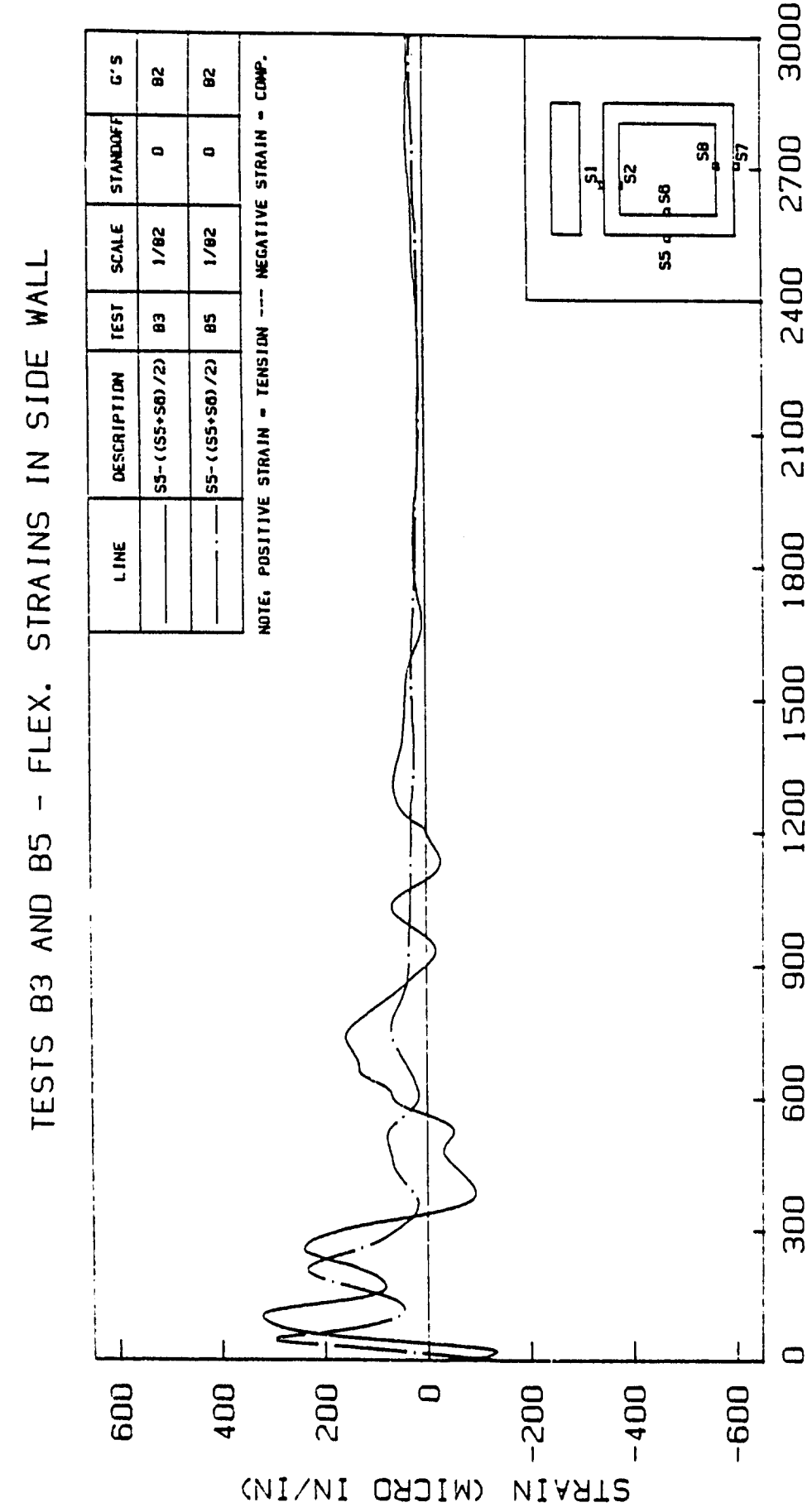

Figure 6.79. Flexural Strains in the Side Wall for Tests B3 and B5

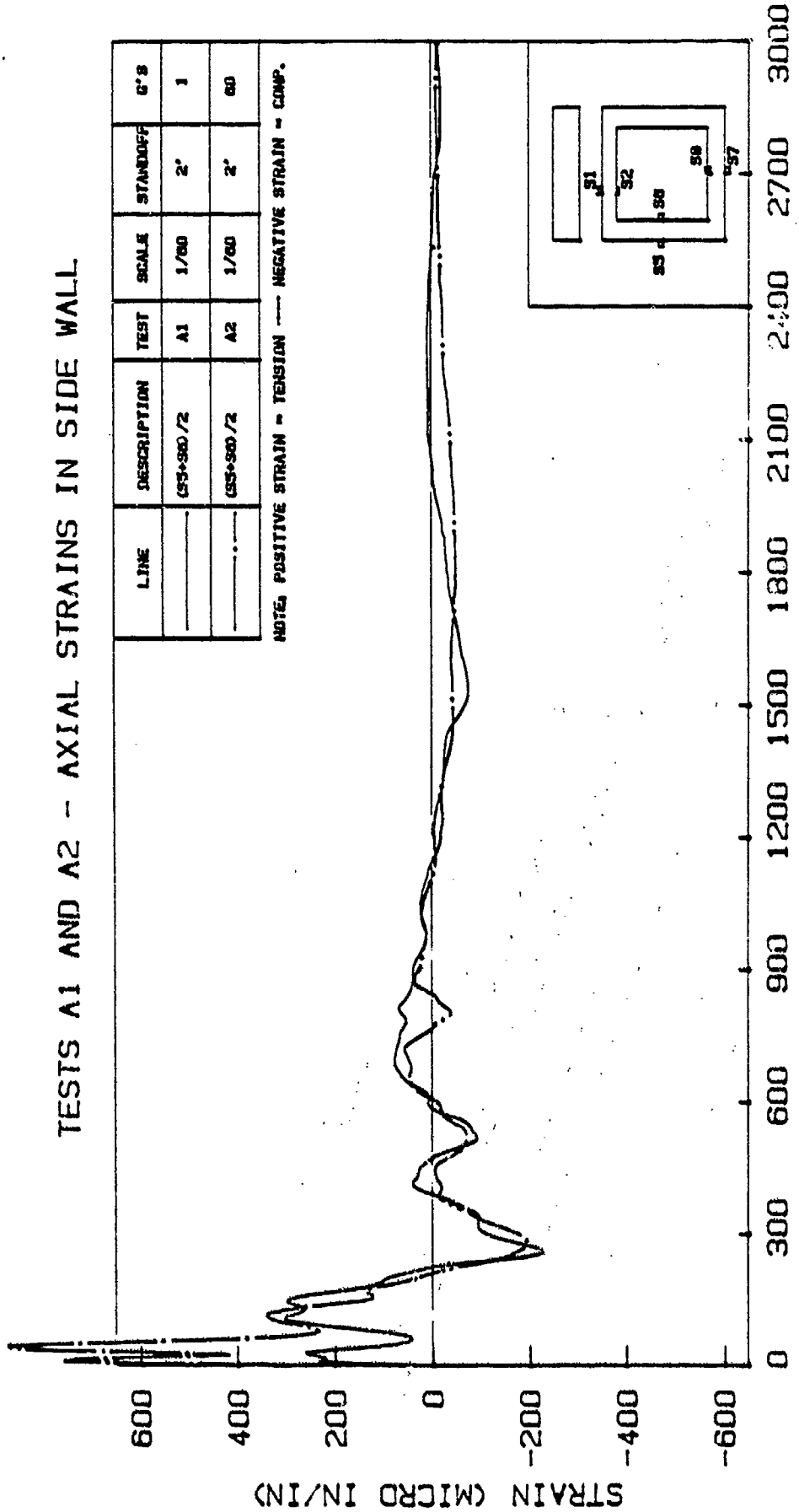

Figure 6.80. Axial Strains in the Side Wall for Tests A1 and A2

larger degree of load transfer to the soil. Figure 6.81 shows axial strains in tests A5 and A6. The magnitudes of strains in this case are smaller compared to tests A1 and A2 (Figure 6.80). However, the first compressive peak is larger in the 60g test (A6) compared to the 1g test (A5).

Figures 6.82 and 6.83 show axial strains for tests B1, B2 and B2, B4 respectively. The magnitudes of these strains are smaller than the corresponding strains in tests on 1/60-scale models (A series).

Figure 6.84 shows axial strains in tests A3 and A4. Test A4 shows slightly larger compressive strains than test A3. Considering larger pressures observed on the top slab in test A3, it is expected that compressive strains in test A3 be larger. This effect can be clearly observed in tests A3 and A7 (Figure 6.85). Tests B3 and B5 (Figure 6.86) show substantially different results. It is believed that this is due to a gage malfunction in test B3.

6.3.3 Strains in Bottom Slab

Figure 6.87 shows flexural strains in the bottom slab for tests A1 and A2. Test A2 shows residual strains after the shock wave has passed. This is due to gravity stresses in the 60g tests which remain after the explosion occurred. Compressive flexural strains on the outside of the bottom slab are consistently and considerably higher in the 60g test (A2). The peak strain in the 60-g test (A2) is 200% larger than the peak strain in the 1g test (A1). Figure

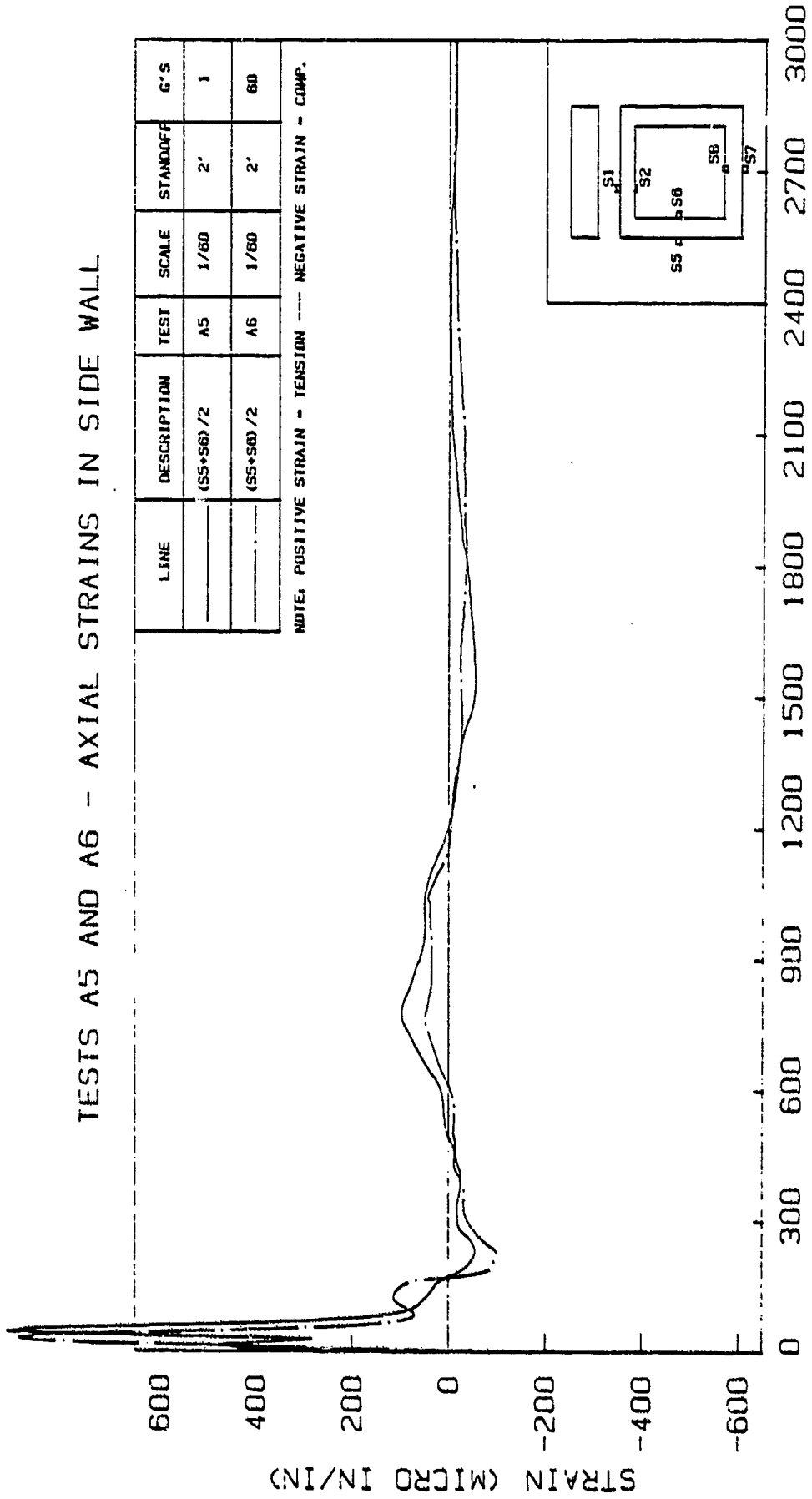

Figure 6.81. Axial Strains in the Side Wall for Tests A5 and A6

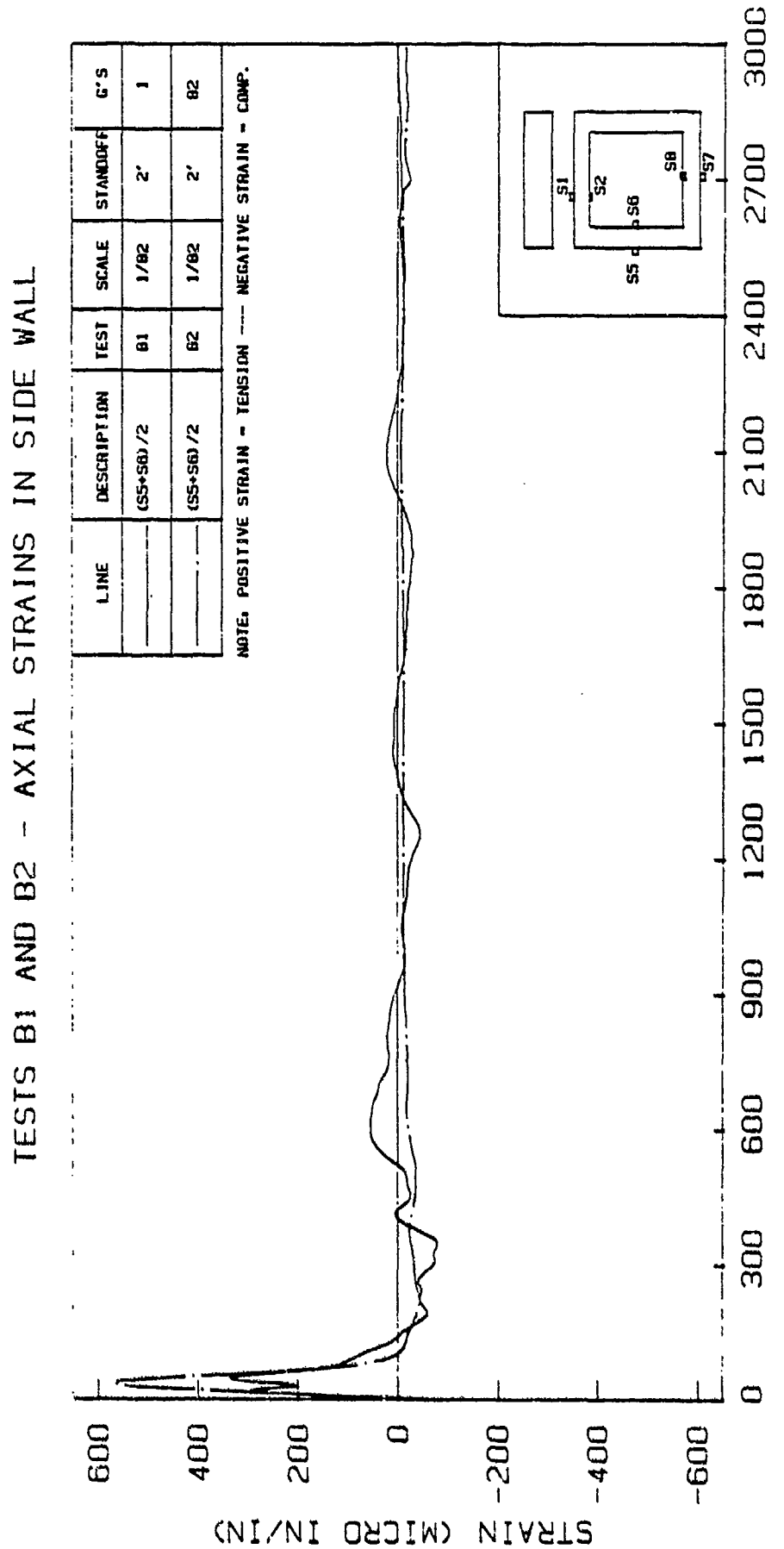

Figure 6.82. Axial Strains in the Side Wall for Tests B1 and B2

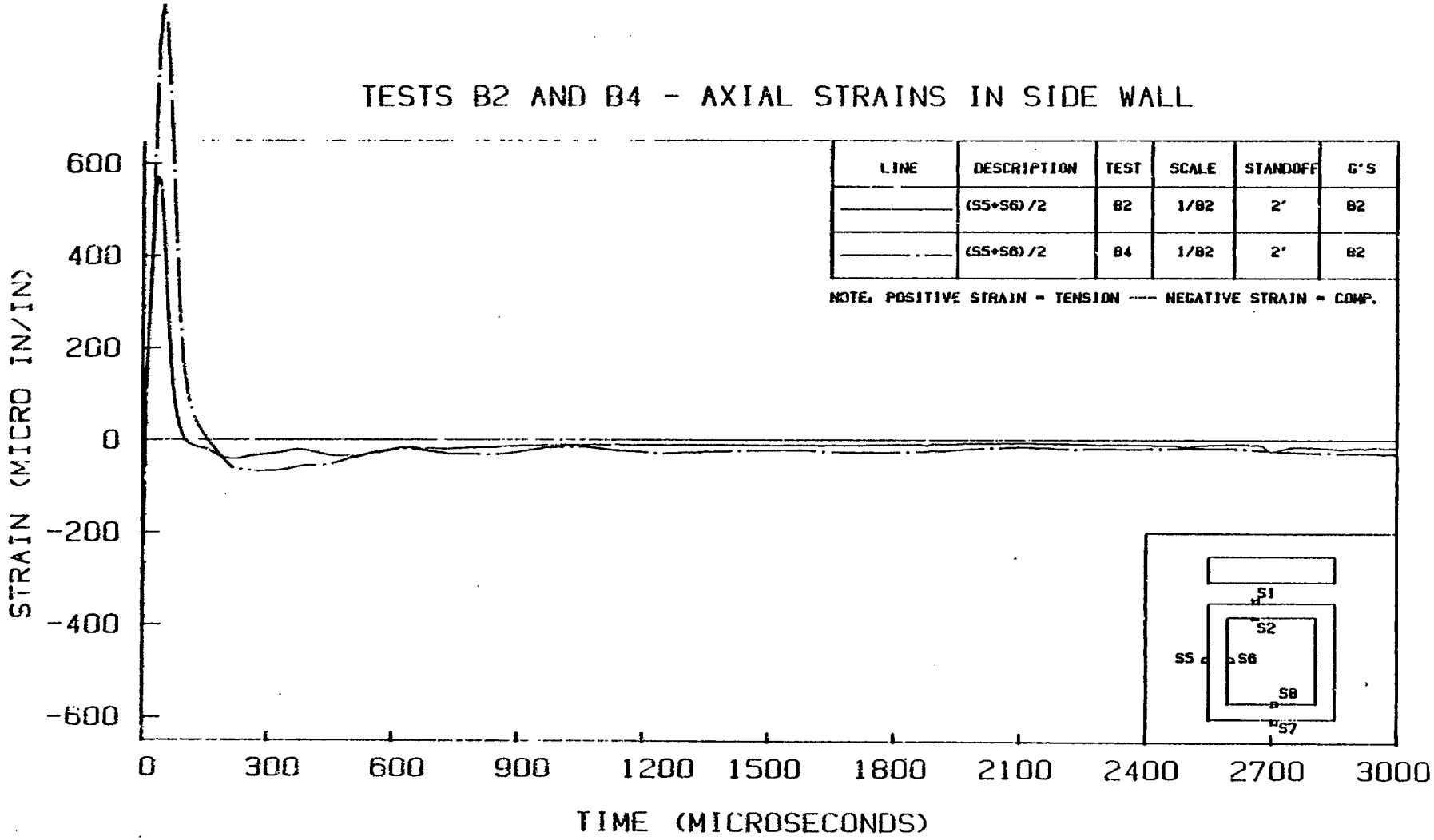

Figure 6.83. Axial Strains in the Side Wall for Tests B2 and B4

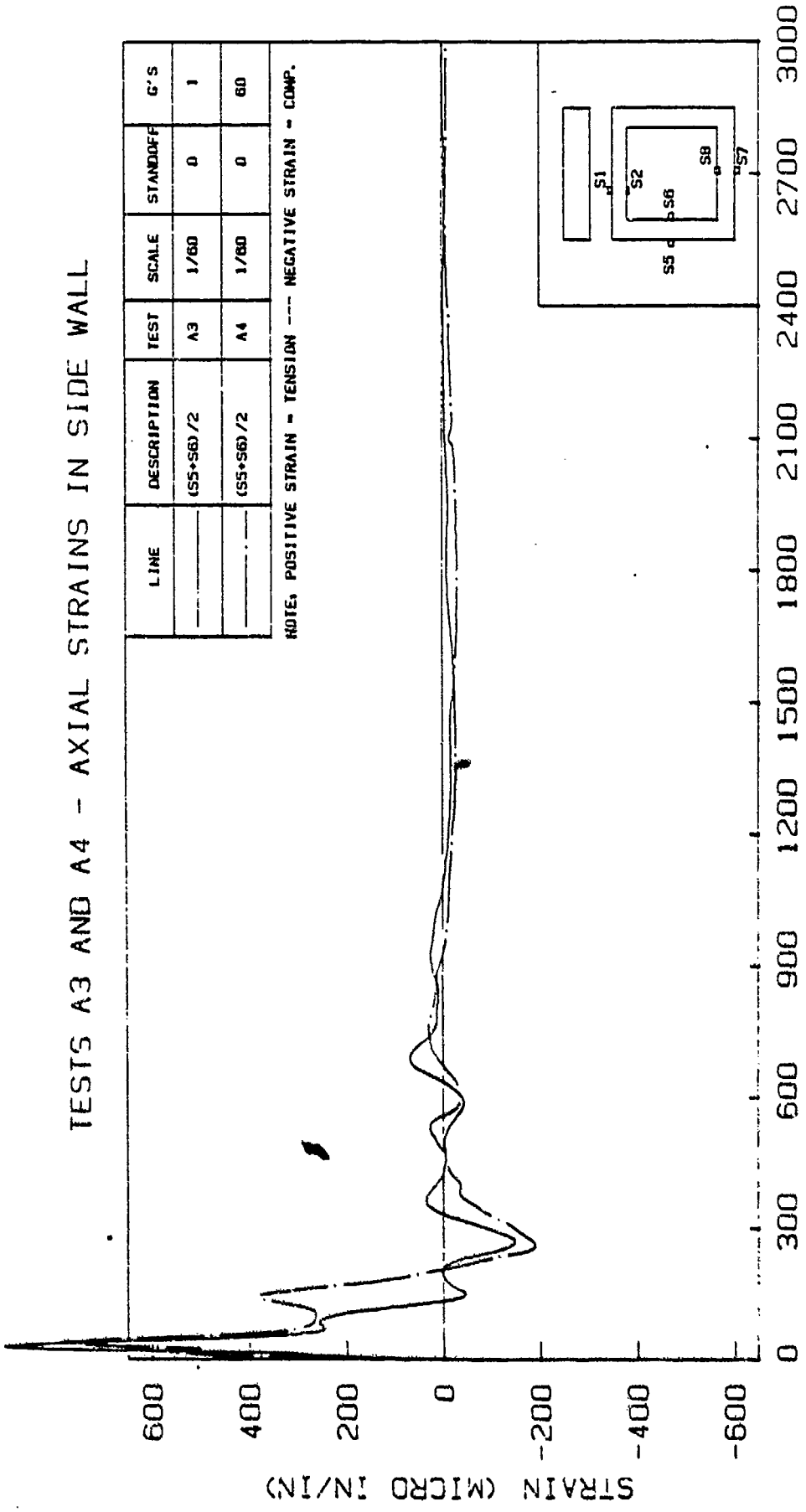

Figure 6.84. Axial Strains in the Side Wall for Tests A3 and A4

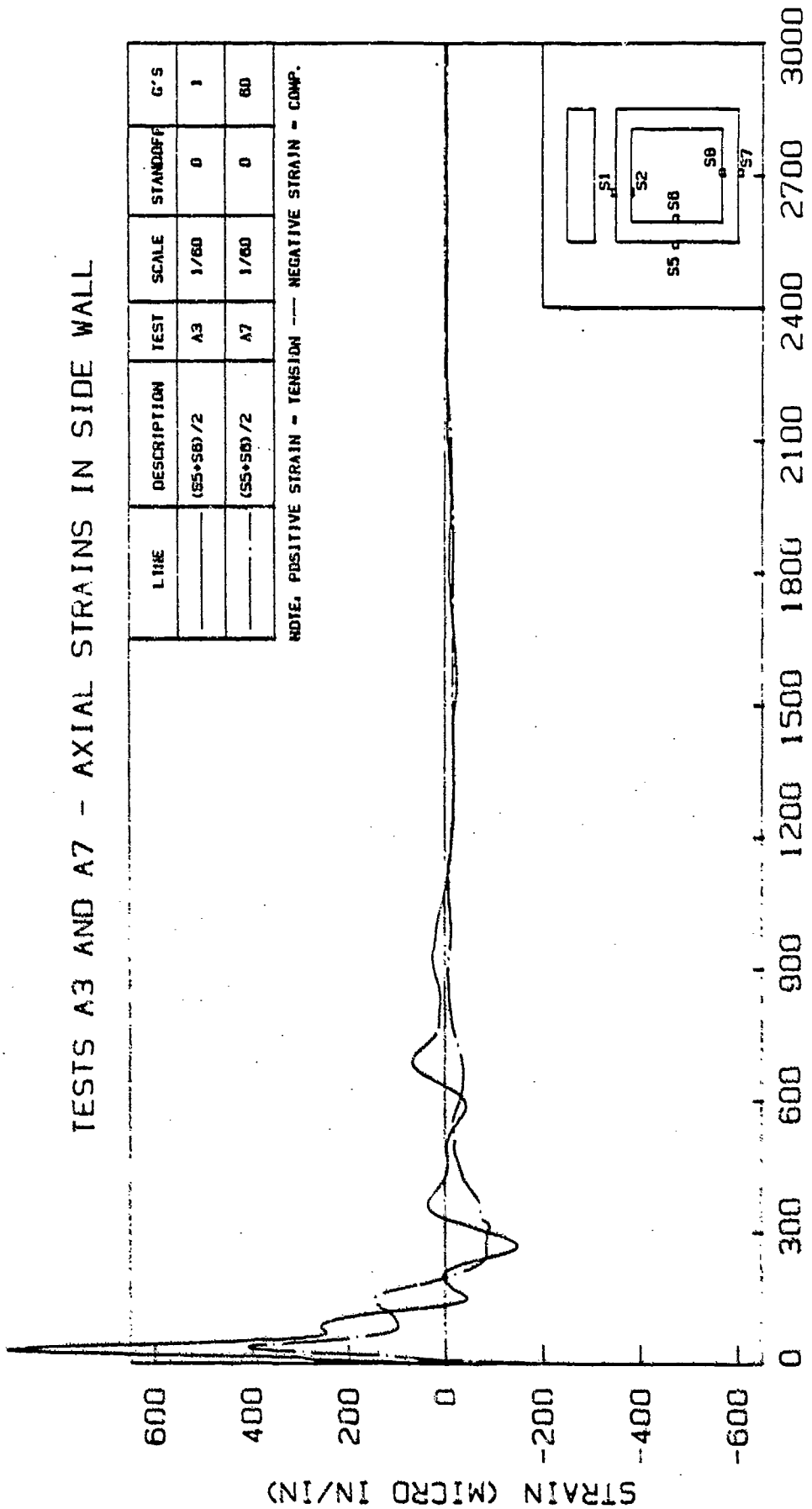

Figure 6.65. Axial Strains in the Side Wall for Tests A3 and A7

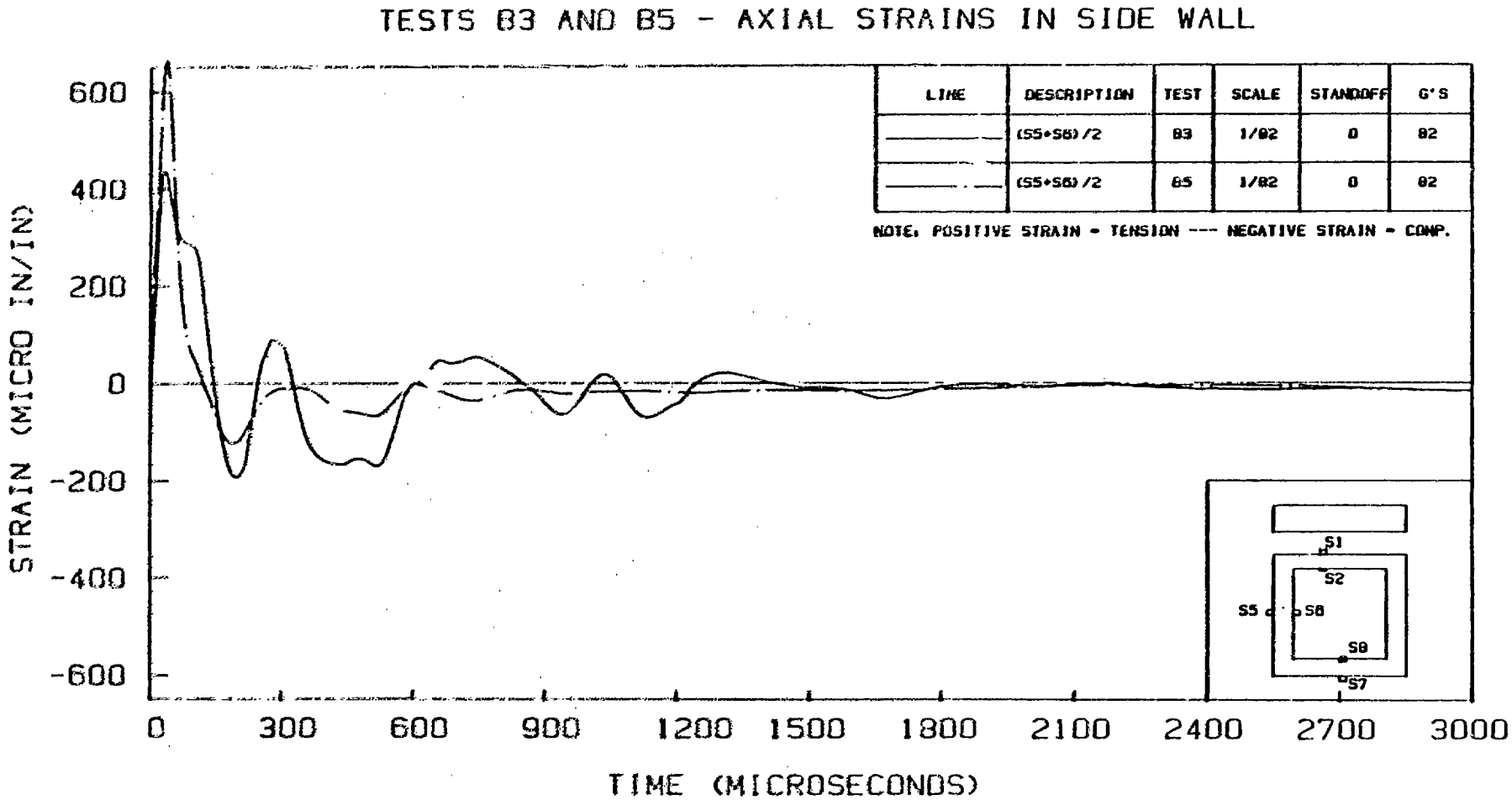

Figure 6.86. Axial Strains in the Side Wall for Tests B3 and B5

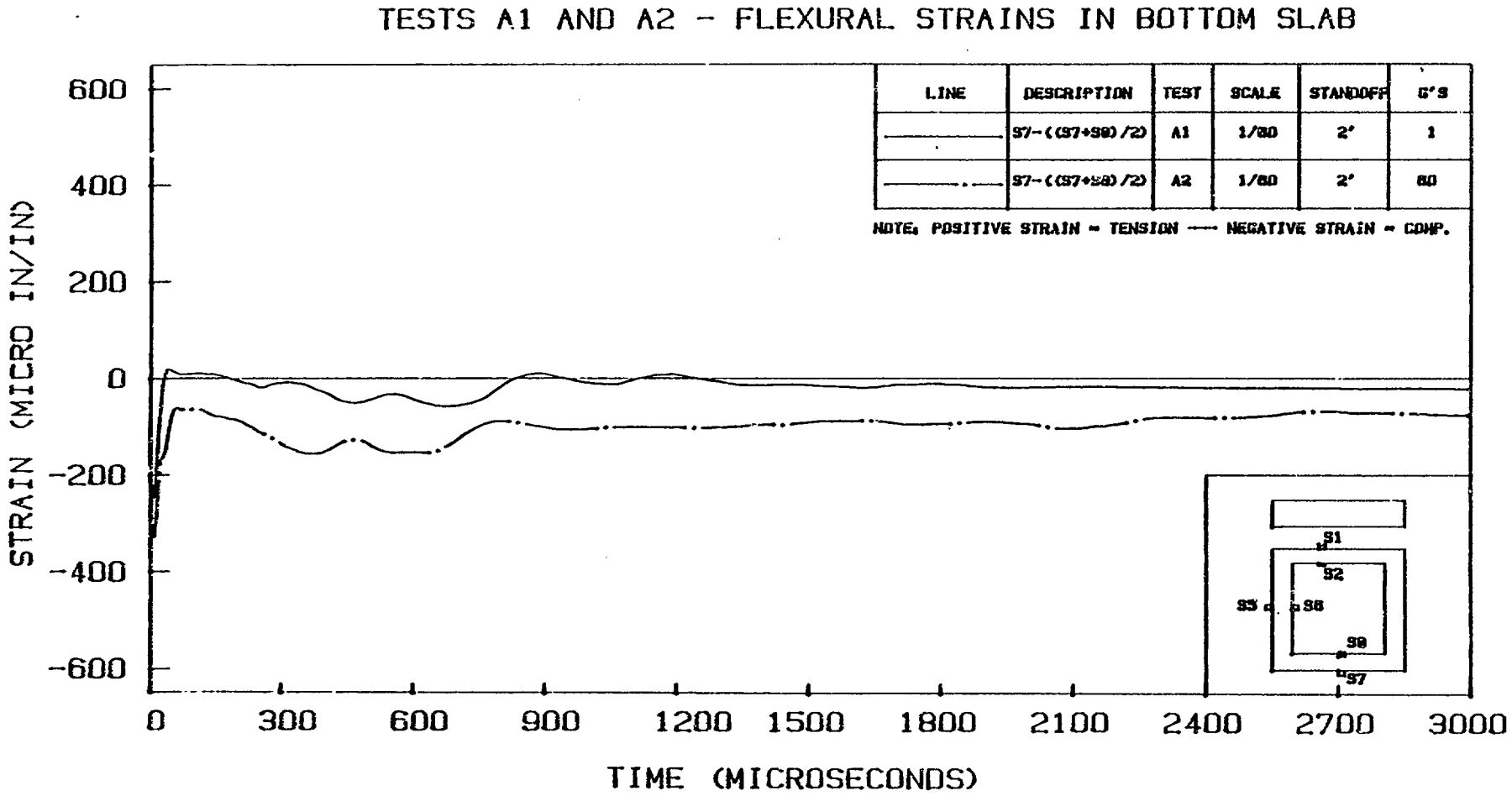

Figure 6.87. Flexural Strains in the Bottom Slab for Tests A1 and A2

6.88 shows flexural strains in tests A5 and A6. Again, flexural compressive strains are larger in the 60g test (A6). The magnitudes of these strains are close to those obtained in tests A1 and A2. Similar tests at 2' standoff on 1/82-scale models (Figure 6.89) exhibit behaviors similar to those observed in tests A1, A2, A5 and A6. Peak strains in test B2 are close to peak strains in test A2. Also, the arrival times for the peak in test B2 is 60/82 times smaller than the corresponding arrival times in test A2. These facts point to the validity of scaling relationships presented in Chapter 2. Tests B2 and B4 which are conducted under similar conditions show very similar responses as shown in Figure 6.90.

Tests on 1/60-scale models at zero standoff distance (A3, A4, A7) also show a response similar to tests at 2' standoff (A1, A2, A5, A6) as shown in Figures 6.91 and 6.92. Test A7 shows slightly larger peak compressive strains than test A4. Figure 6.93 shows flexural responses in tests on 1/82-scale models at zero standoff distance. The do not show similar responses as would be expected and the peak strains are larger than those in tests on 1/60-scale models at zero standoff distance.

Axial strain curves in the bottom slabs for tests on 1/60-scale models (Figures 6.94 and 6.95) are very similar to the axial strain curves in the top slab for the same tests. The reason may be that the axial strains in the top

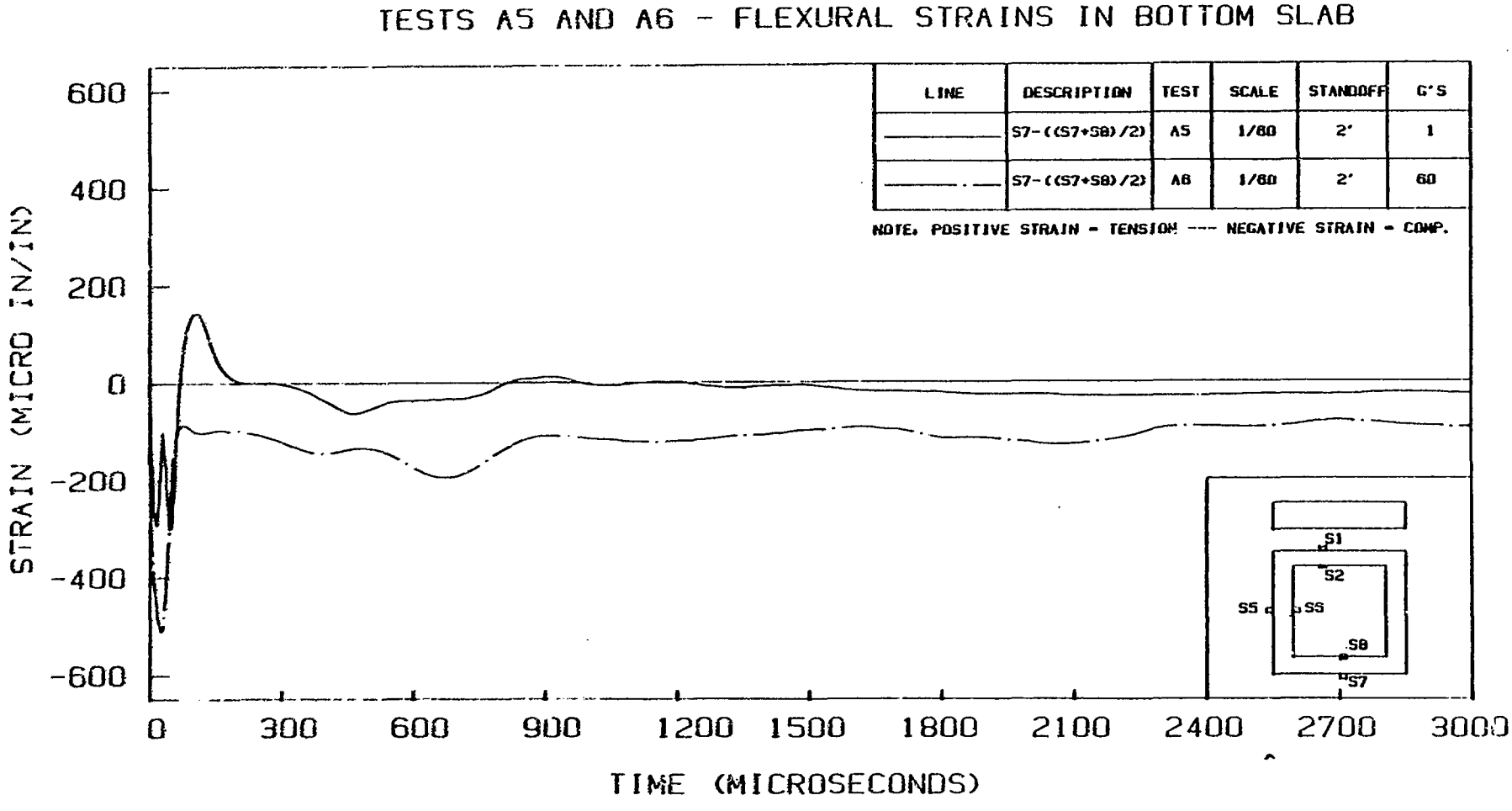

Figure 6.88. Flexural Strains in the Bottom Slab for Tests A5 and A6

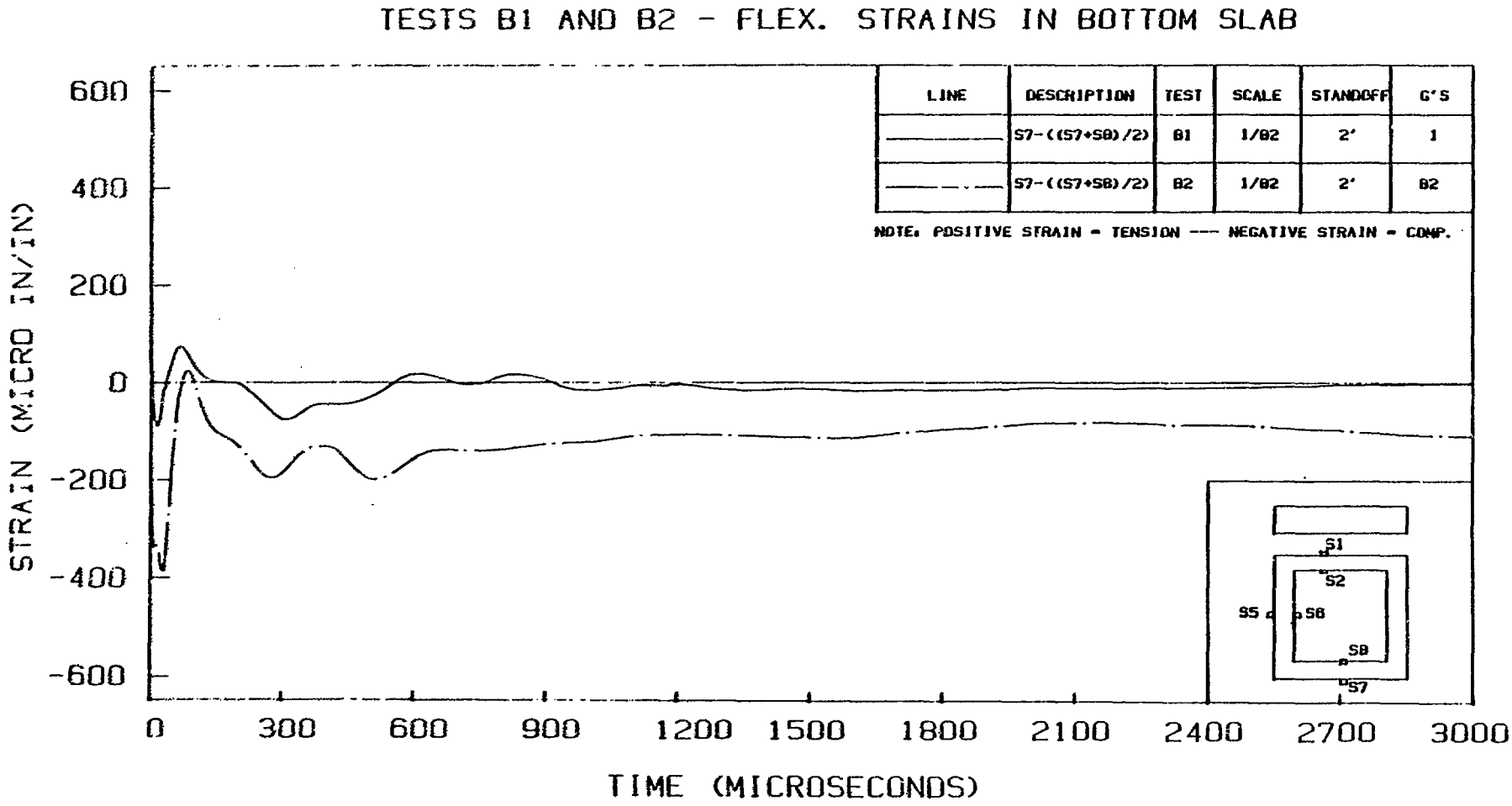

Figure 6.89. Flexural Strains in the Bottom Slab for Tests B1 and B2

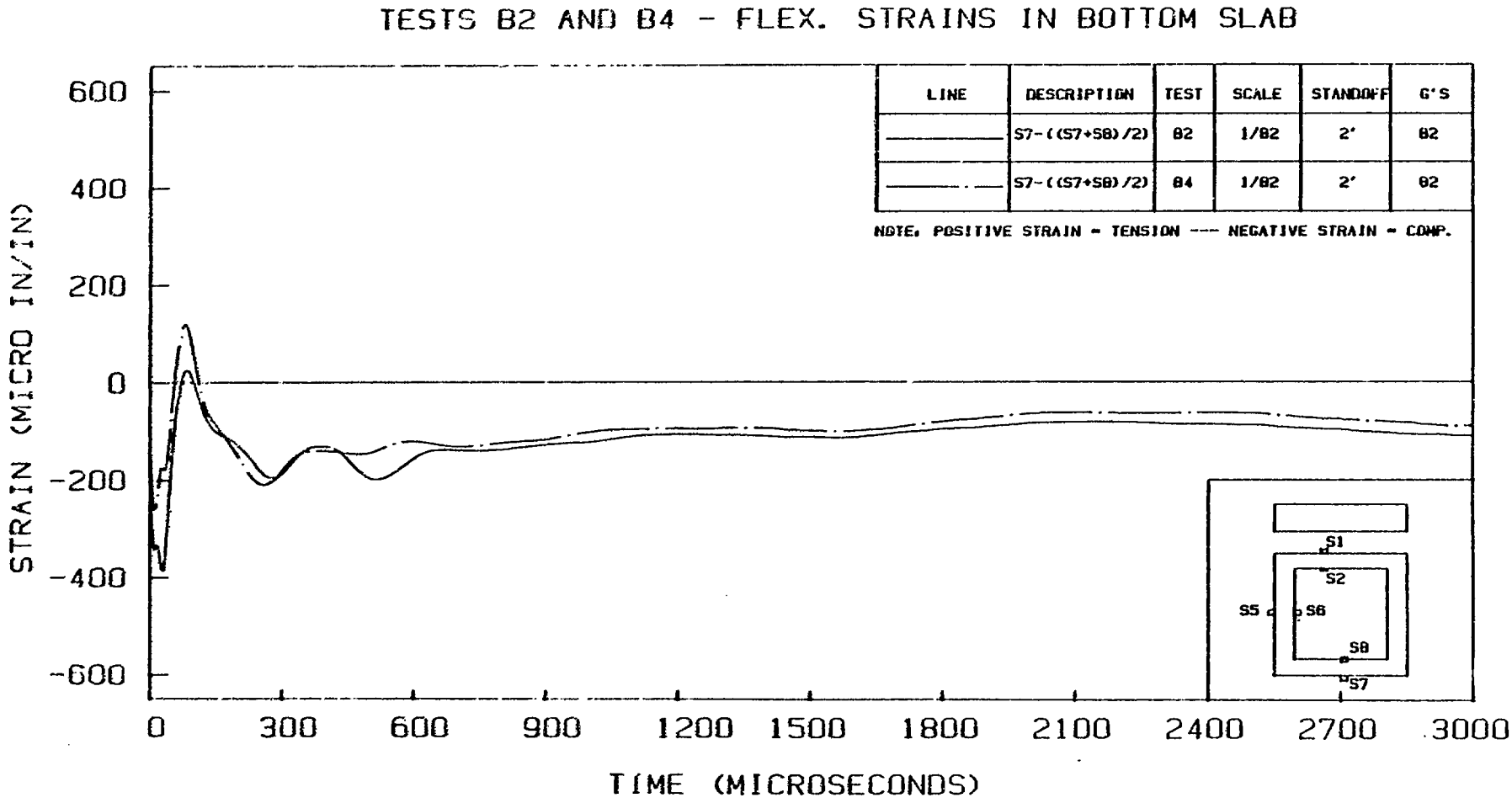

Figure 6.90. Flexural Strains in the Bottom Slab for Tests B2 and B4

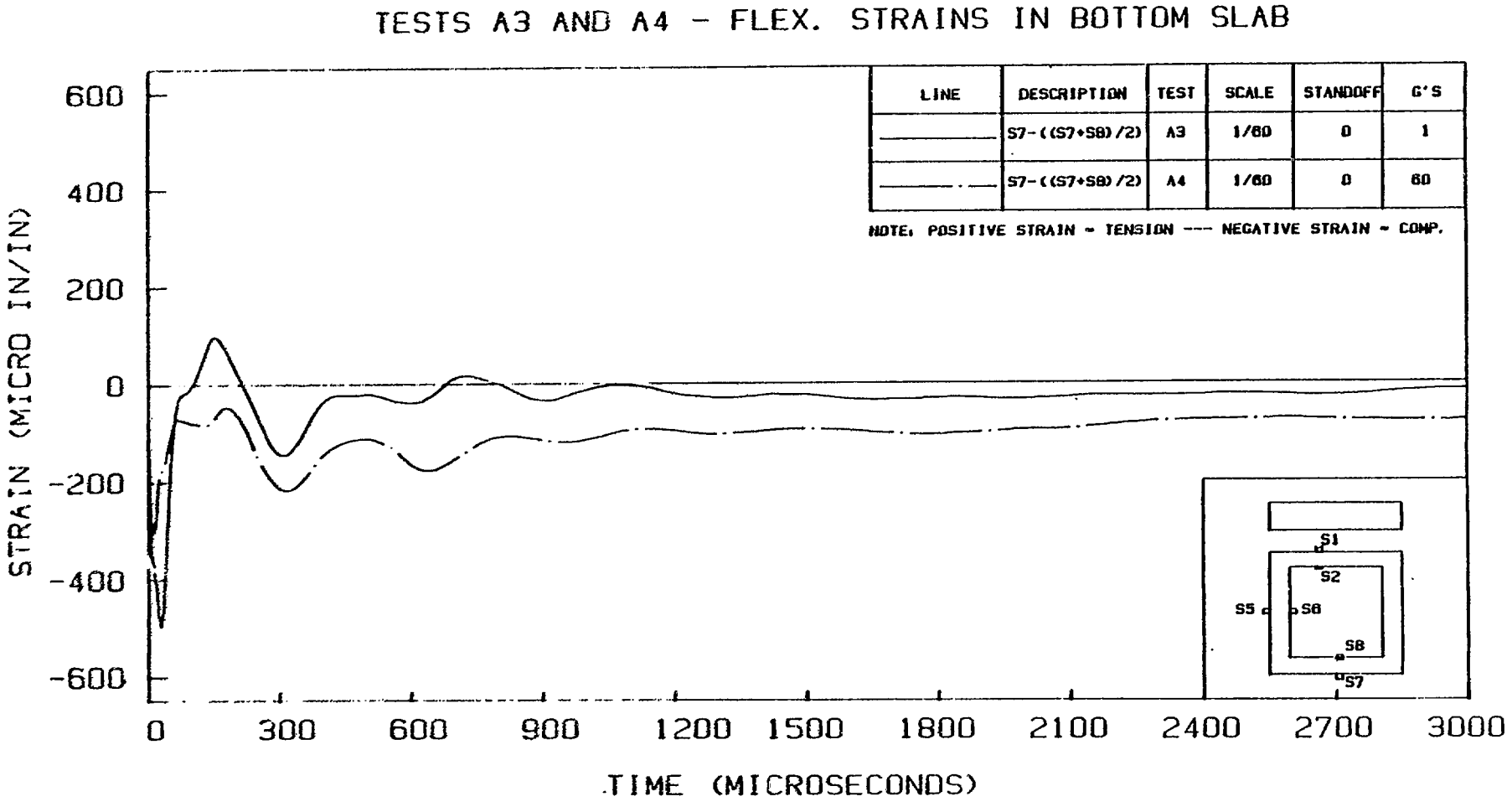

Figure 6.91. Flexural Strains in the Bottom Slab for Tests A3 and A4

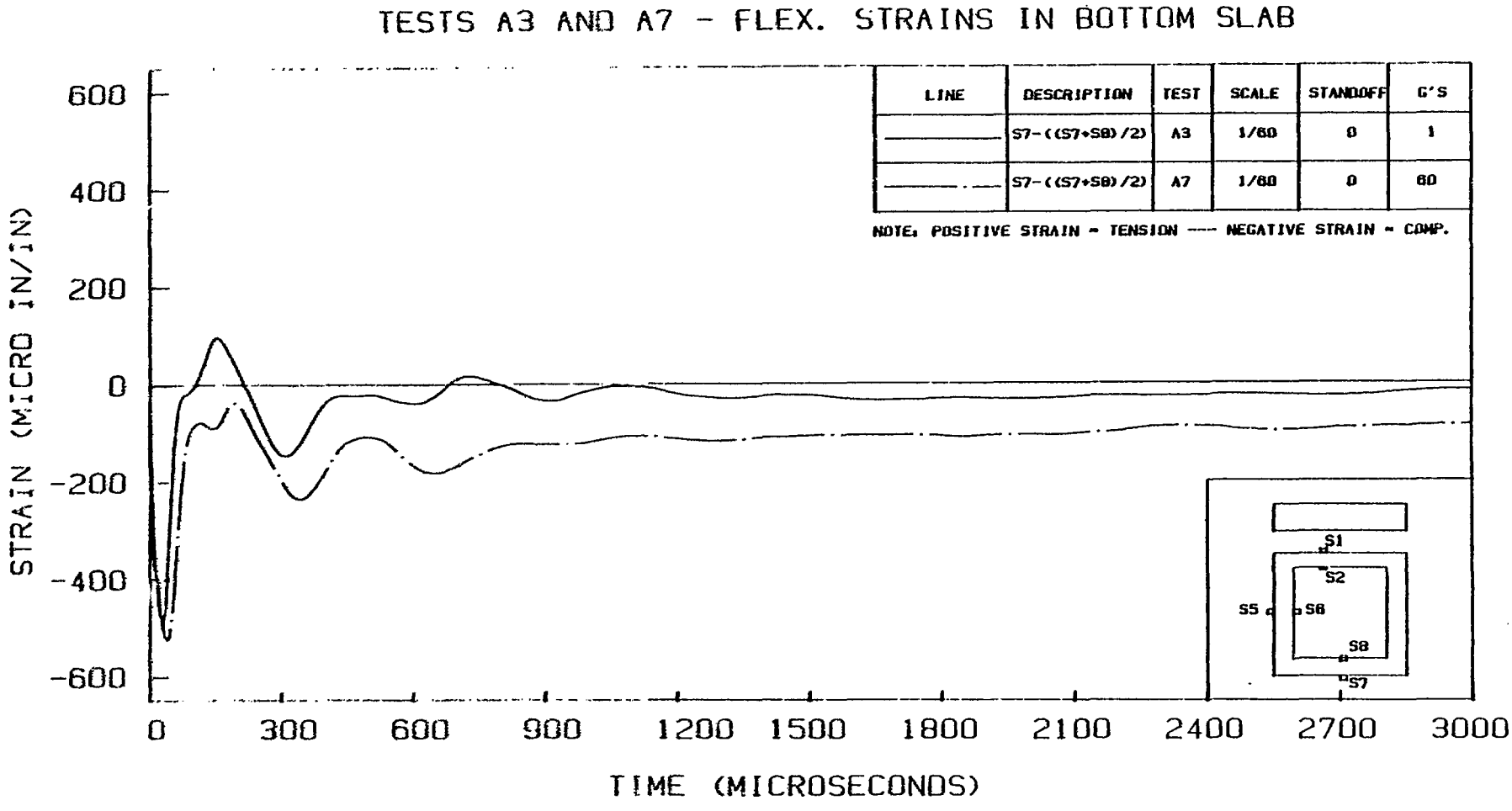

Figure 6.92. Flexural Strains in the Bottom Slab for Tests A3 and A7

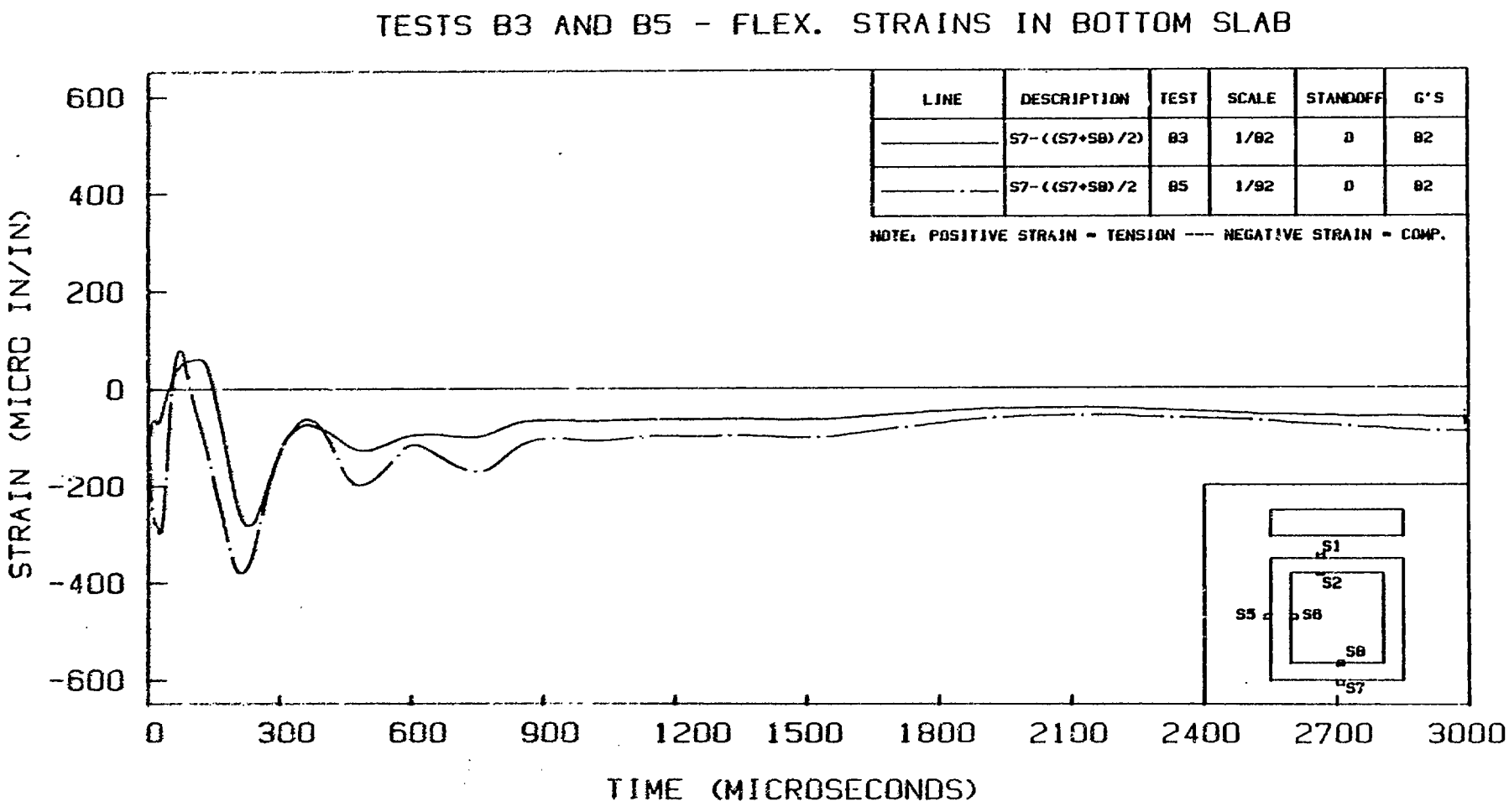

Figure 6.93. Flexural Strains in the Bottom Slab for Tests B3 and B5

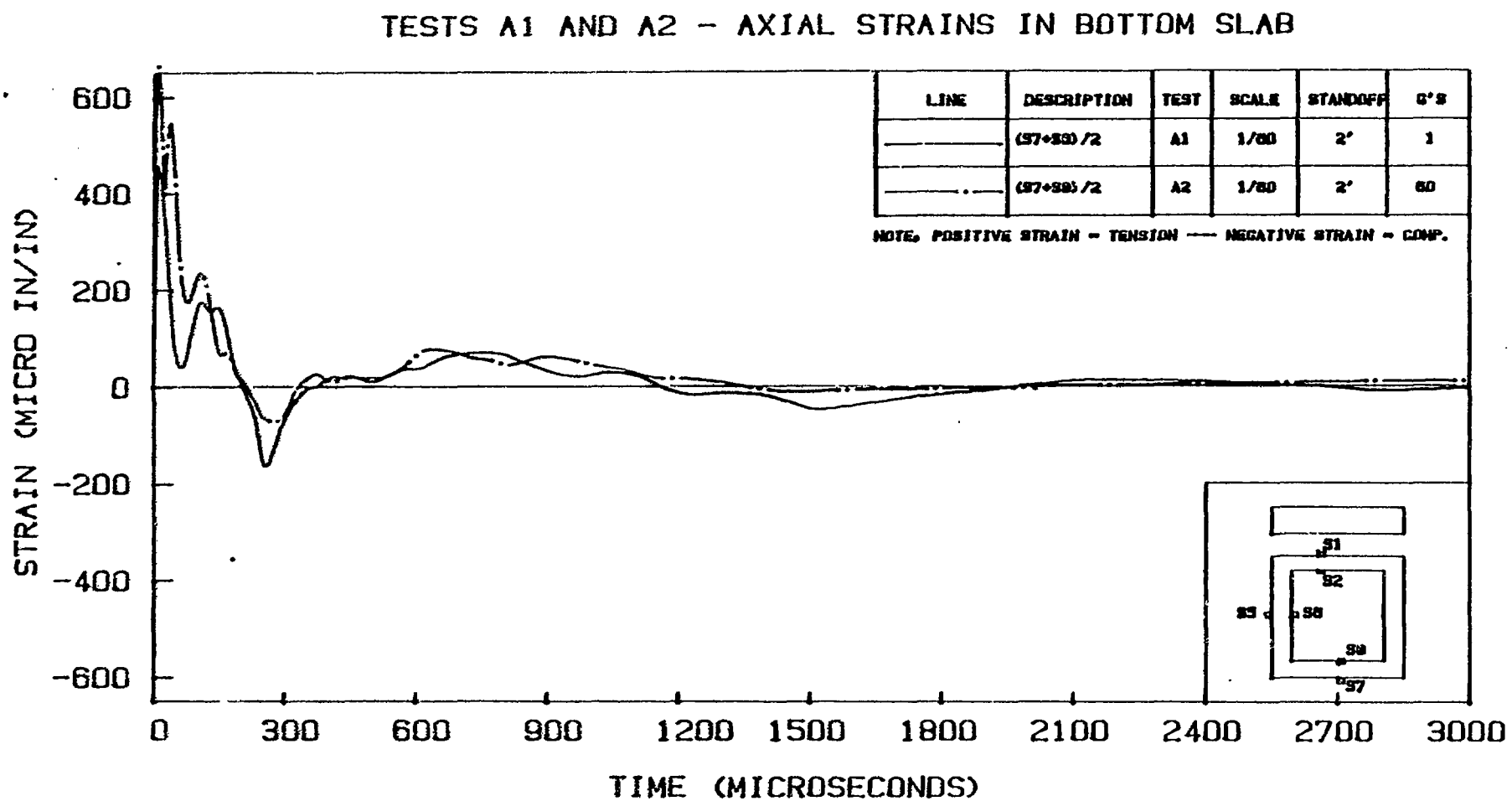

Figure 6.94. Axial Strains in the Bottom Slab for Tests A1 and A2

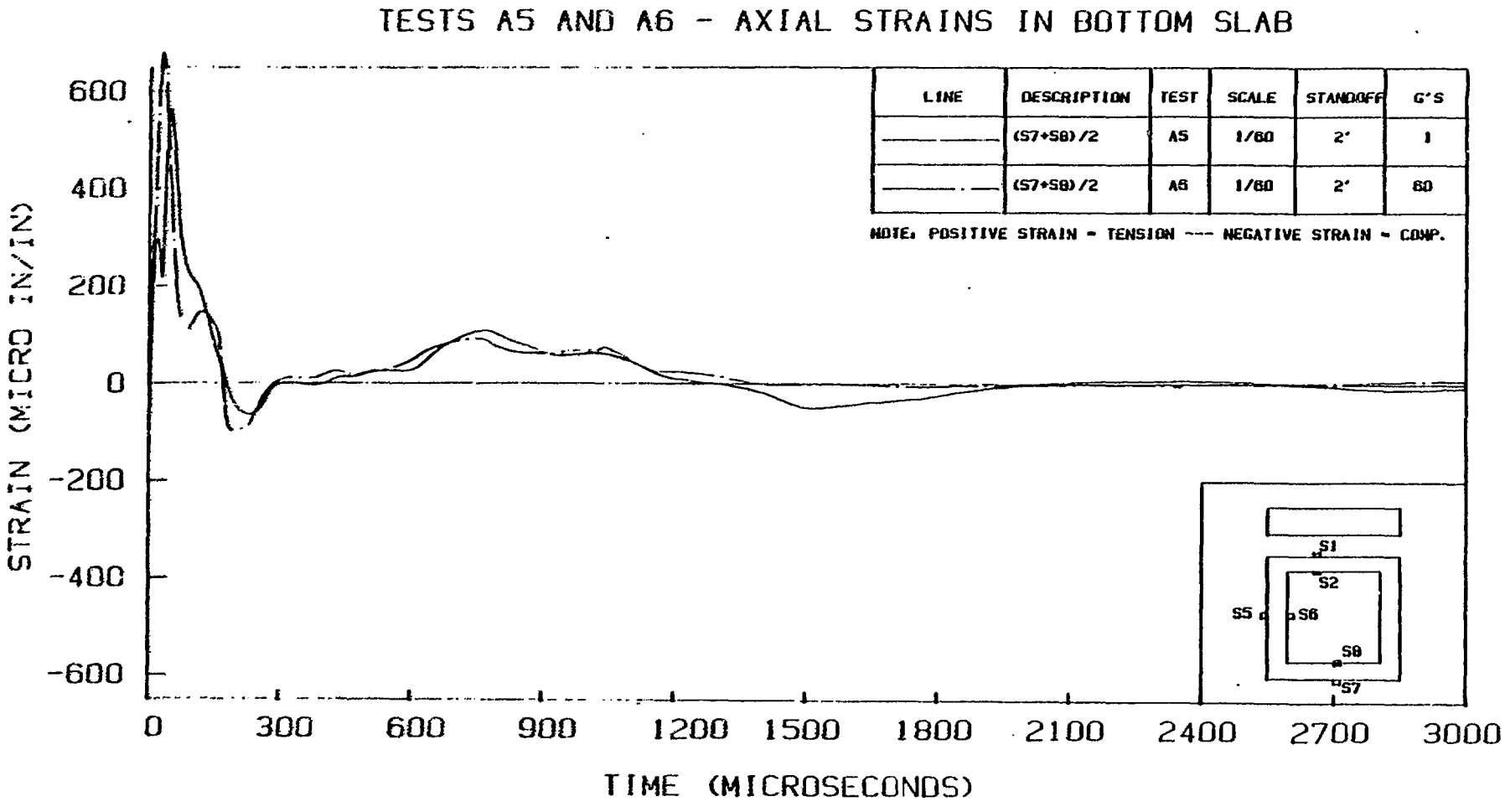

Figure 6.95. Axial Strains in the Bottom Slab for Tests A5 and A6

slab are transferred to the bottom slab through shear waves in the side walls.

Tests on 1/82-scale models at 2' standoff show very little axial strains in the bottom slab (Figures 6.96 and 6.97). Figures 6.98 to 6.100 show axial strains in the bottom slab for tests A3, A4, A7, B3 and B5.

In summary, tests at 60 or 82 g's show substantially higher flexural strains in the top slab, the side wall, and the bottom slab of the box structure as compared to tests at 1g. Again, these facts illustrate the significance of gravity stresses (centrifuge testing) in the response of these structures.

6.4 Velocities

Velocities at the center of the top slab and the side wall are calculated by integrating the responses of Accelerometers A1 and A2, respectively. Because of the observed drift in the accelerometer responses prior to the explosions, the digital zero on the accelerometer responses does not indicate zero acceleration. Therefore, a reference voltage (zero acceleration) has to be established for each accelerometer response. This is equivalent to shifting the accelerometer response by a constant value to account for the drift. The reference voltage is determined through the process of trial and error. The selected reference voltage which results in the convergence of velocity and displacement responses to zero after a relatively long

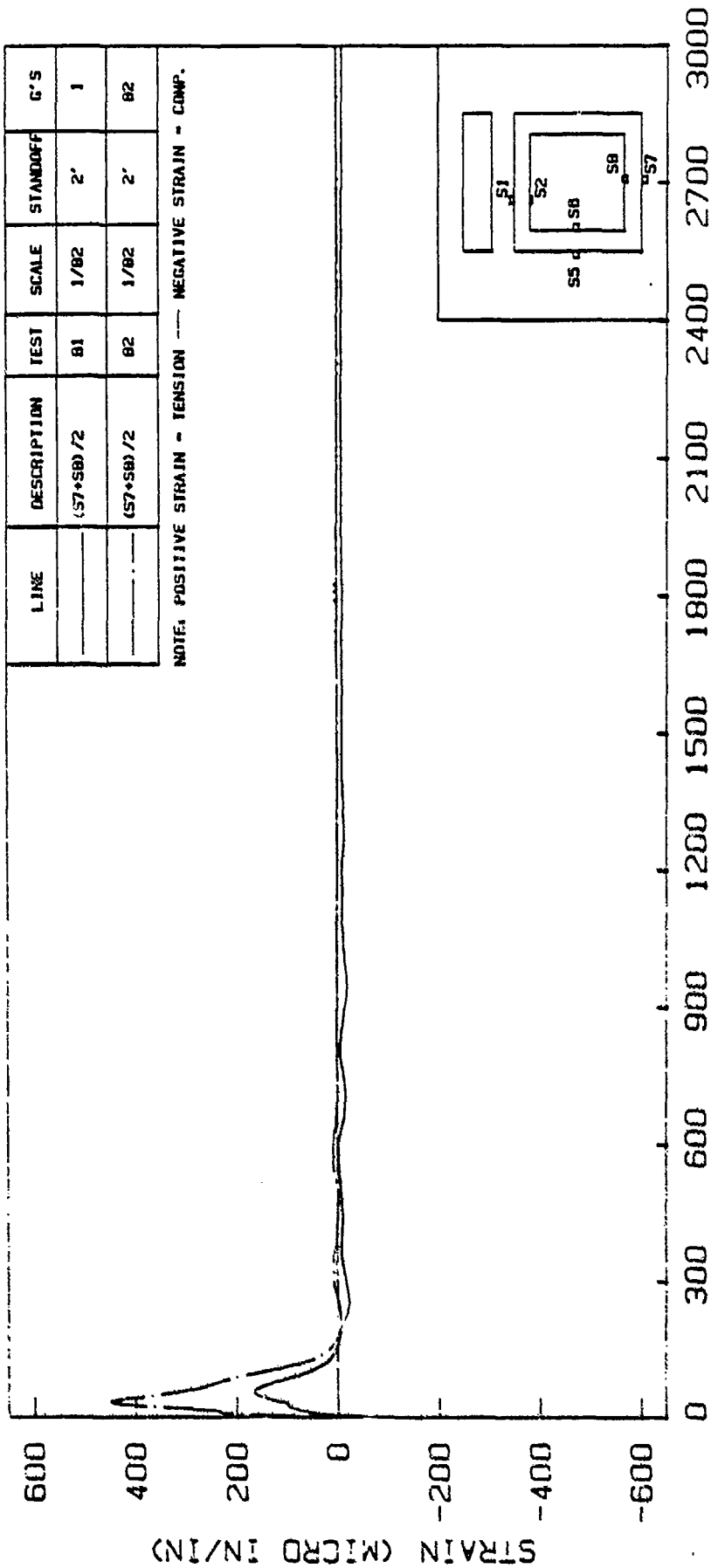

Figure 6.96. Axial Strains in the Bottom Slab for Tests B1 and B2

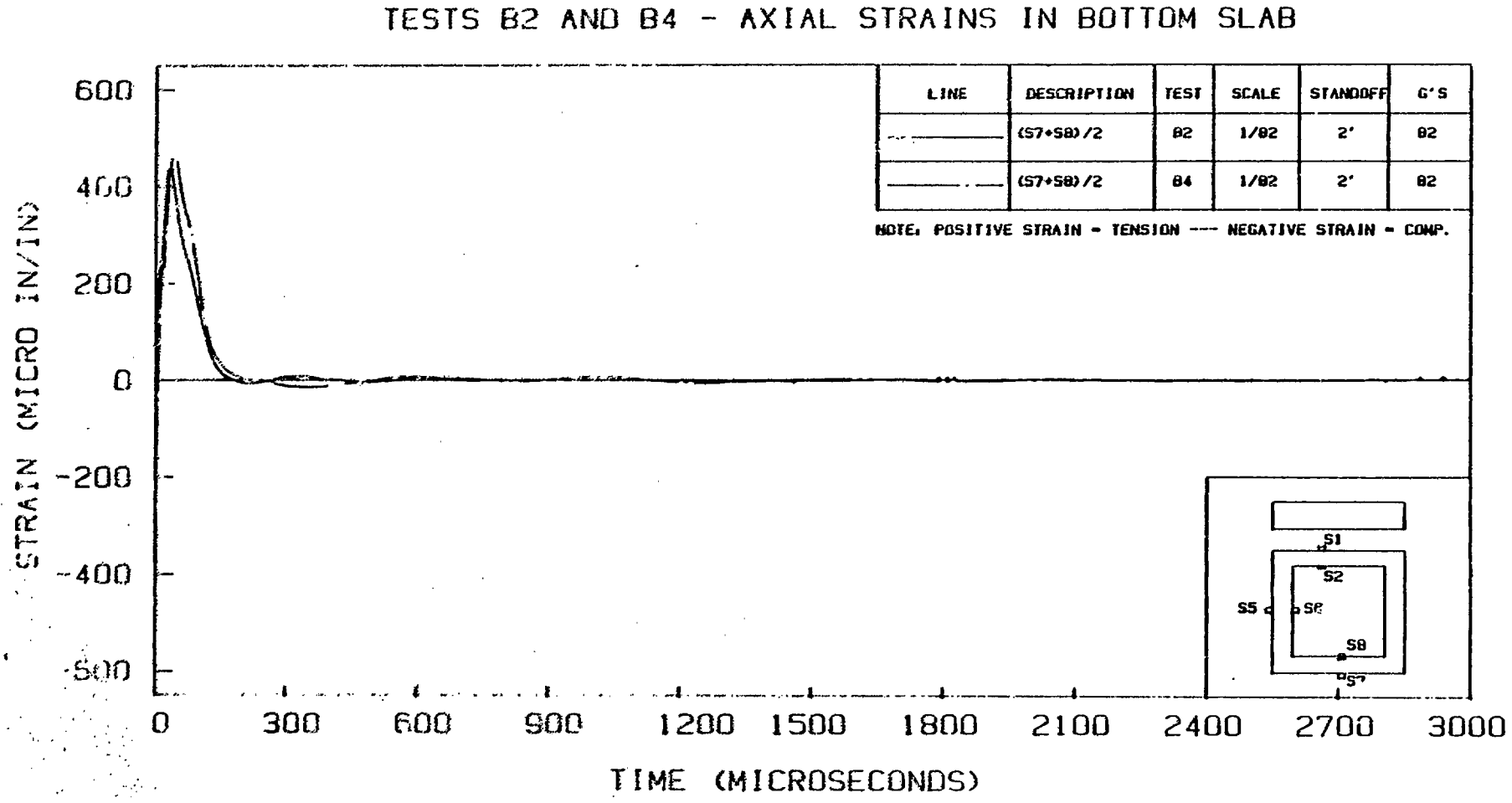

Figure 6.97. Axial Strains in the Bottom Slab for Tests B2 and B4

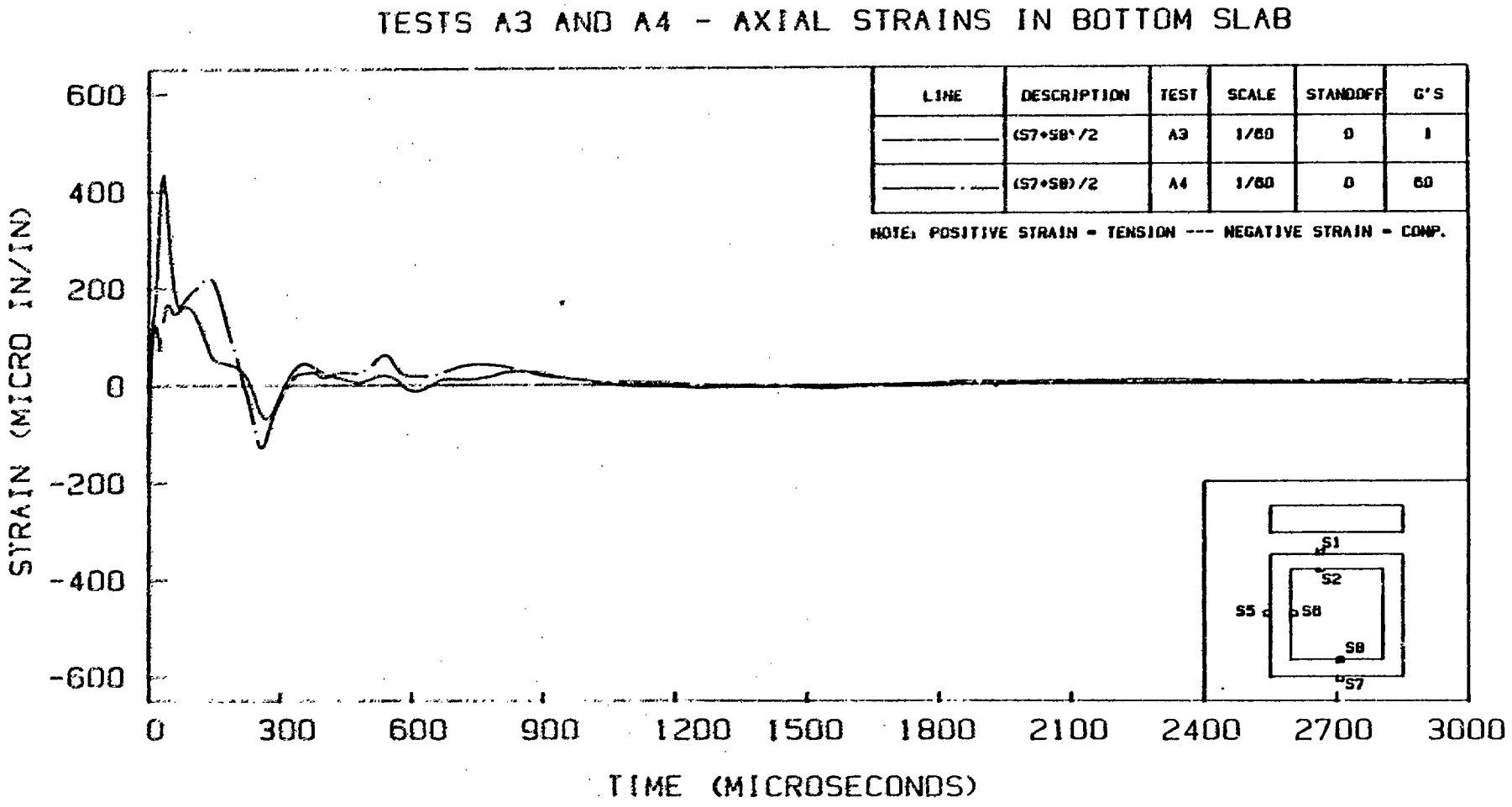

Figure 6.98. Axial Strains in the Bottom Slab for Tests A3 and A4

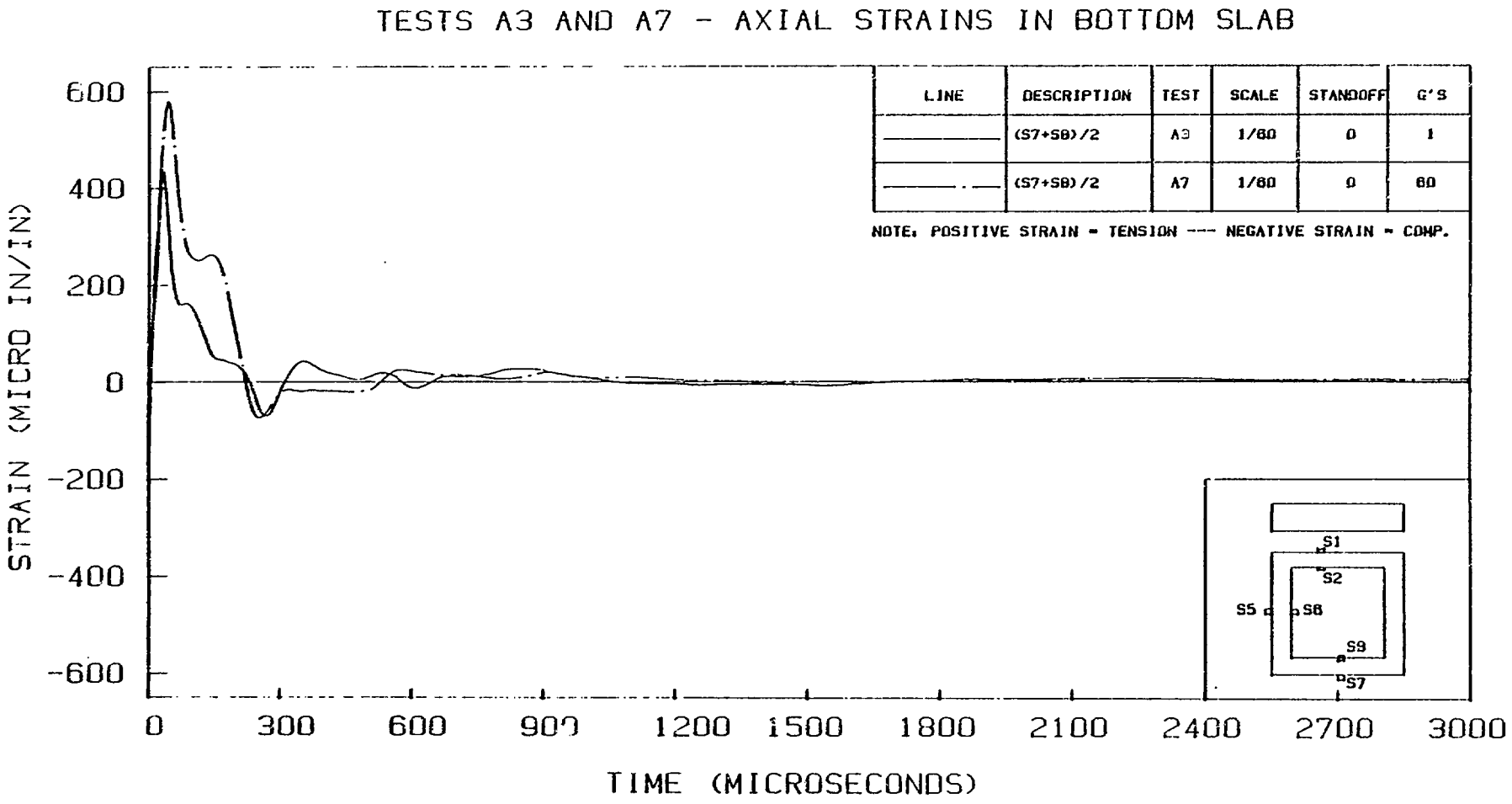

Figure 6.99. Axial Strains in the Bottom Slab for Tests A3 and A7

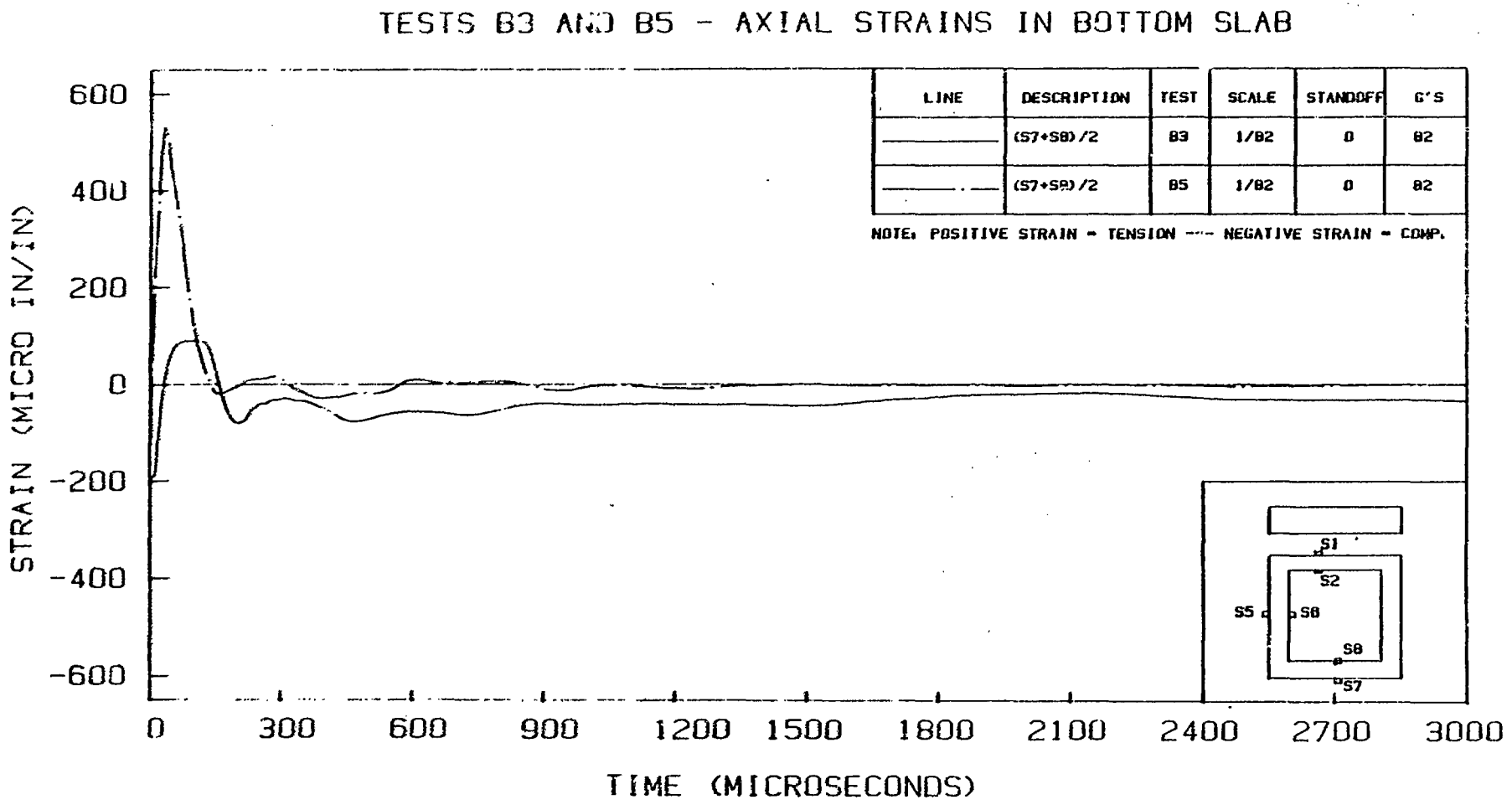

Figure 6.100. Axial Strains in the Bottom Slab for Tests B3 and B5

period of time (5 to 10 ms) is a valid reference point for each accelerometer response.

The first 80 μseconds in the response of each accelerometer was set equal to zero so that the effect of explosion on the instrumentation would not be integrated. Positive velocity is directed downward for the top slab, and inward for the side wall.

6.4.1 Velocity V1

Velocity V1 (top slab) is obtained by integrating the response of accelerometer A1. Figure 6.101 shows Velocity V1 responses in tests A1 (2' standoff, 1g) and A2 (2' standoff, 60 g's). The peak velocity in test A1 (17 in/sec) is larger than the peak velocity in test A2 (14 in/sec) by 21%. The duration of positive velocity in test A1 (2400 μseconds) is larger than the corresponding time in test A2 (1150 μseconds) by 109%. Velocity V1 in test A2 also has a faster arrival time for the first peak, which is expected considering the observed faster arrival time of the pressure wave on the top slab in test A2 (see Figure 6.7). The smaller peak velocity in test A2 may be attributed to larger confinement of the structure by the soil at high gravities. Figure 6.102 shows a very similar type of response for tests A5 (2' standoff, 1g) and A6 (2' standoff, 60 g's).

Figure 6.103 shows Velocity V1 responses for test B1 (2' standoff, 1g) and B2 (2' standoff, 82 g's). The general

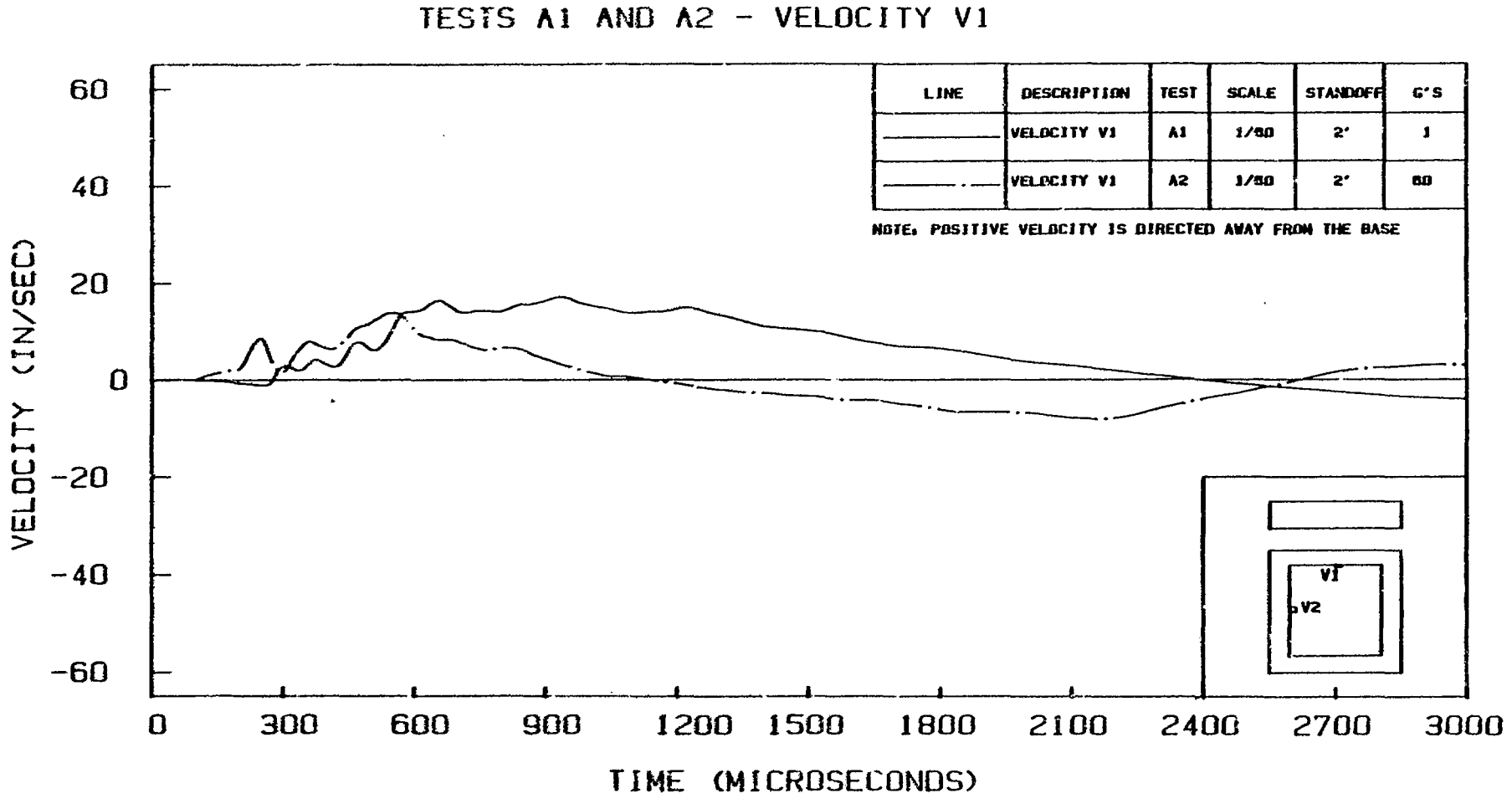

Figure 6.101. Velocity V1 in Tests A1 and A2

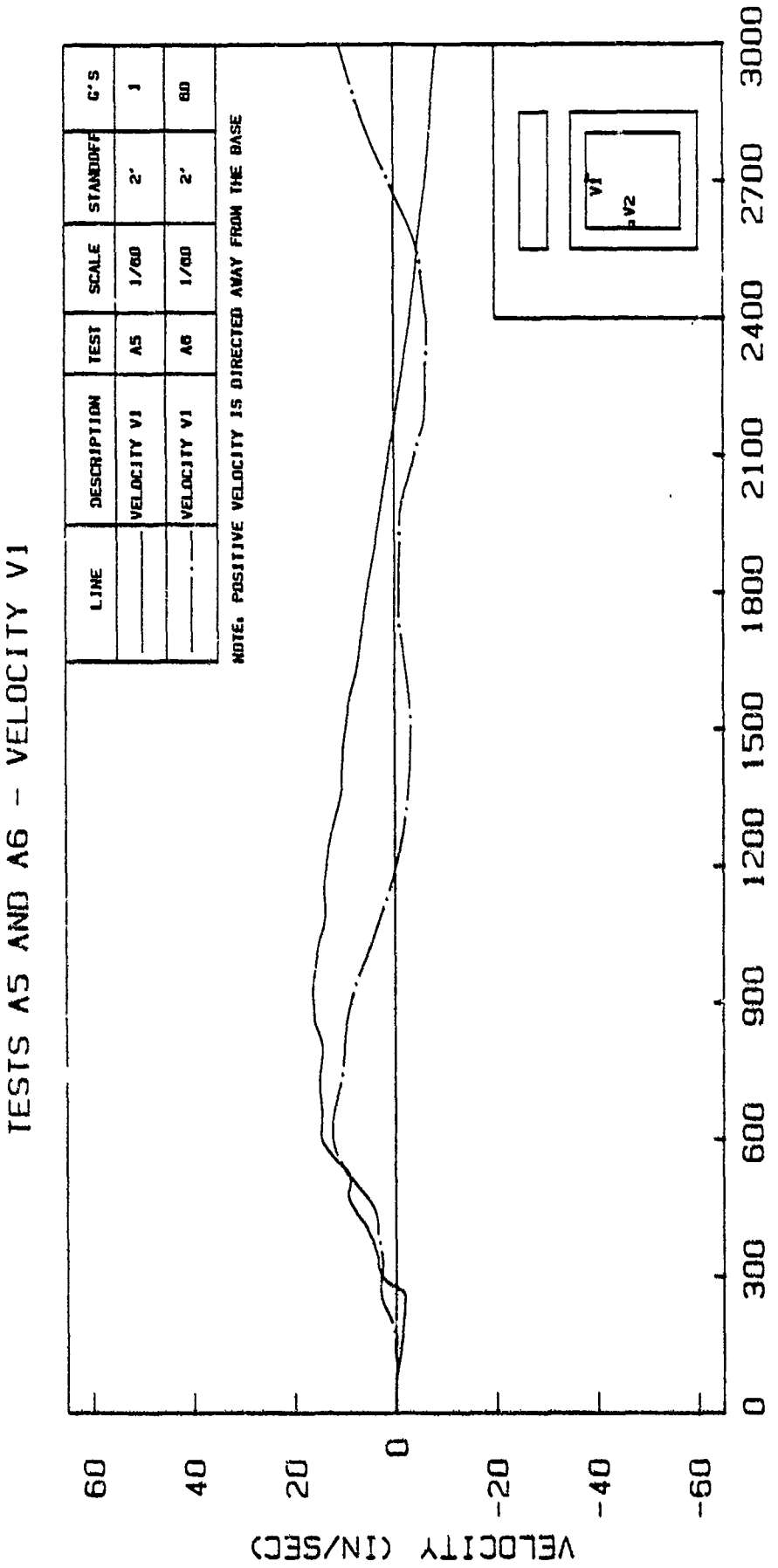

Figure 6.102. Velocity V1 in Tests A5 and A6

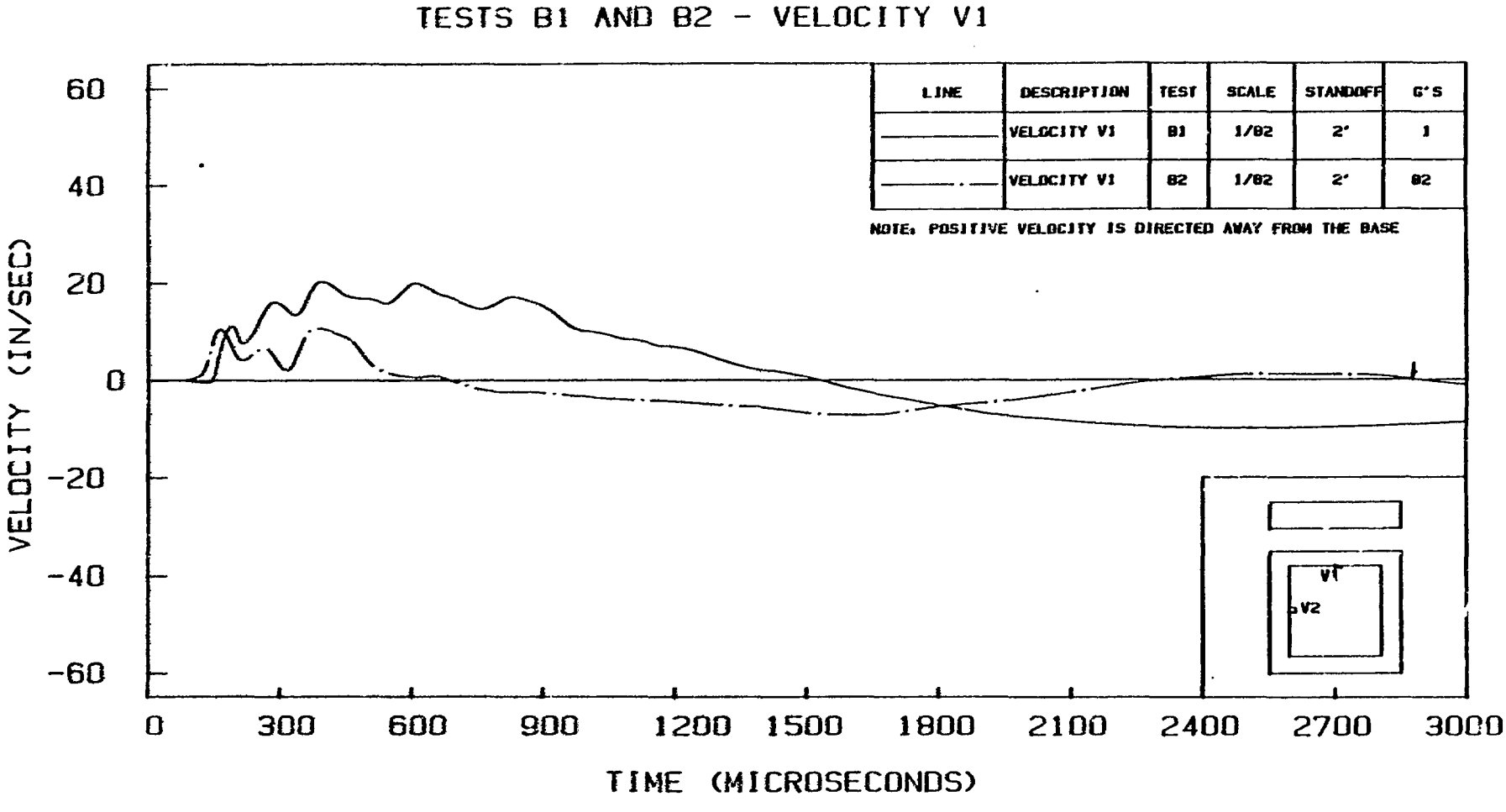

Figure 6.103. Velocity V1 in Tests B1 and B2

shapes of the two curves are similar to the corresponding responses in tests A1, A2, A5, and A6 (Figures 6.101 and 6.102). Based on the scaling relationships (Table 2.3), peak velocities in comparable tests on 1/60- and 1/82-scale models should be equal. However, specific times in tests on 1/82-scale models should be smaller than the corresponding tests on 1/60-scale models by a factor of 60/82. Figure 6.103 shows that the peak velocity in test B1 is 20 in/sec which is slightly larger than the peak velocities in comparable tests A1 and A5 (17 in/sec). The peak velocity in test B2 (11 in/sec) is slightly smaller than the peak velocity in test A2 (14 in/sec) and test A6 (13 in/sec). The adjusted time for the duration of positive velocity in test B1 (1536 x 82/60 = 2100 μseconds) is smaller than the corresponding times in tests A1 (2400 μseconds) and A5 (2170 μseconds) by 12% and 3%, respectively. The adjusted time for the duration of positive velocity in test B2 (696 x 82/60 = 951 μseconds) is also smaller than the corresponding times in tests A1 (1150 μseconds) and A2 (1200 μseconds) by 17% and 21%, respectively.

Figure 6.104 shows the Velocity V1 responses in tests B2 and B4. These two tests were conducted under identical conditions and should yield similar results. The general shapes of the two curves and the magnitudes of the peak positive velocities are in close agreement.

Figure 6.105 shows the Velocity V1 responses in tests A3 and A4. The peak velocity in test A3 (26 in/sec) is larger

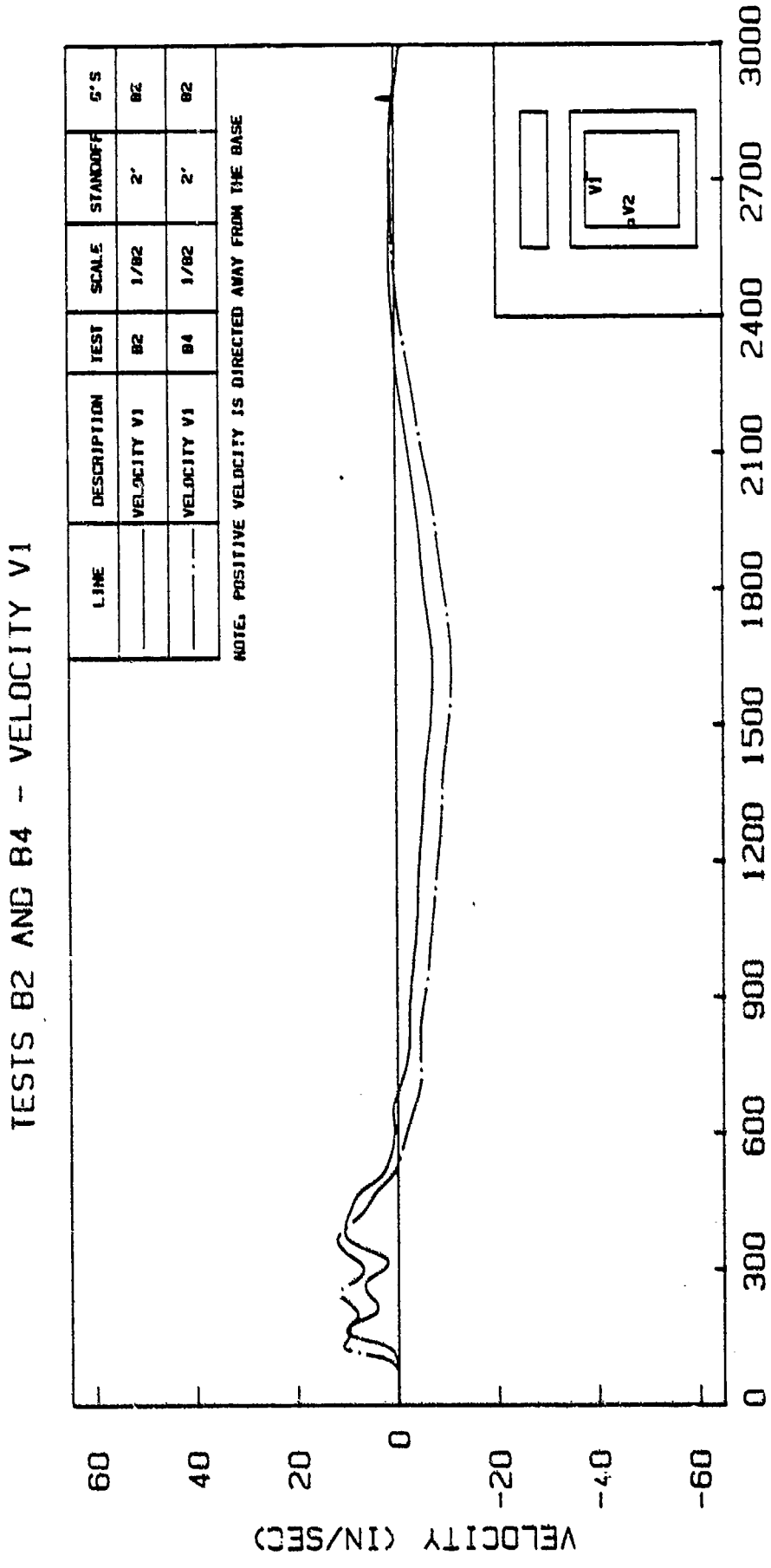

Figure 6.104. Velocity V1 in Tests B2 and B4

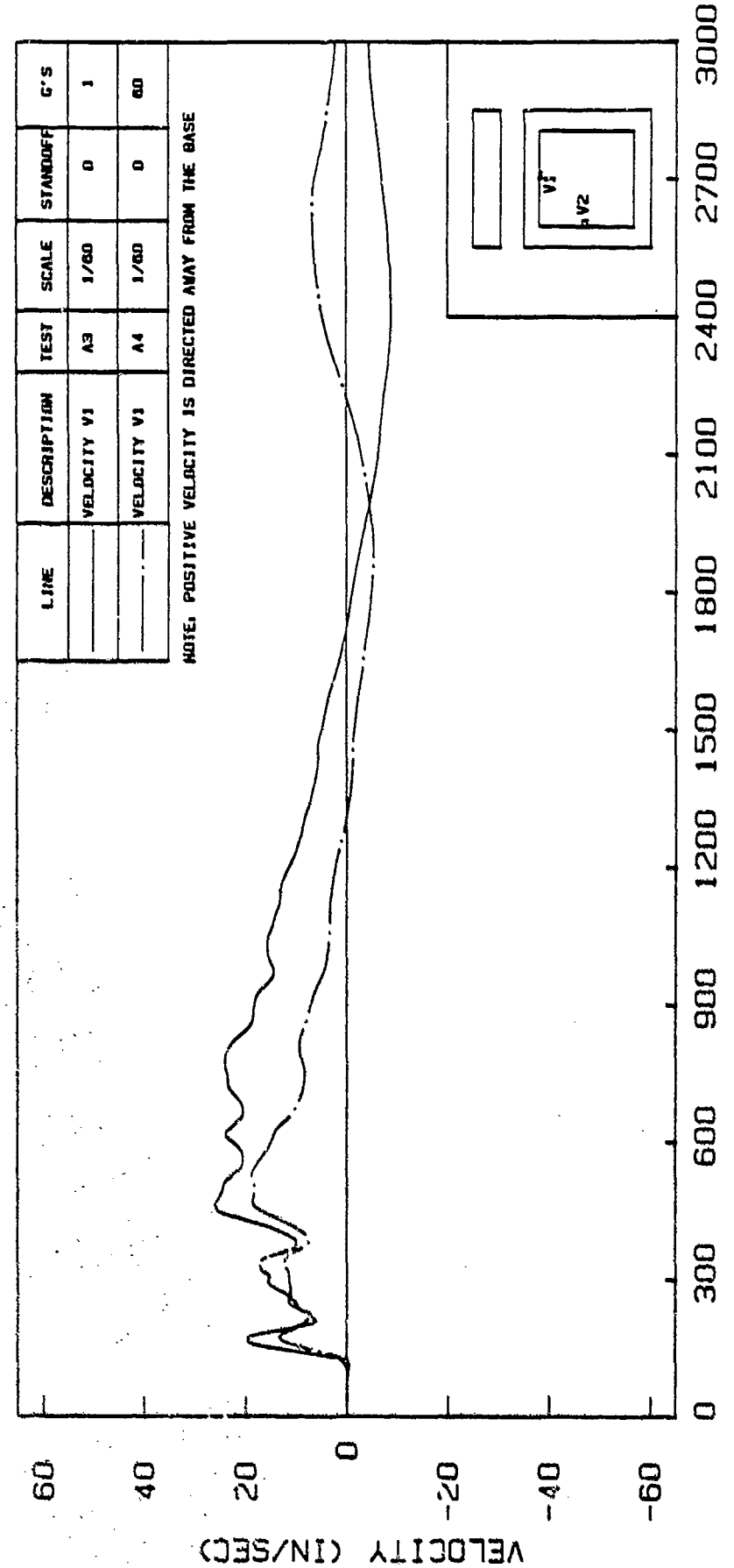

Figure 6.105. Velocity V1 in Tests A3 and A4

than the peak velocity in test A4 (19 in/sec) by 37%. The duration of positive velocity in test A3 (1730 μseconds) is also larger than the corresponding time in test A4 (1310 μseconds) by 32%. Figure 6.106 shows Velocity V1 responses in tests A4 and A7. Tests A7 and A4 were conducted under similar conditions (except for the condition of burster slab explained earlier). Test A7 shows slightly smaller peak velocities as compared to test A4.

Figure 6.107 shows Velocity V1 responses in tests B3 and B5. These two tests are also comparable to tests A4 and A7 (Figure 6.106) except for the size of the model (1/82 versus 1/60). Although, the peak velocities for the 1/82-scale models are larger, the general shape of the response curves are very similar considering that the times in 1/82-scale models are smaller than the corresponding times in 1/60-scale models by a factor of 60/82. For example, the adjusted arrival time of the third peak velocity in test B3 (342 x 82/60 = 467 μseconds) is relatively close to the corresponding arrival time in test A4 (528 μseconds).

In general, for tests conducted on 1/60 and 1/82-scale models, the peak velocities (V1) in tests at 1g are larger than the peak velocities in corresponding tests at 60 and 82 g's. Moreover, the general shape of velocity responses differ significantly for high-gravity and 1g tests. These results are believed to be due to larger confinement of the structure by soil in high-gravity tests. This fact illustrates the significance of gravity stresses

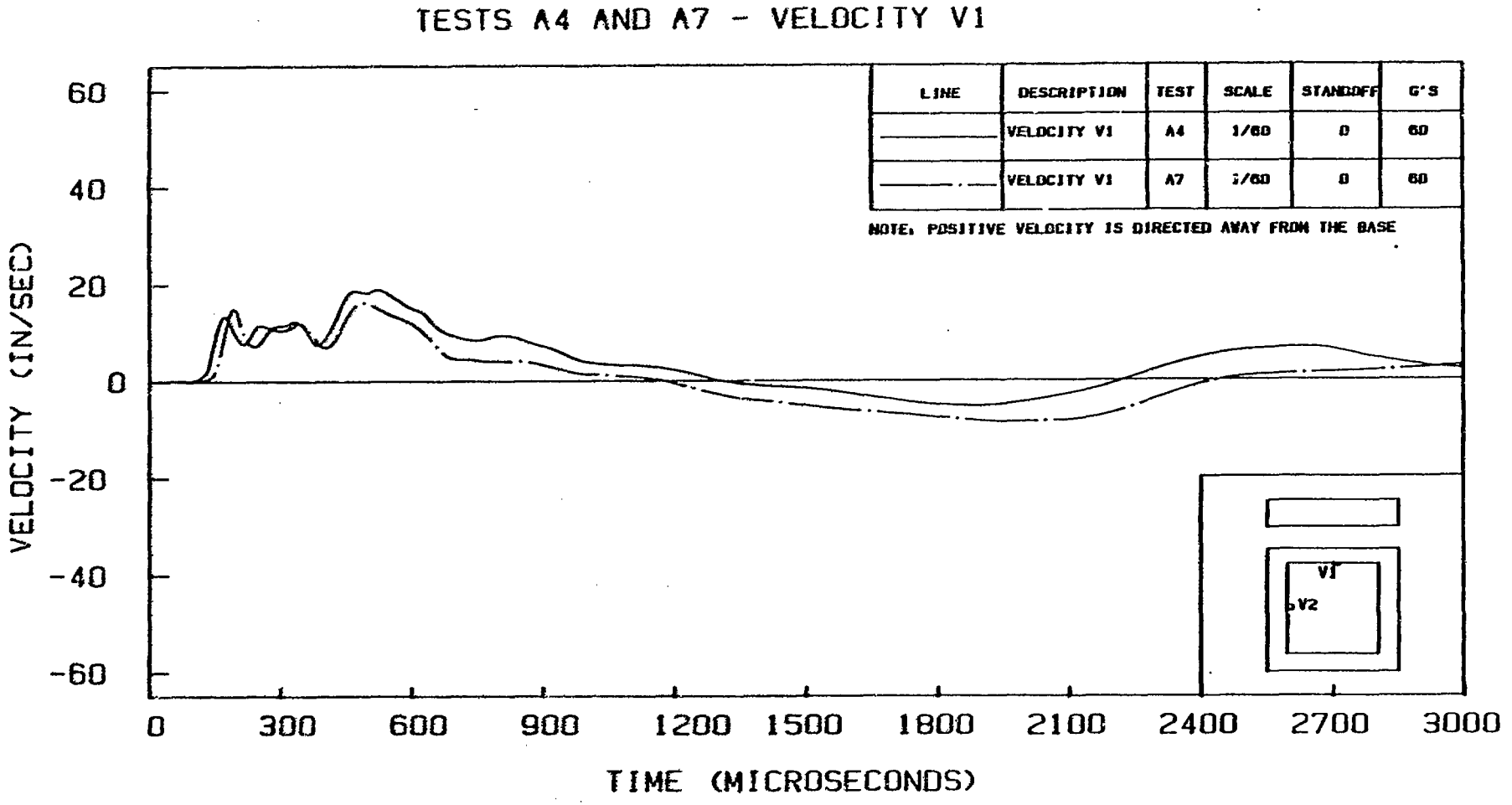

Figure 6.106. Velocity V1 in Tests A4 and A7

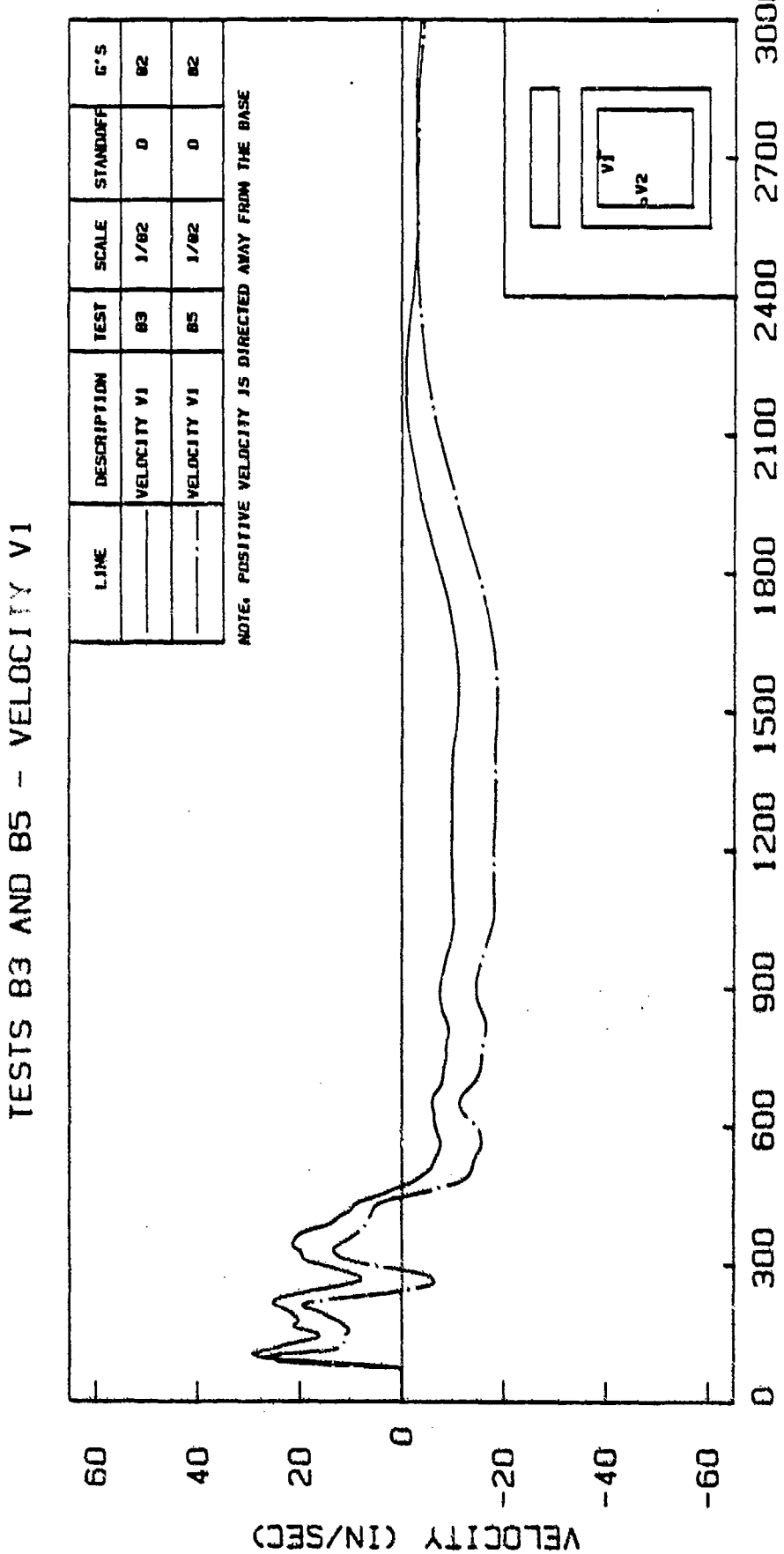

Figure 6.107. Velocity V1 in Tests B3 and B5

(centrifuge testing) with respect to the structural response of such systems. A high degree of repeatability of velocity responses is evident for tests conducted under similar conditions.

6.4.2 Velocity V2

Velocity V2 (side wall) is obtained by integrating the response of Accelerometer A2. Figure 6.108 shows Velocity V2 responses in tests A1 and A2. The magnitude of peak velocities (4 in/sec) is much smaller than the velocity peaks on the top slab (Figure 6.101). As expected, the velocity on the side wall is first directed outward (negative velocity). Figure 6.109 shows Velocity V2 responses in tests A5 and A6 which are in general agreement with the response in tests A1 and A2 (Figure 6.108). There was a problem with the convergence of the velocity response in test A5.

Tests B1 and B2 (Figure 6.110) show slightly different velocity responses. The peak negative velocity in test B1 has a magnitude of 6 in/sec which is larger than the corresponding peaks in tests A1 (4 in/sec) and A5 (5 in/sec). The adjusted arrival time of the peak velocity in test B1 (215 x 82/60 = 294 μseconds) is smaller than the corresponding times in tests A1 and A5 (360 μseconds). Figure 6.111 illustrates that tests B2 and B4, which were conducted under similar conditions, show very similar velocity responses.

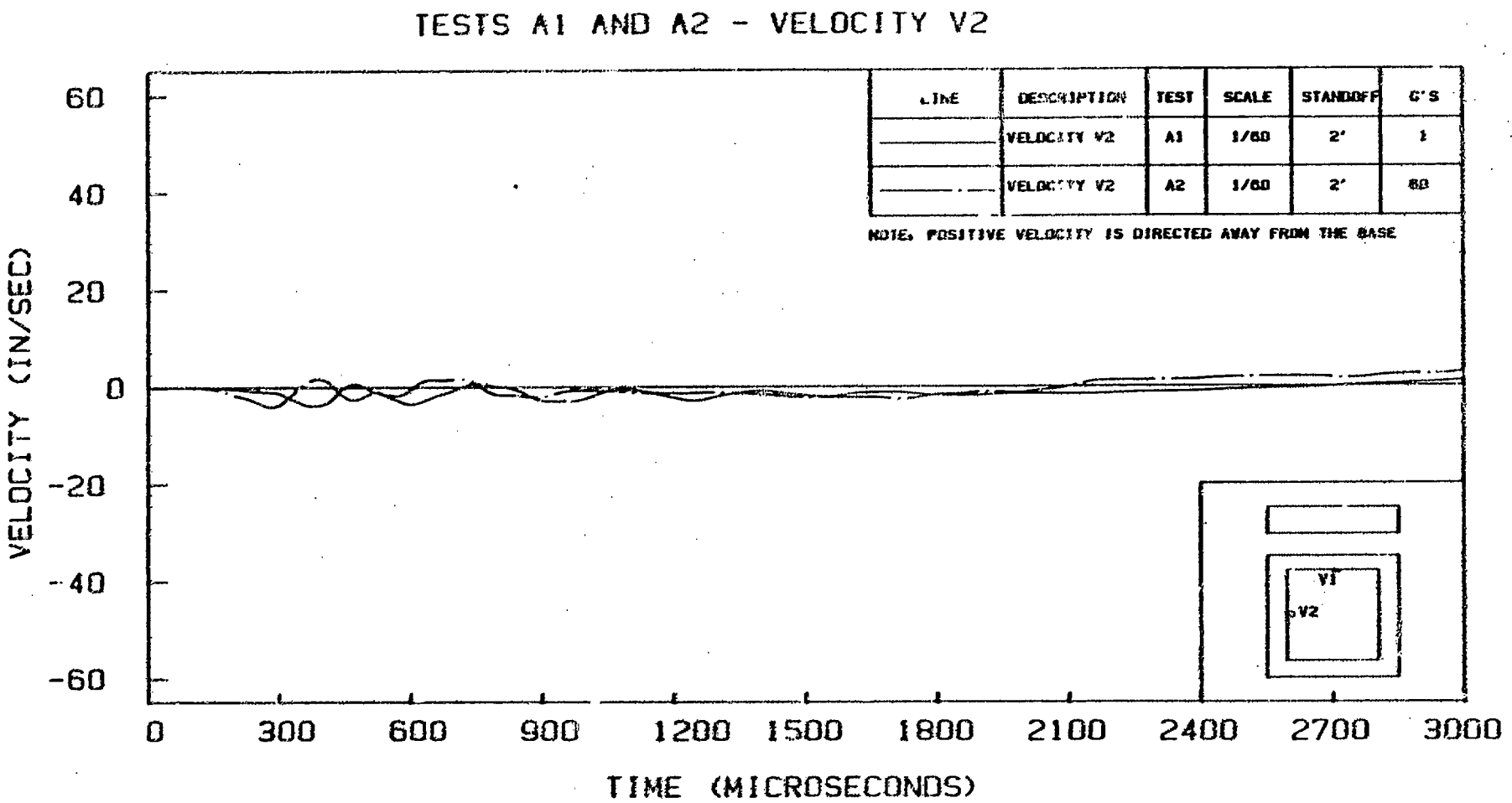

Figure 6.108. Velocity V2 in Tests A1 and A2

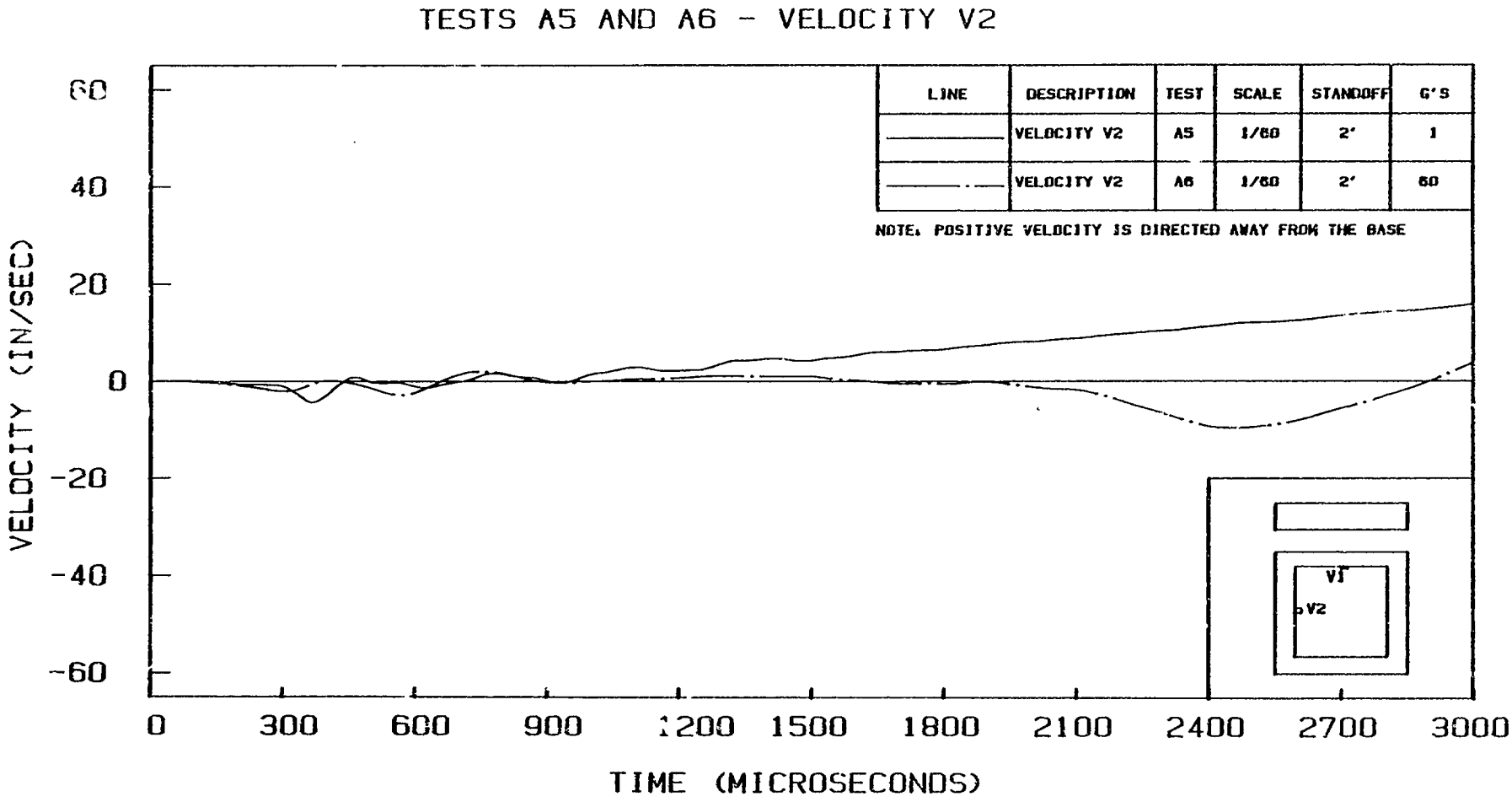

Figure 6.109. Velocity V2 in Tests A5 and A6

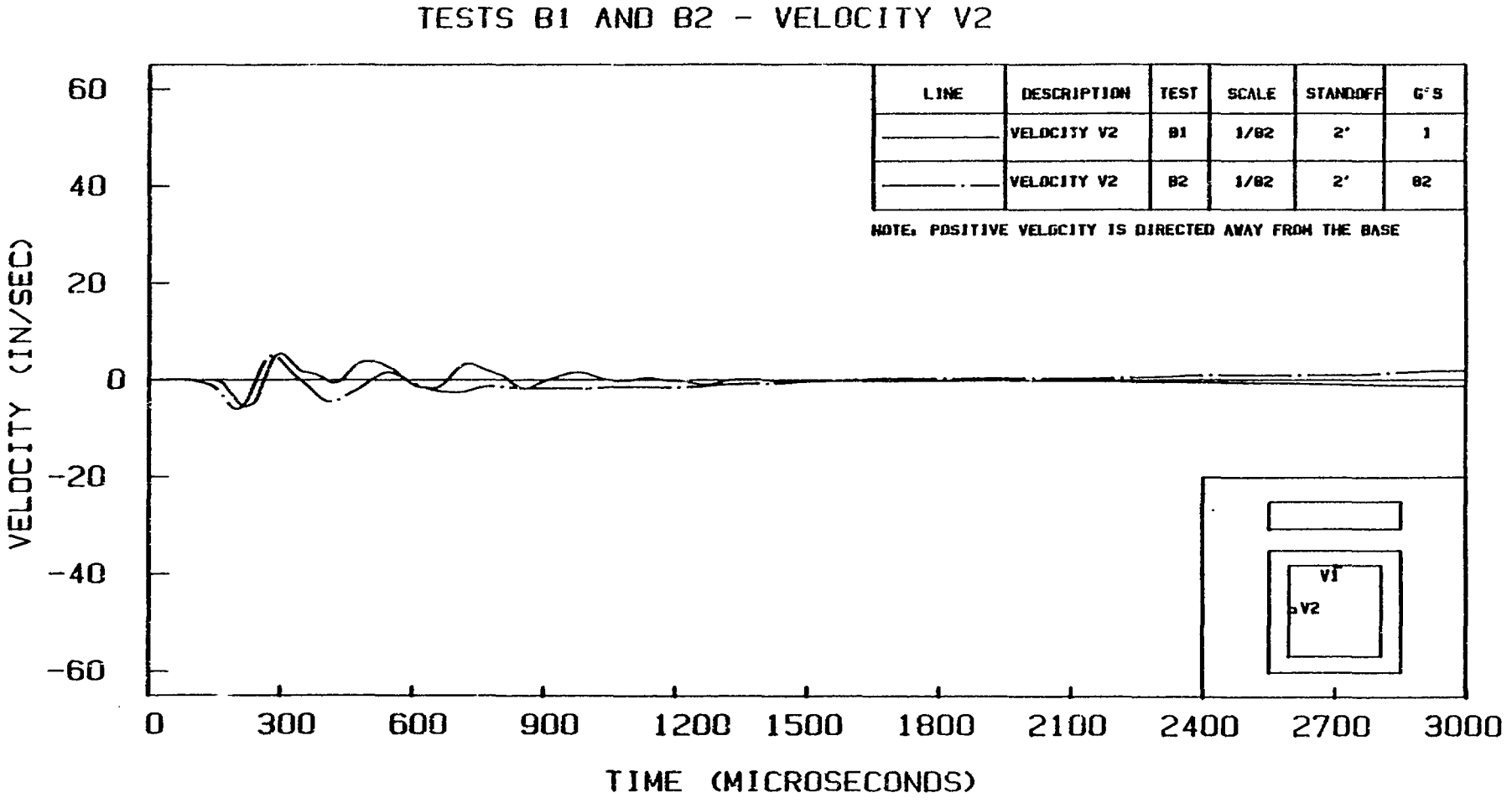

Figure 6.110. Velocity V2 in Tests B1 and B2

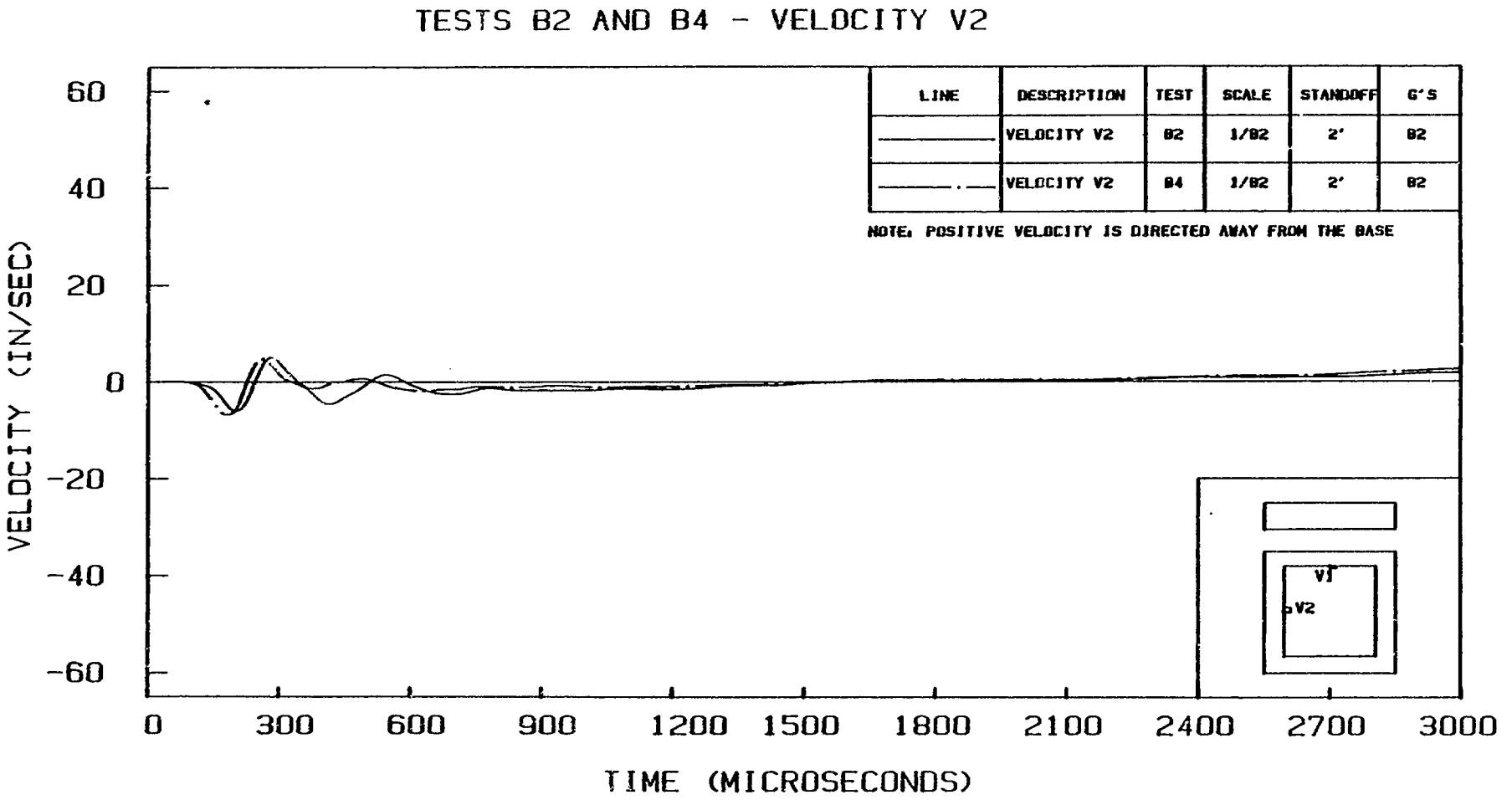

Figure 6.111. Velocity V2 in Tests B2 and B4

Figure 6.112 shows Velocity V2 responses in tests A3 and A4. The first negative peak velocity in test A3 (10 in/sec) is larger than the corresponding peak in test A4 (7 in/sec). However, the arrival times of these two peaks are very close. Velocity responses for tests A4 and A7 are shown in Figure 6.113. As expected, the two curves are very similar because the two tests were conducted under similar conditions. This type of similarity in response can also be seen in tests B3 and B5 (Figure 6.114). The first negative peak velocity in test B3 (17 in/sec) is larger than the coreesponding peak in comparable test A4 (10 in/sec). The adjusted arrival time of this first peak in test B3 (138 x 82/60 = 189 μseconds) is smaller than the corresponding time in test A4 (228 μseconds).

6.5 Displacements

Displacements at the center points of the top slab and the side wall are calculated through double integration of the responses of Accelerometers A1 and A2, respectively. Positive displacement is directed downward for the top slab and inward for the side wall.

6.5.1 Displacement D1

Displacement D1 (top slab) is obtained by integrating the response of Velocity V1. Figure 6.115 shows the Displacement D1 in tests A1 and A2. Test A1 shows a peak displacement of 0.018 in which is larger than the peak in

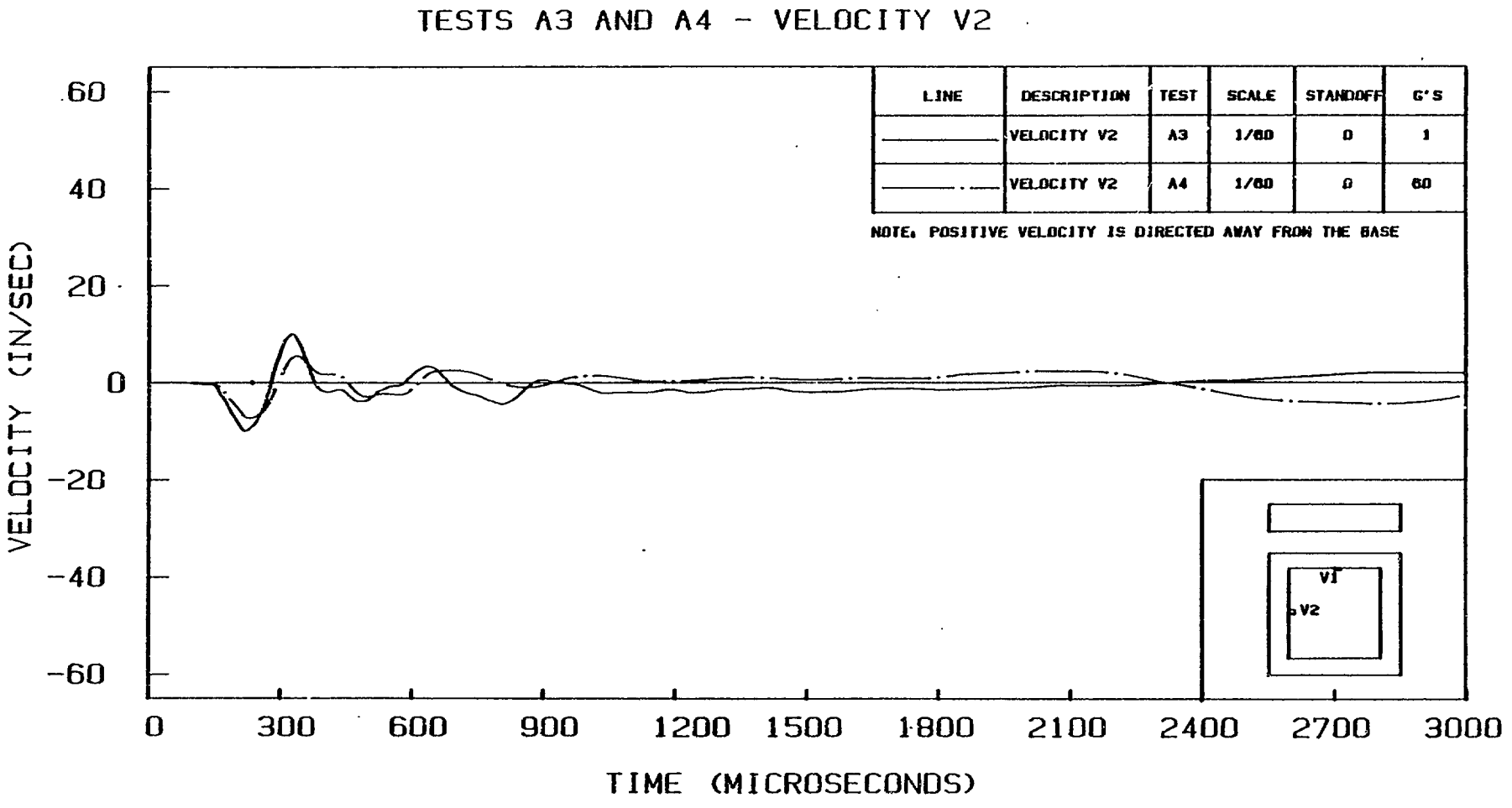

Figure 6.112. Velocity V2 in Tests A3 and A4

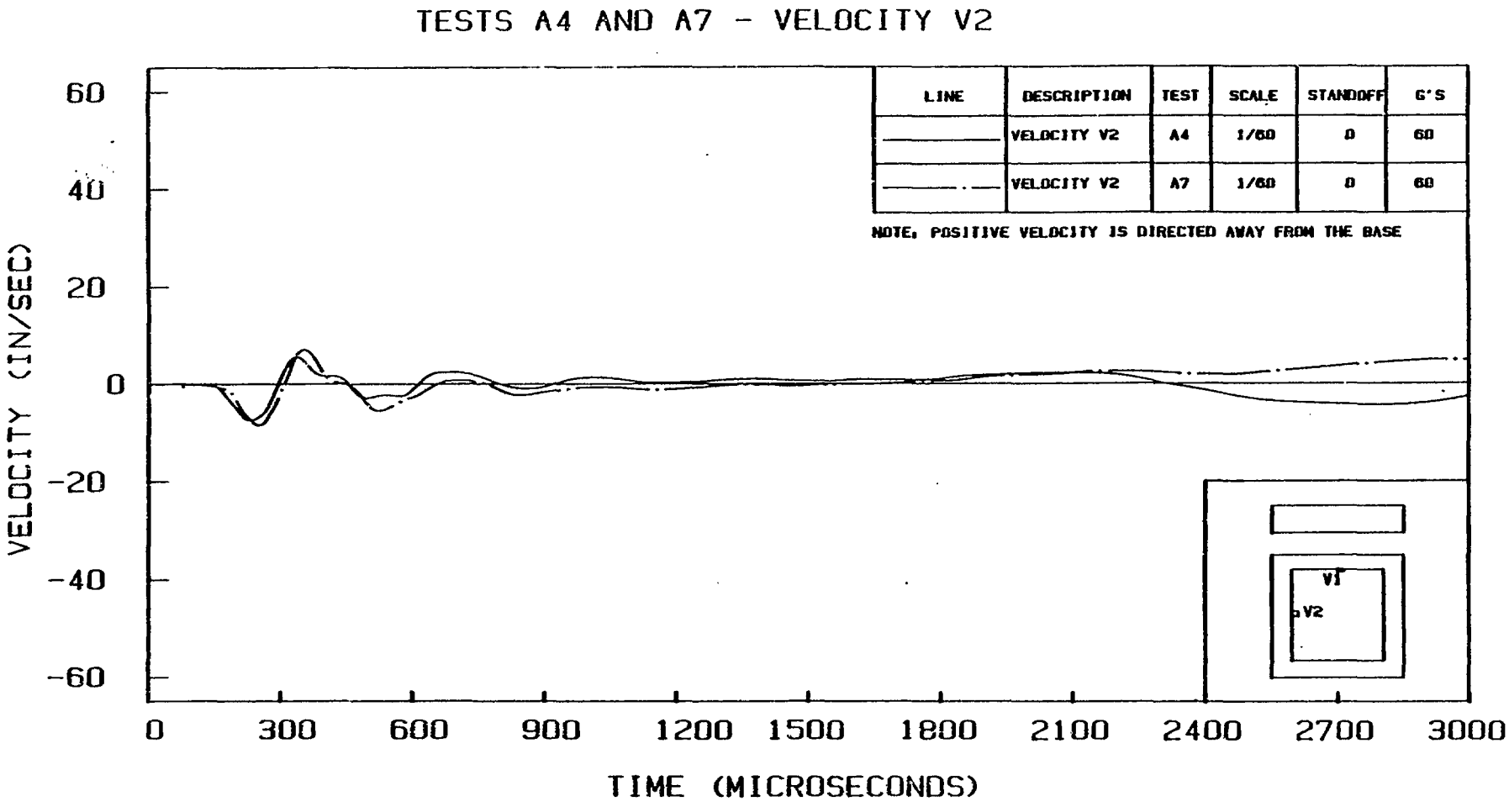

Figure 6.113. Velocity V2 in Tests A4 and A7

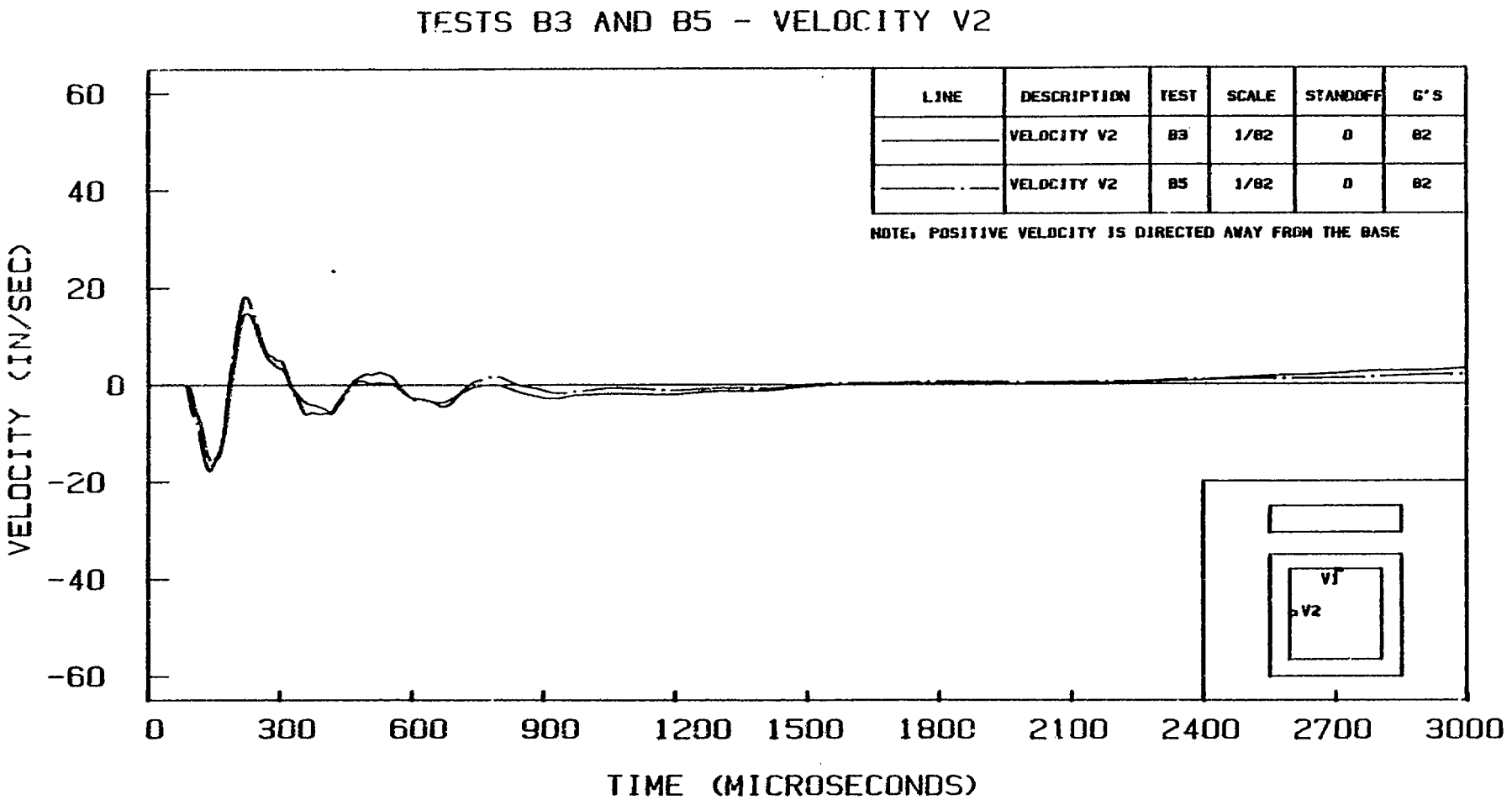

Figure 6.114. Velocity V2 in Tests B3 and B5

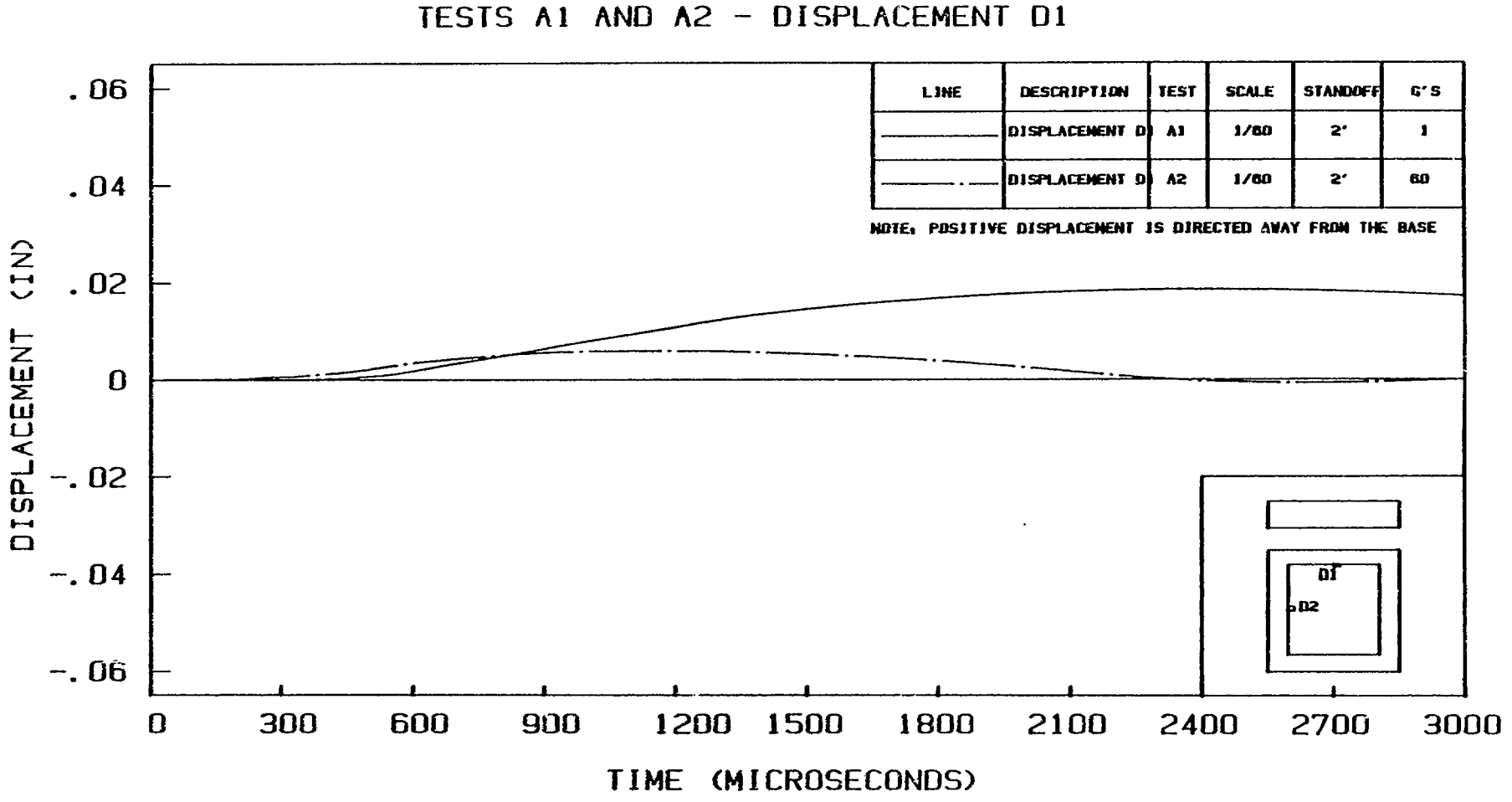

Figure 6.115. Displacement Dl in Tests Al and A2

test A2 (0.005 in). This difference in displacements at 1 and 60 g's is due to a larger confinement of the structure by soil at 60 g's which results in a higher stiffness for the top slab. Figure 6.116 shows a similar-type behavior in tests A5 and A6.

The adjusted peak displacement in test B1 (0.015 x 82/60 = 0.02 in) is slightly larger than the corresponding peak displacements in tests A1 (0.018 in) and A5 (0.017 in). The adjusted peak displacement in test B2 (0.003 x 82/60 = 0.004 in) is smaller than the corresponding peaks in tests A2 (0.005 in) and A6 (0.006 in). Figure 6.118 shows the displacement curves for tests B2 and B4. They show similar responses except for the divergence of the negative displacement in test B4.

Figure 6.119 shows the displacement (D1) curves in tests A3 and A4. The peak displacement in test A3 (0.022 in) is larger than the peak displacement in test A4 (0.010 in). Again, the increased confinement of the structure in test A4 is believed to be the main reason for this observed difference. Test A4 shows a divergence in displacement response. A similar test (A7) is shown in Figure 6.120. The peak displacement in test A7 is 0.006 which is smaller than the peak in test A4 (0.010 in).

In summmary, deflections of the top slab of the structure are much larger in the 1g tests as compared to the tests at high gravities. These observations are believed to be due to larger confinement of the structure

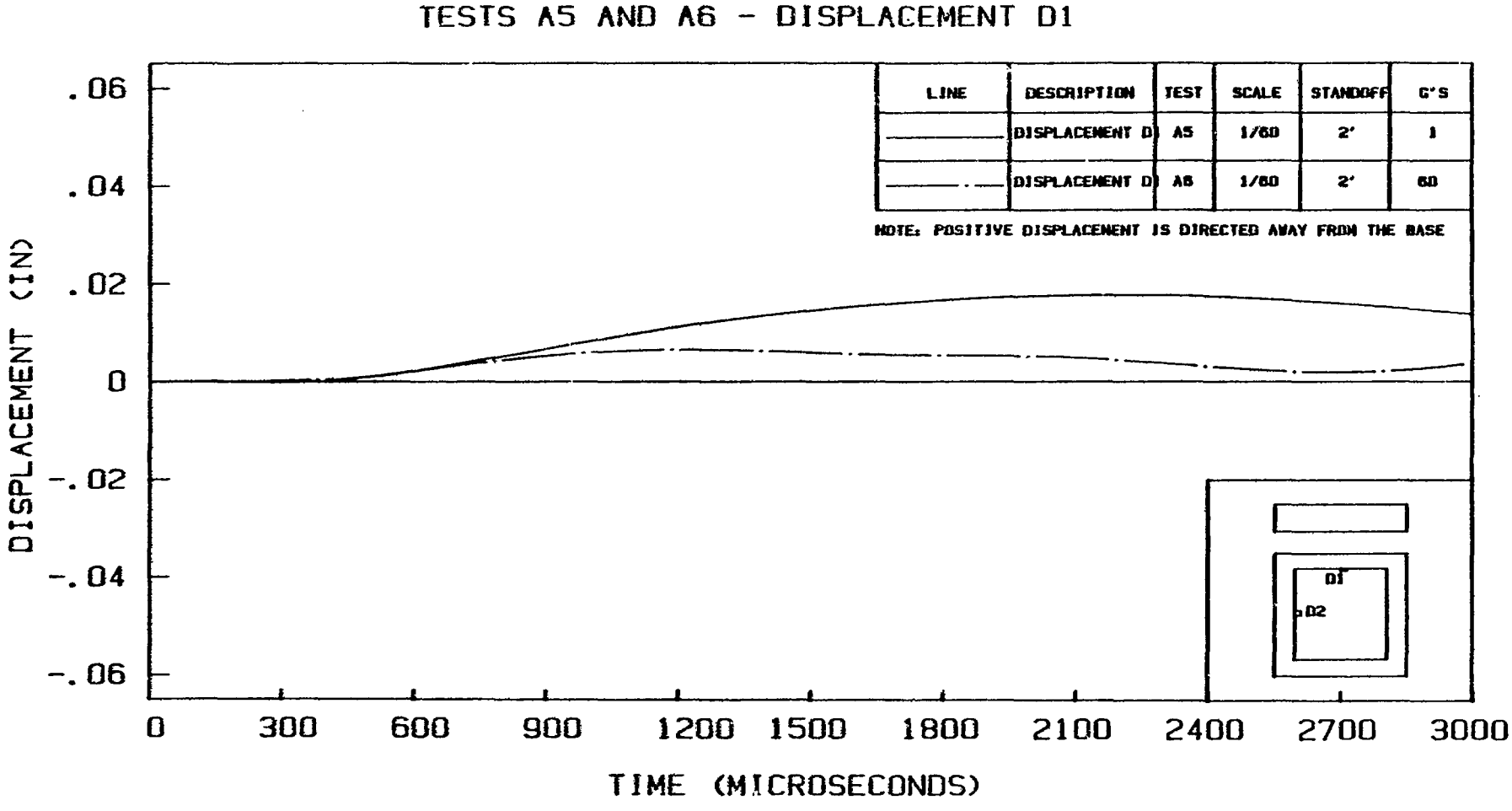

Figure 6.116. Displacement D1 in Tests A5 and A6

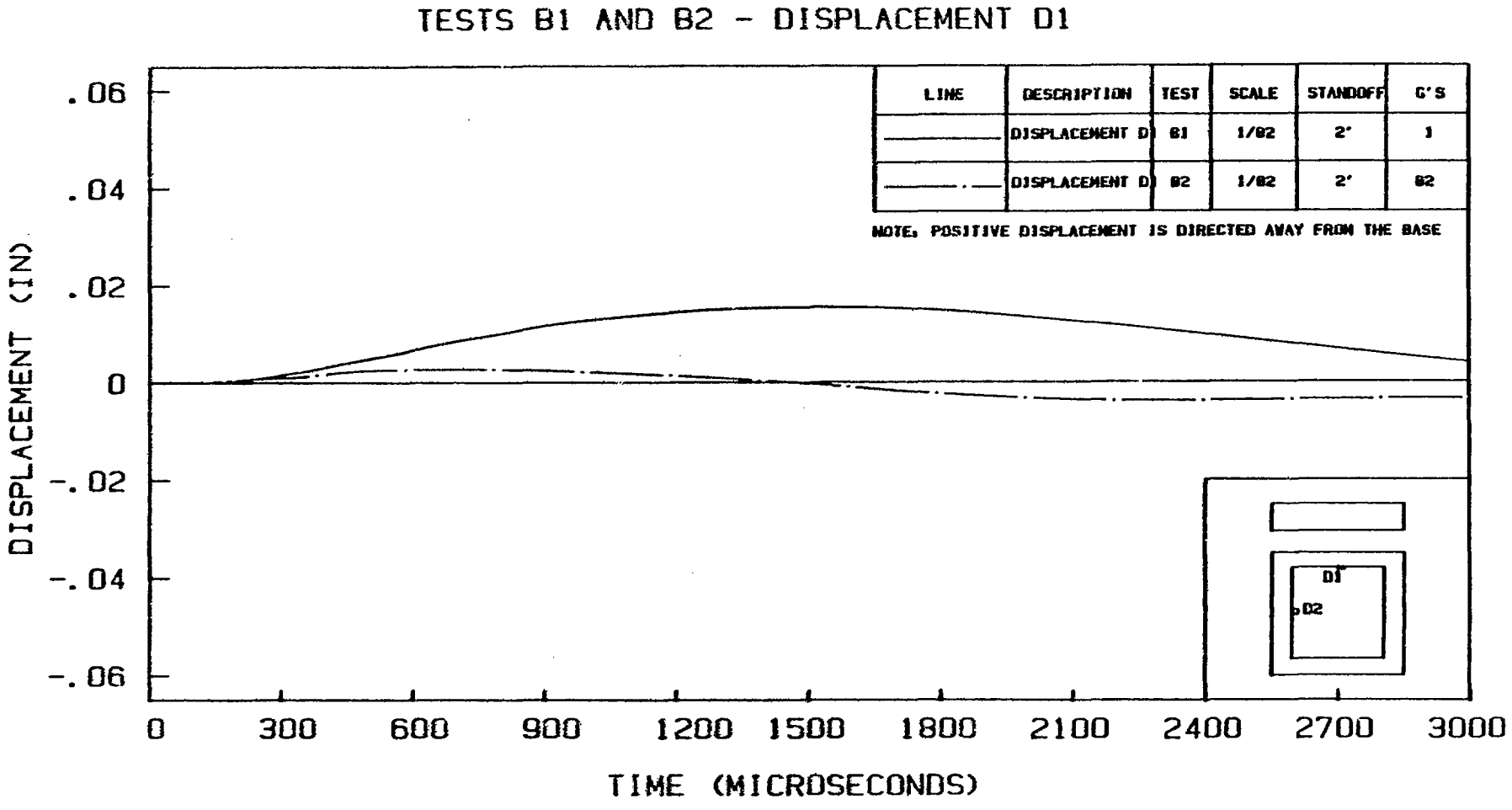

Figure 6.117. Displacement D1 in Tests B1 and B2

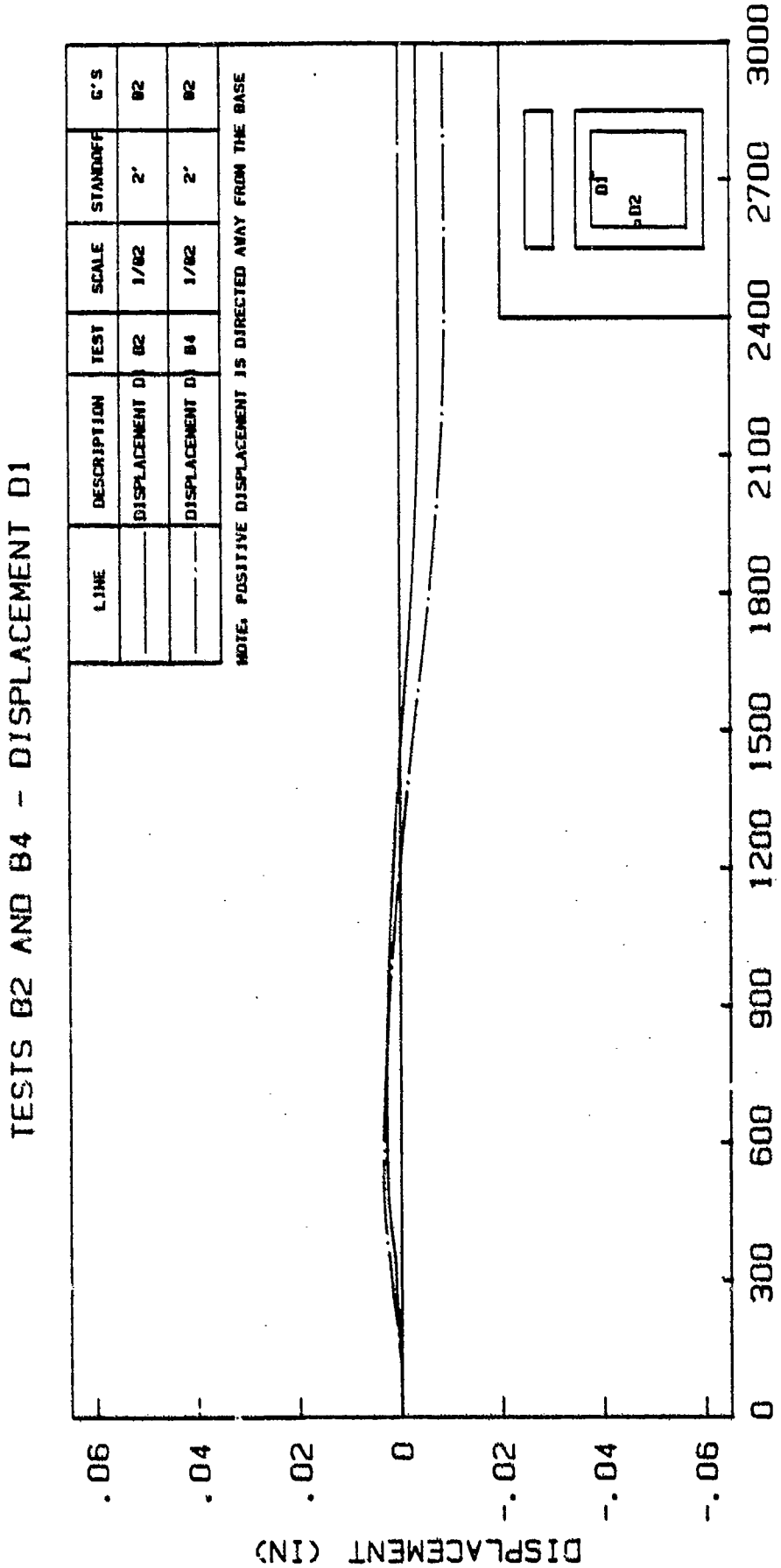

Figure 6.118. Displacement D1 in Tests B2 and B4

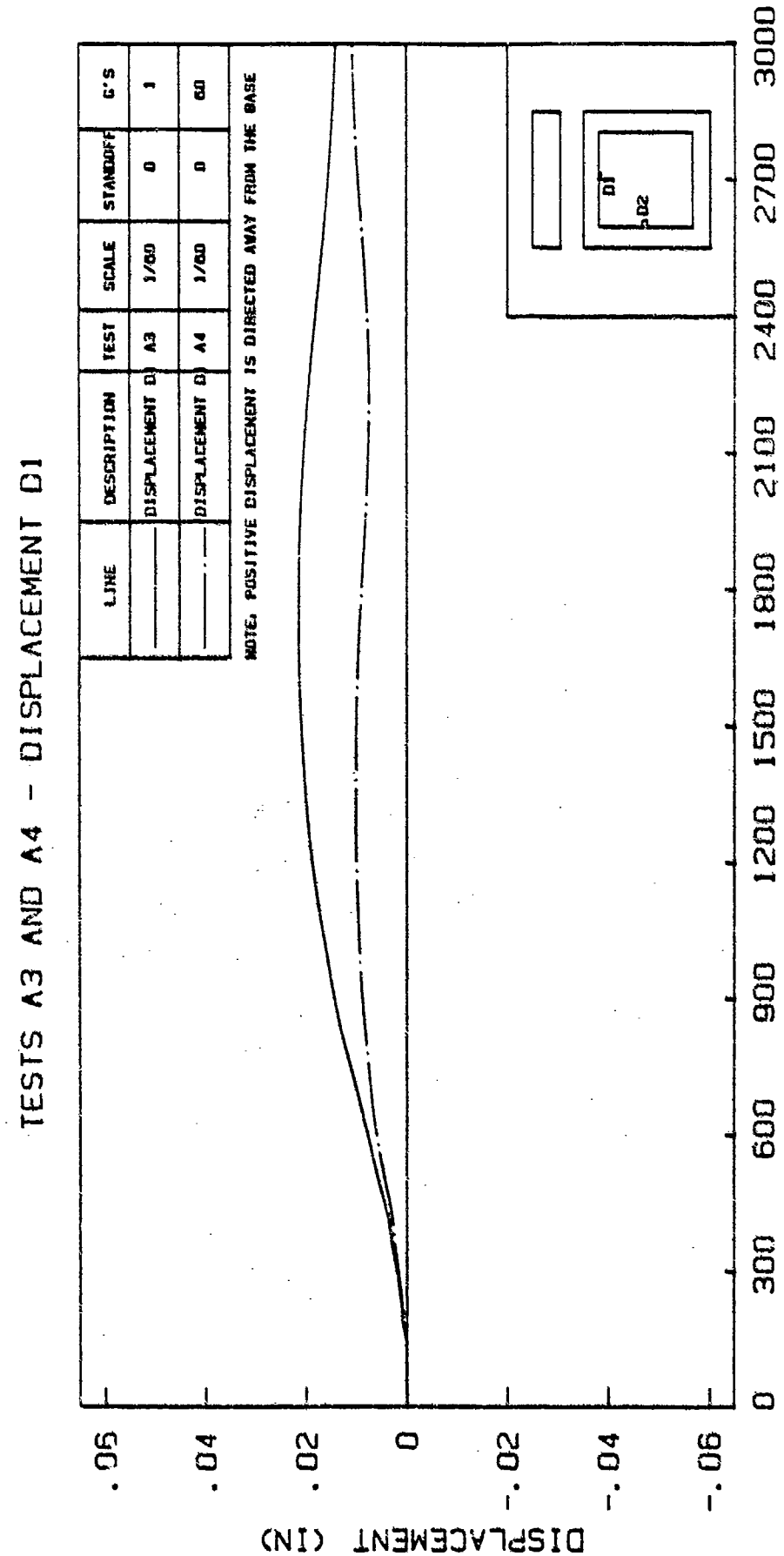

Figure 6.119. Displacement D1 in Tests A3 and A4

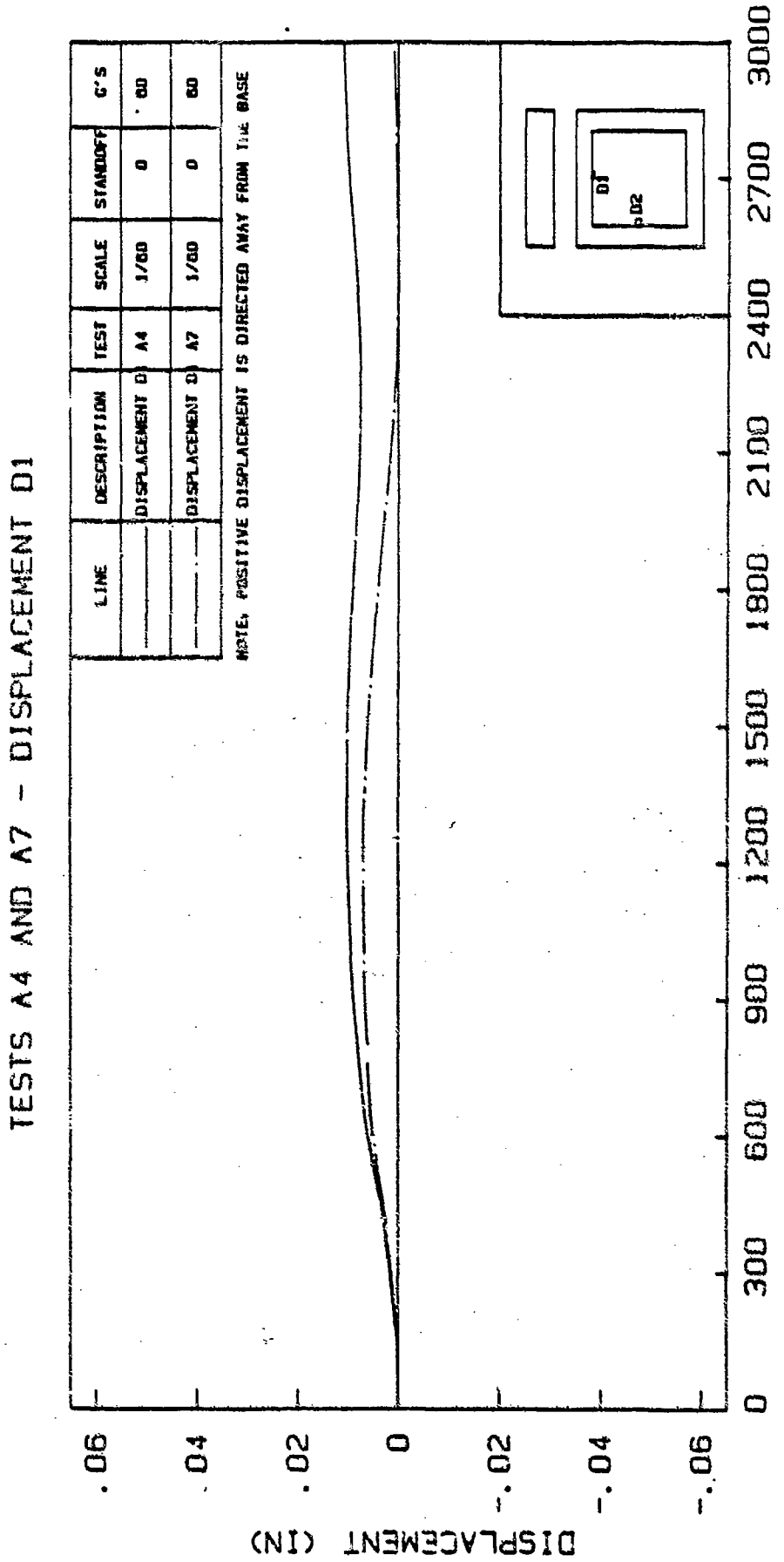

Figure 6.126. Displacement D1 in Tests A4 and A7

by soil (along the side walls) in high-gravity tests resulting in different (more restrictive) boundary conditions for the top slab as compared to tests at 1g. These results clearly indicate the significance of centrifuge testing in terms of the effect of gravity stresses in modifying the structural response of the system. In addition, the repeatability of deflection responses in similar tests are clearly illustrated and the scaling relationships are, to a large extent, verified.

6.5.2 Displacement D2

Displacement D2 (side wall) is obtained by integrating the velocity response V2. Most of the displacement curves for the side wall do not converge to zero displacement. This may be because of very small displacements (less than 0.001 in) involved, and the errors introduced in double integrations to obtain such small displacements. Therefore, only Figures 6.121 and 6.122 which indicate more reasonable responses are shown. Displacement scales in these two figures are different from previous figures.

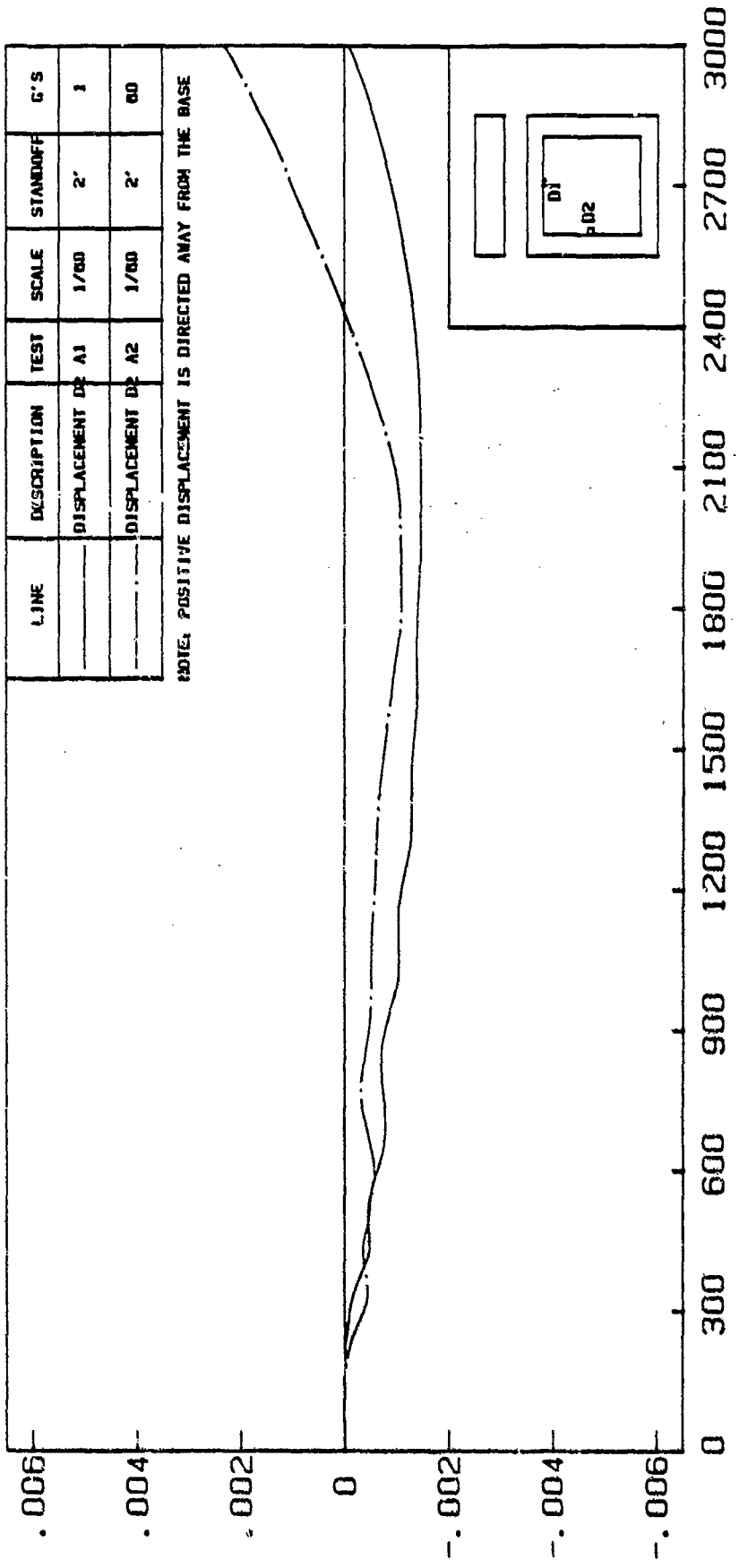

Figure 6.121. Displacement D2 in Tests A1 and A2

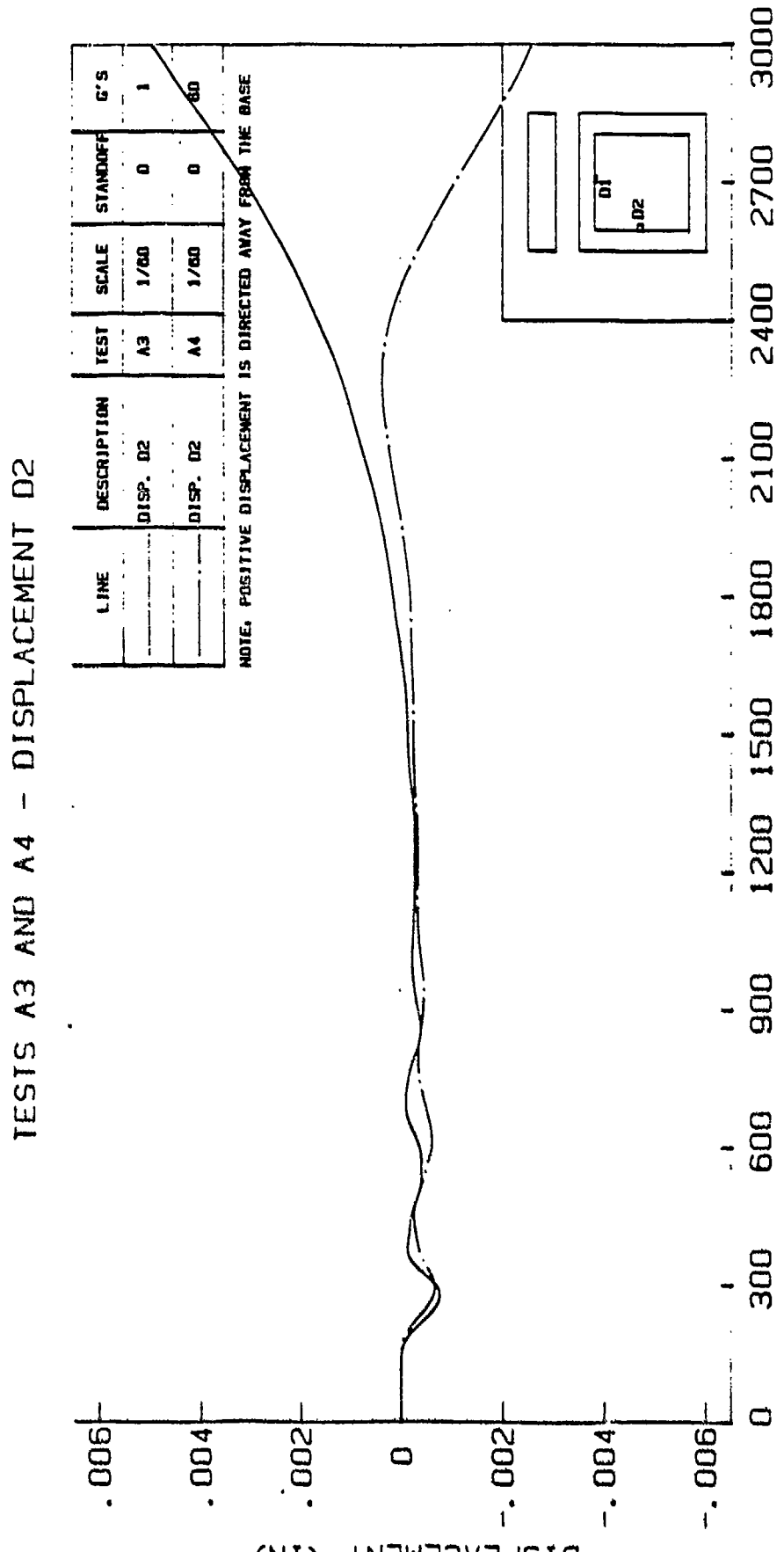

Figure 6.122. Displacement D2 in Tests A3 and A4

CHAPTER 7
CONCLUSIONS AND RECOMMENDATIONS

7.1 Conclusions

Based on the tests performed in this research effort, the following conclusions can be made:

1) An effective instrumentation system including piezoelectric shock pressure transducers, strain gages and accelerometers can be designed and built for centrifuge tests on small-scale models of underground structures subjected to blast loading.

2) For blast tests at a standoff distance of 2 scaled feet, the arrival times of pressure waves on the top slab of the box structure are consistently and substantially faster in the high-gravity tests (both 1/60- and 1/82-scale) as compared to 1g tests. In addition, the peak pressures in high-gravity tests are also higher. These results are believed to be due to larger stiffness of sand in high-gravity tests. Accelerometer and strain gage data also show faster acceleration response times and higher flexural strains in the high-gravity tests.

Tests on 1/82-scale models (2' standoff) show larger pressures than similar tests on 1/60-scale models even though equal pressures were expected according to the

scaling relationships. The reason for this discrepancy is believed to be due to an improper scaling of the explosive, not in terms of total mass, but rather in terms of mass distribution and charge geometry. Also, dimensional tolerances with regard to the building and placement of very small-scale structural models and explosive charges may be a factor. Despite these differences, the arrival times of peaks in most tests on 1/82-scale models were close to 60/82 times smaller than the corresponding times on the 1/60-scale models. This relationship satisfies the basic time scaling relationship. Based on these tests, it appears that 1/82-scale models may be close to the limit in terms of the smallest acceptable size model to be used in such tests.

For blast tests at zero standoff distances, the only test performed at 1g showed larger pressures and accelerations on the top slab of the box structure as compared to high-gravity tests. This condition may be explained by considering that, for tests at higher gravities, the higher soil stiffness (under the burster slab) would distribute the highly localized pressure (zero standoff) more evenly and therefore reduce peak pressures at the center of the top slab of the box structure. In addition, a larger portion of the total explosive energy may be expended in crater formations in tests at high gravities, resulting in smaller energy transmission to the soil. Also, testing errors such as incorrect placement of

the detonator may be a distinct possibility for this specific test. Again, consistent results were obtained for high-gravity tests on 1/60-scale models but tests on 1/82-scale models showed some variations.

Velocity and displacement responses for tests on 1/60 and 1/82-scale models indicate substantially different results between tests conducted at high gravities and at 1g. This fact illustrates the significant effect of gravity stresses (centrifuge testing) on the soil-structure interaction and the structural response of such systems. A high degree of repeatability of velocity and displacement responses is also evident for tests conducted under similar conditions.

3) Based on the test results reported here, it can be concluded that the centrifuge is a necessary and viable tool for blast testing on small-scale models of underground structures. This method of testing can result in substantial cost savings as compared to full-scale tests and would be ideal for parametric studies on underground structures. Ultimate strength (failure) studies on such systems in a centrifuge should be performed only after a sufficient understanding of the dynamic ultimate strength properties of microconcrete and their relationship to regular concrete is achieved.

7.2 Recommendations for Future Studies

Further improvements to the instrumentation system should be directed at eliminating the use of slip rings and multiple oscilloscopes. The use of telemetry to bypass slip rings may not be advisable because of the relatively high costs of such systems specially when signals with wide frequency bandwidths (such as blast) are involved. It is recommended that on-board data capture and storage systems be designed for future tests. These systems are technologically and economically feasible. Multiple high-speed, high-accuracy analog-to-digital converters together with storage modules can be designed to store the waveforms for transfer to a computer at a later time.

Now that the basic methods and devices for blast tests in centrifuge have been developed and the importance of gravity stresses are established, future such tests should, at first, be directed at understanding the major contributing parameters independent from each other. For example, an study of the characteristics of shock wave propagation in different soils (no structure) should be the first step in that process. Next, a structure with a simple geometry such as a slab should be included in the tests. Finally, complex structures such as box-type structures can be tested for parametric studies on the structural performance of such systems. More information is needed on the dynamic ultimate strength (failure) properties of microconcrete compared to regular concrete specially for

the shear failure mode. This information is needed for performing reliable ultimate strength blast tests in a centrifuge.

APPENDIX A
ELECTRONIC COMPONENTS OF THE INSTRUMENTATION SYSTEM

BURR-BROWN®

INA101

Very-High Accuracy INSTRUMENTATION AMPLIFIER

FEATURES

- ULTRA-LOW VOLTAGE DRIFT - 0.25μV/°C
- LOW OFFSET VOLTAGE - 25μV
- LOW NONLINEARITY - 0.002%
- LOW NOISE - 13nV/√Hz at f_o = 1kHz
- HIGH CMR - 106dB at 60Hz
- HIGH INPUT IMPEDANCE - $10^{10}\Omega$
- LOW COST

APPLICATIONS

- AMPLIFICATION OF SIGNALS FROM SOURCES SUCH AS:
  - Strain Gages
  - Thermocouples
  - RTDs
- REMOTE TRANSDUCERS
- LOW LEVEL SIGNALS
- MEDICAL INSTRUMENTATION

DESCRIPTION

The INA101 is a high accuracy, multistage, integrated-circuit instrumentation amplifier designed for signal conditioning requirements where very-high performance is desired. All circuits, including the interconnected thin-film resistors, are integrated on a single monolithic substrate.

A multiamplifier design is used to provide the highest performance and maximum versatility with monolithic construction for low cost. The input stage uses Burr-Brown's ultra-low drift, low noise technology to provide exceptional input characteristics.

Gain accuracy is achieved with precision nichrome resistors. This provides high initial accuracy, low TCR (temperature coefficient of resistance) and TCR matching, with outstanding stability as a function of time.

State-of-the-art wafer-level laser-trimming techniques are used for minimizing offset voltage and offset voltage drift versus temperature. This advanced technique also maximizes common-mode rejection and gain accuracy.

The INA101 introduces premium instrumentation amplifier performance and with the lower cost makes it ideal for even higher volume applications.

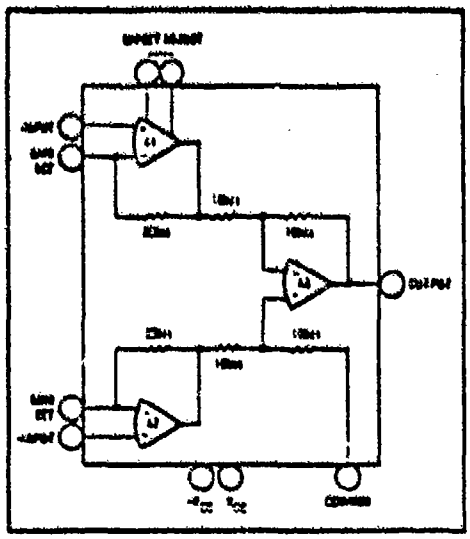

International Airport Industrial Park • P.O. Box 11400 • Tucson, Arizona 85734 • Tel. (602) 746-1111 • Twx: 910-952-1111 • Cable: BBRCORP • Telex: 66-6491

ANALOG DEVICES

Precision, Low-Power FET-Input Electrometer Op Amp

AD515

FEATURES

Ultra Low Bias Current: 0.075pA max (AD515L)
0.150pA max (AD515K)
0.300pA max (AD515J)
Low Power: 1.5mA max Quiescent Current
(0.8mA typ)
Low Offset Voltage: 1.0mV max (AD515 K & L)
Low Drift: 15μV/°C max (AD515K)
Low Noise: 4μV p-p, 0.1 to 10Hz
Low Cost

AD515 FUNCTIONAL BLOCK DIAGRAM

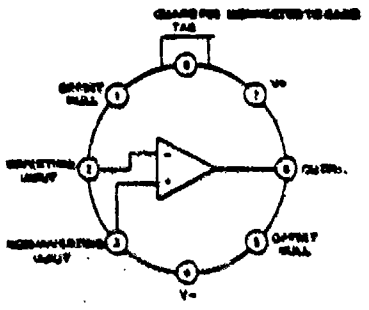

TO-99
TOP VIEW

PRODUCT DESCRIPTION

The AD515 series of FET-input operational amplifiers are second generation electrometer designs offering the lowest input bias currents available in any standard operational amplifier. The AD515 also delivers laser-trimmed offset voltage, low drift, low noise and low power, a combination of features not previously available in ultra-low bias current circuits. All devices are internally compensated, free of latch-up, and short circuit protected.

The AD515 delivers a new level of versatility and precision to a wide variety of electrometer and very high impedance buffer measurement situations, including photo-current detection, vacuum ion-gauge measurement, long term precision integration, and low drift sample/hold applications. The device is also an excellent choice for all forms of biomedical instrumentation such as pH/pion sensitive electrodes, very low current oxygen sensors, and high impedance biological microprobes. In addition, the low cost and pin compatibility of the AD515 with standard FET op amps will allow designers to upgrade the performance of present systems at little or no additional cost. The 10^{14} ohm common mode input impedance, resulting from a solid bootstrap input stage, ensures that the input bias current is essentially independent of common mode voltage.

As with previous electrometer amplifier designs from Analog Devices, the case is brought out to its own connection (pin 8) so that the case can be independently connected to a point at the same potential as the input, thus minimizing stray leakage to the case. This feature will also shield the input circuitry from external noise and supply transients, as well as reducing common mode input capacitance from 0.8pF to 0.2pF.

The AD515 is available in three versions of bias current and offset voltage, the "J", "K", and "L"; all are specified for rated performance from 0 to +70°C and supplied in a hermetically sealed TO-99 package.

PRODUCT HIGHLIGHTS

1. The AD515 provides the lowest bias currents available in an integrated circuit amplifier.
   - The ultra low input bias currents are specified as the maximum measured at either input with the device fully warmed up on ±15 volt supplies at +25°C ambient with no heat sink. This parameter is 100% tested.
   - By using ±5 volt supplies, input bias current can typically be brought below 10fA.
2. The input offset voltage on all grades is laser trimmed to a level typically less than 500μV.
   - The offset voltage drift is the lowest available in an FET electrometer amplifier.
   - If additional nulling is desired, the amount required will have a minimal effect on offset drift (approximately 1μV/°C per millivolt).
3. The low quiescent current drain of 0.8mA typical and 1.5mA maximum, which is among the lowest available in operational amplifier designs of any type, keeps self heating effects to a minimum and renders the AD515 suitable for a wide range of remote probe situations.
4. The combination of low input noise voltage and very low input noise current is such that for source impedances from much over one Megohm up to 10^{11} ohm, the Johnson noise of the source will easily dominate the noise characteristic.

National Semiconductor

Transmission Line Drivers/Receivers

DS1488 Quad Line Driver

General Description

The DS1488 is a quad line driver which converts standard DTL/TTL input logic levels through one stage of inversion to output levels which meet EIA Standard No. RS-232C and CCITT Recommendation V. 24.

Features

- Current limited output ±10 mA typ
- Power-off source impedance 300Ω min
- Simple slew rate control with external capacitor
- Flexible operating supply range
- Inputs are DTL/TTL compatible

Schematic and Connection Diagrams

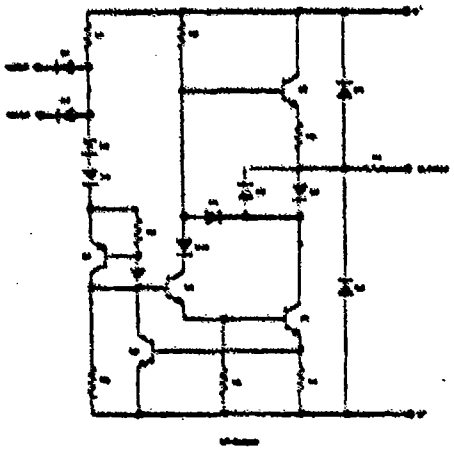

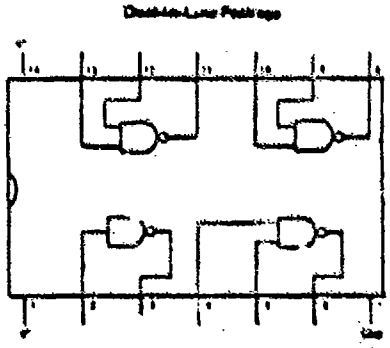

Order Number DS1488J or DS1488N
See NS Package J14A or N14A

Typical Applications

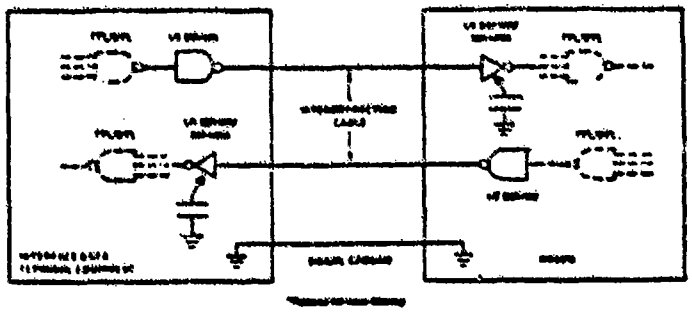

National Semiconductor

Peripheral/Power Drivers

DS55450/DS75450 Series Dual Peripheral Drivers

General Description

The DS55450/DS75450 series of dual peripheral drivers are a family of versatile devices designed for use in systems that use TTL or DTL logic. Typical applications include high speed logic buffers, power drivers, relay drivers, lamp drivers, MOS drivers, bus drivers and memory drivers.

The DS55450/DS75450 series are unique general purpose devices each featuring two standard Series 54/74 TTL gates and two uncommitted, high current, high voltage NPN transistors. These devices offer the system designer the flexibility of tailoring the circuit to the application.

The DS55451/DS75451, DS55452/DS75452, DS55453/DS75453 and DS55454/DS75454 are dual peripheral AND, NAND, OR and NOR drivers, respectively, (positive logic) with the output of the logic gates internally connected to the bases of the NPN output transistors.

Features

- 300 mA output current capability
- High voltage outputs
- No output latch-up at 20V
- High speed switching
- Choice of logic function
- TTL or DTL compatible diode-clamped inputs
- Standard supply voltages
- Replaces TI "A" and "B" series

Connection Diagrams (Dual-In-Line and Metal Can Packages)

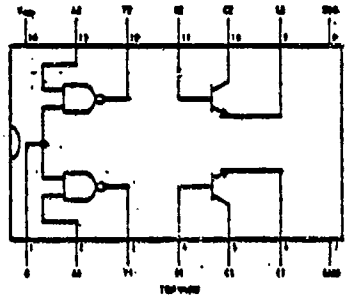

Order Number
DS55450J, DS75450J, or DS7545ON
See NS Package J14A or N14A

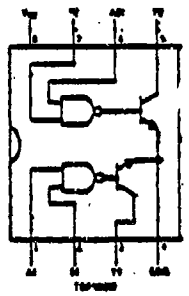

Order Number DS55451J-8,
DS75451J-8 or DS75451N-8

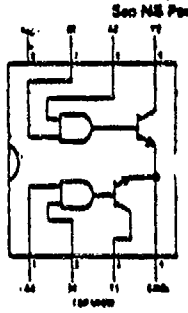

Order Number DS55452J-8,
DS75452J-8 or DS75452N-8

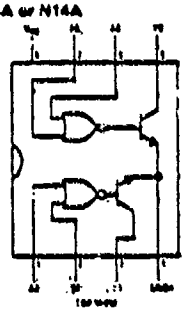

Order Number DS55453J-8,
DS75453J-8 or DS75453N-8

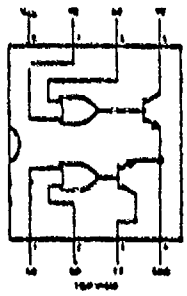

Order Number DS55454J-8,
DS75454J-8 or DS75454N-8

See NS Package J08A or N08A

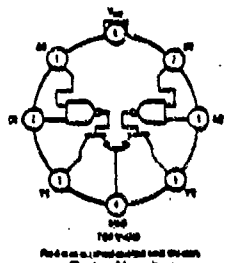

Order Number
DS55451H or DS75451H

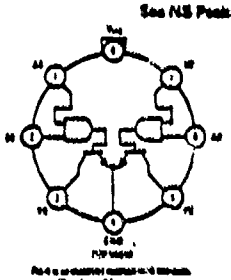

Order Number
DS55452H or DS75452H

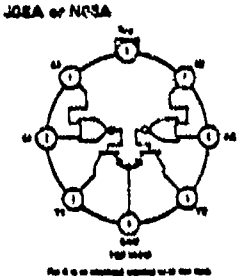

Order Number
DS55453H or DS75453H

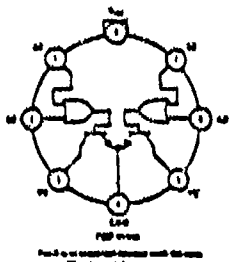

Order Number
DS55454H or DS75454H

See NS Package H08C

National Semiconductor

CD4066BM/CD4066BC Quad Bilateral Switch

general description

The CD4066BM/CD4066BC is a quad bilateral switch intended for the transmission or multiplexing of analog or digital signals. It is pin-for-pin compatible with CD4016BM/CD4016BC, but has a much lower "ON" resistance, and "ON" resistance is relatively constant over the input-signal range.

features

- Wide supply voltage range — 3V to 15V
- High noise immunity — 0.45 V_{DD} typ
- Wide range of digital and analog switching — ±7.5 V_{peak}
- "ON" resistance for 15V operation — 80Ω typ
- Matched "ON" resistance over 15V signal input — ΔR_{ON} = 5Ω typ
- "ON" resistance flat over peak-to-peak signal range
- High "ON"/"OFF" output voltage ratio — 65 dB typ
  @ f_{is} = 10 kHz, R_L = 10 kΩ
- High degree of linearity — <0.4% distortion typ
  @ f_{is} = 1 kHz, V_{is} = 5 Vp-p, $V_{DD} - V_{SS}$ = 10V, R_l = 10 kΩ
- Extremely low "OFF" switch leakage — 0.1 nA typ
  @ $V_{DD} - V_{SS}$ = 10V, T_A = 25°C
- Extremely high control input impedance — 10^{12}Ω typ
- Low crosstalk between switches — −50 dB typ
  @ f_{is} = 0.9 MHz, R_L = 1 kΩ
- Frequency response, switch "ON" — 40 MHz typ

applications

- Analog signal switching/multiplexing
  - Signal gating
  - Squelch control
  - Chopper
  - Modulator/Demodulator
  - Commutating switch
- Digital signal switching/multiplexing
- CMOS logic implementation
- Analog-to-digital/digital-to-analog conversion
- Digital control of frequency, impedance, phase, and analog-signal gain

schematic and connection diagrams

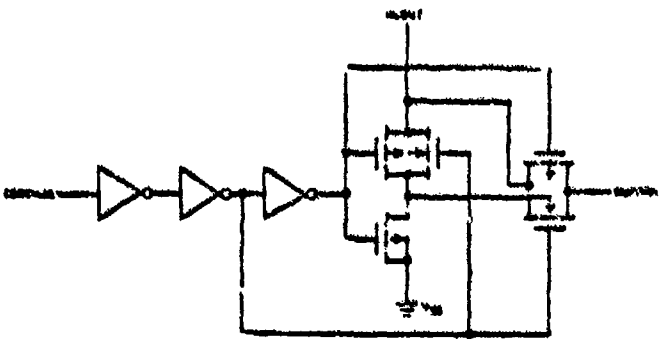

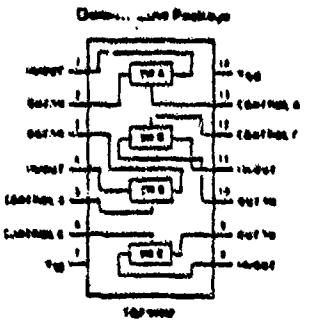

Using the CMOS Dual Monostable Multivibrator

National Semiconductor
Application Note 138
Thomas P. Redfern

INTRODUCTION

The MM54C221/MM74C221 is a dual CMOS monostable multivibrator. Each one-shot has three inputs (A, B and CLR), and two outputs (Q and $\overline{Q}$). The output pulse width is set by an external RC network.

The A and B inputs trigger an output pulse on a negative or positive input transition respectively. The CLR input when low resets the one-shot. Once triggered the A and B inputs have no further control on the output.

THEORY OF OPERATION

Figure 1 shows that in its stable state, the one-shot clamps C_{EXT} to ground by turning N1 ON and holds the positive comparator input at V_{CC} by turning N2 OFF. The prefix N is used to denote N-channel transistors.

The signal, G, gating N2 OFF also gates the comparator OFF thereby keeping the internal power dissipation to an absolute minimum. The only power dissipation when in the stable state is that generated by the current through R_{EXT}. The bulk of this dissipation is in R_{EXT} since the voltage drop across N1 is very small for normal ranges of R_{EXT}.

To trigger the one-shot the CLR input must be high. The gating, G, on the comparator is designed such that the comparator output is high when the one-shot is in its stable state. With the CLR input high the clear input to FF is disabled allowing the flip-flop to respond to the A or $\overline{B}$ input. A negative transition on A or a positive transition on B sets Q to a high state. This in turn gates N1 OFF and N2 and the comparator ON.

Gating N2 ON establishes a reference of 0.63 V_{CC} on the comparator's positive input. Since the voltage on C_{EXT} can not change instantaneously V1 = 0V at this time. The comparator then will maintain its one level on the output. Gating N1 OFF allows C_{EXT} to start charging through R_{EXT} toward V_{CC} exponentially.

Assuming a perfect comparator (zero offset and infinite gain) when the voltage on C_{EXT}, V1, equals 0.63 V_{CC} the comparator output will go from a high state to a low state resetting Q to a low state. *Figure 2* is a timing diagram summarizing this sequence of events.

This diagram is idealized by assuming zero rise and fall times and zero propagation delay but it shows the basic operation of the one-shot. Also shown is the effect of taking the CLR input low. Whenever CLR goes low FF

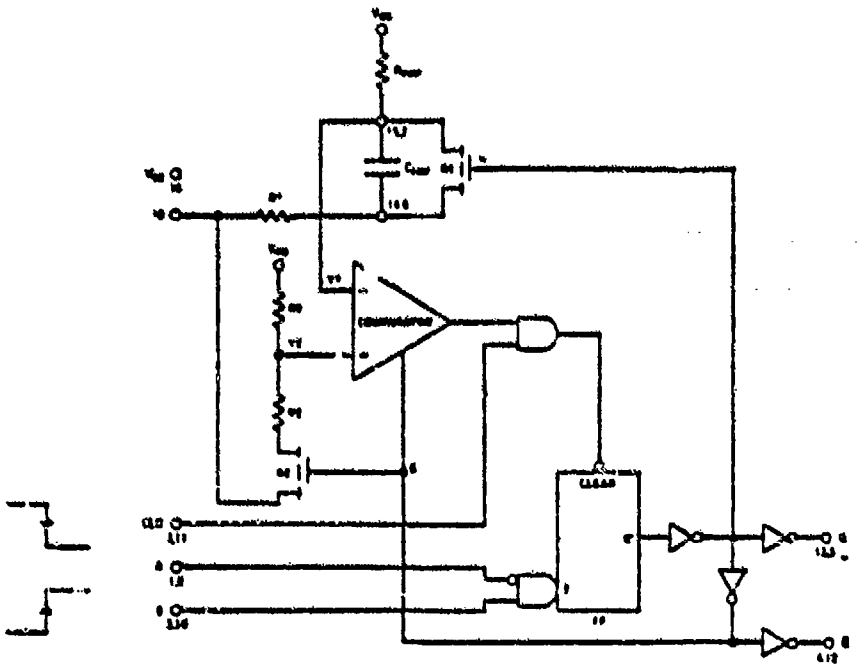

FIGURE 1. Monostable Multivibrator Logic Diagram

National Semiconductor

Voltage Comparators

LM161/LM261/LM361 High Speed Differential Comparators

General Description

The LM161/LM261/LM361 is a very high speed differential input, complementary TTL output voltage comparator with improved characteristics over the SE529/NE529 for which it is a pin-for-pin replacement. The device has been optimized for greater speed performance and lower input offset voltage. Typically delay varies only 3 ns for over-drive variations of 5 mV to 500 mV. It may be operated from op amp supplies (±15V).

Complementary outputs having minimum skew are provided. Applications involve high speed analog to digital converters and zero-crossing detectors in disc file systems.

Features

- Independent strobes
- Guaranteed high speed — 20 ns max
- Tight delay matching on both outputs
- Complementary TTL outputs
- Operates from op amp supplies — ±15V
- Low speed variation with overdrive variation
- Low input offset voltage
- Versatile supply voltage range

Schematic and Connection Diagrams

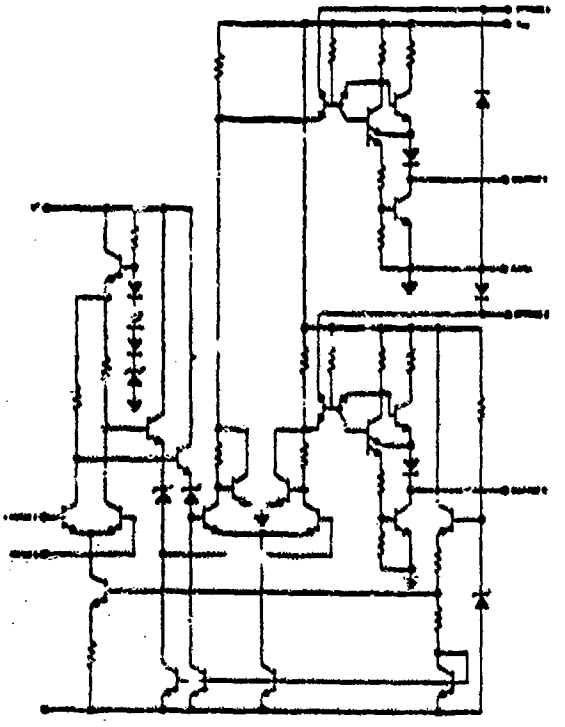

Dual-In-Line Package

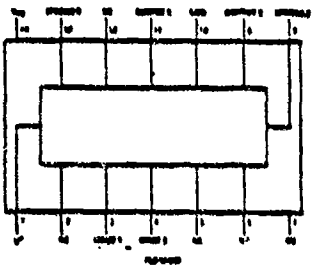

Order Number LM161J, LM261J or LM361J
See NS Package J14A

Order Number LM361N
See NS Package N14A

Metal Can Package

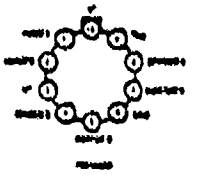

Order Number LM161H, LM261H or LM361H
See NS Package H10C

Logic Diagram

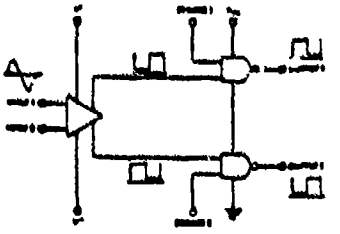

APPENDIX B
COMPUTER PROGRAMS WRITTEN ON HP 9816

The following are several computer programs written on an HP 9816 computer for analysis of the test results. One such program is for the retrieval of waveforms from Nicolet 4094 oscilloscopes and storage of data on computer diskettes. Other programs analyze and plot the results on a digital plotter.

```
10    REM PROGRAM TO RETRIEVE WAVEFORMS FROM NICOLET 4094
20    OUTPUT 714:"C,4,2,13,10"
30    ENTER 714:Z
40    OUTPUT 714:"H,0"
50    ENTER 714:Z
60    DIM N(11)
70    FOR I=1 TO 11
80    ENTER 714:N(I)
90    NEXT I
100   ENTER 714:Z
110   OUTPUT 714:"D,4,0,0,4000,1"
120   ENTER 714:Z
130   REM CONTROL 7,16:0
140   DIM B$[8004] BUFFER
150   ASSIGN @Buf TO BUFFER B$
160   ASSIGN @Wic TO 714
170   RESET @Buf
180   TRANSFER @Wic TO @Buf;COUNT 8000,WAIT
190   REM CONTROL 7,16:2
200   ENTER 714:Z
210   J=1
220   DIM A(2000)
230   DIM B(2000)
240   FOR I=1 TO 7999 STEP 4
250   P=256*MUN(B$[I])+MUN(B$[I+1])-65536*(MUN(B$[I])>=128)
260   A(J)=P
270   J=J+1
280   NEXT I
290   J=1
300   FOR I=2 TO 7999 STEP 4
310   P=256*MUN(B$[I])+MUN(B$[I+1])-65536*(MUN(B$[I])>=128)
320   B(J)=P
330   J=J+1
340   NEXT I
350   INPUT "INPUT FILE NAME 1:",File1$
360   INPUT "INPUT FILE NAME 2:",File2$
370   CREATE BDAT File1$,1,18000
380   CREATE BDAT File2$,1,18000
390   ASSIGN @P1 TO File1$
400   ASSIGN @P2 TO File2$
410   OUTPUT @P1;A(*)
420   PRINT "FIRST WAVEFORM RECORDED ON FILE ",File1$
430   OUTPUT @P2;B(*)
440   PRINT "SECOND WAVEFORM RECORDED ON FILE ",File2$
450   BEEP
460   END
```

```
10    REM ** PROGRAM TO SUBTRACT NOISE FROM STRAIN DATA **
20    REM ** JANUARY 1987 **
30    REM
40    DIM A(2048),B(2048)
50    INPUT "INSERT DATA TAPE AND INPUT STRAIN FILE NAME: ",Fs$
60    ASSIGN @Fs TO Fs$
70    ENTER @Fs:Hnormal,A(*)
80    ASSIGN @Fs TO *
90    INPUT "INSERT 'NOISE' TAPE AND INPUT NOISE FILE NAME: ",F$
100   ASSIGN @F TO F$
110   ENTER @F:Hnormal,B(*)
120   ASSIGN @F TO *
130   FOR I=1 TO 2048
140   A(I)=A(I)-B(I)
150   NEXT I
160   INPUT "INSERT DISK FOR STORAGE OF CORR. DATA IN DRIVE 1 AND PRESS ENTER",Ans
170   File$="ds$"&":"&"HP9122,700,1"
180   CREATE BDAT File$,1,17000
190   ASSIGN @P1 TO File$
200   OUTPUT @P1 Hnormal,A(*)
210   PRINT "CORRECTED STRAIN DATA RECORDED ON FILE: ",File$
220   PRINT "PROGRAM STOP"
230   END
```

```
10    REM ── PROGRAM TO OBTAIN AXIAL AND FLEXURAL STRAINS ──
20    REM ── JANUARY 1987 ──
30    REM
40    DIM A(2048),B(2048),File1$[20],File2$[20]
50    INPUT "INPUT FIRST DATA FILE NAME",File1$
60    INPUT "INPUT SECOND DATA FILE NAME",File2$
70    ASSIGN @F1 TO File1$
80    ASSIGN @F2 TO File2$
90    ENTER @F1;Hnormal,A(*)
100   ENTER @F2;Hnormal,B(*)
110   IF Hnormal=Hnormal THEN 130
120   PRINT "--ERROR--TIME BASES FOR THE TWO WAVEFORM NOT EQUAL"
130   GOTO 640
140   REM
150   REM ── CALCULATE AXIAL STRAIN ──
160   REM ── AXIAL STRAIN = (S1+S2)/2 ──
170   REM
180   FOR I=1 TO 2048
190   B(I)=(A(I)+B(I))/2
200   NEXT I
210   REM
220   REM ── STORE AXIAL STRAIN ──
230   REM
240   File4$="\"&File1$[1,4]&File2$[3,4]&":HP9122,700,1"
250   CREATE BDAT File4$,1,17000
260   ASSIGN @F3 TO File4$
270   OUTPUT @F3;Hnormal,B(*)
280   PRINT "AXIAL STRAIN DATA RECORDED ON FILE: ",File4$
290   REM
300   REM ── CALCULATE FLEXURAL STRAIN ──
310   REM ── FLEXURAL STRAIN = S1-((S1+S2)/2) ──
320   REM
330   File5$="F"&File1$[1,4]&File2$[3,4]&":HP9122,700,1"
340   CREATE BDAT File5$,1,17000
350   ASSIGN @F4 TO File5$
360   FOR I=1 TO 2048
370   A(I)=A(I)-B(I)
380   NEXT I
390   REM
400   REM ── STORE FLEXURAL STRAIN DATA ──
410   REM
420   OUTPUT @F4;Hnormal,A(*)
430   PRINT "FLEXURAL STRAIN DATA RECORDED ON FILE: ",File5$
440   REM
450   REM ── PLOT AXIAL AND FLEXURAL CURVES ──
460   INPUT "INPUT 1 TO SEE PLOT;0 TO EXIT",Ans
470   IF Ans=0 THEN 640
480   GINIT
490   GRAPHICS ON
500   WINDOW 1,2048,-4,4
510   INPUT "PRESS CLR SCR AND THEN ENTER",Ttt
520   FOR I=1 TO 2048
530   PLOT I,A(I)
540   NEXT I
550   INPUT "PRESS ENTER TO SEE FLEXURAL CURVE",Abb
560   GCLEAR
561   GRAPHICS OFF
571   GINIT
572   GRAPHICS ON
573   WINDOW 1,2048,-4,4
574   INPUT "PRESS CLR SCR AND THEN ENTER",Ppp
580   FOR I=1 TO 2048
590   PLOT I,A(I)
600   NEXT I
612   INPUT "PRESS ENTER WHEN READY",Zzz
613   GRAPHICS OFF
614   GCLEAR
615   PRINT "PROGRAM STOP"
616   END
```

```
10    REM ── PROGRAM TO PLOT CALIBRATION CURVES FOR PRESSURE GAGES ──
20    REM ── FEBRUARY 1987
30    REM
40    DIM A(3968),Fc$[50]
50    INPUT "INPUT 1ST FILE NAME AND FREQUENCY",F1$,Fr1
51    INPUT "INPUT 2ND FILE NAME AND FREQUENCY",F2$,Fr2
52    INPUT "INPUT 3RD FILE NAME AND FREQUENCY",F3$,Fr3
53    INPUT "INPUT 4TH FILE NAME AND FREQUENCY",F4$,Fr4
60    ASSIGN @F1 TO F1$
61    ASSIGN @F2 TO F2$
62    ASSIGN @F3 TO F3$
63    ASSIGN @F4 TO F4$
70    ASSIGN @P TO 705
80    OUTPUT @P;"IN;SP1;IP1350,2000,9250,6000;"
90    OUTPUT @P;"SC0,40,-8.0,8.0;"
100   OUTPUT @P;"PD0,-8 PD 40,-8,40,8,0.8,0,-8 PU"
120   OUTPUT @P;"SI.2,.3;TL1,3,0"
130   FOR X=0 TO 40 STEP 10
140   OUTPUT @P;"PA";X,".-8;XT;"
150   OUTPUT @P;"CP-1,-1;LB";X;""
160   NEXT X
170   OUTPUT @P;"PA20,-8;CP-12,-2.3;LBTIME (MILLISECONDS)"
180   OUTPUT @P;"TL1.3,0"
190   FOR Y=-8 TO 8 STEP 2
200   OUTPUT @P;"PA0,";Y,"YT;"
220   NEXT Y
221   OUTPUT @P;"PA0,0 CP-2,-1;DI0,1;LBOUTPUT"
230   INPUT "INPUT GENERAL TITLE FOR GRAPH",Fc$
250   OUTPUT @P;"PA20,8 SI.2,.3 CP2,10"
260   OUTPUT @P;"DI1,0 LB";Fc$;""
261   ENTER @F1;Nmaxm1,A(*)
262   OUTPUT @P;"LT"
263   OUTPUT @P;"SI.1,.15;PA30,7;LBAPPLIED PRESSURE"
264   OUTPUT @P;"PU36,7;PD39,7;PU"
266   OUTPUT @P;"PA0,0 PU"
270   FOR I=1 TO 1968
280   OUTPUT @P;"PA";Nmaxm1*(I-1)*1000;-A(I);"PD"
290   NEXT I
291   OUTPUT @P;"PU"
300   ENTER @F1;Nmaxm1,A(*)
310   OUTPUT @P;"LT6"
311   OUTPUT @P;"SI.1,.15;PA30,6;LBPRESSURE GAGE S1"
312   OUTPUT @P;"PU36,6;PD39,6;PU"
320   OUTPUT @P;"PA0,0 PU"
330   FOR I=1 TO 1968
340   OUTPUT @P;"PA";Nmaxm1*(I-1)*1000;A(I)*10;"PD"
350   NEXT I
351   OUTPUT @P;"PU"
360   ENTER @F2;Nmaxm1,A(*)
370   OUTPUT @P;"LT5"
371   OUTPUT @P;"SI.1, .15;PA30,5;LBPRESSURE GAGE S2"
372   OUTPUT @P;"PU36,5;PD39,5;PU"
380   OUTPUT @P;"PA0,0 PU"
390   FOR I=1 TO 1968
400   OUTPUT @P;"PA";Nmaxm1*(I-1)*1000;A(I)*10;"PD"
410   NEXT I
411   OUTPUT @P;"PU"
412   ENTER @F3,Nmaxm1,A(*)
413   OUTPUT @P;"LT4"
414   OUTPUT @P;"SI.1, .15;PA30,4;LBPRESSURE GAGE S3"
415   OUTPUT @P;"PU36.4,PD39.4;PU"
416   OUTPUT @P;"PA0,0 PU"
420   FOR I=1 TO 1968
430   OUTPUT @P;"PA";Nmaxm1*(I-1)*1000;A(I)*10;"PD"
440   NEXT I
450   OUTPUT @P;"PU"
460   OUTPUT @P;"PA33,-1 LBFREQUENCY = 10 KHZ"
470   OUTPUT @P;"PA30,-4 SI.1, .15;LBVERTICAL DIVISION = 40 PSI FOR APPLIED PRESSURE"
480   OUTPUT @P;"PA30,-7 LBVERTICAL DIVISION = 0.2 VOLT FOR PRESSURE GAGES"
490   END
```

```
REM --- PROGRAM TO PLOT TWO PRESSURE WAVEFORMS ON HP 7470A PLOTTER ---
REM --- FEBRUARY 1987 ---
REM
DIM A(3968),FC$(50),B(3968)
INPUT "INPUT FILE NAME FOR 1ST WAVEFORM",F1$
INPUT "INPUT FILE NAME FOR 2ND WAVEFORM",F2$
INPUT "INPUT GENERAL TITLE FOR GRAPH",FC$
INPUT "INPUT LEGEND TITLE FOR 1ST CURVE",L1$
INPUT "INPUT LEGEND TITLE FOR 2ND CURVE",L2$
INPUT "INPUT TABLE FOR 1ST WAVEFORM",T1$
INPUT "INPUT TABLE FOR 2ND WAVEFORM",T2$
ASSIGN @P TO F1$
ASSIGN @ TO F2$
ASSIGN @P TO 705
OUTPUT @P;"IN;SP1;IPI350,2000,9250,6000;"
OUTPUT @P;"SC0,4000,-300,300;"
OUTPUT @P;"PU0,-100 PD 4000,-100,4000,300,0,300,0,-100 PU"
OUTPUT @P;"SI.2,.3;TL1,3,0"
FOR X=0 TO 4000 STEP 500
OUTPUT @P;"PA";X;",-300;XT;"
IF X=0 THEN OUTPUT @P;"CP-1,-1;LB";X;""
IF X=0 THEN 180
IF X<1000 THEN OUTPUT @P;"CP-2,-1;LB";X;""
IF X=1000 THEN OUTPUT @P;"CP-3,-1;LB";X;""
NEXT X
OUTPUT @P;"PA2000,-400;CP-10,-2.3;LBTIME (MICROSECONDS)"
OUTPUT @P;"TL3,3,0"
FOR Y=-300 TO 300 STEP 100
OUTPUT @P;"PA0,";Y;"YT;"
IF Y=0 THEN OUTPUT @P;"CP-3,-.25;LB";Y;""
IF Y<>0 THEN OUTPUT @P;"CP-5,-.25;LB";Y;""
NEXT Y
OUTPUT @P;"PA0,0 CP-6.0,-3;DI0,1;LBPRESSURE (PSI)"
OUTPUT @P;"PA2300,300 SI.2,.3 CP2.16"
OUTPUT @P;"DI1,0 LB";FC$;""
OUTPUT @P;"PU"
REM
REM --- SHOW STRUCTURE ---
REM
OUTPUT @P;"PU3200,-100 PD3200,-92,4000,-92 PU"
OUTPUT @P;"PU3400,-177 PD 3600,-177,3800,-162,3400,-162,3400,-177 PU"
OUTPUT @P;"PU3440,-161 PD 3740,-161,3740,-175,3440,-175,3440,-161 PU"
OUTPUT @P;"PU3400 -141 PD 3600,-141,3800,-115,3400,-115,3400,-141 PU"
REM
REM --- SHOWING LOCATION OF GAGES ---
REM --- P1
OUTPUT @P;"PU3610,-161 PD 3610,-163,3590,-163,3590,-161 PU"
OUTPUT @P;"SI.2,.13;PA3600,-133;LBP1"
REM --- P2
OUTPUT @P;"PU3610,-162 PD 3610,-158,3590,-158,3590,-162 PU"
OUTPUT @P;"SI.2,.13;PA3610,-136;LBP2"
REM --- P3
OUTPUT @P;"PU3430,-162 PD 3430,-158,3440,-158,3440,-162 PU"
OUTPUT @P;"SI.2,.13;PA3430,-136;LBP3"
REM --- P4
OUTPUT @P;"PU3400,-170 PD 3380,-170,3380,-175,3400,-175 PU"
OUTPUT @P;"SI.2,.13;PA3300,-172;LBP4"
REM --- P5
OUTPUT @P;"PU3400,-210 PD 3400,-213,3380,-213,3380,-210,3400,-210 PU"
OUTPUT @P;"SI.2,.13;PA3300,-210;LBP5"
REM --- P6
OUTPUT @P;"PU3400,-174 PD 3400,-169 3380,-169,3380,-174,3400,-174 PU"
OUTPUT @P;"SI.2,.13;PA3300,-172;LBP6"
REM
REM --- LEGEND ---
REM
!OUTPUT @P;"PU3200,100 PD 3250,162,4000,162 PU"
!OUTPUT @P;"PU3400,100 PD 3600,162 PU"
!OUTPUT @P;"PU3040 100 PD 3040,162 PU"
!OUTPUT @P;"PU3230 100 PD 3230,162 PU"
!OUTPUT @P;"PU3440,100 PD 3440,162 PU"
!OUTPUT @P;"PU3710,100 PD 3710,162 PU"
!OUTPUT @P;"PU3200,234 PD 4000,234 PU"
!OUTPUT @P;"PU3200,208 PD 4000,208 PU"
!OUTPUT @P;"SI.1,.13;PA3300,100;CP2,-1.5;LBLINE     DESCRIPTION   TEXT   SCALE   STANDOFF
!OUTPUT @P;"LT"
!OUTPUT @P;"PU3230,231 PD 3380,231 PU"
!OUTPUT @P;"PA3610,231;LB";L1$;""
!OUTPUT @P;"LT4,6"
!OUTPUT @P;"PU3230,185 PD 3380,185 PU"
!OUTPUT @P;"PA3610,185;LB";L2$;""
!OUTPUT @P;"PA3100,231;LB";T1$(1,2);""
!OUTPUT @P;"PA3300,231;LB";T1$(3,6);""
!OUTPUT @P;"PA3600,231;LB";T1$(7,8);""
!OUTPUT @P;"PA3840,231;LB";T1$(9,10);""
!OUTPUT @P;"PA3100,185;LB";T2$(1,2);""
!OUTPUT @P;"PA3300,185;LB";T2$(3,6);""
!OUTPUT @P;"PA3600,185;LB";T2$(7,8);""
!OUTPUT @P;"PA3840,185;LB";T2$(9,10);""
ENTER @F1,General,A(*)
!OUTPUT @P;"PU"
!OUTPUT @P;"PA0,0 PU"
FOR I=1 TO 1968
!OUTPUT @P;"PA";General*(I-1)*1000000,A(I)*169;"PD"
!NEXT I
!OUTPUT @P;"PU"
!OUTPUT @P;"PA0,0 PU"
ENTER @F2,General,B(*)
!OUTPUT @P;"LT1,6"
FOR I=1 TO 1968
!OUTPUT @P;"PA";General*(I-1)*1000000 B(I)*169;"PD"
!NEXT I
!OUTPUT @P;"PU"
END
```

```
REM ---- PROGRAM TO PLOT PRESSURE IMPULSE WAVEFORMS ON HP PLOTTER ----
REM ---- FEBRUARY 1987 ----
REM
DIM A(3968),Fc$[50],B(3968)
INPUT "INPUT FILE NAME FOR 1ST WAVEFORM",F1$
INPUT "INPUT FILE NAME FOR 2ND WAVEFORM",F2$
INPUT "INPUT GENERAL TITLE FOR GRAPH",Fc$
INPUT "INPUT LEGEND TITLE FOR 1ST CURVE",L1$
INPUT "INPUT LEGEND TITLE FOR 2ND CURVE",L2$
INPUT "INPUT TABLE FOR 1ST WAVEFORM",T1$
INPUT "INPUT TABLE FOR 2ND WAVEFORM",T2$
ASSIGN @F1 TO F1$
ASSIGN @F2 TO F2$
ASSIGN @P TO 705
OUTPUT @P;"IN;SP1;IP1350,2000,9250,6000;"
OUTPUT @P;"SC0.4000,-300,300;"
OUTPUT @P;"PU0,-100 PD 4000,-100,4000,300,0,300,0,-100 PU"
OUTPUT @P;"SI.2,.3;TL1.5,0"
FOR X=0 TO 4000 STEP 500
OUTPUT @P;"PA";X;",-100;XT;"
IF X=0 THEN OUTPUT @P;"CP-1,-1;LB";X;""
IF X=0 THEN 180
IF X<1000 THEN OUTPUT @P;"CP-2,-1;LB";X;""
IF X>=1000 THEN OUTPUT @P;"CP-3,-1;LB";X;""
NEXT X
OUTPUT @P;"PA2000,-300;CP-10,-2.3;LBTIME (MICROSECONDS)"
OUTPUT @P;"TL1.5,0"
FOR Y=-100 TO 300 STEP 100
OUTPUT @P;"PA0,";Y;"YT;"
IF Y=0 THEN OUTPUT @P;"CP-5,-.25;LB";Y*.5;""
IF Y<>0 THEN OUTPUT @P;"CP-5,-.25;LB";Y*.5;""
NEXT Y
OUTPUT @P;"PA0,0 CP-6.0,-5;DI0,1;LBIMPULSE (PSI*SEC X-3)"
OUTPUT @P;"PA2500,300 SI.2,.3 CP2,16"
OUTPUT @P;"DI1,0 LB";Fc$;""
OUTPUT @P;"PU"
REM
REM ---- SHOW STRUCTURE ----
REM
OUTPUT @P;"PU3200,-100 PD3200,-92.4000,-92 PU"
OUTPUT @P;"PU3400,-177 PD 3800,-177,3800,-161,3400,-161,3400,-177 PU"
OUTPUT @P;"PU3440,-261 PD 3760,-261,3760,-175,3440,-175,3440,-261 PU"
OUTPUT @P;"PU3400,-141 PD 3800,-141,3800,-115,3400,-115,3400,-141 PU"
REM
REM ---- SHOWING LOCATION OF GAGES ----
REM ---- P1
OUTPUT @P;"PU3610,-161 PD 3610,-165,3590,-165,3590,-161 PU"
OUTPUT @P;"SI.1,.15;PA3600,-135;LB11"
REM ---- P2
OUTPUT @P;"PU3610,-162 PD 3610,-158,3590,-158,3590,-162 PU"
OUTPUT @P;"SI.1,.15;PA3610,-136;LB12"
REM ---- P3
OUTPUT @P;"PU3430,-162 PD 3430,-158,3440,-158,3440,-162 PU"
OUTPUT @P;"SI.1,.15;PA3430,-134;LB13"
REM ---- P4
OUTPUT @P;"PU3400,-170 PD 3380,-170,3380,-175,3400,-175 PU"
OUTPUT @P;"SI.1,.15;PA3390,-172;LB14"
REM ---- P5
OUTPUT @P;"PU3400,-219 PD 3400,-215,3380,-215,3380,-219,3400,-219 PU"
OUTPUT @P;"SI.1,.15;PA3390,-219;LB15"
REM ---- P6
OUTPUT @P;"PU3400,-174 PD 3400,-169,3380,-169,3380,-174,3400,-174 PU"
OUTPUT @P;"SI.1,.15;PA3390,-172;LB16"
REM
REM ---- LEGEND ----
REM
OUTPUT @P;"PU1400,-100 PD 1200,-100 PU"
OUTPUT @P;"PU1400,-100 PD 1400,-218.1200,-218 PU"
OUTPUT @P;"PU1800,-100 PD 1800,-238 PU"
OUTPUT @P;"PU2240,-100 PD 2240,-238 PU"
OUTPUT @P;"PU2410,-100 PD 2410,-238 PU"
OUTPUT @P;"PU2660,-100 PD 2660,-238 PU"
OUTPUT @P;"PU2910,-100 PD 2910,-238 PU"
OUTPUT @P;"PU1400,-144 PD 1200,-144 PU"
OUTPUT @P;"PU1400,-192 PD 1200,-192 PU"
OUTPUT @P;"SI .1, .15;PA1300,-100;CP2,-1.8;LB1;DE      DESCRIPTION    TEXT   SCALE   STANDOFF
OUTPUT @P;"LT"
OUTPUT @P;"PU1410,-169 PD 1780,-169 PU"
OUTPUT @P;"PA1810,-169;LB";L1$;""
OUTPUT @P;"LT4,4"
OUTPUT @P;"PU1410,-219 PD 1780,-219 PU"
OUTPUT @P;"PA1810,-219;LB";L2$,""
OUTPUT @P;"PA2300,-169;LB";T1$(1,2);""
OUTPUT @P;"PA2300,-169;LB";T1$(3,6);""
OUTPUT @P;"PA2800,-169;LB";T1$(7,8);""
OUTPUT @P;"PA3040,-169;LB";T1$(9,10);""
OUTPUT @P;"PA2300,-219;LB";T2$(1,2);""
OUTPUT @P;"PA2300,-219;LB";T2$(3,6);""
OUTPUT @P;"PA2800,-219;LB";T2$(7,8);""
OUTPUT @P;"PA3040,-219;LB";T2$(9,10);""
OUTPUT @P;"100,+000,-130,130;"
ENTER @F1,Nmaxm1,A(*)
OUTPUT @P;"LT"
OUTPUT @P;"PA0,0 PU"
FOR I=1 TO 3968
Amax=MAX(Amax,ABS(A(I)*Nmaxm1*1000
OUTPUT @P "PA" ,Nmaxm1*I-1,(I)*1000000;"PD"
NEXT I
OUTPUT @P;"PU"
OUTPUT @P;"PA0 0 PU"
ENTER @F2,Nmaxm1,B(*)
OUTPUT @P;"LT4 4"
FOR I=1 TO 3968
Amax=MAX(Amax,ABS(B(I)*Nmaxm1*1000
OUTPUT @P "PA" ,Nmaxm1*I-1,(I)*1000000 ;"PD"
NEXT I
OUTPUT @P "PU"
END
```

```
REM ── PROGRAM TO PLOT STRAIN WAVEFORMS ON HP 7470A PLOTTER ──
REM ── JANUARY 1987 ──
REM
DIM A(2048),B(2048),Fc$[50]
INPUT "INPUT FILE NAME FOR 1ST. WAVEFORM",F1$
INPUT "INPUT FILE NAME FOR 2ND. WAVEFORM",F2$
INPUT "INPUT GENERAL TITLE FOR GRAPH",Fc$
INPUT "INPUT LEGEND TITLE FOR 1ST CURVE",L1$
INPUT "INPUT LEGEND TITLE FOR 2ND CURVE",L2$
INPUT "INPUT TABLE FOR 1ST WAVEFORM",T1$
INPUT "INPUT TABLE FOR 2ND WAVEFORM",T2$
ASSIGN @F1 TO F1$
ASSIGN @F2 TO F2$
ASSIGN @P TO 705
OUTPUT @P;"IN;SP1;IP1250,2000,9250,6000;"
OUTPUT @P;"SC0,2000,-450,650;"
OUTPUT @P;"PU0,-450 PD 2000,-450,2000,650,0,650,0,-450 PU"
OUTPUT @P;"PA0,0 PD 2000,0 PU"
OUTPUT @P;"SI.2,.3;TL1,3,0"
FOR X=0 TO 2000 STEP 200
OUTPUT @P;"PA";X,"-450;XT;"
IF X=0 THEN OUTPUT @P;"CP-1,-1;LB";X;""
IF X=0 THEN 210
IF X<1000 THEN OUTPUT @P;"CP-2,-1;LB";X*1.5;""
IF X>=1000 THEN OUTPUT @P;"CP-3,-1;LB";X*1.5;""
NEXT X
OUTPUT @P;"PA1000,-650;CP-10,-2.5;LBTIME (MICROSECONDS)"
OUTPUT @P;"TL1,3,0"
FOR Y=-400 TO 400 STEP 100
OUTPUT @P;"PA0,";Y,"YT;"
IF Y=0 THEN OUTPUT @P;"CP-3,-.25;LB";Y;""
IF Y<>0 THEN OUTPUT @P;"CP-3,-.25;LB";Y;""
NEXT Y
OUTPUT @P;"PA0,0 CP-4.0,-3;DI0,1;LBSTRAIN (MICRO IN/IN)"
OUTPUT @P;"PA1250,650 SI.2,.3 CP2,1;"
OUTPUT @P;"SI1,0 LB";Fc$;""
OUTPUT @P;"PU1600,-650 PD1600,-100,2000,-200 PU"
OUTPUT @P;"PU1700,-600 PD 1900,-600,1900,-130,1700,-130,1700,-600 PU"
OUTPUT @P;"PU1730,-565 PD 1870,-565,1870,-180,1730,-180,1730,-565 PU"
OUTPUT @P;"PU1700,-103 PD 1900,-103,1900,-230,1700,-230,1700,-103 PU"
REM
REM ── SHOWING LOCATION OF TEST GAGES ──
REM ── 12
OUTPUT @P;"PU1770,-180 PD 1780,-180,1780,-185,1770,-185,1770,-180 PU"
OUTPUT @P;"SI.1,.15;PA1740,-410;LB12"
REM ──11
REM ── 13
OUTPUT @P;"PU1770,-330 PD 1780,-330,1780,-340,1770,-345,1770,-340 PU"
OUTPUT @P;"SI.1,.15;PA1740,-335;LB11"
REM ── 15
OUTPUT @P;"PU1700,-475 PD 1700,-465,1690,-465,1690,-475,1700,-475 PU"
OUTPUT @P;"SI.1,.15;PA1650,-475;LB13"
REM ── 16
OUTPUT @P;"PU1730,-475 PD 1730,-465,1740,-465,1740,-475,1730,-475 PU"
OUTPUT @P;"SI.1,.15;PA1750,-475;LB14"
REM ── 17
OUTPUT @P;"PU1600,-600 PD 1610,-600,1610,-610,1600,-610,1600,-600 PU"
OUTPUT @P;"SI.1,.15;PA1613,-623;LB17"
REM ── 18
OUTPUT @P;"PU1600,-370 PD 1610,-370,1610,-360,1600,-360,1600,-370 PU"
OUTPUT @P;"SI.1,.15;PA1613,-350;LB18"

REM
REM ── LEGEND ──
REM
OUTPUT @P;"PU1100,410 PD 1100,350,1500,350 PU"
OUTPUT @P;"PU1100,410 PD 1100,350 PU"
OUTPUT @P;"PU1320,410 PD 1320,350 PU"
OUTPUT @P;"PU1610,410 PD 1610,350 PU"
OUTPUT @P;"PU1740,410 PD 1740,350 PU"
OUTPUT @P;"PU1871,410 PD 1871,350 PU"
OUTPUT @P;"PU1100,330 PD 1000,330 PU"
OUTPUT @P;"PU1120,-10 PD 1500,-10 PU"
OUTPUT @P;"SI .1, .15;PA1130,610;CP2,-1.5;LB1/8"     DESCRIPTION   TEST   SCALE   TRANSDUCER
OUTPUT @P;"PA1120,100;LBNOTE: POSITIVE STRAIN = TENSION ... NEGATIVE STRAIN = COMP."
OUTPUT @P;"
OUTPUT @P;"PU1113,100 PD 1190,100 PU"
OUTPUT @P;"PA1110,100;LB";L1$,""
OUTPUT @P;"SI .1 ;"
OUTPUT @P;"PU1113,-30 PD 1190,-30 PU"
OUTPUT @P;"PA1110,-30;LB" L2$,""
OUTPUT @P;"PA1310,100;LB";T1$(1,2),""
OUTPUT @P;"PA1610,100;LB";T1$(3,4),""
OUTPUT @P;"PA1800,100;LB";T1$(5,6),""
OUTPUT @P;"PA1910,100;LB";T1$(9,10),""
OUTPUT @P;"PA1310,-30;LB";T2$(1,2),""
OUTPUT @P;"PA1610,-30;LB";T2$(3,4),""
OUTPUT @P;"PA1800,-30;LB";T2$(5,6),""
OUTPUT @P;"PA1910,-30;LB";T2$(9,10),""
OUTPUT @P;"SC0,2000,-410,690"
ENTER @F1,Header$,A(*)
OUTPUT @P;"SP2"
OUTPUT @P;"PA0,0;PD"
FOR I=1 TO 2048
OUTPUT @P;"PA";I*(2000/2048),A(I)*(1000/4095);"PD"
NEXT I
OUTPUT @P;"PU"
ENTER @F2,Header$,B(*)
OUTPUT @P;"SP3"
OUTPUT @P;"PA0,0;PD"
FOR I=1 TO 2048
OUTPUT @P;"PA";I*(2000/2048),B(I)*(1000/4095);"PD"
NEXT I
OUTPUT @P;"PU"
END
```

```
10    REM ── PROGRAM TO PLOT ACCELERATION WAVEFORMS ON HP 7470A PLOTTER ──
20    REM ── FEBRUARY 1987 ──
30    REM
40    DIM A(2048),B(2048),Fn$[30]
50    INPUT "INPUT FILE NAME FOR LST. WAVEFORM",Fl$
70    ASSIGN @F1 TO Fl$
80    ASSIGN @P TO 705
100   OUTPUT @P;"IN;SP1;IP1350,2000,9250,6000;"
110   OUTPUT @P;"SC0,2000,-650,650;"
120   OUTPUT @P;"PD0,-650 PD 2000,-650,2000,650,0,650,0,-650 PU"
130   OUTPUT @P;"PA0,0 PD 2000,0 PU"
140   OUTPUT @P;"SI.2,.3;TL1,3,0"
150   FOR X=0 TO 2000 STEP 200
160   OUTPUT @P;"PA";X,",-650;XT;"
170   IF X=0 THEN OUTPUT @P;"CP-1,-1;LB";X;""
180   IF X=0 THEN 210
190   IF X<1000 THEN OUTPUT @P;"CP-2,-1;LB";X*1.5;""
200   IF X>=1000 THEN OUTPUT @P;"CP-3,-1;LB";X*1.5;""
210   NEXT X
260   OUTPUT @P;"PA1000,-650;CP-10,-2.5;LB(TIME (MICROSECONDS))"
270   OUTPUT @P;"TL1,3,0"
280   FOR Y=-600 TO 600 STEP 200
290   OUTPUT @P;"PA0,";Y,"YT;"
300   IF Y<0 THEN OUTPUT @P;"CP-3,-.25;LB";Y;""
310   IF Y>=0 THEN OUTPUT @P;"CP-3,-.25;LB";Y*1;""
320   NEXT Y
370   INPUT "INPUT GENERAL TITLE FOR GRAPH",Ft$
384   OUTPUT @P;"PA0,0 CP-6.0,-3;DI0,1;LB ACCELERATION (G'S) "
390   OUTPUT @P;"PA1250,650 SI.1,.3 CP2,16"
400   OUTPUT @P;"DI1,0 LB";Ft$;""
410   OUTPUT @P;"PU1600,-650 PD1600,-200,2000,-200 PU"
420   OUTPUT @P;"PU1700,-600 PD 1900,-600,1900,-150,1700,-150,1700,-600 PU"
430   OUTPUT @P;"PU1730,-565 PD 1870,-565,1870,-180,1730,-180,1730,-565 PU"
440   OUTPUT @P;"PU1700,-503 PD 1900,-503,1900,-150,1700,-150,1700,-503 PU"
450   REM
460   REM ── MOVING LOCATION OF TEXT CASES ──
461   REM ── A1
470   OUTPUT @P;"PU1800,-180 PD 1810,-180,1810,-185,1800,-185,1800,-,88 PU"
471   OUTPUT @P;"SI.1,.15;PA1780,-410;LBA1"
486   REM ── A2
488   OUTPUT @P;"PU1730,-475 PD 1730,-465,1760,-465,1760,-475,1730,-475 PU"
489   OUTPUT @P;"SI.1,.15;PA1750,-475;LBA2"
503   REM
504   REM ── LEGEND ──
505   REM
506   INPUT "INPUT LEGEND TITLE FOR 1ST CURVE",L1$
507   INPUT "INPUT CALIBRATION VALUE:",F$$$
509   OUTPUT @P;"PU1100,650 PD 1100,650,2000,650 PU"
510   OUTPUT @P;"PU1300,650 PD 1300,650 PU"
511   OUTPUT @P;"PU1520,650 PD 1520,650 PU"
512   OUTPUT @P;"PU1610,650 PD 1610,650 PU"
513   OUTPUT @P;"PU1760,650 PD 1760,650 PU"
514   OUTPUT @P;"PU1873,650 PD 1873,650 PU"
515   OUTPUT @P;"PU1100,350 PD 2000,350 PU"
516   OUTPUT @P;"PU1100,450 PD 2000,450 PU"
517   OUTPUT @P;"SI.1,.15;PA1130,550;CP2,-1.5;LB1,INS      DESCRIPTION   TEST   SCALE   STANDOFF
518   OUTPUT @P;"PA1100,-400;LBNOTE: POSITIVE ACCELERATION IS DIRECTED AWAY FROM THE BASE"
519   INPUT "INPUT TABLE FOR 1ST WAVEFORM",T1$
522   OUTPUT @P;"LT"
523   OUTPUT @P;"PU1113,350 PD 1290,300 PU"
524   OUTPUT @P;"PA1310,300;LB";L1$;""
525   OUTPUT @P;"PA1330,300;LB";T1$[1,2];""
529   OUTPUT @P;"PA1610,300;LB";T1$[3,6];""
530   OUTPUT @P;"PA1890,300;LB";T1$[7 8];""
531   OUTPUT @P;"PA1910,300;LB" T1$[9,10];""
534   OUTPUT @P;"SC0 1000,-1200,1200"
537   ENTER @F1 #wave1,A(*)
538   OUTPUT @P;"SI"
539   OUTPUT @P;"PA0 0 PU"
540   FOR I=1 TO 400
541   OUTPUT @P;"PA" #wave1*(I-1)*1000000;A(I)*F$$$;"PD"
549   NEXT I
551   OUTPUT @P;"PU"
553   END
```

```
10    REM --- PROGRAM TO PLOT VELOCITY WAVEFORMS ON HP 7470A PLOTTER ---
11    REM --- THIS PROGRAM INTEGRATES ACCELERATION WAVEFORMS ---
20    REM --- FEBRUARY 1987 ---
30    REM
40    DIM A(2048),Fc$(50),B(2048)
50    INPUT "INPUT ACCEL. FILE NAME FOR 1ST. WAVEFORM",F1$
51    INPUT "INPUT ACCEL. FILE NAME FOR 2ND. WAVEFORM",F2$
53    INPUT "INPUT GENERAL TITLE FOR GRAPH",Fc$
54    INPUT "INPUT LEGEND TITLE FOR 1ST CURVE",L1$
55    INPUT "INPUT LEGEND TITLE FOR 2ND CURVE",L2$
57    INPUT "INPUT CALIBRATION VALUE:",Ffff
58    INPUT "INPUT TABLE FOR 1ST WAVEFORM",T1$
59    INPUT "INPUT TABLE FOR 2ND WAVEFORM",T2$
64    INPUT "INPUT CORRECTION VALUE FOR 1ST CURVE",Xmm
65    INPUT "INPUT CORRECTION VALUE FOR 2ND CURVE",Xmm1
70    ASSIGN @F1 TO F1$
80    ASSIGN @F2 TO F2$
90    ASSIGN @P TO 705
100   OUTPUT @P;"IN;SP1;IP1350,2000,9250,6000;"
110   OUTPUT @P;"SC0,2000,-450,650;"
120   OUTPUT @P;"PU0,-450 PD 2000,-450,2000,650,0,650,0,-450 PU"
130   OUTPUT @P;"PA0,0 PD 2000,0 PU"
140   OUTPUT @P;"SI.2,.3;TL1.5,0"
150   FOR X=0 TO 2000 STEP 200
160   OUTPUT @P;"PA";X,",-450;XT;"
170   IF X=0 THEN OUTPUT @P;"CP-1,-1;LB";X;""
180   IF X=0 THEN 210
190   IF X<1000 THEN OUTPUT @P;"CP-2,-1;LB";X*1.3;""
200   IF X>=1000 THEN OUTPUT @P;"CP-3,-1;LB";X*1.3;""
210   NEXT X
260   OUTPUT @P;"PA1000,-450;CP-10,-2.5;LBTIME (MICROSECONDS)"
270   OUTPUT @P;"TL1.5,3"
280   FOR Y=-400 TO 600 STEP 100
290   OUTPUT @P;"PA0,";Y,"YT;"
300   IF Y=0 THEN OUTPUT @P;"CP-3,-.25;LB";Y;""
310   IF Y<>0 THEN OUTPUT @P;"CP-5,-.25;LB";Y/100;""
320   NEXT Y
384   OUTPUT @P;"PA0,0 CP-6.0,-3;DI0,1;LB VELOCITY (CM/SEC) "
390   OUTPUT @P;"PA1250,650 SI.2,.3 CP2,.4"
400   OUTPUT @P;"DI1,0 LB";Fc$;""
410   OUTPUT @P;"PU1600,-450 PD1600,-100,2000,-100 PU"
420   OUTPUT @P;"PU1700,-400 PD 1900,-400,1900,-330,1700,-330,1700,-400 PU"
430   OUTPUT @P;"PU1730,-165 PD 1870,-165,1870,-100,1730,-100,1730,-165 PU"
440   OUTPUT @P;"PU1700,-165 PD 1900,-165,1900,-130,1700,-130,1700,-165 PU"
450   REM
460   REM --- SHOWING LOCATION OF TEST CASES ---
461   REM --- A1
473   OUTPUT @P;"PU1800,-180 PD 1810,-180,1810,-165,1800,-165,1800,-180 PU"
475   OUTPUT @P;"SI.1,.15;PA1780,-410;LBA1"
484   REM --- A2
488   OUTPUT @P;"PU1730,-475 PD 1710,-465,1740,-465,1740,-475,1730,-475 PU"
489   OUTPUT @P;"SI.1,.15;PA1750,-475;LBA2"
103   REM
104   REM --- LEGEND ---
108   REM
109   OUTPUT @P;"PU1100,450 PD 1100,350,2000,350 PU"
110   OUTPUT @P;"PU1300,450 PD 1300,350 PU"
111   OUTPUT @P;"PU1520,450 PD 1520,350 PU"
112   OUTPUT @P;"PU1610,450 PD 1610,350 PU"
112   OUTPUT @P;"PU1740,450 PD 1740,350 PU"
114   OUTPUT @P;"PU1875,450 PD 1875,350 PU"
115   OUTPUT @P;"PU1130 110 PD 1300 110 PU"
116   OUTPUT @P;"PU1130,-10 PD 1330 -10 PU"
[illegible] OUTPUT @P;"SI .1,.15;PA1110 510 CP2,-1,4;LBCURVE      DESCRIPTION   TEST   SCALE   STANDOFF"
[illegible] OUTPUT @P;"PA1100 300;LBNOTE: POSITIVE VELOCITY IS DIRECTED AWAY FROM THE BASE"
[illegible] OUTPUT @P;"SP2"
[illegible] OUTPUT @P;"PU1113,100 PD 1290 100 PU"
[illegible] OUTPUT @P;"PA1310,100;LB";L1$;""
[illegible] OUTPUT @P;"SP3"
[illegible] OUTPUT @P;"PU1113 -40 PD 1290 -40 PU"
[illegible] OUTPUT @P;"PA1310 -40;LB";L2$;""
[illegible] OUTPUT @P;"PA1310,100;LB";T1$[1,2];""
[illegible] OUTPUT @P;"PA1610 100;LB";T1$[3,4];""
[illegible] OUTPUT @P;"PA1600 100;LB";T1$[5,8];""
[illegible] OUTPUT @P;"PA1920 100;LB";T1$[9,10];""
[illegible] OUTPUT @P;"PA1310 -40;LB";T2$[1,2];""
[illegible] OUTPUT @P;"PA1610 -40;LB";T2$[3,4];""
[illegible] OUTPUT @P;"PA1600 -40;LB";T2$[5,8];""
[illegible] OUTPUT @P;"PA1920 -40;LB";T2$[9,10];""
[illegible] OUTPUT @P;"SC0 1280 -45 3.85 0"
[illegible] ENTER @F1 Amerma,A(*)
[illegible] OUTPUT @P;"SP2"
[illegible] OUTPUT @P;"PA0 0 PD"
[illegible] [illegible]
[illegible] FOR I=1 TO 400
[illegible] IF I=1 THEN [illegible] Ffff
[illegible] [illegible] Ffff [illegible] Amerma [illegible]
[illegible] OUTPUT @P;"PA" Amerma [illegible] 1000000 [illegible]
[illegible] NEXT I
[illegible] OUTPUT @P;"PU"
[illegible] ENTER @F2 Amerma,B(*)
[illegible] OUTPUT @P;"SP3"
[illegible] OUTPUT @P;"PA0 0 PD"
[illegible]
[illegible] FOR I=1 TO 400
[illegible] [illegible] Ffff
[illegible] [illegible] Ffff [illegible] Amerma [illegible]
[illegible] OUTPUT @P;"PA" Amerma [illegible] 1000000 [illegible]
[illegible] NEXT I
[illegible] OUTPUT @P;"PU"
END
```

```
REM ── PROGRAM TO PLOT DISPLACEMENT WAVEFORMS ON HP 7470A PLOTTER ──
REM ── THIS PROGRAM DOUBLE INTEGRATES ACCELERATION WAVEFORMS ──
REM ── FEBRUARY 1987 ──
REM
DIM A(2048),Z$(501,8(2048)
INPUT "INPUT ACCEL. FILE NAME FOR 1ST. WAVEFORM",F1$
INPUT "INPUT ACCEL. FILE NAME FOR 2ND. WAVEFORM",F2$
INPUT "INPUT GENERAL TITLE FOR GRAPH",T$
INPUT "INPUT LEGEND TITLE FOR 1ST CURVE",L1$
INPUT "INPUT LEGEND TITLE FOR 2ND CURVE",L2$
INPUT "[ENTER CALIBRATION VALUE:",.FFFF
INPUT "INPUT TABLE FOR 1ST WAVEFORM",T1$
INPUT "INPUT TABLE FOR 2ND WAVEFORM",T2$
INPUT "INPUT CORRECTION VALUE FOR 1ST CURVE",Xm
INPUT "INPUT CORRECTION VALUE FOR 2ND CURVE",Xm1
ASSIGN @F1 TO F1$
ASSIGN @F2 TO F2$
ASSIGN @P TO 705
OUTPUT @P:"IN;SP1;PI1350,2000,9250,4000;"
OUTPUT @P:"SC0,2000,-650,650;"
OUTPUT @P:"FOO,-650 PD 2000,-650,2000,650,0,650,0,-650 PD"
OUTPUT @P:"PA0,0 PD 2000,0 PU"
OUTPUT @P:"SI.2,.3;TL1,3.0"
FOR X=0 TO 1000 STEP 200
OUTPUT @P:"PA":X,",-650;ST;"
IF X=0 THEN OUTPUT @P:"CP-1,-1;LB":X;""
IF X=0 THEN 110
IF X<1000 THEN OUTPUT @P:"CP-2,-1;LB":X*1.3;""
IF X=1000 THEN OUTPUT @P:"CP-3,-1;LB":X*1.3;""
NEXT X
OUTPUT @P:"PA1000,-650;CP-10,-3.5;LBTIME (MICROSECONDS)"
OUTPUT @P:"TL1,3.0"
FOR Y=-600 TO 600 STEP 100
OUTPUT @P:"PA0,";Y;"PY;"
IF Y=0 THEN OUTPUT @P:"CP-3,-.25;LB";Y;""
IF Y<>0 THEN OUTPUT @P:"CP-3,-.25;LB";Y* 0001;""
NEXT Y
OUTPUT @P:"PA0,0 CP-6.0,-3;SI0.1;LB DISPLACEMENT (IN) "
OUTPUT @P:"PA1350,650 SI.2,.3 CP3,1A"
OUTPUT @P:"SI1.0 LB" F$@;""
OUTPUT @P:"PU1600,-650 PD1600,-200,2000,-200 PU"
OUTPUT @P:"PU1700,-600 PD 1900,-600,1950,-150,1700,-150,1700,-600 PU"
OUTPUT @P:"PU1730,-165 PD 1870,-165,1870,-300,1730,-150,1730,-165 PU"
OUTPUT @P:"PU1790,-165 PD 1900,-165,1900,-150,1790,-150,1790,-300 PU"
REM
REM ── SHOWING LOCATION OF TEXT CARDS ──
REM ── A1
OUTPUT @P:"PU1800,-100 PD 1810,-100,1810,-150,1800,-150,1800,-100 PU"
OUTPUT @P:"SI.1, 12:DA1700,-410:LBA1"
REM ── A2
OUTPUT @P:"PU1730,-475 PD 1730,-465,1740,-465,1740,-475,1730,-475 PU"
OUTPUT @P:"SI.1, 13:DA1730,-475;LBA2"
REM
REM ── LEGEND ──
REM
OUTPUT @P:"PU1100,650 PD 1100,250,2000,250 PU"
OUTPUT @P:"PU1300,650 PD 1300,250 PU"
OUTPUT @P:"PU1320,650 PD 1320,250 PU"
OUTPUT @P:"PU1610,650 PD 1610,250 PU"
OUTPUT @P:"PU1740,650 PD 1740,250 PU"
OUTPUT @P:"PU1870,650 PD 1870,250 PU"
OUTPUT @P:"PU1900,650 PD 1900,250 PU"
OUTPUT @P:"PU1920,650 PD 1900,250 PU"
OUTPUT @P:"SI .  .3 PA1130,650;CP2.-1 3;LB[ENT      DESCRIPTION   TEXT   SCALE   STANDARD
OUTPUT @P:"PA1100,200 LBNOTE: POSITIVE DISPLACEMENT IS DIRECTION AWAY FROM THE BASE"
OUTPUT @P:"LT"
OUTPUT @P:"PU1910,100 PD 1990,100 PU"
OUTPUT @P:"PA1910,100 LB" L1$,""
OUTPUT @P:"LT4,3"
OUTPUT @P:"PU1910,-50 PD 1990,-50 PU"
OUTPUT @P:"PA1910,-50 LB" L2$,""
OUTPUT @P:"PA1930,150 LB" T1$(1,2);""
OUTPUT @P:"PA1930,100 LB" T1$(3,6);""
OUTPUT @P:"PA1940,150 LB" T2$(1,2);""
OUTPUT @P:"PA1940,100 LB" T2$(3,6);""
OUTPUT @P:"PA1930,-50 LB" T1$(1,2);""
OUTPUT @P:"PA1930,-100 LB" T1$(3,6);""
OUTPUT @P:"PA1940,-50 LB" T2$(1,2);""
OUTPUT @P:"PA1940,-100 LB" T2$(3,6);""
OUTPUT @P:"PA1920,-150 LB" T$(1,20);""
OUTPUT @P:"SC0 2000  65 0.65 0"
ENTER @F1 Xm,Ym,A1,**
OUTPUT @P:"LT"
OUTPUT @P:"PA0,0 PU"
[Xm]
Ym=0
FOR I=1 TO 4096
IF I=1 THEN A(I)=-Ym/FFFF
A(I)=A(I-1)+FFFF*(-Ym+A(I))/2^12
Ym=(Ym+A(I))*FFFF
OUTPUT @P "PA" Xm*1.3;A(I)*1000000 Ym*1000;"PD"
EXIT I
OUTPUT @P ;"PU"
ENTER @F2 Xm,Ym,A1,**
OUTPUT @P "LT4,3"
OUTPUT @P "PA0,0 PU".
[Xm]
Ym=0
FOR I=1 TO 4096
IF I=1 THEN A(I)=-Ym/FFFF
A(I)=A(I-1)+FFFF*(-Ym+A(I))/2^12
Ym=(Ym+A(I))*FFFF
OUTPUT @P "PA" Xm*1.3;A(I)*1000000 Ym*1000 "PD"
EXIT I
OUTPUT @P ;"PU"
END
```

REFERENCES

Al-Hussaini, M.M.; Goodings, D.J.; Scofield, A.N.; Townsend, F.C., "Centrifuge Modeling of Coal Waste Embankments," ASCE Journal of the Geotechnical Engineering Division, Vol. 107, No. GT4, April, 1981, pp 481-499.

Baird, G.T., Instrumentation for Centrifugal Testing, Task Report, E. H. Wang Civil Engineering Laboratory, Kirtland AFB, New Mexico, 1984.

Baker, W.E.; Westine, P.S.; Dodge, F.T., Similarity Methods In Engineering Dynamics, Hayden Book Company, Rochelle Park, New Jersey, 1973.

Bloomquist, D., Centrifuge Modeling of Large Strain Consolidation Phenomena in Phosphatic Clay Retention Ponds, Ph.D. Dissertation, University of Florida, Gainesville, Florida, 1982.

Bradley, D.M., Centrifugal Scaling Laws For Ground Launch Cruise Missile Shelter, Master's Report, University of Florida, Gainesville, Florida, December, 1983.

Bur, A.J.; Roth, S.C., "A Polymer Pressure Gage for Dynamic Pressure Measurements," Proceedings of the Second Symposium on the Interaction of Non-nuclear Munitions With Structures, Panama City Beach, Florida, April 15-18, 1985.

Cady, W.G., Piezoelectricity; An Introduction to the Theory and Applications of Electromechanical Phenomena in Crystals, 2nd ed., Vol. 1, McGraw-Hill Book Company, 1964.

Chung, R.M.; Bur, A.J.; Holder, J.R.,"Laboratory Evaluation of an NBS Polymer Stress Gage," Proceedings of the Second Symposium on the Interaction of Non-nuclear Munitions with Structures, Panama City Beach, Florida, April 15-18, 1985.

Craig, W.H., "Modeling Pile Installations in Centrifuge Experiments," Proceedings of the 11th International Conference on Soil Mechanics and Foundation Engineering,

Vol. 2, San Francisco, 1985.

Cunningham, C.H.; Townsend, F.C.; Fagundo, F.E., The Development Of Micro-concrete For Scale Model Testing Of Buried Structures, ESL-TR-85-49, Air Force Engineering And Services Center, Tyndall Air Force Base, Florida, January, 1986.

Denton, D.R.; Flathau, W.J., "Model Study of Dynamically Loaded Arch Structures," ASCE Journal Of Engineering Mechanics, Vol. 92, No. EM3, June, 1966, pp 17-32.

Dove, R.C.; Adams, P.H., Experimental Stress Analysis and Motion Measurements, C.E. Merrill Books, Columbus, Ohio, 1964.

Dragnich, R.G.; Calder, C.A.,"A Sandwich-transducer Technique for Measurement of Internal Dynamic Stress," Experimental Mechanics, May 1973, pp 199-203.

D'Souza A.F.; Garg V.K., Advanced Dynamics: Modeling and Analysis, Prentice-Hall, Englewood Cliffs, N.J., 1984.

Endevco General Catalog, Endevco Corporation, San Juan Capistrano, California, 1986.

Endevco, TP101, Endevco Technical Paper 101, Endevco Corporation, San Juan Capistrano, California, 1986.

Fiodorov, I.S.; Melnik, V.G.; Teitelbaum, A.I.; Sarrina, V.A.; Vogdeo, V.N.; Vutsel, V.I.; Schcherbina, V.I.; Yakoleva, T.G., "Centrifugal Tests of Embankment Dams and Dikes," Proccedings of the 11th International Conference on Soil Mechanics and Foundation Engineering, Vol. 2, San Francisco, 1985.

FS10 Owners Manual, Operation of EBW Firing System, Model FS-10, Reynolds Industries, Inc., San Ramon, California, 1981.

Gill, J.J., Centrifugal Modeling Of A Subterranean Structure Subjected To Blast Loading, Master's Report, University of Florida, Gainesville, Florida, December, 1985.

Gran, J.K.; Bruce, J.R.; Colton, J.A., "Scale Modeling Of Buried Reinforced Concrete Structures Under Air-Blast Loading," ACI Special Publication SP 73-7, 1973, pp 125-142.

Gurtin, M.E., "The Effect of Accelerometer Low-Frequency Response on Transient Measurements," Experimental Mechanics, Vol. 18, No. 1, June, 1961, pp 206-208.

Hetenyi, M.I., Handbook of Experimental Stress Analysis,

Wiley, New York, 1950.

Holder, J.R.; Chung, R.M.; Bur, A.J., "Field Evaluation of the Polymer Stress Gage," Proceedings of Second Symposium on the Interaction of Non-nuclear Munitions with Structures, Panama City Beach, Florida, April 15-18, 1985.

Kantrowitz, P.; Kousourou, G.; Zucker, L., Electronic Measurements, Prentice-Hall, Englewood Cliffs, N.J., 1979.

Krauthammer, T., "Shallow-Buried RC Box-Type Structures," ASCE Journal Of Structural Engineering, Vol. 110, No. 3, March, 1984, pp 637-651.

Krawinker H.; Moncarz, P.D., "Similitude Requirements for Dynamic Models," ACI Special Publication SP 73-1, 1973.

Kulkarni, K.R.; Chandrasekaran, V.S.; King, G.J.W., "Centrifugal Model Studies on Laterally Loaded Pile Groups in Sand," Proceedings of the 11th International Conference on Soil Mechanics and Foundation Engineering, Vol. 2, San Francisco, 1985.

Kutter, B.L.; O'Leary, L.M.; Thompson, P.Y., "Centrifugal Modeling of the Effect of Blast Loading on Tunnels," Proceedings of Second Symposium on the Interaction of Non-Nuclear Munitions with Structures, Panama City Beach, Florida, April 15-18, 1985.

Langhaar, H.L., Dimensioal Analysis and Theory of Models, John Wiley and Sons, New York, 1951.

Malmstadt, H.V.; Enke, C.G.; Crouch, S.R., Electronics and Instrumentation for Scientists, Benjamin/Cummings Pub. Co., Reading, Mass., 1981.

McVay, M.C.; Papadopoulos, P.C., "Long-Term Behavior of Buried Large-Span Culverts," ASCE Journal of Geotechnical Engineering, Vol. 112, No.4, April, 1986, pp 424-442.

Meeks, S.W.; Ting, R.Y., "Effects of Static and Dynamic Stress on the Piezoelectric and Dielectric Properties of PVF2," J. Acoust. Soc. Am., Vol. 74, No. 6, Dec. 1983, pp 1681-1686.

Meeks, S.W.; Ting, R.Y., "The Evaluation of PVF2 for Underground Shock-wave Sensor Application," J. Acoust. Soc. Am., Vol. 75, No. 3, March, 1984, pp 1010-1012.

Murphy, G., Similitude in Engineering, Ronald Press Co., New York, 1950.

Nielsen, J.P., The Centrifugal Simulation Of Blast Parameters, ESL-TR-83-12, Air Force Engineering And Services Center, Tyndall Air Force Base, Florida, December, 1983.

Nye, J.F., Physical Properties of Crystals, Their Representation by Tensors and Matrices, Clarenden Press, Oxford, 1957.

Pan, F., "Analysis of Variation of Poisson's Ratio with Depth of Soil," Proceedings of the International Conference on Recent Advances In Geotechnical Earthquake Engineering a. Soil Dynamics, Vol. 1, St. Louis, April, 1981.

Pan, F., "The Relation Between Dynamic Elastic Parameters and Depth of Soil," Proceedings of Conference on Soil Dynamics a. Earthquake Engineering, Vol. 1, Southampton, U.K., July, 1982.

Prevost, J.H.; Cury, B.; Scott, R.F., "Offshore Gravity Structures: Centrifugal Modeling," ASCE Journal of the Geotechnical Engineering Division, Vol. 107, No. GT2, February, 1981, pp 125-141.

Randolph, M.F.; Ah-Tech, C.Y.; Murray, R.T., "Centrifuge Study of Spill-Through Abutments," Proceedings of the 11th International Conference on Soil Mechanics and Foundation Engineering, Vol. 2, San Francisco, 1985.

Riedel, J., "The Accurate Measurement of Shock Phenomena," Endevco Technical Paper 214, Endevco Corporation, San Juan Capistrano, California, 1986.

Sabnis, G.M.; White, R.N.; "A Gypsum Mortar For Small-Scale Models," ACI Journal, Vol. 64, No. 11, November, 1967, pp 767-774.

Sabnis, G.M.; Harris,H.G.; White, R.N.; Mirza, M.S., Structural Modeling and Experimental Techniques, Prentice-Hall, Englewood Cliffs, N.J., 1983.

Schmidt, R.M.; Holsapple, K.A., "Theory and Experiments on Centrifuge Cratering," Journal of Geophysical Research, Vol. 85, No. B1, January, 1980, pp 235-251.

Tener, R.K., "The Application of Similitude to Protective Construction Research," Proceedings of the Symposium on Soil-Structure Interaction, Tucson, Arizona, September, 1964.

THORN EMI notes, Information supplied by THORN EMI Central Research Laboratories, Dawley Road, Hayes, Middlesex, England, 1986.

Williams, M.; McFetridge, G., "Unbalanced-bridge Computational Techniques and Accuracy for Automated Multichannel Strain-measuring Systems," Experimental Techniques, April 1983, pp 32-37.

Wong, F.S.; Weidlinger, P., "Design Of Underground Protective Structures," ASCE Journal Of Structural Engineering, Vol. 109, No. 8, August, 1983, pp 1972-1979.

Young, D.F.; Murphy, G., "Dynamic Similitude Of Underground Structures," ASCE Journal Of Engineering Mechanics, Vol. 90, No. EM3, June, 1964, pp 111-131.

(The reverse of this page is blank.)

DISCLAIMER NOTICE

THIS DOCUMENT IS BEST QUALITY PRACTICABLE. THE COPY FURNISHED TO DTIC CONTAINED A SIGNIFICANT NUMBER OF PAGES WHICH DO NOT REPRODUCE LEGIBLY.